Design and elaboration of anti-corrosion hybrid bio-sourced coatings for aircraft industries via EISA methodology

Gabriel Cardoso Gonçalves

THÈSE

UNIVERSITE DE PAU ET DES PAYS DE L'ADOUR

École doctorale des Sciences Exactes et leurs Applications

Présentée et soutenue le 16 décembre 2022

par **Gabriel CARDOSO GONÇALVES**

pour obtenir le grade de docteur
de l'Université de Pau et des Pays de l'Adour

Spécialité : Chimie-Physique

Design and elaboration of anti-corrosion hybrid bio-sourced coatings for aircraft industries via EISA methodology

MEMBRES DU JURY

RAPPORTEURS

• Jalel LABIDI	Professeur / Université du Pays Basque
• Marie France THEVENON	Dr. HDR / Unité de recherche BioWoodEB, CIRAD

EXAMINATEURS

• Corinne NARDIN	Professeure / Université de Pau et des Pays de l'Adour
• Renata ANTON SIMAO	Professeure / Université Fédérale de Rio de Janeiro

DIRECTEURS

• Fatima CHARRIER EL-BOUHTOURY	Maître de Conférences / Université de Pau et des Pays de l'Adour
• Jean-Charles DUPIN	Maître de Conférences / Université de Pau et des Pays de l'Adour
• Joachim ALLOUCHE **(Encadrant)**	Chargé de Recherche CNRS / Université de Pau et des Pays de l'Adour

UNIVERSITÉ DE PAU ET DES PAYS DE L'ADOUR

Acknowledgements

Firstly, I would like to thank Jalel Labidi, Marie-France Thevenon and Corinne Nardin for accepting to participate in the jury and to evaluate my thesis I would also like to make a special thanks to Renata Simão, who since my start in the Engineering school in 2012 have been helping and guiding me with and discussions, thanks a lot for your participation in the jury Renata.

A special thanks to Fatima Charrier and Joachim Allouche for have trusted and accepted me as their PhD student during these years, always giving me important information and helping to achieve the best result.

Jean-Charles Dupin, thank you for all this time as my thesis director. During the thesis, I was able to talk, get advice, and laugh with you many times. You were vital throughout these years, and I will never forget the counseling and discussions we had. As I have already told you personally, I hope very much to keep you as a friend. Thank you very much for everything, JC.

Thanks to all the team of the PCM that I had the chance to know and share these last 3 years and to all the other members of the other teams that I knew during my PhD and that could have helped me. Special thanks to Yann for all discussions and help during my period in the laboratory.

To the Barbek team, thank you very much for all the friendship inside and outside the lab. For sure, nothing would have been the same without our "soirées", barbecues, parties, festivals, and everything else we have been together. Matt, Ma, Marine, Manon, Laure, Parnian, Helo, Jojo, Matheus and all the others, you are awesome.

The “bureau” E020, the best office! Laure and Parnian, what can I say? I can not imagine my PhD without our conversations about the most random and bizarre subjects, people hiding behind the door, going to the dentist every day and everything else. I can easily write two other manuscripts just to summarize our history. Thank you, a lot, I will never forget it.

To my friends Matheus Gariglio and Giopatto, many thanks for everything! The parties and discussions were always amazing. Gariglio and Ma, we must travel together again, we have the best stories after! To my friends in Brazil that I had the chance to see in 2022 and for those that I could not see but that are always with me, you are the best. Thanks Biel, Aline, Vitor, Garcia, João and all the others.

Finally, my parents, you the most important thing in my life and I know that I can count on you. I have no words to describe how important you are for me and how you have been helping me to surpass all the hard moment. Thanks, I love you.

“When you want something, all the universe conspires in helping you to achieve it”

Paulo Coelho, The Alchemist

Summary

Abbreviations Table

At. Conc – Atomic Concentration

ATR – Attenuated Total Reflectance

BE – Binding Energy

CCC – Chromium conversion coatings

CVD - Chemical Vapor Deposition

DLS – Dynamic Light Scattering

DR – Direct Route

ECHA – European Chemicals Agency

EISA – Evaporation Induced Self-Assembly

IM – Intermetallic

IPCC – Intergovernmental Panel on Climate Change

IR - FTIR – Infrared Attenuated Total Reflection Spectroscopy

NDR – Non-Direct Route

PECVD - Plasma-Enhanced Chemical Vapor Deposition

REACH – Registration, Evaluation, Authorization and Restriction of Chemicals

RED – Relative Energy Difference

SEM – Scanning Electron Microscopy

Sq – Root main square height

SSSS – Supersaturated Solid Solution

TESPSA – 3-(triethoxysilyl)propylsuccinic

VOC – Volatile Organic Compounds

w.s. – Withdrawal speed

WCA – Water Contact Angle

XPS – X-ray photoelectron spectroscopy

General Introduction & Context

Context

Fossil fuels have been the engine of the industrialized world and its economy since the beginning of the industrial revolution. However, due to the ungoverned use during all these years, we are currently at a critical moment regarding these resources. The prospect of depletion of fossil reserves within fifty years and its direct connection with environmental issues, particularly global warming, requires the creation of new solutions based on the reduction of energy consumption, raw materials, and the development of new resources, new materials, and recycling techniques[1,2].

Recent studies by the Intergovernmental Panel on Climate Change (IPCC) have shown that the main source of CO_2 emissions comes from the burning of fossil fuels and industry. The IPCC warns that fossil fuel emissions must be halved within 10 years for global warming to be limited to 1.5°C above pre-industrial levels[3].

These numbers and new demands served to alert governments and industrial sectors of the need for new measures to protect the environment and people's health, and restrictions on products that, even if industrially consolidated, could be harmful in the medium/long term. One of these measures was the creation of the European agreement REACH (Registration, Evaluation, Authorization and Restriction of Chemicals) in 2006[4].

This legislation, signed by all European countries and administered by the European Chemicals Agency (ECHA), aims to increase the sustainable use of chemicals by banning hazardous ones until 2030. One of the direct objectives is then to encourage concerned actors to develop some alternatives that are less harmful to life and the environment. Among the targeted banned products are the Chrome VI based entities, the most common chemicals applied for the protection of aluminum alloys used in the aircraft industry[5,6].

Aluminum alloys are often one of the preferred materials for aerospace projects, since they fulfil the required properties and engineering demands, such as corrosion resistance properties and high mechanical strength capabilities. Compared to steel it is a lightweight option, and an ideal material for a wide range of aircraft components and aerospace applications. Indeed, Aluminum alloys combine good mechanical properties such as for example ductility, thermal conductivity and tensile strength with a low density, what it makes them extremely attractive for parts of an aircraft[7].

The Al 2000 series of alloys are a set of hard alloys widely used for the manufacture of structural parts of airplanes, such as the wing and engine support, as well as for the fuselage of the aircraft itself[8]. These aluminum-copper alloys, which include some of the highest strength heat treatable aluminum alloys, typically contain between 2 to 10% copper, with smaller additions of other elements (e.g. magnesium in Al2024). The copper provides substantial increase in strength and facilitates precipitation hardening. However, despite the good mechanical behavior, the presence of copper in these alloys reduces the ductility and corrosion resistance, and the application of a protective layer over the material becomes mandatory[9]. The susceptibility of these alloys to the phenomenon of solidification cracking is increased, consequently, some of these alloys can be the most challenging aluminum alloys to weld.

Chromium VI conversion layers (CCC), some extremely toxic products with genotoxic and carcinogenic effects[10], were for years applied as the main anti-corrosion solution in the aeronautics industry[11]. However, with the REACH agreement they will be permanently banned.

In this current context, the total investment in the aerospace coatings market has reached a sum of $1.7 billion by 2020[12] and an increased demand for new alternatives of metals and organic compounds is expected. Among new developments, inhibitor based on rare earth elements such as cerium[13], transition metals such as titanium and manganese[14], and even chromium III (Cr III)[15], a non-toxic species of Cr, are some of the options studied in the "metal field".

As an alternative to the "inorganic options", materials of biological origin are emerging as possible organic solutions, since when incorporated into inorganic protective systems[16]. They can confer interesting physicochemical properties (e.g. adhesion and hydrophobicity) and can even contribute to sustainable and eco-friendly anti-corrosion solutions[17,18].

As the second most abundant biopolymer on Earth, lignin is a promising candidate in the future vision of safe implemented component and can be extracted from a wide range of biomass resources that makes it a renewable feedstock. It has an important structural role in wood cells, providing mechanical stability against environmental stresses and allowing water transport inside the cell once it has a hydrophobic behavior[19]. Due to the enormous variety from which it can be obtained, lignin generally presents a heterogeneous molecular structure, varying its mass, bonding types and organic functions depending on the vegetable from which it will be obtained, and the type of purification and extraction performed[20]. Then, this molecular entity is generally not easy to include in high valued technologies.

Moreover, despite the rise of lignin market, that reached an amount of almost 611 million dollars in 2019, the biggest part of lignin production consists of low-purity materials[21] mainly used in the form of combustion for heat recovery, a low-value utilization. However, over the last few years, a part of ©Kraft type lignin, a kind of industrial lignin obtained from Kraft pulp, which accounts for about 85% of the total lignin production in the world, is directed to biochemicals and biomaterials[22,23]. Today, the emergence of these new demands for the lignin comes from new organizations such as The International Lignin Institute[25] that promotes the possibilities and interests of new high technological applications in which lignin plays a main role[26].

Research aim

The aeronautic industry is constantly striving to reduce the aircraft operating costs, increase their payload and reduce the environmental impact during the whole life of the product[27].

With the use of light alloys, such as aluminum, new applications have been discovered to rapidly improve existing designs. The disadvantage of using these materials is that they are particularly susceptible to corrosion. Environmental degradation is a limiting factor for aluminum alloys in outdoor applications. An effective way to protect alloys from rapid degradation or to reduce the rate of degradation is the preservation of the surface with an appropriate coating and pretreatment, in accordance with a sustainable philosophy.

In this context, the Nouvelle-Aquitaine Region (where is located the University of Pau and Pays de l'Adour), has created some innovation policies concerning the stimulation of a circular economy action plan[28] and by the technological valorization of some local resources (e.g., wood and its derivatives) in the context of sustainable management and new innovative technologies. The regional competitiveness hub, Xylofutur[29], for example, aims to catalyze the territory efforts and allow an effective synergy between the different actors of the ecosystem (research laboratory, technology transfer organizations, companies...), creating specific areas of action for the development of wood source fibers as a raw material for the paper industry, process panels or even bio-sourced complex systems, context in which this thesis is comprehended.

Some lignin-based materials (composites, films) have already been developed and tested. In the case of biofilms, some simple deposition techniques were investigated with varying degrees of success. Drop casting method, for instance, was proved inefficient for creating a mechanically stable coating under more severe conditions[30]. However, more versatile techniques in which parameters like temperature, relative humidity, deposition speed, among others, could be controlled have found a much more positive echo, significantly improving the coatings properties[31,32]. Among these alternatives, the dip coating has emerged as a good choice for combining the deposition method with other areas, such as the manufacture of hybrid systems, which require specific parameters to be formulated, but can be obtained in a "simple" way through these techniques.

The preparation of surfaces prior to bonding is another aspect of interest in metal protection, once it is also becoming progressively more constrained, due to environmental and health and safety legislation. In addition, as these pre-treatments use a considerable amount of time and energy, there is the necessity for more research to solve these issues and reduce overall process time.

The alloys protection against corrosion could even find help with the use of gas-phase processes (such as plasma) that starts on interesting aircraft industry for surface pre-treatment. Plasma pre-treatment offers significant cost and time savings, less energy consumption, application accuracy, no debris/dust generated during the process, and can be easily applied.

Objectives

This thesis work is part of this whole regional framework and was initiated with the E2S program of the University of Pau (UPPA) that tends to support the energy and environmental transition of local businesses and communities. The UPPA research teams are thus mobilized on issues related to energy and the environment. More specifically, the objective of the PhD work was to bring together two IPREM research skills (Surface treatments technology and Valorization of pine tree bio resources) for a common benefit, the development of new means of protection of Aluminum alloys from the territorial bio resources.

In this context, a series of Lignin-silica hybrid coatings covering an Al 2024 alloy substrate was fabricated by the dip-coating method through the EISA (Evaporation Induced Self-Assembly) strategy. EISA is a powerful chemical method that is widely used to design well-organized nanostructured hybrid and nanostructured materials[26]. Classically, the process, based on the self-assembly of organic and inorganic matters, leads to a nanoscale patterning of metal oxides by the structuring of organic mesophases originating from inorganic precursors in solution and triggered by the evaporation of solvents. Combining this approach with the dip coating process would allow the structure and the morphology of future hybrid coatings to be optimized by controlling experimental conditions such as the relative humidity and the deposition temperature[33].

Finally, the EISA method was used to fabricate some lignin-silica hybrid nanocomposites with a potential anti-corrosion purpose. Two synthetic routes were selected to fulfill these expectations with the prior functionalization of the substrate or a direct deposition onto the metal. Once coatings were designed, supplementary plasma treatments were tested in order to improve the hydrophobic properties and then to increase the protective barrier characteristics. A general illustrated synopsis :of the work is presented here below.

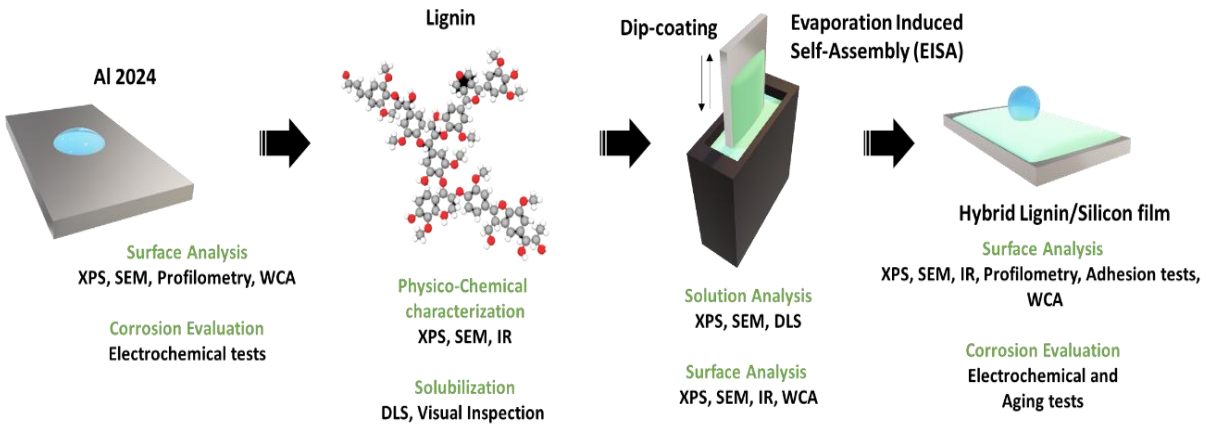

Scope of the work

The work of this thesis is presented in five chapters, which, in addition to the discussion of the results obtained, will present a bibliographical study and the methodology applied to the topics covered. The following chapters are going to be presented:

Chapter 1 - Raw materials and experimental procedure

This chapter describes the experimental methodology followed during this research, and the materials and equipment used are listed. A description of the topic under investigation is presented with a bibliographic focus about the materials studied in this work, (e.g. aluminum 2024 alloy, the lignocellulosic biomass their properties and applications, the sol-gel and Evaporation Induced Self-Assembly (EISA) methodologies. Some elements of these materials' characterization are discussed through a combination of several physicochemical techniques: XPS, FTIR, Ellipsometry and DLS measurement.

Chapter 2 - Hybrid Lignin/Silicon coatings elaboration

This chapter discusses the elaboration of lignin/silicon hybrid coatings over Al 2024 alloy. It focusses on the importance of pre-treating the metal surface with a molecular layer that will be an anchoring site for the hybrid coating. A systematic analysis of surfaces is reported to better understand wettability and adhesion properties measured for any developed coatings. Some coatings designs have been selected from this study.

Chapter 3 - Surface Modification of hybrid bio coatings by plasma

This part analyzes the possibility to improve the hydrophobicity character of lignin/silicon coatings in relation with the anti-corrosion expectation. A complete survey of the coatings surface is reported to value th impact of such a treatment and the wettability evolution is presented.

Chapter 4 - Ageing and Corrosion Tests of Lignin/Silicon hybrid coatings

First attempts of corrosion and UV exposure are reported in this chapter for the selected coatings. Both electrochemical measurements and salt fog experiment were done to assess the protective behavior of the coatings.

Chapter 5 - Conclusions

This chapter summarizes the findings of this investigation, highlighting the limitations of the material/technology under study and presents the perspectives to the work continuation.

Annexes

At the end of the dissertation, different appendices are included to deeply describe techniques of characterization.

References

1. Höök, M., & Tang, X. (2013). Depletion of fossil fuels and anthropogenic climate change—A review. Energy Policy, 52, 797–809. https://doi.org/https://doi.org/10.1016/j.enpol.2012.10.046
2. Galgani, P., Woltjer, G., Toorop, R. de A., & Ruiz, A. de G. (2021). Fossil fuel and other non-renewable material depletion (Issue December).
3. ClientEarth Communications. Fossil fuels and climate change: the facts. 2022 [Online]. Available: https://www.clientearth.org/latest/latest-updates/stories/fossil-fuels-and-climate-change-the-facts/.
4. Carneiro, E., Castro, J. D., Marques, S. M., Cavaleiro, A., & Carvalho, S. (2021). REACH regulation challenge: Development of alternative coatings to hexavalent chromium for minting applications. Surface and Coatings Technology, 418(May). https://doi.org/10.1016/j.surfcoat.2021.127271
5. European Chemicals Agency, Understanding REACH [Online]. Available: https://echa.europa.eu/regulations/reach/understanding-reach, 2016
6. Mandard, S. . L'Europe lance un plan d'interdiction massive de substances chimiques toxiques pour la santé et l'environnement. Le Monde (online), 2020, Available : https://www.lemonde.fr/planete/article/2022/04/25/l-europe-lance-un-plan-d-interdiction-assive-de-substances-chimiques-toxiques-pour-la-sante-et-l-environnement_6123596_3244.html
7. Sankaran, K. K.; Mishra, R. S. Chapter 4 - Aluminum Alloys; Sankaran, K. K., Mishra, R. S. B. T.-M. and D. of A. with H. M., Eds.; Elsevier, 2017; pp 57–176. https://doi.org/https://doi.org/10.1016/B978-0-12-812068-2.00004-7
8. Totten, G. E., Tiryakioğlu, M., & Kessler, O. (2018). Encyclopedia of Aluminum and Its Alloys (G. E. Totten, M. Tiryakioğlu, & O. Kessler (eds.)). CRC Press. https://doi.org/10.1201/9781351045636
9. Xiao, X., Zhou, Z., Liu, C., & Cao, L. (2022). Microstructure and Its Effect on the Intergranular Corrosion Properties of 2024-T3 Aluminum Alloy. Crystals, 12(3), 1–11. https://doi.org/10.3390/cryst12030395
10. Chromium (VI) Substance Inforcard, European Chemicals Agency ECHA (online), Available: https://echa.europa.eu/substance-information/-/substanceinfo/100.132.559
11. Carreira, A. F.; Pereira, A. M.; Vaz, E. P.; Cabral, A. M.; Ghidini, T.; Pigliaru, L.; Rohr, T. Alternative Corrosion Protection Pretreatments for Aluminum Alloys. J. Coatings Technol. Res. 2017, 14 (4), 879–892. https://doi.org/10.1007/s11998-017-9922-9
12. Market Report. Aerospace Coatings Market by Resin Type, Technology User Type, End Use Industry, Application - Global Opportunity Analysis and Industry Forecast, 2022 – 2030. 2022
13. Schuman, T. P. (2018). Protective coatings for aluminum alloys. Handbook of Environmental Degradation of Materials: Third Edition, 423–448. https://doi.org/10.1016/B978-0-323-52472-8.00021-6
14. Stoica, A. I.; Światowska, J.; Romaine, A.; Di Franco, F.; Qi, J.; Mercier, D.; Seyeux, A.; Zanna, S.; Marcus, P. Influence of Post-Treatment Time of Trivalent Chromium Protection Coating on Aluminium Alloy 2024-T3 on Improved Corrosion Resistance. Surf. Coatings Technol. 2019, 369, 186–197. https://doi.org/10.1016/j.surfcoat.2019.04.051

15. Liang, A., Li, Y., Liang, H., Ni, L., & Zhang, J. (2017). A favorable chromium coating electrodeposited from Cr(III) electrolyte reveals anti-wear performance similar to conventional hard chromium. Materials Letters, 189, 221–224. https://doi.org/10.1016/j.matlet.2016.12.022
16. Coquery, C.; Carosio, F.; Negrell, C.; Caussé, N.; Pébère, N.; David, G. New Bio-Based Phosphorylated Chitosan/Alginate Protective Coatings on Aluminum Alloy Obtained by the LbL Technique. Surfaces and Interfaces 2019, 16, 59–66. https://doi.org/10.1016/j.surfin.2019.04.010Sd
17. Dastpak, A.; Yliniemi, K.; Monteiro, M. C. de O.; Höhn, S.; Virtanen, S.; Lundström, M.; Wilson, B. P. From Waste to Valuable Resource: Lignin as a Sustainable Anti-Corrosion Coating. Coatings 2018, 8 (12). https://doi.org/10.3390/COATINGS8120454.
18. Dastpak, A.; Ansell, P.; Searle, J. R.; Lundström, M.; Wilson, B. P. Biopolymeric Anticorrosion Coatings from Cellulose Nanofibrils and Colloidal Lignin Particles. ACS Appl. Mater. Interfaces 2021, 13 (34), 41034–41045. https://doi.org/10.1021/ACSAMI.1C08274/SUPPL_FILE/AM1C08274_SI_001.PDF.
19. Vanholme, R.; Demedts, B.; Morreel, K.; Ralph, J.; Boerjan, W. Lignin Biosynthesis and Structure. Plant Physiol. 2010, 153 (3), 895–905. https://doi.org/10.1104/pp.110.155119. 0).
20. Bruijnincx, P., Gruter, G.-J., Westenbroek, A., & Engelen-Smeets, E. (2016). Lignin Valorisation - the importance of a full value chain Bruijnincx, P., Gruter, G.-J., Westenbroek, A., & Engelen-Smeets, E. (2016). Lignin Valorisation - the importance of a full value chain approach, (June), 22. http://www.dutchbiorefi.June,22.http://www.dutchbiorefinerycluster.nl/download/413/documenten/Lignin_valorisation_-_APC_June_2016.pdf
21. Kraft Lignin Market Research Report by Application (Binders And Resins, Pesticides And Fertilizers, and Thermoplastic Polymers), by Region (Americas, Asia-Pacific, and Europe, Middle East & Africa) - Global Forecast to 2026 - Cumulative Impact of COVID-19 https://www.researchandmarkets.com/reports/4905005/kraft-lignin-market-research-report-by
22. Chakar, F. S., & Ragauskas, A. J. (2004). Review of current and future softwood kraft lignin process chemistry. Industrial Crops and Products, 20(2), 131–141. https://doi.org/https://doi.org/10.1016/j.indcrop.2004.04.016
23. Siddiqui, H., Mahmood, N., Yuan, Z., Crapulli, F., Dessbesell, L., Rizkalla, A., Ray, A., & Xu, C. (Charles). (2017). Sustainable Bio-Based Phenol-Formaldehyde Resoles Using Hydrolytically Depolymerized Kraft Lignin. In Molecules (Vol. 22, Issue 11). https://doi.org/10.3390/molecules22111850
24. Wang, H., Pu, Y., Ragauskas, A., & Yang, B. (2019). From lignin to valuable products–strategies, challenges, and prospects. Bioresource Technology, 271(September), 449–461. https://doi.org/10.1016/j.biortech.2018.09.072
25. Abaecherli, A., Gosselink, R., de Jong, E., & Guran, B. (2004). A new starting point for powerful lignin promotion: Eurolignin and linked activities. Cellulose Chemistry and Technology, 38, 5–6.
26. Demuner, I. F., Colodette, J. L., Demuner, A. J., & Jardim, C. M. (2019). Biorefinery review: Wide-reaching products through kraft lignin. BioResources, 14(3), 7543–7581. https://doi.org/10.15376/biores.14.3.demuner
27. Martin, D., & Cruickshank, R. (2022). Ready for take-off : creating aviation ' s greener future.

28. EC. (2020). Circular Economy Action Plan. European Commission. Available: https://ec.europa.eu/environment/circular-economy/pdf/new_circular_economy_action_plan.pdf
29. Xylofutur. Plan d' action 2021. http://xylofutur.fr/
30. S.B. Lee, P. Luner, The wetting and interfacial properties of lignin, Tappi J. 55 (1), 1972, 16–21
31. Alwadani, N.; Ghavidel, N.; Fatehi, P. Surface and Interface Characteristics of Hydrophobic Lignin Derivatives in Solvents and Films. Colloids Surfaces A Physicochem. Eng. Asp. 2021, 609 (October 2020), 125656. https://doi.org/10.1016/j.colsurfa.2020.125656.
32. Li, J.; Wang, M.; She, D.; Zhao, Y. Structural Functionalization of Industrial Softwood Kraft Lignin for Simple Dip-Coating of Urea as Highly Efficient Nitrogen Fertilizer. Ind. Crops Prod. 2017, 109 (July), 255–265. https://doi.org/10.1016/j.indcrop.2017.08.011.
33. Grosso, D. How to Exploit the Full Potential of the Dip-Coating Process to Better Control Film Formation. J. Mater. Chem. 2011, 21 (43), 17033–17038. https://doi.org/10.1039/c1jm12837j.

Chapter I.

Raw materials and experimental procedure

Figure List

Table List

This chapter will cover the study of the raw componential materials exploited for the preparation of the hybrid lignin/silicon coatings. Initially, a state of art is developed, highlighting the most important theoretical points about the Aluminum, Al 2024 alloy. A detailed procedure of the metal surface preparation and the solutions synthesis (blending of lignin with silica network precursor) are given. The lignocellulosic biomass specificities and the extraction methods are even detailed as such finally the Evaporation Induced Self-Assembly method (a derivative from Sol-Gel) which has been adapted for the purpose of this work through an *in-situ* auto-assembly process.

In a second time, both the composition (XPS chemical analysis) and the morphology (SEM survey) of the ©Kraft lignin bio source material will be presented and compared to the relevant literature. Following, a study performed on the lignin solubilization stage will be indicated and discussed. The solubility level is verified by a visual inspection and then confirmed by a DLS analysis.

The Al 2024 alloy substrate is even fully described in term of: i) chemical composition, *via* XPS, with the highlight of the native Al_2O_3 oxide layer and its estimated thickness, ii) morphology through the microscopic observation (SEM) of the raw and the "chemically prepared" surface. A complementary optical profilometry observation has been carried out to quantify the initial roughness.

Finally, a first prospect of the EISA method to design lignin/silicon hybrid systems in a glass beaker is tested to anticipate the next morphologies expected when the EISA will be associated with dip-coating methodology onto the Al 2024 substrate.

1. State of the Art

1.1. Aluminum and the 2024 Aluminum Alloy

Discovered in 1825 by a Danish scientist called Christian Oersted, the commercially pure aluminum (Al) is a non-ferrous metal that is obtained from the alumina (Al_2O_3) reduction and along the years has been vastly used in the aircraft industry in the form of alloys[1].

The pure aluminum has one of the smallest densities among the metals with 2.7g /cm^3, what represents his main advantages when compared with other elements like iron (Fe) or cupper (Cu), with densities of 7.9 g/cm^3 and 8.9 g/cm^3 respectively. Other remarkable properties of the Al are the heat and electrical conductivity, high ductility and conformability[2]. But despite these good aspects, the pure aluminum does not present all required properties to fill the growing demands of the airspace industry[3], which could be observed in Table I-1. For instance, the elasticity modulus of the Al is around 70 GPa while copper and steel, also commonly present in aircraft fabrications, have elasticity modulus close to 110 GPa and 210 GPa respectively. Among other points, this explicits the necessity of the creation of alloys that could improve the mechanical needs[4].

Table I-1: Al requirements for the Aerospace Industry over the years. Adapted from Sankaran, K. K., Mishra, R.[3].

Time Frame	Principal Design Drivers
Pre-1930s	Static strength
1930s-1960s	Static strength, corrosion resistance, fatigue
1960-1970s	Static strength, corrosion resistance, stable elevated temperature properties, durability, damage tolerance, good properties in thick sections
1980s	All the above and dramatic weight savings
1990s	Static strength, corrosion resistance, durability, damage tolerance, good properties in thick sections, highly balanced properties, low manufacturing, acquisition and maintenance (ownership) costs, high level of safety
2000s-present	Above as for 1990s and amenability to revolutionary processing such as additive manufacturing
Future	Above plus breakthrough structural weight and cost savings, extended maintenance/inspection intervals, passenger comfort, green aerostructures

In this scenario, aluminum alloys were developed from the addition of hetero elements to the Al matrix often followed by a heat post treatment for the consolidation of various series of alloys containing intermetallic (IM) particles[5] responsible for the mechanical properties' enhancement.

The heat post treatment phase is generally performed into three important stages: the first consists in the formation of a monophase solution containing all components, then this solution goes through a rapid cooling until it forms a supersaturated solid solution (SSSS), and finally, this SSSS is submitted to a specific temperature ageing and the precipitates can be formed[6]. The formed intermetallic particles are classified into 3 groups according to Brooks, C. R.[7], depending on the built-up phase and on their size. The **Coarse Intermetallic Particles** vary in size from 1 to 30 micrometers and are formed during the solidification stage from the combination of alloying elements and impurities present in the alloy[8]. **Dispersoids** are between 20nm to 2µm big and have elevated fusion points[9]. The **Hardening precipitates** the smallest encountered particles (10-200nm) and generally stand at grain boundaries inducing material hardening[10].

In the scope of this work, the alloy 2024-T3 is a ternary Al-Cu-Mg series vastly used for fuselages and upper wing in airplanes structures due to its high resistance to cracks propagation and to fatigue[11]. The T3 mention in the alloy label refers to the temper code : solution is heat treated, cold worked, and naturally aged to a

substantially stable condition. Applies to products that are cold worked to improve strength, or in which the effect of cold work associated with flattening or straightening is recognized in applicable specifications[12]. The present alloy integrates the family of materials hardened by precipitation, being commercialized with a significant amount of magnesium and copper and minor presence of elements like Zn, Mn and Fe. Expected composition of 2024 alloy can be found in Table I-2 with elements amounts variation range according to suppliers.

Table I-2: Aluminum 2024 alloy commercial ranges composition. Data obtained at [13].

	Components								
	Al	Cu	Mg	Cr	Fe	Mn	Ti	Zn	Others
Wt. %	Matrix	3,8-4,9	1,2-1,8	≤ 0,1	≤ 0,5	0,3-0,9	≤ 0,15	≤ 0,25	≤ 0,15

The mechanical properties and hardening of this alloy will be defined by the presence (individual or simultaneous) of heterogeneous equilibrium phases, in which α(Al),θ(Al_2Cu) and S(Al_2CuMg) are the most relevant, but others like Al_6CuMg_4 and Al_3Mg_2 can also be presents in determinates ranges of temperatures[14,].

The commercial 2024-T3 alloy will be inserted in the α+ θ+ S zone, presenting the main intermetallic from these phases and dispersoids and precipitates that will also contain minor compounds, for instance Al_8Fe_2Si, Al_7CuFe_2 and Al_6MnFe_2, that will also contribute for the mechanical composition enhancement[15].

1.2. Lignocellulose Biomass

As defined by Houghton, R.A.[16], biomass can be described as "the mass of living organisms, including plants, animals, and microorganisms, or, from a biochemical perspective, cellulose, lignin, sugars, fats, and proteins. Biomass includes both the above- and belowground tissues of plants, for example, leaves, twigs, branches, boles, as well as roots of trees and rhizomes of grasses". Among all these kinds of biomass, those obtained from plants (specially from trees), are the most abundant representing around 70% of total.

Wood is one of the vital structural components of trees, being responsible for the circulation of fluids and nutrients that will be further used in the photosynthesis[17]. Wood is classified into two large groups called Gymnosperms (Softwood) and Dicotyledonous Angiosperms (Hardwood), varying from their cellular composition. In both groups, cellular walls are constituted of the so-called Lignocellulosic biomass, an assembly of Cellulose, Hemicellulose and Lignin that confers the final mechanical and physico-chemical properties of the wood[18,19].

These three biopolymers are found in different concentration according to the type of wood, the wall cell position and the extractive materials (e.g. tannin, resins, fatty acids...). The Figure I-1 below represents an overview of the wood cell wall composition.

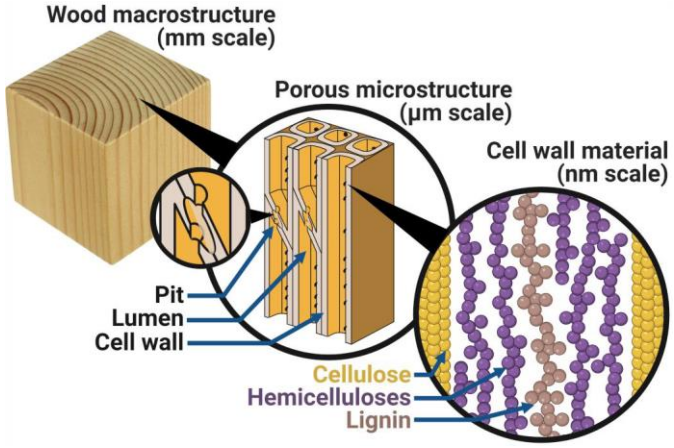

Figure I-1: Wood composition from the macro to the nanoscale. Obtained from Thybring, E.E. and Fredriksson, M.[20].

1.2.1. Cellulose

The most abundant biopolymer on Earth and principal compound of wood cellular wall, around 40-50% content (in relation of the total dried mass), is the cellulose. This mostly crystal homopolymer belongs to the polysaccharide family and generally forms by aligned linear chains settling the molecular formula of $(C_6H_{10}O_5)_m$. Molecular structure consists of more than 10000 repetitive units of D-glucose (specifically D-anhydroglucopyranose (AGU)) linked by so-called β (1-4) bonds. Each AGU groups possess 3 hydroxyl functions, in the repetitive block, justifying a reported hydrophilic character of the molecule[21] (Figure I-2).

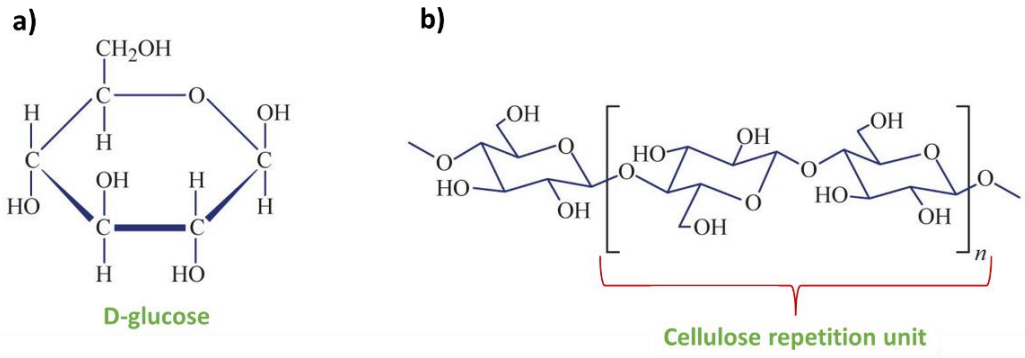

Figure I-2: a) Main forming unit from Cellulose molecule and b) Cellulose molecule model. Adapted from[22].

The cellulose molecules associate with each other by Van der Walls and hydrogen bonds, reaching a microfibrillar structures that can interact to form a crystalline cellulose fiber. The final polysaccharide shows important properties for its uses, the most important in the paper industry, such as degradability and chirality[23].

Because of the huge amount of free OH groups present in the cellulose macromolecule, its pseudo-crystalline arrangement can vary in terms of orientation, form, purity and size what will produce new forms of cellulose[24]. The polymorphism is listed in four different forms (Cellulose I, II, III or IV)[25] and will differ from each other through the way they are obtained (i.e. experimental temperature and pressure), and the crystalline like arrangement.

1.2.2. Hemicellulose

The hemicellulose, also called of heteropolysaccharide, is a polysaccharide that corresponds to 20-35% of total vegetal wall mass. It connects the cellulose and lignin, strengthening the cell wall[26].Differently of the cellulose, the amorphous structure is formed by short-small groups and a low molecular weight, resulted from a small polymerization degree among of 50-300 units of different types of polysaccharides (e.g., xyloglucan, xylans, mannans, glucomannans, and β-(1→3,1→4)-glucans) depending on the bio source[27].

Softwood hemicelluloses (normally labeled Galactoglucomannans) and hardwood hemicelluloses strongly differ from their molecular structure and weight deeply affecting their solubility and dispersion in various solvents[26, 28] .

Although they develop in the mutual environment, cellulose and hemicellulose have clear morphological and chemical differences. While cellulose is a linear homopolymer, with high molecular weight and huge chains, hemicellulose gets small chains with low molecular weight formed by different sugars[19]. In turn, its reactivity will be much higher than that of cellulose, due to the presence of substituent side groups and the presence of free OH along the chain[26]. Due to its relatively easy biodegradation, the hemicellulose has been used as an eco-friendly alternative to plastic packages and as energy source to replace some petroleum[29,30].

1.2.3. Lignin

Discovered in 1838 by Anselme Payen and studied in a fundamental way until 1940, when Peter Schulze identified its tridimensional structure, lignin is considered as the second renewable biopolymer plus abundant on Earth and one of the major contents of wood in association with cellulose and hemi-cellulose[31].

Present in medium lamella (ML) of wood cell walls, its content varies according to studied vegetal species, being around 24-33% in softwood and 19-28% in hardwood (both values in relation to dried weight). Besides the structural function in wall cell, once it acts like a cement for the walls and helps in the vascular system through the water and ions transport[32], this bio compound also provides mechanical resistance to compression and traction and act as a barrier against the attack of parasites[33].

The lignin morphology is a complex amorphous three-dimensional system, highly aromatic and with a diversity of bonds and chemical functions changing under the extraction source. Considering this compositional complexity,it is known that the final structure consists of the radical interaction of three phenolic monomers (called Monolignols): the p-coumaryl alcohol, the coniferyl alcohol and the sinapyl alcohol that once incorporated in the lignin respectively form p-hydroxyphenyl (H), guaiacyl (G) and syringyl (S)[34].

These three major constituents come from phenylalanine ammonia-lyase (PAL), which forms the monolignols after a sequence of enzymatic / addition reactions, such as methylation and hydroxylation[35].

Finally, the angiosperms family possess both G and S units, with some few traces of H when gymnosperms essentially have guaiacyl in their formation and a “more branched” arrangement[36]. Table I-3 below indicates the H, G and S content variation in both hardwood and softwood classes.

Table I-3: Monolignols content in Softwood and Hardwood families, readapted from Constant, S. et al.[36].

Unit	Gymnosperms ("Softwood")	Angiosperms ("Hardwood")
p-hydroxyphenyl (H)	0 – 1 %	50 – 75 %
Guaiacyl (G)	90 – 95 %	25 – 50 %
Syringyl (S)	0,5 – 3,4 %	Few Traces

1.2.3.1. Lignin Linkages

Lignin's biosynthesis route is known to be an endwise radical polymerization among monolignols. The following pathways are identified before the final structure obtention[37]:

a) **Radical Oxidation:** during this phase there is the radical species formation, resulting of a dehydrogenation process. This step is controlled by oxidative enzymes like laccase and peroxidases.
b) **Radical species stabilization:** free electron delocalization process occurs to stabilize formed structures.
c) **Species Bonding:** stabilized units formed during the second step will interact among then by different types of bonds (in different positions) resulting in a Dimer.
d) **Dimer Dehydrogenation (not mandatory):** previous formed dimer can be dehydrogenated once again and interact with a new phenol radical.

The bonds generated through this route exist in the form of two large groups: the carbon-carbon and the carbon-oxygen bonds. In addition, the following naming was adopted for each element: all carbons (C) of aromatic rings are numbered from 1 to 6 and C from aliphatic chains are labeled as alpha (C_α), beta (C_β) and gamma (C_γ)[37].

- **Condensed Bonds:** these units are in the form of carbon-carbon (C-C) bonds and have a higher resistance to degradation, requiring greater dissociative energies to be broken[38].
- **Ether Linkages:** bonds in the form of C-O-C linkages and most abundant in lignin's final molecule. Carbon Beta (C_β) higher reactivity allows an easy formation of aryl-ether bonds with a phenoxy oxygen[39].

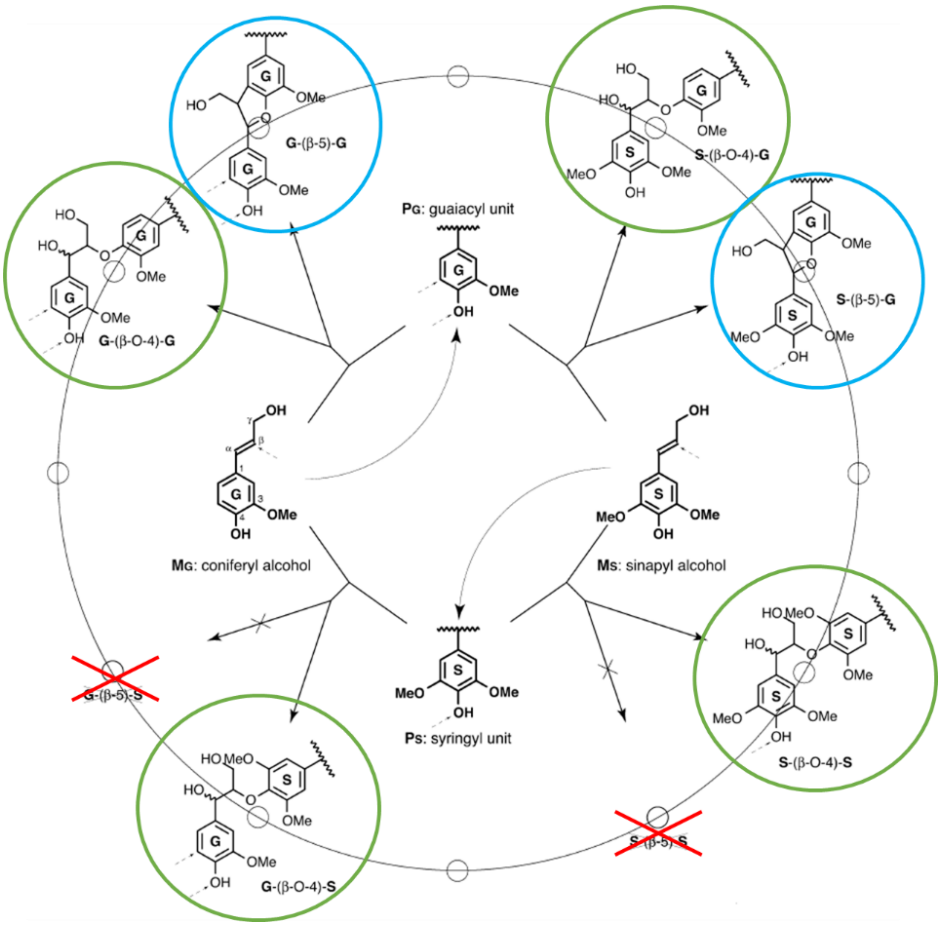

Figure I-3: H, G and S unit possible interaction and the resulting linkages. Extracted and adapted from Ralph, J. et al.[40].

As stated by Ralph, J. et al.[40], the β position is the most favorable for the units coupling increasing the amount of β-O-4, β-β and β-5 bond types in lignin molecule. Angiosperms, on the other hand, show less interactions of types β-5, 4-O-5' and 5-5' since the syringyl units do not have favorable pathways to create these types of links, as indicated in the diagram from Figure I-3.

The β-O-4 bond is the most important and abundant bonding type, representing between 40-60% of linkages totality, as indicated in Figure I-4 alongside all possible link types[41]. This majority comes from the different possibilities that these aryl ether unit can be formed once interactions between G-G, S-G and S-S created the unit. The lignin depolymerization/extraction process is initiated from the break of this bond.

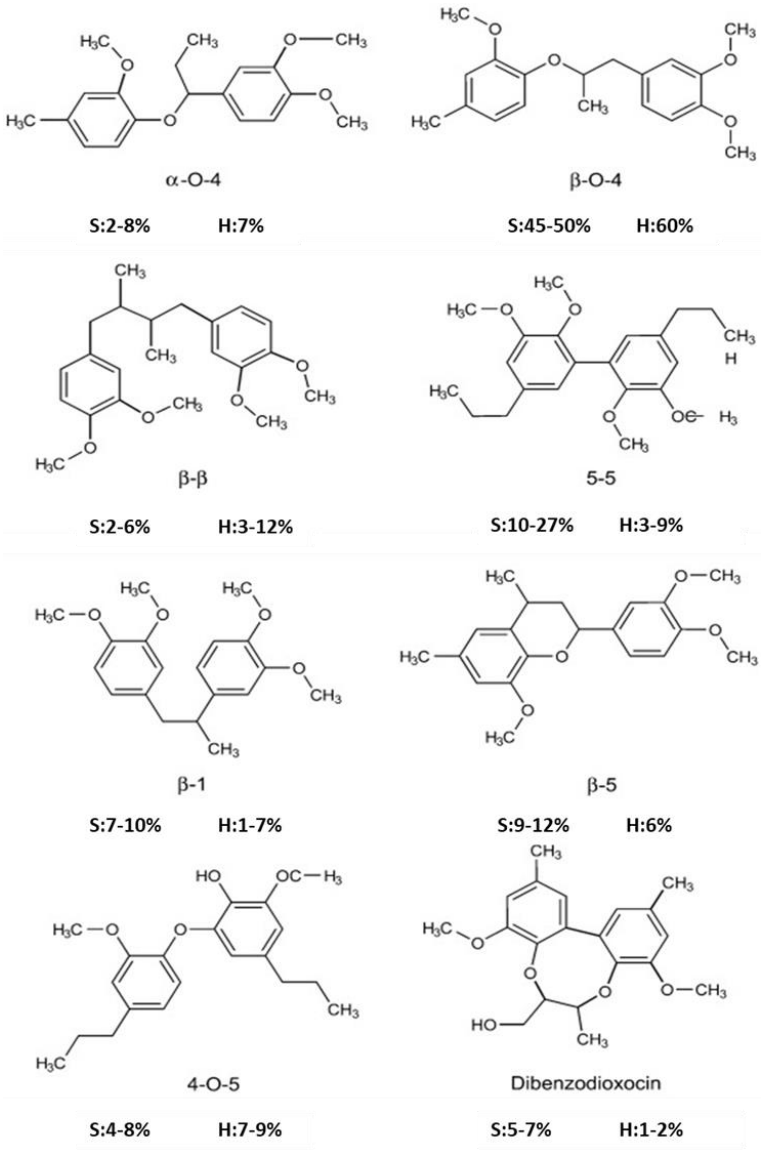

Figure I-4: Possible bond types present in the lignin molecule and their respective percentages in softwoods (S) and hardwoods (H). Adapted from[41].

In reason of the huge number of variables, it is not easy to really precise final lignin molecule nature. Therefore, in the next section, most usual extraction pathways will be presented in relation with some final possible molecules' properties and architectures.

1.2.3.2. Lignin Extraction Process

Two broad categories of lignin obtention are often indicated. The first group (1) comes from the lignin break down into soluble fragments, Kraft © and lignosulphonate methods belong to this group. The second (2) category consists in the selectively lignin hydrolysis with different solvents. The organosolv process is the most well-known of this group.

– Kraft © Process

The most common and industrial type of lignin, representing almost 80% of all production, is produced after a series of "Kraft Cooking" steps, in which wood chips are treated in a $NaOH/Na_2S$ alkaline solution at approximatively 170°C under pressure (between 6 bar - 10.5 bar) for 1-2 hours, generating a "White Liquor"[42].

This liquor then goes through a series of chemical reactions activated by ions (hydroxides and hydrosulfides) that starts on the delignification process. During this step, the chemical bonds are broken (mainly the β-aryl type) and consequently the structure of the lignin is altered, obtaining an increase of condensed bonds, phenolic groups formation and the implementation of sulfur (R-S-H groups). After these evolutions, the "white liquor" is enriched with approximately 40% lignin, hemicellulose and other wood components, and then progress towards the "Black Liquor"[42,43,44].

The final stage is lignin isolation from Black Liquor, a process based on the phase precipitation by the acidification of the medium from the action of sulphuric acid (H_2SO_4) or CO_2 and followed by filtration and washing steps [43,44]. The lignin obtained in this process will possess a high molecular weight and a moderate purity, (containing sulfur as main impurity - about 1.5% of the total content) and normally it would be soluble into water at a basic pH and in some organic solvents like THF and HMDSO[45].

– Lignosulphonate Process

Developed around 1930 to be used as plasticizer and dispersant[46], this kind of lignin gets a high molecular weight, an elevated impurity concentration (between 6-8% of sulfur in the final composition) and is soluble in water[47].

The chemical pathway, called "sulfite pulping", is based on the cleavage of α-O-4 bonds aiming a final molecule containing multiple chemical functions, like carbonyl and hydroxyl[48]. For this, the initial biomaterial is treated in an elevated temperature (between 140-170°C) in a solution containing some sulphate (HSO_3^-) and bi-sulphate (SO_3^{2-}) salts. Ester bonds in the lignin are broken and sulfur in the final molecule (sulphonation process)[49]. Finally, as in the kraft process, the sulfonated lignin is separated from the rest of the components through filtration.

Unlike the Kraft type that is classically burned as an energy source, *lignosulphonate* lignin has a particular use in low-tech[50]. This makes sulfonated lignin the largest market share of all lignin types, accounting for approximately 70% of the total market, according to a study by Global Market Insights in 2020 (mainly due to the oil & gas and concrete sectors)[51].

– Organosolv Process

Generally recognized by the low productivity and consequently small industrial usage, this process was created in between1980-1990 and results in the purest final product among all possible extractions, with no traces of sulfur and a composition closer from native lignin[52].

The extraction route consists of the separation of cellulose, hemicellulose and lignin via a solubilization process in an organic solvent (methanol, ethanol, organic acids and others)[53] or a mixture of organic solvent and

water in high temperature (around 200 °C). The obtained cellulose is digested through an enzymatic hydrolysis reaction and at the same moment hemicellulose is hydrolyzed. During this step, the most important reaction is the cleavage of alpha-aryl ether bonds present in the structure[54]. In sequence, hemicellulose is precipitated in ethanol and an extremely pure lignin is recovered.

Organosolv process is the "greener" way to recover lignin, causing less environmental impacts and it produces a material with low molecular mass with chemical functions abundancy[55]. The works of A. Xu et al.[56] and Sillero, L. et al.[57] , for instance, demonstrates and evaluates the possibility of the usage of bio-derived solvents (for organosolv lignin recovery).

The Table I-4 below shows a short comparison between the tree most important obtained lignin types in each process, concerning their molecular weight, purity and solubility.

Table I-4: Most important lignin types comparation, adapted from Rakotovelo, A. et al.[37] .

Property	Lignin Type		
	Kraft	Lignosulphonate	Organosolv
Molar Mass [g/mol]	2000 - 5000	20000 - 50000	Less than 2000
Dispersity	180	215 - 254	188
Sulfur Percentual [%]	1 - 1,5	4 - 8	0
Solubility	Alkaline water (pH>10) and some organic solvents (e.g. THF)	Water	Organic Solvents & Mixture Organic Solvent + Water

1.2.3.3. Lignin Applications

As mentioned in the previous topic, several types of lignin are present in the market, with specific characteristics for each application. Although it is not normally destined to applications of great intellectual value; recent studies, such as that of Han, Z. J. et al.[58] demonstrated the possibility of inserting lignosulphonate lignin in the manufacture of bio-foams, which requires the presence of sulfur during its synthesis.

Moreover, the organosolv lignin will present its main applications in laboratory studies due to its extremely high purity but unfortunately a low yield of production. This lignin is deeply discussed in the works of Parot, M. et al.[59], Bello, F. and Chimphango, A.[60], de Sousa Nascimento, L. et al.[61] and Qin, Z. et al.[62] in which the extreme purity of the chain allows the evaluation of extraction processes with new solvents. More recently, the organosolv lignin got more attention due to its incorporation in biofuels fabrication, increasing the interest of this material for future fine chemistry applications[63, 64].

Finally, the Kraft © lignin is the industrially most produced type, corresponding to about 80% of the lignin global production. Along years, the main use was as a source of heat and energy for the paper industry[65]. However, uses with associated high technological value have started to be developed over the last decade aiming to take advantage of the high carbon content and aromaticity of the molecule. Works, related to batteries[66], composites and nanocomposites[67,68] and even coatings, have been gaining prominence in the scientific community. As can be seen in the graph below (Figure I-5), the number of articles published since 2010 related Kraft © lignin and coatings has exponentially increased (x10 over 10 years).

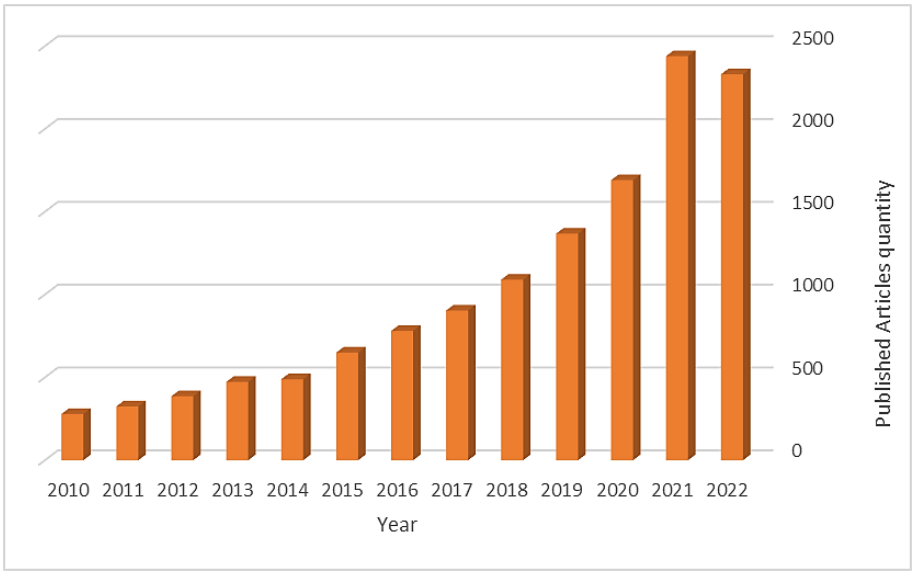

Figure I-5: Published articles correlation Kraft © lignin and Coatings. Obtained from Science Direct platform[69] .

When incorporated into anticorrosion systems, the valuable interest for Kraft © lignin appears equally pronounced, attesting of the recent innovative character of the bio resource (Figure I-6).

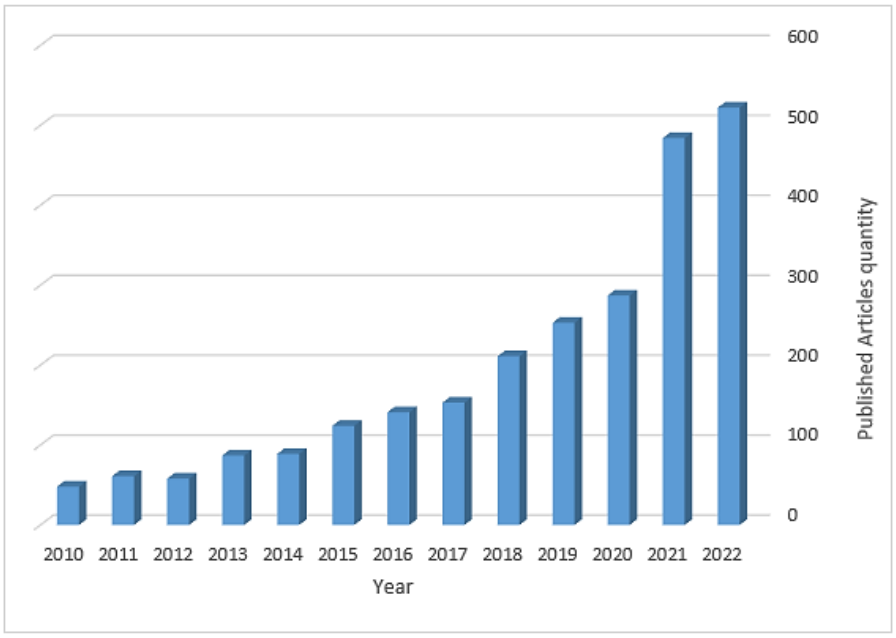

Figure I-6: Published articles correlation Kraft © lignin and anticorrosion coatings. Obtained from Science Direct Platform[70].

1.3. Sol-Gel

The history of sol-gel initially dates to the 1940s, when Geffcken and Bergen[71] managed to synthesize single oxide coatings by the sol-gel, but it was only 10 years later that some of these products started to be commercialized. Even later, around 1969, Dislich and Hinz[72] elaborated and published the chemical basis that proved that multicomponent oxides could be produced by this methodology. This caused a global boom in sol-gel processing approach, which was then seen as a new and quite easy way to produce homogeneous glass and ceramics at low temperatures compared to traditional melting and sintering processes.

However, the sol-gel fabrication of inorganic-organic hybrid materials was only proposed in the 80's due to the difficulty to make various phases interacting; from that period, it gained an attracted attention in various fields of materials technology, including electronics, chemistry, machinery, pharmaceuticals and medicine as reported in a very recent review[73].

Currently, the sol-gel keeps getting more industrial and scientific concern, once it is a greener alternative (so called "soft chemistry") to classical routes used for the development of anti-corrosion systems with less hazardous constraints. The sol-gel, associated with dip-coating deposition, fit in the green chemistry context to replace the conversion processes using hexavalent chromium[74,75]. The work of Huang, Y. et al.[76] highlights this possibility from sol-gel method aiming a green approach, once it shows the elaboration of possible anti-corrosive coatings on aluminum alloys, free of chrome and VOC.

1.3.1. Sol-Gel principles

The sol-gel process can be considered a wet-chemical methodology capable to create structured inorganic polymers or hybrid organic/inorganic materials that could be incorporated into fibers, coatings among others.

Briefly, the sol-gel process initiates with the hydrolysis of metal or silico-alkoxides precursors in colloidal solutions (gels) and a condensation step leads to the formation of colloidal clusters (micelles) that result in the formation of polymer chains with solvent trapped between them. Finally, the chains are washed and dried to eliminate the solvent and create xerogels or aerogels that can later be incorporated into other systems[77].

Deeply into the process, the whole sol-gel mechanism can be sequenced into different steps[78]:

a) Activation (hydrolysis) of the molecular precursor.
b) Polycondensation of the active species into micelles until the formation of a colloidal solution "sol".
c) Gelation "gel".
d) Aging.
e) Washing.
f) Dry.
g) Stabilization.

The two initial steps occur simultaneously. An alkoxide precursor with a main structure $M(OR)_x$, in which M is usually a metal or metalloid (silicon in this thesis) (and R is an alkyl group (C_nH_{2n+1}) is placed into water (or a

mixture of water and another solvent). The Hydrolysis sets up and alkyl groups are replaced with OH. Simultaneously and competitively, a condensation step occurs with the hydrolyzed active species and/or the initial precursor itself, creating an M-O-M network[79]. The following equations represent both hydrolysis and condensation process for a $Si(OR)_x$ precursor:

- **Hydrolysis** : $Si - OR + H2O \rightarrow Si - OH + ROH$ Equation I-1
- **Condensation** : $Si - OH + Si - OR \rightarrow Si - O - Si + ROH.$ Equation I-2

These reactions keep on happening repeatedly to gradually increase the amount of Si-O-Si bonds present in the solution until the system starts to act cooperatively with colloidal particles, which is called “sol”. The characteristics of the "sol" will vary according to factors such as pH, temperature, volume of precursor inserted among others[80].

After a period, called “gelation time”, the obtained colloidal particles grow enough to bond and create a 3D network able to elastically resist to mechanical stress. The created gel, made from the crosslinking of the particles and the spreading of the solvent between chains, presents a higher viscosity and a more solid aspect[78, 80].

So, the gel is left ageing (syneresis or weeping process)[81] and viscosity keeps o, increasing along time. Finally, the gel is washed to eliminate main part of impurities and dried. The drying step eliminates the solvent entrapped in the chains and allows the material solidification. Two main methods are related to the sol-gel drying:

- Xerogel: consists of a dry process in normal conditions, creating stronger gels but with a volume loss between 5 and 10 percent[82].
- Aerogel: drying in extreme conditions (in an autoclave) without volume loss, but more fragile[83].

The main advantage of sol-gels, when compared to other processes is the good capacity to create strong homogeneous layers from a vast range of precursors, leading to the combination of different properties in a single procedure.

1.3.2. Sol-Gel parameters influence

The physico-chemical route to obtain a sol-gel material depends on several factors that can influence the velocity, availability, and final morphological configuration.

The temperature plays a key role along the whole process, once its increase favors both condensation and hydrolysis reactions. During the aging phase, higher temperatures can speed the gel stiffness preventing a shrinkage process. Another role of the temperature is in the drying phase, which is shorter in higher temperatures[78,84,85].

The second important parameter to be considered is the pH once it can dislocate chemical reactions equilibrium to favorize the reaction products creation[86]. As can be observed in Figure I-7, the acid pH favors the hydrolysis phase, producing the so-called “Polymeric-Gel” and the basic pH induces the formation of more viscous “Colloidal-Gel”, made of highly branched particles.

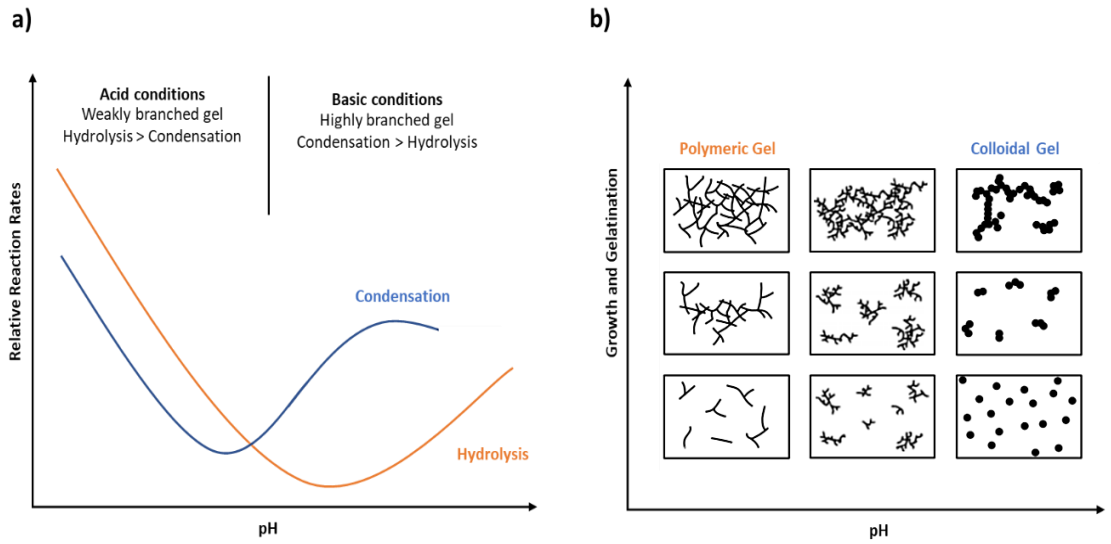

Figure I-7: Relation between the pH and the reaction rates (a) and the obtained morphology (b). Redrawn from Cushing, B.L. et al.[86].

The concentration of the precursors is selected according to the reactivity of the precursor chosen for the elaboration of a given material. The concentration within the "sol", is particularly important throughout condensation: the lower it is, the farther the molecules capable of binding are from each other, slowing down the reaction rate. This parameter was important for the processing of the present PhD work.

Finally, the last to be examined is the solvent nature. In the case of alkoxide precursors, which are immiscible or only slightly miscible with water, it is preferable to use alcohols (or other organic solvents) mixed with water, thus hydrogen bonds can be formed with H_2O. Usually, the solvent is chosen to have the same like carbon chain as the ligands in the alkoxide, avoiding the possibility of ligand exchange[86,87,88].

1.3.3. Sol-Gel deposition via EISA method

The EISA consists of a simple, fast and effective technique based on the controlling of the solvent evaporation rate in a way that the micellar concentration of the solution (that increases during the polycondensation phase) surpass the critical micellar concentration (CMC). Once it happens, the particles organize themselves as micelles and start to assume an auto-organized pattern[89].

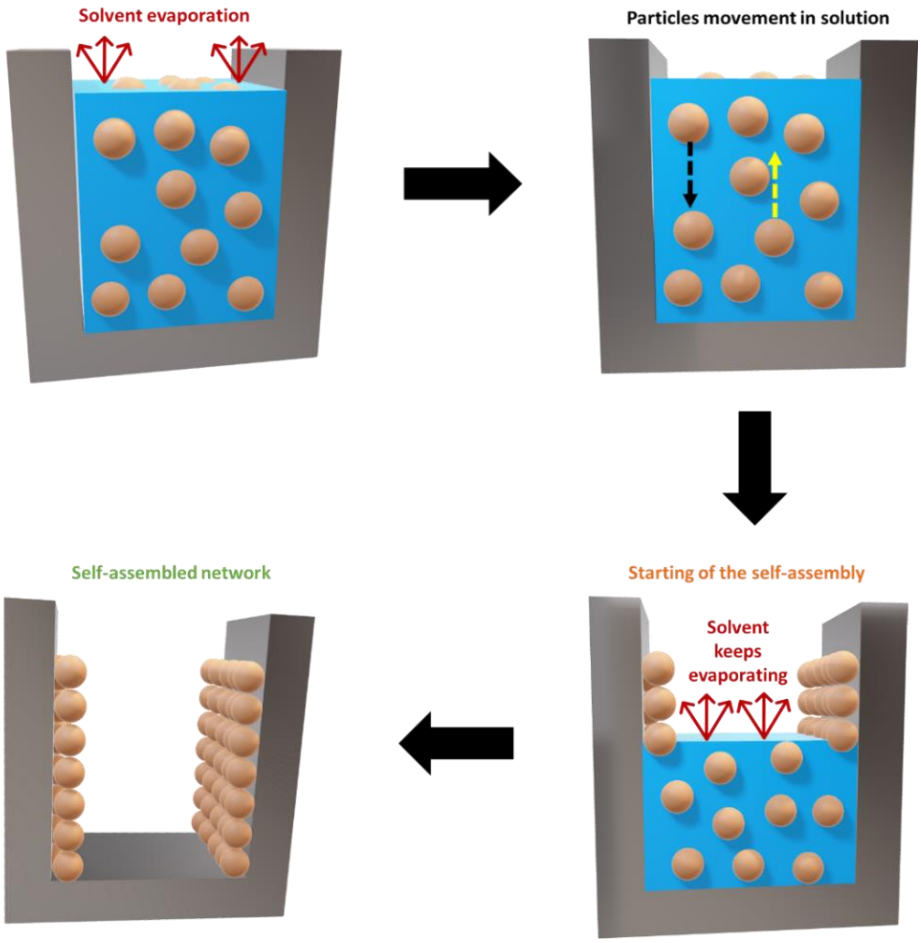

Figure I-8: EISA schematic representation. Based on Xu,X. and Li,L.[90].

In the schema of Figure I-8, the EISA process can be divided in the four main sequential stages[91]:

a) **Solvent Evaporation:** it should be the fastest possible, avoiding possible any phases separation.

b) **Relative Humidity equilibrium with the film:** during this phase, there is the equilibrium between the amounts of water entrapped inside the film with the atmospheric level of water. Like the first point, it should be the fastest possible.

c) **Mesophase stabilization:** it is the moment when the film stabilizes its morphology and composition in relation to the environment. During this moment, deposition parameters change (for instance RH variations) could deeply transform the created organization.

d) **Network stiffening:** the last point concerns the film stiffening, being promoted through thermal treatments or other methods that could modify the physical properties of the material.

Due to the versatility and speed of this methodology, it has been gradually incorporated into the field of biomass-based coatings, allowing the production of hybrid layers with desired properties.

In relation with the present work, the research of Cusola, O. et al.[92] deserves special emphasis due to the experimental and computational proof of the production capacity of lignin particles via EISA and its subsequent use as coatings. On the same terms, but with a more targeted approach to anticorrosive applications, the article

from de Haro, J.C. et al.[93], achieved the elaboration of an anti-corrosive hybrid coating on aluminum substrates from a pre-esterified lignin.

In this new research field for lignocellulosic biomass materials, we will present the effectiveness and reproducibility of this methodology (associated with dip-coating/EISA deposition) for future possible industrial perspectives of lignin-silicon coatings development.

2. Materials & Methods

2.1. Aluminum 2024: mechanical and chemical preparation

The Aluminum 2024, a common feature in aircraft industry applications, has been chosen as substrate in this work. Some rectangular alloy plates were provided by Goodfellow Cambridge Ltd. initially in the dimensions 300 mm x 300 mm x 1.60 mm, plates were then cut into the 3 dimensions for different prospects of the study: rectangles of 60 mm x 20 mm x 1.60mm used for the electrochemical salt spray test and ellipsometry evaluations, rectangles of 20 mm x 10 mm x 1.60mm used in all microscopy and spectroscopy analyses and disks of 5.5 mm diameter x 1.6mm thickness, which were used specifically for the electrochemical tests. The various samples panels are presented in Figure I-9 and the nominal composition given by the supplier is reported in the Table I-5 below.

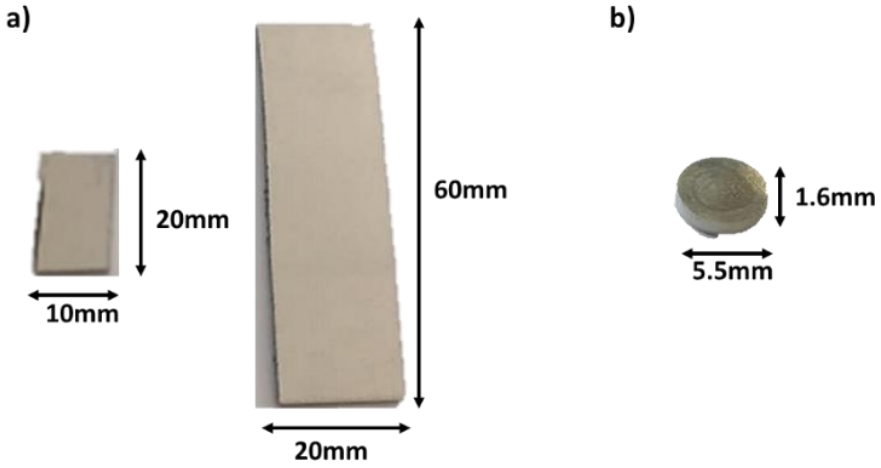

Figure I-9: Al 2024 after cut. A) rectangular form and b) disk geometry.

Table I-5: Nominal composition of the Al 2024 alloy, provided by Goodfellow Cambridge Ltd.

Element	Al	Cu	Mg	Mn
Weight Percentual (wt. %)	93.5	4.5	1.5	0.5

Once cut into appropriated dimensions, the plates were firstly subjected to a chemical cleaning supposed to remove surface rubbles and impurities coming from machining operations. This step of preparation even induces a subsequent surface hydroxylation and generally an increase of surface roughness. According to a procedure already experienced and optimized for metal alloys in the laboratory[94], the chemical attack consists in a sequential reaction of Acetone 99.5% (CAS: 67-64-1), Nitric Acid (HNO3) 65.0% (CAS: 7697-37-2) (both provided by Merck) and Sodium Hydroxide (NaOH) 97.0% (CAS: 1310-73-2) from PROLABO. The preparation route used in the present work concerns the following sequency:

a) **Organic degreasing:** immersion in acetone bath of the plate under sonication during 10 min at room temperature.
b) **Alkaline pickling:** immersion in a NaOH 2.5 M during 1min in a temperature of 45°C then rinsing thoroughly with demineralized water.
c) **Acid etching:** immersion in a HNO_3 1.6 M bath for 30 minutes at room temperature then rinsing thoroughly with demineralized water.
d) **Drying** under air flow.

2.2. Lignin solubilization test

The Kraft © lignin used was bought from UPM Biochemicals (UPM BiopivaTM 100 – CAS: 8068-05-01) with a nominal molecular weight of 5000g/mol. This model lignin was extracted from softwood and can be studied as a close replica of lignin coming from pine trees of the Nouvelle Aquitaine forest. For the solubility tests done in the first part of the work, a specific protocol was decided as followed:

a) Lignin was blended with the tested solvent in 10mg/ml amount.
b) A preliminary visual evaluation was done to get a first opinion.
c) The solution was then sonicated (frequency 50 KHz) during 10 min.
d) More solvent is added in the solution until the initial concentration is divided by 2.
e) A second visual evaluation was then performed.
f) The so diluted solution was once more sonicated during 10 min and then re-evaluated.
g) From the comparison of the different solutions observation, adequate solubility conditions were finally selected considering the most appropriated solvent.

During this phase, different solvents were evaluated : milli Q distilled water (pH 7), acetone 99.5% (CAS: 67-64-1), dimethyl sulfoxide 99.7% (CAS: 67-68-5) (DMSO), ethanol 99.9% (CAS: 64-17-5), methyl THF 99.0% (CAS: 96-47-9) (2-MTHF) and THF 99.9% (CAS: 109-99-9) (all bought from Merck). After the visual phase for the choice of solvent, a DLS analysis was performed to corroborate the first set of results. The conclusion of experiments reported the good efficiency of THF, and this point will be presented further in this chapter.

2.3. Hybrid Lignin/Silicon solution preparation

Two solutions were used in the research: - one containing Lignin and TEOS diluted in different concentrations in the selected solvent (Solution A – viscosity 1.5 mPa.s (Anton Paar MCR 302e Rheometer)), - the other only concerning the dilution of lignin (Solution B - viscosity 1.3 mPa.s) to better apprehend its behavior without the TEOS interaction.

In preparation, Kraft © lignin was solubilized in the solvent selected from the solubility test (see section 3.2). The solution was then acidified by Hydrochloric Acid (HCl) 37% (CAS: 7647-01-0) (Merck) and finally the inorganic source Tetraethyl orthosilicate (TEOS) 98% (CAS: 78-10-4) (Merck) was added. The detailed synthesis route used for the hybrid solution (Figure I-10) elaboration is the following:

a) 0.12g of the Kraft © lignin is solubilized in 23.60mL of THF in room temperature.
b) The mixture is then sonicated for 45 minutes (room temperature) for the complete solubility.
c) The obtained brown solution is left for cooling for 5 min in the fumehood.
d) The solution is acidified with the addition of 5.83 mL of 2M HCl (End of preparation for Solution B).
e) 0.97 mL of TEOS are finally added.
f) Left under stirring and aging 24h to provide a complete TEOS hydrolysis (End of preparation for Solution A).

A pre-study was carried out at the very beginning of this PhD work in order to value the EISA potential to promote a structured Lignin/Silicon material out of the "dip coating" process. To this end, the "selected" solution was left to dry in a beaker under the fumehood. Our starting point was adapted from the work of J. Wei et al.[95] in which a 3D highly ordered mesoporous silica is produced *via* the EISA method. The mass ratio among the products used is 1/175/50/7.5 for Lignin/THF/2M HCl/TEOS respectively and correspond to the following molar proportion: $1/8.6x10^{-5}/1.5x10^{-4}/5.8x10^{-3}$.

The resulting material is a consistent solid (no powdering aspect) as shown in Figure I-10.

Figure I-10: Hybrid Lignin/Silicon solubilized and after dry, forming a dark brown powder.

2.4. Techniques of characterization: some notions and important points

In this sub-topic, some notions and the most fundamental points are briefly detailed to allow the reader to understand the first results collected. The complete description and scientific background of those methods are reported in the thesis Appendix.

2.4.1. X-Ray Photoelectron Spectroscopy

X-ray photoelectron spectroscopy (XPS) is a quantitative and qualitative spectroscopic technique sensitive to extreme surfaces (10 nm maximum) that allows to determine the chemical state and the electronic structure of a material. This analysis is based on the irradiation of X-rays on a material, which will then eject an electron with a specific kinetic energy (KE). The law of conservation of energy (Equation I-3) will correlate the KE of the emitted photoelectron, the energy of the applied X-ray source and the binding energy of this same photoelectron[96].

$$h\nu + E_I^K(N) = E_I^K(N-1) + KE \qquad \text{Equation I-3}$$

$$BE = E_I^K(N-1) - E_I^K(N) = h\nu - KE \qquad \text{Equation I-4}$$

$E^k(N)$ is the energy of the initial neutral ground state system with N electrons and $E^k(N - 1)$ is the energy of the system in the final state, after ionization (ionized by N-1 electrons). Therefore, the measurement principle is based on determining the kinetic energy of the emitted photoelectrons to derive the binding energy (BE) for the chemical properties of the sample surface. The interest in determining the binding energy of an atom lies in the possibility to quantity and understand the chemical environment of that atom in relation to its neighbors.

XPS spectra appear as lines emerging from a continuous background due to inelastic collisions that some electrons undergo as they travel through the solid. The core peaks typically have binding energies between 30 and 1000 eV, representing extreme surface chemistry. The valence band (BE = 0 to 30 eV) is more representative of the sample volume. Each line is identified by its position on the energy scale[97]. A deeper explanation can be found in the Appendix – Topic 1.

2.4.2. Scanning Electron Microscopy (SEM)

The Scanning Electron Microscope (SEM) is an electron microscope that creates an image of a sample by scanning the surface with a focused electrons beam. Electrons interact with atoms in the sample and generate various signals that contain information about the topography and composition of the sample's surface. The sample surface is raster scanned and the position of the electron beam is combined with the intensity of the detected signal (emitted secondary electrons) to create the morphology image. The number of detectable secondary electrons, and thus the signal strength, depends on the topography of the sample and SEM observation can be achieved with a resolution around 1 nm[98]. The most detailed concept of this method and the experimental conditions are presented in Appendix– Topic 2.

2.4.3. Infrared Attenuated Total Reflection Spectroscopy (IR - ATR)

The principle of the infrared spectroscopy is based on the interaction between the infrared radiation and a molecule. The molecules will absorb the energy provided by the IR radiation and will start to vibrate in specific frequencies that are characteristic of their structure. Each vibration frequency will then correspond to a

determinate bond movement (e.g. symmetric and asymmetric stretching) possibly identified in the intensity *vs* vibration wavenumber.

The ATR mode is a variation of the methodology that allows the samples to be examined directly in the solid or liquid state without further preparation[99]. The developed explanation of the IR-ATR method and the experimental conditions are reported in Appendix – Topic 3.

2.4.4. Dynamic Light Scattering (DLS)

Dynamic Light Scattering (DLS) is one of the most popular light scattering techniques because it allows particle sizing down to 1 nm diameter. The technique is based on the use of a monochromatic beam, which is incident on a solution containing dispersed macromolecules. The light is then scattered in all directions, depending on the size and shape of the macromolecules. The intensity of the scattered light is analyzed in relation to time, which provides useful information about the molecular weight and radius of gyration of the macromolecules.

Another possible field to explore the DLS is the qualitative evaluation of a solution concentration/solubility, once for more concentrated solutions there will be a faster and higher intensity detected. On the other hand, for well dissolved mixtures, there will be almost no signal detection[100].

3. Results and Discussion

3.1. Kraft © Lignin: morphology and chemical composition

SEM images shown that the Kraft © lignin from UPM Biochemicals is organized as big dense non-uniform agglomerates structure (Figure I-11 a)). Once zoomed, these clusters appear constituted of micron sized spherical particles (Figure I-11 b)). This morphology was also identified in the works of Hararak, B. et al.[101] and Goliszek ,M. et al.[102], confirming this preferable arrangement adopted in Kraft © lignin organization.

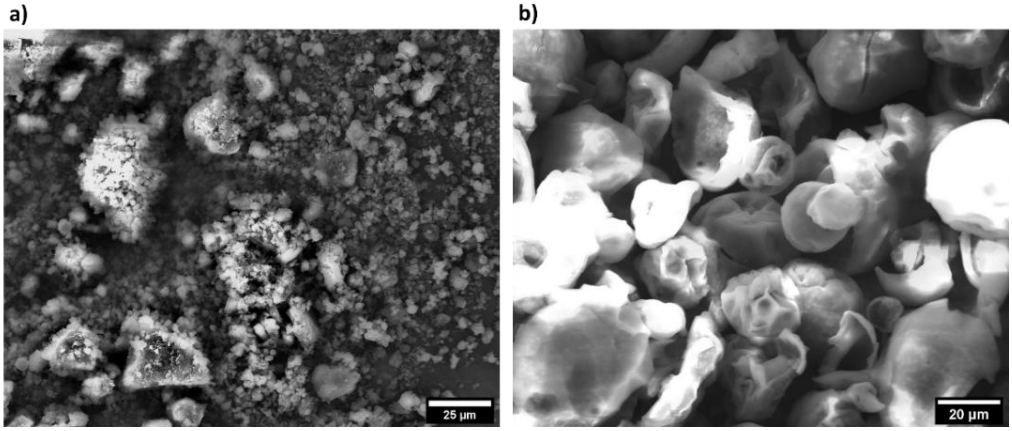

Figure I-11: SEM of Kraft © lignin morphology. a) big agglomerates constituted of smaller particles (x600) and b) higher magnification of these particles, showing the globular morphology (x750).

In summary, chemical composition of the Kraft © lignin determined with XPS data is presented in Figure I-12 a). In the general XPS spectrum, as expected for the Kraft type, some traces of sodium (1072.9 eV) and sulfur (S 2p around 165.0 eV and S 2s around 229.0 eV) seemed to be incorporated in the structure. This incorporation is reported in the literature[103,104,105] and is justified by the use of NaOH and Na_2S during the pulping extraction process in Chapter I -1.3.2). The sulfur exists in two chemical environments, thiol ($2p_{3/2}$ 164.5 eV and $2p_{1/2}$ 165.8 eV) and as sulfate ($2p_{3/2}$ 169.7 eV and $2p_{1/2}$ 170.8 eV)[106].

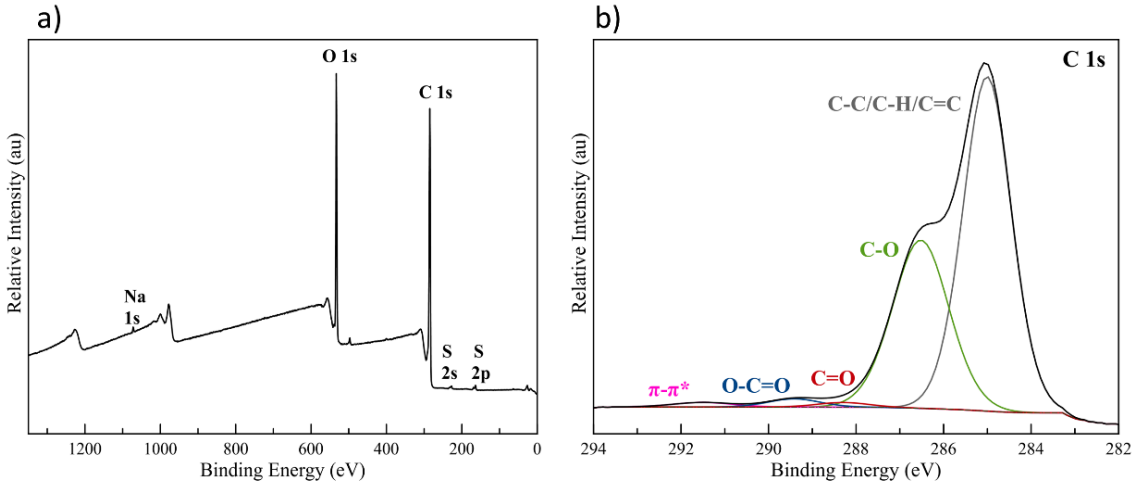

Figure I-12: Kraft © lignin general spectrum (a) and C 1s core level spectrum (b).

Most intense peaks in the XPS survey are associated with carbon and oxygen, representing almost 99% of the total composition (Table I-6). The chemical convolution of C1s peak (Figure I-12 b)) is a multiple with 4 different components which reflects the molecular intricacy. The main and most intense one refers to the aliphatic carbon, aromatic C=C and C-H bonds (285.0 eV). The C-O bond at 286.5 eV concerns 27.7% of the relative carbon composition. These two chemical environments constitute the main types of carbon in lignin, as demonstrated by Brazil T.R. et al.[107] and due to the β-O-4 bonding, the most abundant link in Kraft © lignin[108] .

The other two components identified are C=O and O-C=O bonds, at 288.3 eV and 289.4 eV respectively, just counting for 2% of the carbon amount. Finally, the last signal attribution refers to the π–π* transition at 291.5 eV in relation with the aromaticity of the structure.

Table I-6: XPS quantitative analysis of Kraft © lignin .

Core Peak	Kraft © lignin		
	BE (eV)	at. %	Total At. Conc (%)
C 1s	285.0	47.4	77.9
	286.5	27.7	
	288.3	0.7	
	289.4	1.3	
	291.5	0.8	
O 1s	532.9	3.5	20.8
	534.2	17.3	
N 1s	401.0	0.1	0.1
Na 1s	1072.9	0.3	0.3
S 2p	164.5	0.4	0.9
	165.8	0.2	
	169.7	0.2	
	170.8	0.1	

Corroborating the XPS results, ATR-FTIR study carried out presents the most important bands relate to lignin, Figure I-13. The aromatic groups, present in high quantity in lignin molecule, are identified in the bands at 1510 cm^{-1} and 1600 cm^{-1}. The guaiacyl structure, one of the main formation units, is identifiable at 1260 cm^{-1} as precisely discussed in the work of Nada, A.A.M.A. et al. [109]. The OH bonds stretching are marked at 3350 cm^{-1}, whereas stretching movement of methyl groups is identified at 2930 cm^{-1} and the C-H bonds stretching at 1030 cm^{-1} [110,111].

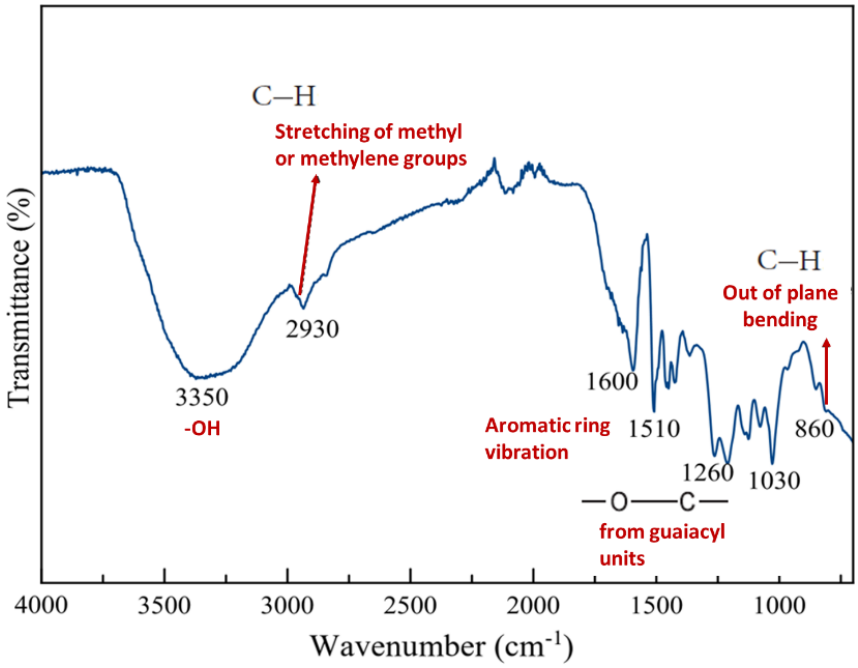

Figure I-13: ATR-FTIR spectrum of Kraft © lignin .

3.2. Lignin solubilization

Once the chemical and morphological identity of the Kraft © lignin was finalized, studies of best solvent selection in terms of lignin solubilization were carried out.

Visual evaluation of the solvents, indicated in Figure I-15, quickly showed that distilled water, acetone, ethanol and methyl-THF would not be able to dissolve the lignin efficiently, leaving many solid particles in suspension. This non soluble fractions aspect, in solvents like acetone and ethanol, had already been reported in some recent researches[112,113]. The poor capacity of these two solvents to solubilize lignin has also been highlighted in the abacus of the Hansen Sphere[114]. This theory, one of the most appropriate for the solubilization of lignin[115], reported that at room temperature, these solvents show high values of RED, the determinant parameter of Hansen theory[116],, which is the opposite trend of what is expected for good solvents (the closer to 0, the better the solubilization capacity of the solvent).

On the other hand, both THF and DMSO were extremely effective in solubilizing the lignin, with no apparent suspended particles and an apparent homogeneity. These results are also corroborated by a rich literature on the topic, with for instance research of Mattinen, M.-L. et al.[117] that used and Sadeghifar, H. and Ragauskas, A.[113] that attests the efficiency of same solvents. However, due to its faster evaporation compared to dimethyl sulfoxide, a major parameter in the EISA methodology, THF solvent was finally selected. The DLS analysis done in the THF with the solubilized lignin shown almost no laser deviation (no laser intensity changes during the experiment - Figure I-14, confirming the absence of big particles and then, corroborating the previous assumption. The results also indicated the presence of some nanometer size particles (about 95 ± 5 nm), what can be explain by the incapacity of the lignin to be one hundred percent dissolved due to its natural composition; however, these nanoparticles did not affect the coating elaboration, as it will be pointed out in the next chapters.

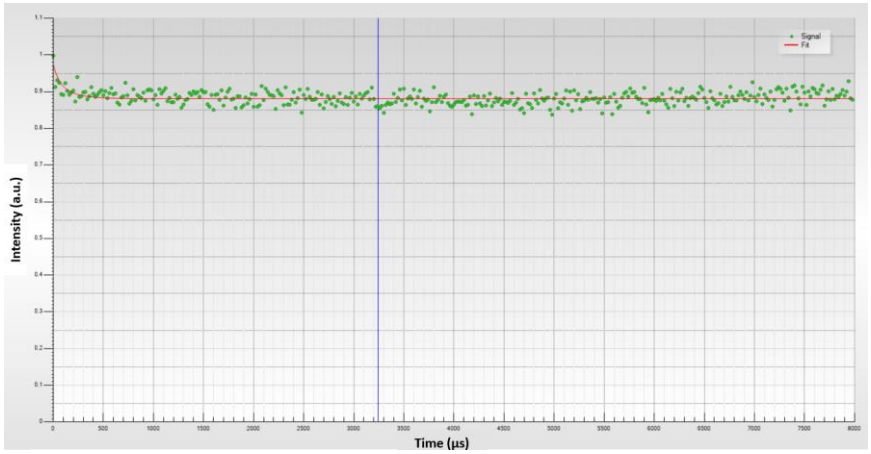

Figure I-14: DLS analysis of lignin solubilization in THF.

One surprising result was the non-solubility of lignin in methyl-THF (deliberately tested as it is considered as "green" solvent from renewable resources[118]), while tetrahydrofuran was very efficient. The work of Weidener, D. et al.[119] showed that it is able to dissolve lignin in 2-MTHF but under extremely specific conditions, such as the addition of CO_2 to the solution.

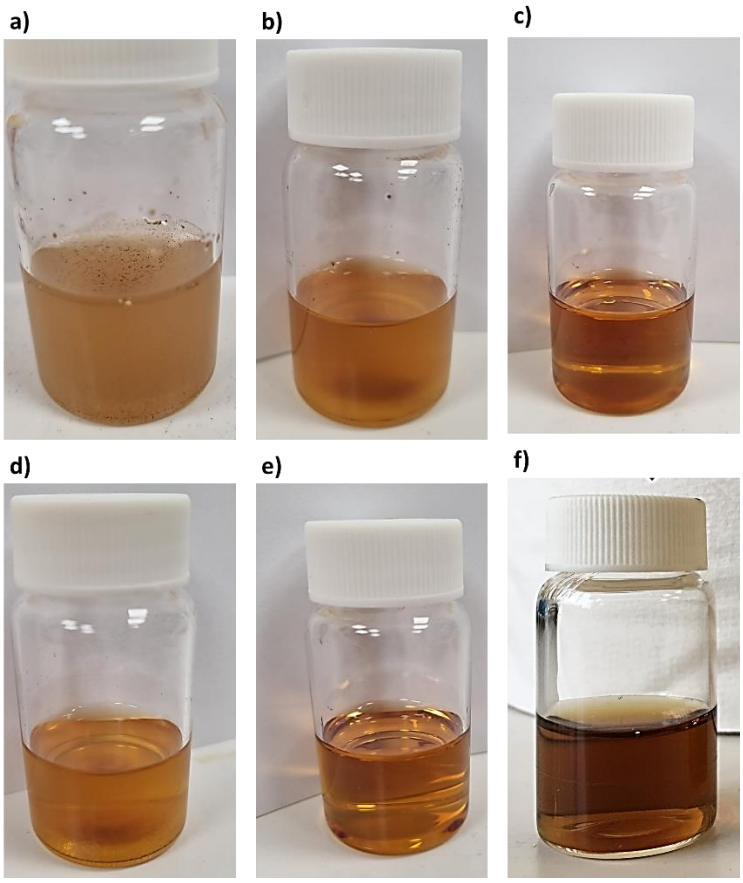

Figure I-15: Visual test evaluation to define the best solvent for the Kraft © lignin solubilization. Solvents: a) milli Q distilled water,b) Ethanol,c) Acetone,d) 2-MTHF,e) DMSO and f) THF.

3.3. Aluminum 2024: morphology and chemical composition before and after the surface preparation

The raw Al 2024 plates had their chemical composition identified by XPS before the surface cleaning stage. Results show the small presence of Si (0.4 %) and Zn (0.3 %) (Table I-7 and Figure I-16 a)) with peaks at respectively 102.8 eV (Si2p) and 1022.2 eV (Zn2p); these elements exist on surface despite they are not cited in the supplier nominal composition and are related to the 2024 alloy intermetallic (IM) particles constituents[120].

Table I-7: Al 2024 chemical composition as received.

Core Peak	Al 2024 alloy raw		
	BE (eV)	at.%	Total At. Conc (%)
Al 2p	73.1	0.6	9.0
	73.5	0.3	
	74.2	0.6	
	75.4	7.5	
C 1s	285.0	66.0	74.7
	286.3	5.4	
	287.9	1.2	
	289.1	2.1	
O 1s	532.2	14.1	14.1
Mg 2p	51.5	0.7	0.7
Si 2p	102.8	0.4	0.4
Na 1s	1072.0	0.4	0.4
N 1s	399.7	0.4	0.4
Zn 2p	1022.2	0.3	0.3

The small Al content (9.0%) is attributed to the surficial contamination of the sample specially related to the high amount of hydrocarbon species (74.7 %). However, the Al 2p signal is clear enough to discriminate 3 chemical environments (Figure I-16 b)): Al metal (Al°) at 73.1eV-73.5eV ($2p_{3/2-1/2}$ components), $Al(OH)_3$/AlO(OH) at 74.2 eV and Al_2O_3 at 75.4 eV[121,122]. For these last two Al surroundings, a single component is classically reported to traduce the expected $2p_{3/2-1/2}$ doublet as their width is bigger than Al° one and does not allow to differ $2p_{3/2}$ and ½ components.

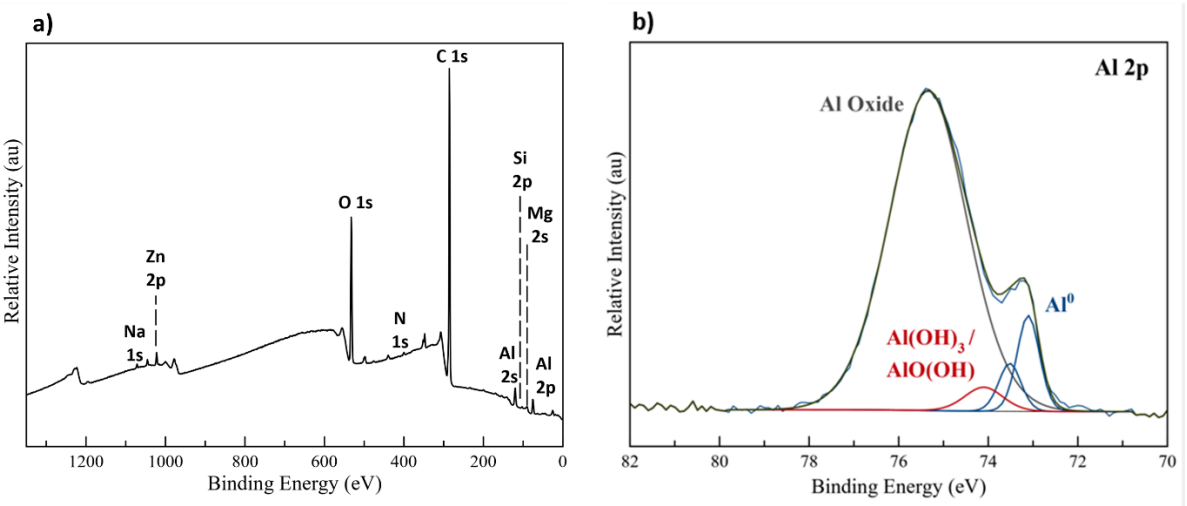

Figure I-16: General spectrum (a) and Al 2p core level spectrum (b) from Al 2024 as received.

As explained in Chapter I - Topic 1.1., the alumina layer (Al_2O_3) naturally grows up over the metallic surface, what explains the important content beyond 80% of total Al 2p content. From the XPS signal, the thickness of the alumina layer can be approximatively calculated (following the Equation 5 presented in Appendix) and is valued to 12.1 nm for the as received Al 2024 substrate. In the chemical composition, the presence of N and Na is related to surficial the impurities over the surface.

The scanning electron images of the surface demonstrated that before the surface preparation, the raw material surface does not present a lot of visible IM particles (Figure I-17 a)) even if the machining scratches are easily identifiable (Figure I-17 b)).

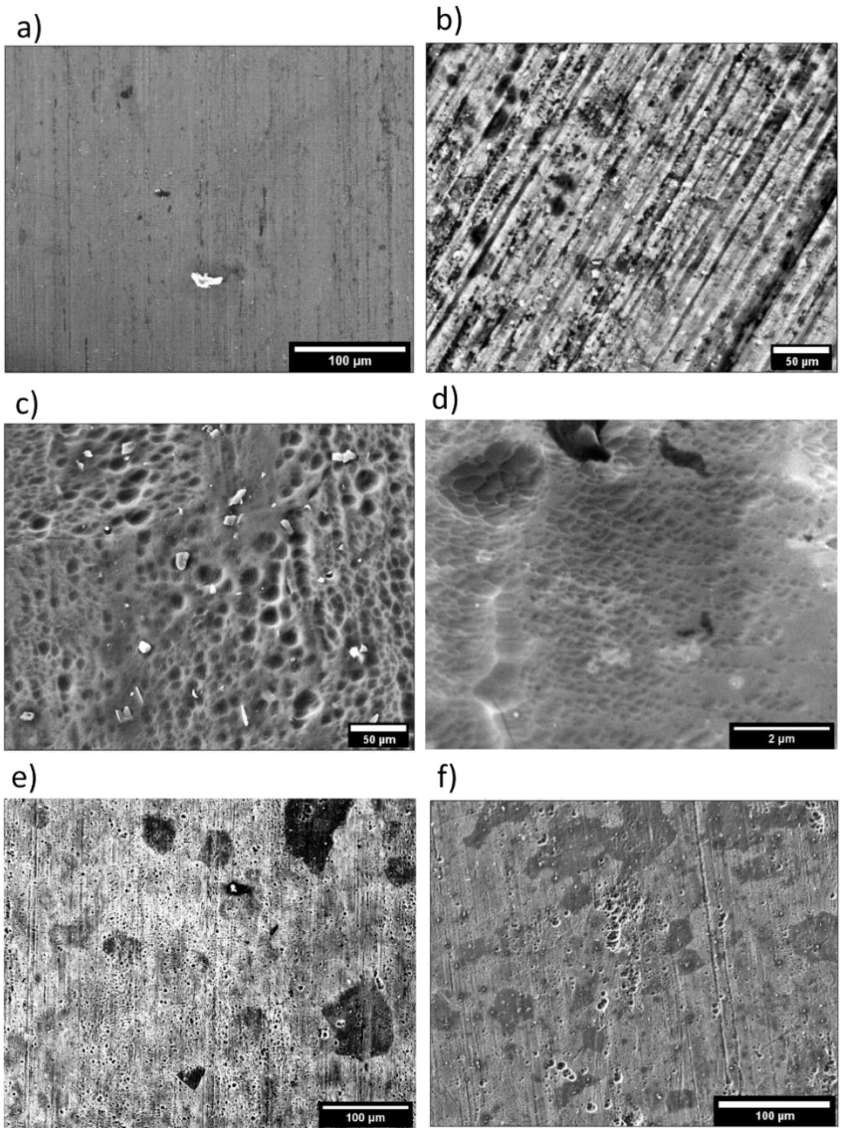

Figure I-17: SEM images from Al 2024 substrate: Raw material at a x300 (a) and x800 magnification (b) respectively, Raw material after preparation process at a x300 (c) and x16000 magnification (d), highlighting a clear roughness and at x250 (e) and x2000 (f) magnification, showing the grain boundaries observation.

After the surface preparation, SEM images evidence a typical rough surface (Figure I-17 c) and d)) and the identification of grain boundaries (Figure I-17 e) and f)). It was also verified the mitigation of the machining marks, previously found.

The chemical composition achieved with XPS has corroborated the SEM images and has confirmed the preparation process drastically reduced the carbon content at the same time it increased the Al signal (Figure I-18 a)). After the alkali and acid treatments, copper signals (Cu2p3/2 at 933.6 eV and Cu3p3/2 at 77.9 eV) began to appear in the XPS profile as expected for this major constituent of the Al 2024 family[123]. The copper enrichment is, as matter of fact, associated with the partial dissolution of the Al_2O_3 layer, exposing alloying elements that are present in small amounts.

The Al 2p component (Figure I-18 b)) is much more intense than before, representing 35.5 % of the total composition (Table I-8), with a still intense alumina component (75.4 eV). However, the Al_2O_3/Al2p ratio decreases slightly from 0.83 to 0.70 in relation with the partial release of the oxide layer. Both Al(OH)3/AlO(OH) at 74.5 eV and Al0 at 73.0 eV – 73.5 eV are now better visible anticipating the good scenario for a subsequent functionalization of the substrate[124]. The native oxide layer thickness calculation shows that the alumina layer was significantly reduced (around 40%) from 12.1 nm to 7.2 nm after surface treatment.

The strong carbon content reduction (more than 3 times, Table I-8) at 285.0 eV also justified the efficient surface "cleaning". On the contrary to the Cu, Mg and Zn elements almost completely disappeared from the surface composition (Table I-8) with removal of intermetallic particles such as ZnO and $Zn(OH)_2$[125]. Finally, the chlorine was also present as an impurity alongside nitrogen.

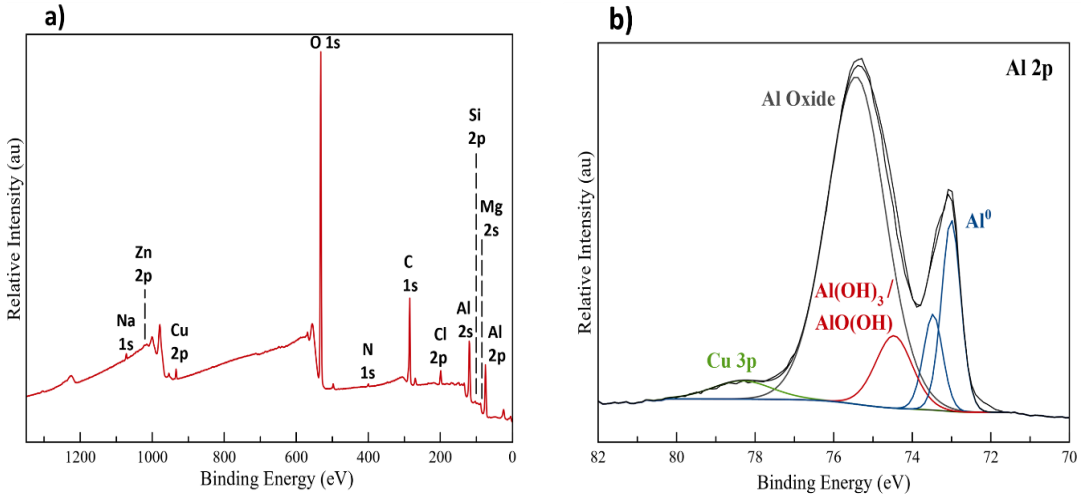

Figure I-18: XPS spectra of Al2024 after preparation: a) general survey and (b) Al 2p core level .

Table I-8: XPS quantification of raw Al 2024 and after chemical treatments.

Core Peak	Al 2024 alloy raw			Al 2024 alloy prepared		
	BE (eV)	at.%	Total At. Conc (%)	BE(eV)	at.%	Total At. Conc (%)
Al 2p	73.1	0.6	9.0	73.0	4.8	35.5
	73.5	0.3		73.5	2.4	
	74.2	0.6		74.3	3.5	
	75.4	7.5		75.4	24.8	
C 1s	285.0	66.0	74.7	285.0	17.8	22.8
	286.3	5.4		286.6	2.9	
	287.9	1.2		288.1	0.5	
	289.1	2.1		289.4	1.6	

O 1s	532.2	14.1	14.1	532.0	38.3	38.3
Mg 2p	51.5	0.7	0.7	-	-	-
Si 2p	102.8	0.4	0.4	104.3	0.9	0.9
Na 1s	1072.0	0.4	0.4	-	-	-
N 1s	399.7	0.4	0.4	400.2	0.5	0.5
Zn 2p	1022.2	0.3	0.3	1022.5	0.1	0.1
Cl 2p	-	-	-	199.1	1.3	1.9
				200.5	0.6	

As a last characterization of the Al2024 substrate, the wettability of the samples was evaluated by the WCA method (see Appendix). After the surface preparation, the test showed an extremely hydrophilic behavior, with an average angle of 28°. This is probably due to the surface hydroxylation, as hydroxyl groups have a high affinity for water, thus increasing the wettability of the material[126].

3.4. EISA dried solution: morphology and chemical composition

The lignin/silicon "sol", ready to be used in the dip-coating campaign, was firstly just dried according to the EISA methodology (topic 2.3 on this chapter). A pre-analysis of the hybrid morphology and of its chemical composition was done to anticipate the global hybrid aspect (morphology, homogeneity, phases observation, possible powdering…).

With SEM, the dried product unambiguously revealed a bi-phasic morphology, with a dense smooth matrix, certainly assigned to Si inorganic phase, and a nodular external layer partially wrapping the central matrix (Figure I-19 a) and b)). After a comparison with Kraft © lignin SEM analysis (Figure I-11), it is possible to consider that the aggregated globules of the nodular phases could correspond to lignin micro particles. These microscopic observations attest the association of lignin and silica phases into a bi-phasic composite arrangement that could make possible the combination of their own properties (mechanical and hydrophobicity) for an efficient protective coating.

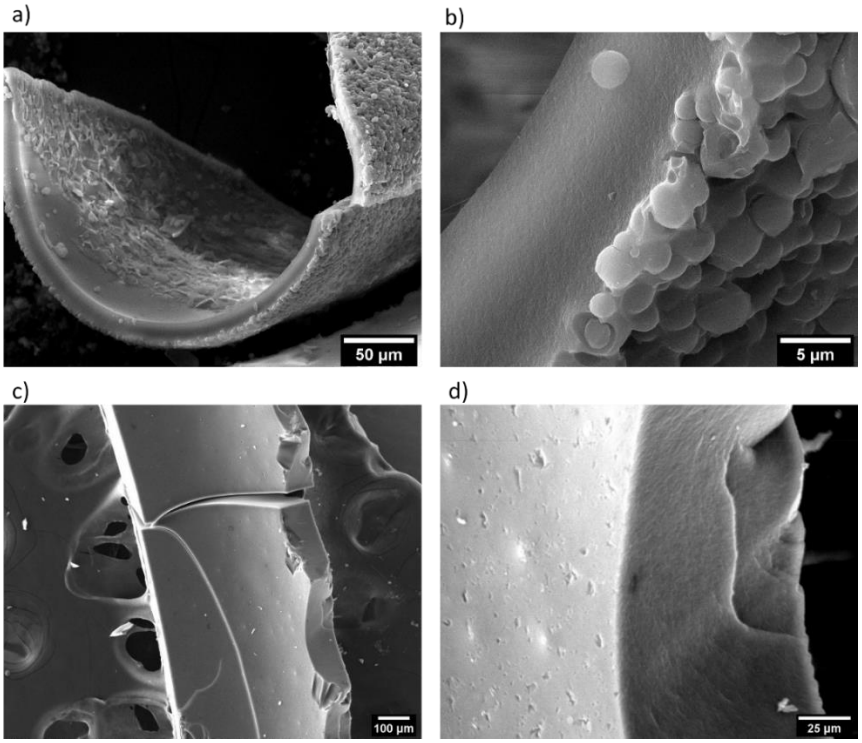

Figure I-19:SEM images of Lignin/Silicon hybrid: a) general overview, x400 magnification, b) Dense smooth matrix/nodules interface, x4000 magnification, c) after burning 2h at 600 °C, x90 and d) after burning 2h at 600 °C, x600 magnification.

To precise the nature of the identified phases, the lignin/silicon hybrid was burnt at 600°C for 2h in an air ambient oven (temperature ramp: 150°C/h). The previously brown material turned white and kept only the central dense morphology (Figure I-19 c) and d)). No more nodules were still visible.

The white color traduces the conversion of hydrolyzed-condensed (H-C) TEOS network into SiO_2 dense material with the heat treatment. As stated by Adam, M. et al.[127], during the progressive pyrolysis of lignin, the weak bonds firstly break at low temperature, and above 500 °C the carbon units disassembled releasing H_2 and other volatile molecules. On the other hand, TEOS-like networks are condensed under thermal treatment producing the appearance of a dense SiO_2 phase, but even of silanols ($Si(OH)_x$ and $SiH_x(OH)_y$) and some volatile products[128,129].

The XPS analysis confirmed both the presence of the organic and inorganic phases. The XPS general survey, for the dried hybrid (Figure I-20 a)), shows an intense C 1s orbital peak around 284.9 eV in accordance with to the presence of the Lignin (almost 60 at. %). The components of the C 1s core level spectrum (Figure I-20 b)) confirm the complex chemical composition of the biopolymer with several carbon chemical environments (C-C/C=C/C-H, C-O, C=O, O-C=O). A Si 2p core level peak appears at 104.0 eV corresponding to O-Si-O bonds, of silicon oxide[130].

Another key point is that Lignin/Silicon hybrid survey does not show the minor elements found into Kraft © lignin as sulfur and sodium for instance.

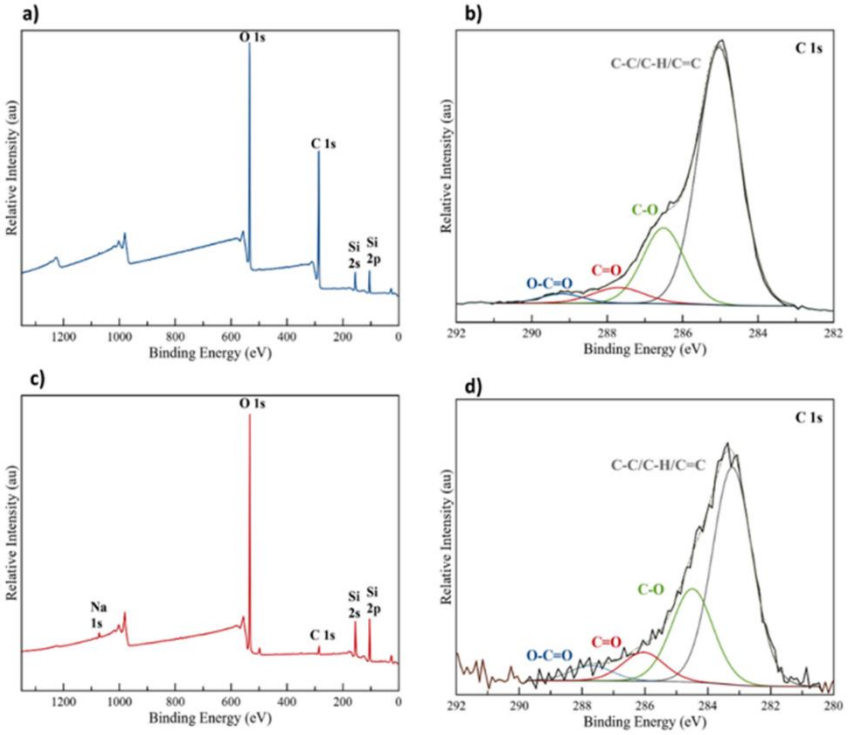

Figure I-20: XPS spectra of Lignin/Silicon hybrid: (a) general survey of dried material, (b) C1s core peak of dried material, (c) general survey of burnt material and (d) C1s core peak of burnt material.

After burning at 600°C, the Lignin/Silicon product general spectrum (Figure I-20 c)) shows that both O 1s and Si 2p signals are more intense (Table I-9) and the C 1s component drastically goes down, indicating the elimination of the organic part of the hybrid (lignin) (Figure I-20 d)).

Table I-9: XPS Quantitative data from Lignin/Silicon Hybrids before and after burning.

Core Peak	Lignin/Silicon hybrid			Lignin/Silicon hybrid after burning at 600°C		
	BE (eV)	at.%	Total At. Conc (%)	BE (eV)	at.%	Total At. Conc (%)
C 1s	285.0 286.5 288.0 289.4	41.5 13.6 2.7 1.4	59.2	284.9 286.1 287.4 289.2	3.8 1.6 0.6 0.3	6.3
O 1s	531.6 533.3 -	0.9 29.8 -	30.7	531.2 533.1 534.2	1.6 38.9 16.1	56.6
Si 2p	104.0	10.1	10.1	104.0	36.1	36.1
Na 1s	-	-	-	1072.1 1073.5	0.6 0.4	1.0
C/Si		5.9			0.2	

Despite the increase of silicon amount after calcination, the binding energy of the Si2p signal remains identical (Table I-9) confirming that the SiO_2 network originating from TEOS condensation sets up from the end of the EISA method. The evaporation method would then generate a dense inorganic matrix decorated with lignin micro particles.

Chapter Summary

This chapter presents and discusses the results for the reference materials of this thesis, the pure Kraft © lignin, aluminum alloy 2024 and the hybrid Lignin/Silicon obtained after the complete evaporation of the solvent. The chemical composition of the samples and their morphological aspect were verified. The most relevant points to be retained from these results are:

- SEM characterization of the pure Kraft © lignin has allowed the observation of a particular morphology in its organization, with large and dense agglomerates that, when further investigated, reveal to be composed of micrometric globules of lignin.
- The chemical analysis carried out by XPS confirmed the presence of mostly carbon and oxygen in its chemical composition, with traces of impurities remaining from the extraction processes, what has already been reported in the literature.
- Kraft © lignin solubilization was inefficient in distilled water, acetone, ethanol and me-THF.
- THF was the solvent most capable to combine an efficient dissolution of the lignin, forming a homogeneous solution, and a good evaporation rate, essential character for the EISA methodology that will be applied. It was then selected for the continuation of the work.
- The raw Al 2024alloy presented mostly residual carbon on surface, indicating a high degree of contamination, which was readily confirmed by SEM images.
- On the other hand, after the preparation, , a great roughness is created simultaneously to the removal of impurities and the reduction of the alumina layer, confirming the efficiency of the chemical treatments for the subsequent steps.
- Screening of the Lignin/Silicon hybrid solution morphology left to dry) has shown a self-organization into an organic/organic bilayer. It is now expected to find at least a similar organization after fabrication of the coating on the Al 2024 substrate.

References

1. Mondolfo, L. F. (1976). Composition. In *Aluminum Alloys* (pp. 3–10). Elsevier. https://doi.org/10.1016/B978-0-408-70932-3.50007-3
2. Totten, G. E., Tiryakioğlu, M., & Kessler, O. (2018). *Encyclopedia of Aluminum and Its Alloys*). CRC Press. https://doi.org/10.1201/9781351045636
3. Sankaran, K. K., & Mishra, R. S. (2017). *Chapter 4 - Aluminum Alloys* (K. K. Sankaran & R. S. B. T.-M. and D. of A. with H. M. Mishra (eds.); pp. 57–176). Elsevier. https://doi.org/https://doi.org/10.1016/B978-0-12-812068-2.00004-7
4. ASM International Handbook Committee. (1990). Properties and Selection: Nonferrous Alloys and Special-Purpose Materials. In *European Journal of Pediatrics* (Vol. 2). ASM International. https://doi.org/10.31399/asm.hb.v02.9781627081627
5. Davis, J. R. (2001). *Alloying* (J. R. Davis (ed.)). ASM International. https://doi.org/10.31399/asm.tb.aub.9781627082976
6. Andersen, S. J., Marioara, C. D., Friis, J., Wenner, S., & Holmestad, R. (2018). Precipitates in aluminium alloys. *Advances in Physics: X*, *3*(1), 790–814. https://doi.org/10.1080/23746149.2018.1479984
7. Brooks, C. R. (1982). Heat Treatment: Structure and Properties of Nonferrous Alloys. Asm Intl.
8. Blanc, C., Freulon, A., Lafont, M. C., Kihn, Y., & Mankowski, G. (2006). Modelling the corrosion behaviour of Al2CuMg coarse particles in copper-rich aluminium alloys. *Corrosion Science*, *48*(11), 3838–3851. https://doi.org/10.1016/j.corsci.2006.01.012
9. Parvizi, R., Marceau, R. K. W., Hughes, A. E., Tan, M. Y., & Forsyth, M. (2014). Atom Probe Tomography Study of the Nanoscale Heterostructure around an Al20Mn3Cu2 Dispersoid in Aluminum Alloy 2024. *Langmuir*, *30*(49), 14817–14823. https://doi.org/10.1021/la503418u
10. Cochard, A., Zhu, K., Joulié, S., Douin, J., Huez, J., Robbiola, L., Sciau, P., & Brunet, M. (2017). Natural aging on Al-Cu-Mg structural hardening alloys – Investigation of two historical duralumins for aeronautics. *Materials Science and Engineering A*, *690*, 259–269. https://doi.org/10.1016/j.msea.2017.03.003
11. Liu, J., & Kulak, M. (2000). New paradigm in the design of aluminum alloys for aerospace applications. *Materials Science Forum*, *331*, 127–141. https://doi.org/10.4028/www.scientific.net/msf.331-337.127
12. Systems, T. D., & Cayless, R. B. C. (2013). Alloy and Temper Designation Systems for Aluminum and Aluminum Alloys. 9–22. https://doi.org/10.1361/iaat2000p009
13. ASM Aerospace Specification Metals, Inc. Subcategory: 2000 Series Aluminum Alloy; Aluminum Alloy; Metal; Nonferrous Metal [Online]. Available: https://asm.matweb.com/search/SpecificMaterial.asp?bassnum=ma2024t4.
14. DeRose, J. A., Bałkowiec, A., Michalski, J., Suter, T., Kurzydlowski, K. J., & Schmutz, P. (2012). Microscopic and Macroscopic Characterisation of an Aerospace Aluminium Alloy (AA2024). 6, 23–38. https://doi.org/10.2495/978-1-84564-752-0/03

15. Huda, Z., Taib, N. I., & Zaharinie, T. (2009). Characterization of 2024-T3: An aerospace aluminum alloy. *Materials Chemistry and Physics*, *113*(2–3), 515–517. https://doi.org/10.1016/j.matchemphys.2008.09.050
16. Houghton, R. A., & Hole, W. (2008). Biomass. In S. E. Jørgensen & B. D. B. T.-E. of E. Fath (Eds.), *Encyclopedia of Ecology* (Issue 1990, pp. 448–453). Academic Press. https://doi.org/https://doi.org/10.1016/B978-008045405-4.00462-6
17. B Thibaut, J. G. and B. C. (2001). Wood Growth and Development. *Elsevier*, 96–105.
18. Niaounakis, M. (2013). 1 - Introduction to Biopolymers. In M. B. T.-B. R. Niaounakis Recycling, and Disposal (Ed.), *Plastics Design Library* (pp. 1–75). William Andrew Publishing. https://doi.org/https://doi.org/10.1016/B978-1-4557-3145-9.00001-4
19. Patachia, S., & Croitoru, C. (2016). Biopolymers for wood preservation. In *Biopolymers and Biotech Admixtures for Eco-Efficient Construction Materials*. Elsevier Ltd. https://doi.org/10.1016/B978-0-08-100214-8.00014-2
20. Thybring, E., & Fredriksson, M. (2021). Wood Modification as a Tool to Understand Moisture in Wood. *Forests*, *12*, 372. https://doi.org/10.3390/f12030372
21. Pérez, J., Muñoz-Dorado, J., De La Rubia, T., & Martínez, J. (2002). Biodegradation and biological treatments of cellulose, hemicellulose and lignin: An overview. *International Microbiology*, *5*(2), 53–63. https://doi.org/10.1007/s10123-002-0062-3
22. Britannica, T. Editors of Encyclopaedia. "cellulose." Encyclopedia Britannica, September 20, 2022. https://www.britannica.com/science/cellulose.
23. Klemm, D., Heublein, B., Fink, H. P., & Bohn, A. (2005). Cellulose: Fascinating biopolymer and sustainable raw material. *Angewandte Chemie - International Edition*, *44*(22), 3358–3393. https://doi.org/10.1002/anie.200460587
24. Kumar Gupta, P., Sai Raghunath, S., Venkatesh Prasanna, D., Venkat, P., Shree, V., Chithananthan, C., Choudhary, S., Surender, K., & Geetha, K. (2019). An Update on Overview of Cellulose, Its Structure and Applications. *Cellulose*, 1–21. https://doi.org/10.5772/intechopen.84727
25. Pérez, S., & Samain, D. (2010). Structure and Engineering of Celluloses. In *Advances in Carbohydrate Chemistry and Biochemistry* (Vol. 64, Issue C). https://doi.org/10.1016/S0065-2318(10)64003-6
26. Scheller, H. V., & Ulvskov, P. (2010). Hemicelluloses. *Annual Review of Plant Biology*, *61*(1), 263–289. https://doi.org/10.1146/annurev-arplant-042809-112315
27. Balli, B., Calimli, M. H., Kuyuldar, E., & Sen, F. (2019). Synthesis, characterization, and applications of hemicellulose based eco-friendly polymer composites. *Sustainable Polymer Composites and Nanocomposites*, 293–311. https://doi.org/10.1007/978-3-030-05399-4_10
28. Edwards, M. E., Dickson, C. A., Chengappa, S., Sidebottom, C., Gidley, M. J., & Reid, J. S. (1999). Molecular characterisation of a membrane-bound galactosyltransferase of plant cell wall matrix polysaccharide biosynthesis. *The Plant Journal : For Cell and Molecular Biology*, *19*(6), 691–697. https://doi.org/10.1046/j.1365-313x.1999.00566.x
29. Mckendry, P. (2002). Energy production from biomass (part 1): overview of biomass. Bioresource Technology, 83(1), 37–46. https://doi.org/https://doi.org/10.1016/S0960-8524(01)00118-3

30. Abe, M. M., Branciforti, M. C. M., & Brienzo, M. (2021). Biodegradation of Hemicellulose-Cellulose-Starch-Based Bioplastics and Microbial Polyesters. Recycling, 6, 22. https://doi.org/10.3390/recycling6010022
31. Mccarthy, J. L., & Islam, A. (2000). Lignin Chemistry , Technology , and Utilization : A Brief History.
32. Donaldson, L., Hague, J., & Snell, R. (2001). Lignin Distribution in Coppice Poplar, Linseed and Wheat Straw. *Holzforschung*, *55*, 379–385. https://doi.org/10.1515/HF.2001.063
33. Zhou, G., Sun, X., Zhang, L., Zeng, X., Liu, G., & Sheng, O. (2022). Lignin metabolism plays an essential role in the formation of corky split vein caused by boron deficiency in 'Newhall' navel orange (Citrus sinensis Osb.). *Scientia Horticulturae*, *294*, 110763. https://doi.org/https://doi.org/10.1016/j.scienta.2021.110763
34. Katahira, R., Elder, T. J., & Beckham, G. T. (2018). Chapter 1: A Brief Introduction to Lignin Structure. *RSC Energy and Environment Series*, *2018-Janua*(19), 1–20. https://doi.org/10.1039/9781788010351-00001
35. Barros, J., Serk, H., Granlund, I., & Pesquet, E. (2015). The cell biology of lignification in higher plants. *Annals of Botany*, *115*(7), 1053–1074. https://doi.org/10.1093/aob/mcv046
36. Huijgen, W. J. J., Gosselink, R. J. A., & Bruijnincx, P. C. A. (2016). *New insights into the structure and composition of technical lignins: a comparative characterisation study*. *18*(9). https://doi.org/10.1039/c5gc03043a
37. Rakotovelo, A., Peruch, F., & Grelier, S. (2019). Lignine : structure, production et valorisation chimique. *Meteriaux: Bois et Papiers*, *33*(0). https://www.techniques-ingenieur.fr/base-documentaire/materiaux-th11/applications-du-bois-42654210/lignine-structure-production-et-valorisation-chimique-in235/
38. Aminzadeh, S., Zhang, L., & Henriksson, G. (2017). A possible explanation for the structural inhomogeneity of lignin in LCC networks. *Wood Science and Technology*, *51*(6), 1365–1376. https://doi.org/10.1007/s00226-017-0941-6
39. Witzler, M., Alzagameem, A., Bergs, M., Khaldi-hansen, B. El, Klein, S. E., Hielscher, D., Kamm, B., & Kreyenschmidt, J. (2018). *Lignin-Derived Biomaterials for Drug Release and Tissue Engineering*. 1–23. https://doi.org/10.3390/molecules23081885
40. Ralph, J., Lundquist, K., Brunow, G., Lu, F., Kim, H., Paul, F., Marita, J. M., Hatfield, R. D., Ralph, S. A., Christensen, J. H., Boerjan, W., Schatz, P. F., Marita, J. M., Hatfield, R. D., Ralph, S. A., Christensen, J. H., & Boerjan, W. (2004). Lignins: Natural polymers from oxidative coupling of 4-hydroxyphenyl- propanoids. *Phytochemistry Reviews*, *3*(1), 29–60. https://doi.org/10.1023/B:PHYT.0000047809.65444.a4
41. Abdelaziz, O. Y., Brink, D. P., Prothmann, J., Ravi, K., Sun, M., García-Hidalgo, J., Sandahl, M., Hulteberg, C. P., Turner, C., Lidén, G., & Gorwa-Grauslund, M. F. (2016). Biological valorization of low molecular weight lignin. *Biotechnology Advances*, *34*(8), 1318–1346. https://doi.org/10.1016/j.biotechadv.2016.10.001
42. Chakar, F. S., & Ragauskas, A. J. (2004). Review of current and future softwood kraft lignin process chemistry. *Industrial Crops and Products*, *20*(2), 131–141. https://doi.org/10.1016/j.indcrop.2004.04.016
43. Fernández-Rodríguez, J., Erdocia, X., Hernández-Ramos, F., Alriols, M. G., & Labidi, J. (2018). Lignin separation and fractionation by ultrafiltration. In *Separation of Functional Molecules in Food by Membrane Technology*. https://doi.org/10.1016/B978-0-12-815056-6.00007-3

44. Huber, P., Burnet, A., & Petit-Conil, M. (2014). Scale deposits in kraft pulp bleach plants with reduced water consumption: A review. *Journal of Environmental Management*, *141*, 36–50. https://doi.org/https://doi.org/10.1016/j.jenvman.2014.01.053
45. Galkin, M. V, & Samec, J. S. M. (2016). Lignin Valorization through Catalytic Lignocellulose Fractionation: A Fundamental Platform for the Future Biorefinery. *ChemSusChem*, *9*(13), 1544–1558. https://doi.org/https://doi.org/10.1002/cssc.201600237
46. Plank, J. (2005). Applications of Biopolymers in Construction Engineering. In *Biopolymers Online*. https://doi.org/https://doi.org/10.1002/3527600035.bpola002
47. Gelardi, G., Mantellato, S., Marchon, D., Palacios, M., Eberhardt, A. B., & Flatt, R. J. (2016). Chemistry of chemical admixtures. In *Science and Technology of Concrete Admixtures*. Elsevier Ltd. https://doi.org/10.1016/B978-0-08-100693-1.00009-6
48. Gellerstedt, G. (2009). 8. Cellulose Products and Chemicals from Wood. In M. Ek, G. Gellerstedt, & G. Henriksson (Eds.), *Volume 1 Wood Chemistry and Wood Biotechnology* (pp. 173–194). De Gruyter. https://doi.org/doi:10.1515/9783110213409.173
49. Doherty, W. O. S., Mousavioun, P., & Fellows, C. M. (2011). Value-adding to cellulosic ethanol : Lignin polymers. *Industrial Crops & Products*, *33*(2), 259–276. https://doi.org/10.1016/j.indcrop.2010.10.022
50. Beckham, G. T. (2018). *Lignin Valorization*. The Royal Society of Chemistry. https://doi.org/10.1039/9781788010351
51. Grand View Research, Market Analysis Report - Kraft Lignin Market Research Report by Application (Binders And Resins, Pesticides And Fertilizers, and Thermoplastic Polymers), by Region (Americas, Asia-Pacific, and Europe, Middle East & Africa) - Global Forecast to 2026 - Cumulative Impact of COVID-19.Available :https://www.researchandmarkets.com/reports/4905005/kraft-lignin-market-research-report-by
52. Luo, H., & Abu-Omar, M. M. (2017). *Chemicals From Lignin* (M. A. B. T.-E. of S. T. Abraham (Ed.); pp. 573–585). Elsevier. https://doi.org/https://doi.org/10.1016/B978-0-12-409548-9.10235-0
53. Liu, B., & Abu-Omar, M. M. (2021). Chapter Five - Lignin extraction and valorization using heterogeneous transition metal catalysts. In P. C. Ford & R. B. T.-A. in I. C. van Eldik (Eds.), *Catalysis in Biomass Conversion* (Vol. 77, pp. 137–174). Academic Press. https://doi.org/https://doi.org/10.1016/bs.adioch.2021.02.001
54. Muurinen, E. (2000). Organosolv pulping- a review and distillation study related to peroxyacid pulping. In *Http://Jultika.Oulu.Fi/Files/Isbn9514256611.Pdf*. https://doi.org/10.1016/0960-8524(91)90105-S
55. Lora, J. H., & Glasser, W. G. (2002). Recent Industrial Applications of Lignin: A Sustainable Alternative to Nonrenewable Materials. *Journal of Polymers and the Environment*, *10*(1), 39–48. https://doi.org/10.1023/A:1021070006895
56. Xu, A., Guo, X., Zhang, Y., Li, Z., & Wang, J. (2017). Efficient and sustainable solvents for lignin dissolution: Aqueous choline carboxylate solutions. *Green Chemistry*, *19*(17), 4067–4073. https://doi.org/10.1039/c7gc01886j

57. Sillero, L., Prado, R., Welton, T., & Labidi, J. (2021). Extraction of flavonoid compounds from bark using sustainable deep eutectic solvents. Sustainable Chemistry and Pharmacy, 24, 100544. https://doi.org/https://doi.org/10.1016/j.scp.2021.100544

58. Han, Z. J., Levchenko, I., Kumar, S., Yajadda, M. M. A., Yick, S., Seo, D. H., Martin, P. J., Peel, S., Kuncic, Z., & Ostrikov, K. (2011). Plasma nanofabrication and nanomaterials safety. *Journal of Physics D: Applied Physics*, *44*(17), 174019. https://doi.org/10.1088/0022-3727/44/17/174019

59. Parot, M., Rodrigue, D., & Stevanovic, T. (2022). High purity softwood lignin obtained by an eco-friendly organosolv process. *Bioresource Technology Reports*, *17*(October 2021), 100880. https://doi.org/10.1016/j.biteb.2021.100880

60. Bello, F., & Chimphango, A. (2021). Optimization of lignin extraction from alkaline treated mango seed husk by high shear homogenization-assisted organosolv process using response surface methodology. *International Journal of Biological Macromolecules*, *167*, 1379–1392. https://doi.org/10.1016/j.ijbiomac.2020.11.092

61. de Sousa Nascimento, L., da Mata Vieira, F. I. D., Horácio, V., Marques, F. P., Rosa, M. F., Souza, S. A., de Freitas, R. M., Uchoa, D. E. A., Mazzeto, S. E., Lomonaco, D., & Avelino, F. (2021). Tailored organosolv banana peels lignins: Improved thermal, antioxidant and antimicrobial performances by controlling process parameters. *International Journal of Biological Macromolecules*, *181*, 241–252. https://doi.org/10.1016/j.ijbiomac.2021.03.156

62. Qin, Z., Yang, Q., Cheng, X., Liu, H., & Wang, X. (2021). Industrial Crops & Products Structural features , chemical composition , antioxidant activities of organosolv lignins extracted from black and white sesame capsules and stalks. *Industrial Crops & Products*, *169*(May), 113677. https://doi.org/10.1016/j.indcrop.2021.113677

63. Park, N., Kim, H., Koo, B., Yeo, H., & Choi, I. (2010). Bioresource Technology Organosolv pretreatment with various catalysts for enhancing enzymatic hydrolysis of pitch pine (Pinus rigida). *Bioresource Technology*, *101*(18), 7046–7053. https://doi.org/10.1016/j.biortech.2010.04.020

64. Galbe, M., & Zacchi, G. (2007). Pretreatment of Lignocellulosic Materials for Efficient Bioethanol Production BT - Biofuels (L. Olsson (Ed.); pp. 41–65). Springer Berlin Heidelberg. https://doi.org/10.1007/10_2007_070

65. Kamm, B., Gruber, P. R., & Kamm, M. (2007). Biorefineries – Industrial Processes and Products. In Ullmann's Encyclopedia of Industrial Chemistry. https://doi.org/https://doi.org/10.1002/14356007.l04_l01

66. Jung, H. Y., Lee, J. S., Han, H. T., Jung, J., Eom, K., & Lee, J. T. (2022). Lignin-Based Materials for Sustainable Rechargeable Batteries. Polymers, 14(4), 1–23. https://doi.org/10.3390/polym14040673

67. Polat, Y., Stojanovska, E., Negawo, T., DÖNER, E., & Kilic, A. (2017). Lignin as an Additive for Advanced Composites. In *Green Energy and Technology* (pp. 71–89). https://doi.org/10.1007/978-3-319-46610-1_4

68. Jesionowski, T., Klapiszewski, Ł., & Milczarek, G. (2014). Kraft lignin and silica as precursors of advanced composite materials and electroactive blends. *Journal of Materials Science*, *49*. https://doi.org/10.1007/s10853-013-7822-7

69. Science Direct, Available: https://www.sciencedirect.com/search?qs=Kraft%20lignin%20coatings

70. Science Direct, Available: https://www.sciencedirect.com/search?qs=Kraft%20lignin%20coatings%20anticorrosion
71. Burger, M. J., Robinson, B. J., & Pease, L. F. (2016). Sol-Gel-Derived Nanoscale Materials BT - Handbook of Nanoparticles (M. Aliofkhazraei (ed.); pp. 691–714). Springer International Publishing. https://doi.org/10.1007/978-3-319-15338-4_7
72. Dislich, H., & Hinz, P. (1982). History and principles of the sol-gel process, and some new multicomponent oxide coatings. *Journal of Non-Crystalline Solids*, *48*(1), 11–16. https://doi.org/https://doi.org/10.1016/0022-3093(82)90242-3
73. Sakka, S. (2022). Birth of the sol–gel method: early history. *Journal of Sol-Gel Science and Technology*, *102*(3), 478–481. https://doi.org/10.1007/s10971-021-05640-9
74. Figueira, R. B. (2021). *Chapter 14 - Greener synthesis and applications of hybrid sol–gel-processed materials* (B. Kharisov & O. B. T.-H. of G. S. of N. and C. Kharissova (eds.); pp. 459–490). Elsevier. https://doi.org/https://doi.org/10.1016/B978-0-12-821938-6.00014-1
75. Ciriminna, R., Pagliaro, M., & Palmisano, G. (2015). Sol-Gel for Environmentally Green Products. *The Sol-Gel Handbook*, *3–3*(August), 1055–1070. https://doi.org/10.1002/9783527670819.ch34
76. Huang, Y., Zheng, H., Yang, C.J., Wei, Q., van Ooij, W., Palanivel, V., and Osborne, J. (2003) Non-VOC water-based sol–gel/ silane-based corrosion protection coating. Surface Engineering Coatings and Heat Treatments 2002. Proceedings of the 1st ASM International Surface Engineering and the 13th IFHTSE Congress (ASM References 1069International), October 7–10, 2002, Columbus, Ohio, pp. 115–121.
77. Bokov, D., Turki Jalil, A., Chupradit, S., Suksatan, W., Javed Ansari, M., Shewael, I. H., Valiev, G. H., & Kianfar, E. (2021). Nanomaterial by Sol-Gel Method: Synthesis and Application. *Advances in Materials Science and Engineering*, *2021*. https://doi.org/10.1155/2021/5102014
78. Landau, M. V. (2008). Sol-Gel Process. In *Handbook of Heterogeneous Catalysis*. Wiley-VCH Verlag GmbH & Co. KGaA. https://doi.org/10.1002/9783527610044.hetcat0009
79. Nassar, E., Ciuffi, K., Calefi, P., Rocha, L., De Faria, E., Silva, M., Luz, P., Bandeira, L., Cestari, A., Fernandes, C., Achparaki, M., Thessalonikeos, E., Tsoukali, H., Mastrogianni, O., Zaggelidou, E., Chatzinikolaou, F., Vasilliades, N., Raikos, N., Isabirye, M., … J. Poesen Additional. (2011). Biomaterials and Sol-Gel Process: A Methodology for the Preparation of Functional Materials. In *Intech* (p. 13). https://doi.org/10.5772/23202
80. Hench, L. L., & West, J. K. (1990). The Sol-Gel Process. *Chemical Reviews*, *90*(1), 33–72. https://doi.org/10.1021/cr00099a003
81. Klein, L. (2004). Handbook of zeolite science and technology. In *Focus on Catalysts* (Vol. 2004, Issue 2). https://doi.org/10.1016/s1351-4180(04)00164-3
82. Nayak, A. K., & Das, B. (2018). 1 - Introduction to polymeric gels. In K. Pal & I. B. T.-P. G. Banerjee (Eds.), *Woodhead Publishing Series in Biomaterials* (pp. 3–27). Woodhead Publishing. https://doi.org/https://doi.org/10.1016/B978-0-08-102179-8.00001-6

83. Barrios, E., Fox, D., Li Sip, Y. Y., Catarata, R., Calderon, J. E., Azim, N., Afrin, S., Zhang, Z., & Zhai, L. (2019). Nanomaterials in Advanced, High-Performance Aerogel Composites: A Review. In *Polymers* (Vol. 11, Issue 4). https://doi.org/10.3390/polym11040726
84. Hatte, Q., Dubos, P. A., Guitter, N., Richard-Plouet, M., & Casari, P. (2019). Influence of relative humidity and temperature on the sol-gel transition of a siloxane surface treatment. *Journal of Sol-Gel Science and Technology*, *90*(2), 230–240. https://doi.org/10.1007/s10971-019-04929-0
85. Twej, W. (2009). TEMPERATURE INFLUENCE ON THE GELATION PROCESS OF TETRAETHYLORTHOSILICATE USING SOL-GEL TECHNIQUE. *Iraqi Journal of Science*, *50*, 43–49.
86. Cushing, B. L., Kolesnichenko, V. L., & O'Connor, C. J. (2004). Recent Advances in the Liquid-Phase Syntheses of Inorganic Nanoparticles. *Chemical Reviews*, *104*(9), 3893–3946. https://doi.org/10.1021/cr030027b
87. Moore, G. S. (1985). The Role of the Solvent in Sol-Gel Processing of Silica Glass.
88. Artaki, I., Zerda, T. W., & Jonas, J. (1986). Solvent effects on the condensation stage of the sol-gel process. *Journal of Non-Crystalline Solids*, *81*(3), 381–395. https://doi.org/https://doi.org/10.1016/0022-3093(86)90504-1
89. Pignataro, B. (2014). *Discovering the Future of Molecular Sciences* (B. Pignataro (ed.)). Wiley - VCH. https://doi.org/10.1002/9783527673223
90. Xu, X., & Li, L. (2012). Organic Semiconductor Nanoparticle Film: Preparation and Application (A. Hashim (ed.); p. Ch. 25). IntechOpen. https://doi.org/10.5772/34136
91. Sanchez, C., Rozes, L., Ribot, F., Laberty-Robert, C., Grosso, D., Sassoye, C., Boissiere, C., & Nicole, L. (2010). "Chimie douce": A land of opportunities for the designed construction of functional inorganic and hybrid organic-inorganic nanomaterials. *Comptes Rendus Chimie*, *13*(1–2), 3–39. https://doi.org/10.1016/j.crci.2009.06.001
92. Cusola, O., Kivistö, S., Vierros, S., Batys, P., Ago, M., Tardy, B. L., Greca, L. G., Roncero, M. B., Sammalkorpi, M., & Rojas, O. J. (2018). Particulate Coatings via Evaporation-Induced Self-Assembly of Polydisperse Colloidal Lignin on Solid Interfaces. *Langmuir*, *34*(20), 5759–5771. https://doi.org/10.1021/acs.langmuir.8b00650
93. Carlos De Haro, J., Magagnin, L., Turri, S., & Griffini, G. (2019). Lignin-Based Anticorrosion Coatings for the Protection of Aluminum Surfaces. *ACS Sustainable Chemistry and Engineering*, *7*(6), 6213–6222. https://doi.org/10.1021/acssuschemeng.8b06568
94. Pommiers-Belin, S., Frayret, J., Uhart, A., Ledeuil, J., Dupin, J.-C., Castetbon, A., & Potin-Gautier, M. (2014). Determination of the chemical mechanism of chromate conversion coating on magnesium alloys EV31A. Applied Surface Science, 298, 199–207. https://doi.org/https://doi.org/10.1016/j.apsusc.2014.01.162
95. Wei, J., Wang, H., Deng, Y., Sun, Z., Shi, L., Tu, B., Luqman, M., & Zhao, D. (2011). Solvent evaporation induced aggregating assembly approach to three-dimensional ordered mesoporous silica with ultralarge accessible mesopores. Journal of the American Chemical Society, 133(50), 20369–20377. https://doi.org/10.1021/ja207525eD

96. Hüfner, S. (2003). Introduction and Basic Principles BT - Photoelectron Spectroscopy: Principles and Applications (S. Hüfner (ed.); pp. 1–60). Springer Berlin Heidelberg. https://doi.org/10.1007/978-3-662-09280-4_1

97. Major, G. H., Fairley, N., Sherwood, P. M. A., Linford, M. R., Terry, J., Fernandez, V., & Artyushkova, K. (2020). Practical guide for curve fitting in x-ray photoelectron spectroscopy. Journal of Vacuum Science & Technology A, 38(6), 061203. https://doi.org/10.1116/6.0000377

98. Stokes, D. J. (2008). Principles and Practice of Variable Pressure/Environmental Scanning Electron Microscopy (VP-ESEM). In John Wiley & Sons.

99. Doyle, W. M. (2017). Principles and Applications of Fourier Transform Infra-red (FTIR) Process Analysis.

100. Salzman, G. C. (1999). Light Scatter: Detection and Usage. Current Protocols in Cytometry, 9(1), 1.13.1-1.13.8. https://doi.org/https://doi.org/10.1002/0471142956.cy0113s09

101. Hararak, B., Winotapun, C., Inyai, J., Wannid, P., & Prahsarn, C. (2021). Production of UV-shielded spherical lignin particles as multifunctional bio-additives for polyvinyl alcohol composite films. Journal of Nanoparticle Research, 23. https://doi.org/10.1007/s11051-021-05308-z

102. Goliszek, M., Podkościelna, B., Fila, K., Riazanova, A. V., Aminzadeh, S., Sevastyanova, O., & Gun'ko, V. M. (2018). Synthesis and structure characterization of polymeric nanoporous microspheres with lignin. Cellulose, 25(10), 5843–5862. https://doi.org/10.1007/s10570-018-2009-7

103. Ház, A., Jablonský, M., Šurina, I., Kačík, F., Bubeníková, T., & Ďurkovič, J. (2019). Chemical composition and thermal behavior of kraft lignins. Forests, 10(6), 1–12. https://doi.org/10.3390/f10060483

104. Fang, W., Alekhina, M., Ershova, O., Heikkinen, S., & Sixta, H. (2015). Purification and characterization of kraft lignin. Holzforschung, 69(8), 943–950. https://doi.org/10.1515/hf-2014-0200

105. Borella, M., Casazza, A. A., Garbarino, G., Riani, P., & Busca, G. (2022). A Study of the Pyrolysis Products of Kraft Lignin. Energies, 15(3). https://doi.org/10.3390/en15030991

106. Siril, P., Raveendran, S., Brown, D., & Wilson, K. (2009). Optimising catalytic properties of supported sulfonic acid catalysts. *Applied Catalysis A-General - APPL CATAL A-GEN*, *364*, 95–100. https://doi.org/10.1016/j.apcata.2009.05.032

107. Brazil, T. R., Costa, R. N., Massi, M., & Rezende, M. C. (2018). Structural, morphological, and thermal characterization of kraft lignin and its charcoals obtained at different heating rates. *Materials Research Express*, *5*(4), 45502. https://doi.org/10.1088/2053-1591/aab7c2

108. Chatel, G., & Rogers, R. D. (2014). Review: Oxidation of Lignin Using Ionic Liquids—An Innovative Strategy To Produce Renewable Chemicals. *ACS Sustainable Chemistry & Engineering*, *2*(3), 322–339. https://doi.org/10.1021/sc4004086

109. Nada, A. A. M. A.; El-Sakhawy, M.; Kamel, S. M. Infra-Red Spectroscopic Study of Lignins. Polymer Degradation and Stability 1998, 60 (2–3), 247–251. https://doi.org/10.1016/s0141-3910(97)00072-4.

110. Sillero, L., Prado, R., Welton, T., & Labidi, J. (2021). Extraction of flavonoid compounds from bark using sustainable deep eutectic solvents. Sustainable Chemistry and Pharmacy, 24, 100544. https://doi.org/https://doi.org/10.1016/j.scp.2021.100544

111. Grosse, C., Noël, M., Thévenon, M. F., Rautkari, L., & Gérardin, P. (2018). Influence of water and humidity on wood modification with lactic acid. Journal of Renewable Materials, 6(3), 259-269. https://doi.org/10.7569/JRM.2017.634176

112. Carvalho, L., Araújo, P., Yamaji, F. M., Lima, V. H., & Botaro, V. R. (2020). Bioresource Technology Kraft lignin fractionation by organic solvents : Correlation between molar mass and higher heating value. *Bioresource Technology*, *314*(June), 123757. https://doi.org/10.1016/j.biortech.2020.123757

113. Sadeghifar, H., & Ragauskas, A. (2020). Perspective on Technical Lignin Fractionation. *ACS Sustainable Chemistry & Engineering*, *8*(22), 8086–8101. https://doi.org/10.1021/acssuschemeng.0c01348

114. Díaz de los Ríos, M., & Hernández Ramos, E. (2020). Determination of the Hansen solubility parameters and the Hansen sphere radius with the aid of the solver add-in of Microsoft Excel. SN Applied Sciences, 2(4), 676. https://doi.org/10.1007/s42452-020-2512-y

115. Pereira Novo, L., & Curvelo, A. (2019). Hansen Solubility Parameters: A Tool for Solvent Selection for Organosolv Delignification. Industrial & Engineering Chemistry Research, 58. https://doi.org/10.1021/acs.iecr.9b00875

116. Ni, H., Ren, S., Fang, G., & Ma, Y. (2016). Determination of Alkali Lignin Solubility Parameters by Inverse Gas Chromatography and Hansen Solubility Parameters. BioResources; Vol 11, No 2 (2016). https://ojs.cnr.ncsu.edu/index.php/BioRes/article/view/BioRes_11_2_4353_Ni_Alkali_Lignin_Solubility_Parameters/4368

117. Mattinen, M.-L., Riviere, G., Henn, A., Nugroho, R. W. N., Leskinen, T., Nivala, O., Valle-Delgado, J. J., Kostiainen, M. A., & Österberg, M. (2018). Colloidal Lignin Particles as Adhesives for Soft Materials. In *Nanomaterials* (Vol. 8, Issue 12). https://doi.org/10.3390/nano8121001

118. Slater, C. S., Savelski, M. J., Hitchcock, D., & Cavanagh, E. J. (2016). Environmental analysis of the life cycle emissions of 2-methyl tetrahydrofuran solvent manufactured from renewable resources. Journal of Environmental Science and Health, Part A, 51(6), 487–494. https://doi.org/10.1080/10934529.2015.1128719

119. Weidener, D., Klose, H., Westarp, W. G. Von, Jupke, A., Leitner, W., María, P. D. De, & Grande, P. M. (2021). *Selective lignin fractionation using CO2-expanded 2-methyltetrahydrofuran (2-MTHF)*. 6330–6336. https://doi.org/10.1039/d1gc01651b

120. Hughes, A. E.; Boag, A.; Glenn, A. M.; McCulloch, D.; Muster, T. H.; Ryan, C.; Luo, C.; Zhou, X.; Thompson, G. E. Corrosion of AA2024-T3 Part II: Co-Operative Corrosion. Corros. Sci. 2011, 53 (1), 27–39. https://doi.org/10.1016/j.corsci.2010.09.030.

121. Reddy N.; Bera, P.; Reddy, V. R.; Sridhara, N.; Dey, A.; Anandan, C.; Sharma, A. K. XPS Study of Sputtered Alumina Thin Films. Ceramics International 2014, 40 (7 PART B), 11099–11107. https://doi.org/10.1016/j.ceramint.2014.03.133.

122. Zähr, J.; Oswald, S.; Türpe, M.; Ullrich, H. J.; Füssel, U. Characterisation of Oxide and Hydroxide Layers on Technical Aluminum Materials Using XPS. In Vacuum; 2012; Vol. 86, pp 1216–1219. https://doi.org/10.1016/j.vacuum.2011.04.004.

123. Ghosh, K. S., Hilal, M., & Bose, S. (2013). Corrosion behavior of 2024 Al-Cu-Mg alloy of various tempers. Transactions of Nonferrous Metals Society of China, 23(11), 3215–3227. https://doi.org/https://doi.org/10.1016/S1003-6326(13)62856-3

124. Kameshima, Y.; Yasumori, A.; Okada, K. XPS and X-ray AES (XAES) Study of Various Aluminate Compounds. Hyomen Kagaku. 2000, 21(8),481-487

125. Nelson, K. J. H.; Hughes, A. E.; Taylor, R. J.; Hinton, B. R. W.; Wilson, L.; Henderson, M. Characterisation of Aluminium Alloys after HNO3/HF–NaOH–HNO3/HF Pretreatment. Mater. Sci. Technol. 2001, 17 (10), 1211–1221. https://doi.org/10.1179/026708301101509287.

126. Muñoz, E., Díaz, C., Navarrete, E., Henríquez, R., Schrebler, R., Córdova, R., Marotti, R., & Heyser, C. (2016). Characterization of Surface Changes on Silicon and Porous Silicon after Interaction with Hydroxyl Radicals. Arabian Journal of Chemistry, 12. https://doi.org/10.1016/j.arabjc.2016.11.008

127. Adam, M.; Ocone, R.; Mohammad, J.; Berruti, F.; Briens, C. Kinetic Investigations of Kraft Lignin Pyrolysis. Ind. Eng. Chem. Res. 2013, 52 (26), 8645–8654. https://doi.org/10.1021/ie400979x.

128. Van Der Vis, M. G. M.; Cordfunke, E. H. P.; Konings, R. J. M. The Thermodynamic Properties of Tetraethoxysilane (TEOS) and an Infrared Study of Its Thermal Decomposition. J. Phys. IV JP 1993, 3 (3), 75–82. https://doi.org/10.1051/jp4:1993309.

129. Phadungsukanan, W.; Shekar, S.; Shirley, R.; Sander, M.; West, R. H.; Kraft, M. First-Principles Thermochemistry for Silica Species in the Decomposition of Tetraethoxysilane. J. Phys. Chem. A 2009, 113 (31), 9041–9049. https://doi.org/10.1021/jp905494s

130. Lu, Z. H.; Graham, M. J.; Jiang, D. T.; Tan, K. H. SiO2/Si(100) Interface Studied by Al Kα x-Ray and Synchrotron Radiation Photoelectron Spectroscopy. Applied Physics Letters. 1993, pp 2941–2943. https://doi.org/10.1063/1.110279.

Chapter II.

Hybrid Lignin/Silicon coatings elaboration

Figure List

Table List

This chapter compiles the study of the lignin/silicon coatings elaboration and their physicochemical characterization. As done before, an important bibliography focus is inserted prior to the experimental section. Here, it is intended to give an overview of the manner to protect coatings designed on Al2024 and to look ahead in the field with the opportunity of bio sources. Afterwards, the experimental procedure to prepare lignin/silicon coatings is also presented. More precisely, two routes of preparation have been detailed considering the pre functionalization (NDR coatings), or not (DR coatings), of the Al2024 surface with a molecular layer. Some chemical mechanisms are proposed in that case. The chapter begins with the optimization of the "dip coating" conditions for direct deposits onto the metal substrate (DR coatings): relative humidity in the deposit chamber (varying from 5% to 70%) and sample withdraw speed (varying from 0.05mm/s to 5.0mm/s). Morphology (SEM) and chemical composition (XPS) of the produced materials were attentively analyzed to define the most appropriate experimental conditions and their effects on surface wettability.

In a second time, the results of the non-direct route (NDR) coatings will be discussed in terms of chemical composition, morphology and visual aspect before a comparison with the previous DR coatings. The aim of this comparative study is to bring the most adequate coating type out on the sole basis of material structuring *vs* wettability.

1. State of the art

1.1. Anti-corrosion coatings: Main strategies for corrosion inhibition in aluminum

To reduce the corrosion damage and the repair costs on the aluminum-based materials, different strategies are used to protect it. It is important to point out that these actions increase the value of a project once some design adaptations or changes in used materials are done.

There are three main strategies usually adopted to constrain corrosion effects: two of them are based on studies before the achievement of the final structure assemble and the last one is instituted in the final step. They belong to a general way of thinking called "Compound's Design, Material's Selection and Protective Coatings"[1].

The first method consists of an analysis of Compound's Design, seeking to avoid points that could concentrate tension and then act as regions of cracks formations (facilitator of some types of corrosion). Independently of the environment, two considerations will be made: definition of material function and required properties and the type of environment (temperature, presence or not of fluids, strain and stress).

The second strategy starts with the end of design definition; it is based on the material's choice, once each kind of different metals and alloys will possess characteristics and microstructures that would be able to replace others in the same usage. Factors like material cost, production route and availability are important for the decision and the final cost increase.

Finally, the last type of protection thinking against corrosion is the addition of a protective layer over a material surface (primer layer). This layer should act like a very first active barrier and is designed to reduce the

corrosive effects if the final paint layers are defective. As quoted in the introduction, the most regular "primer" systems laid down on the metal surface are chromate layers as schematized in the Figure II-1 below.

Since a few years, for Al 2024 alloy, the first phase of classical protection, but that is not mandatory, consisted of an anodizing process, i.e. the formation of a porous oxide layer due to the application of electrical currents[2]. This process aims to further increase the material's passive resistance to corrosion, the adhesion between the substrate and the next applied layer. If this step is not realized, the thinner natural oxide layer replaces the anodized layer over the substrate, but this solution does not present the same guarantees, once the anodization can form an oxide layer with a thickness up to 20 micrometers against just some few nanometers of the natural Al_2O_3 layer[3].

Sequentially to the anodization, there is the primer coat, which will vary its thickness between 2 µm to 30 µm[4],and that besides the adhesion function (assuring the good bond between anodization/Al substrate and the intermediate coat), will act as an active layer, providing the anticorrosive protection in case of failure of the intermediate and topcoat layers[5]. The objective of the present work is precisely to propose a new generation of primer.

During years, the chromate conversion coating was usually incorporated in this stage, due to its impressive corrosion inhibiting capacity. However, with the near future ban of the Cr VI, the primer coat has been tested with new formulations containing elements like Zn, Mg and epoxy resin among other components that can replace the chromium and has shown satisfactory results in recent research, resisting long time to extreme conditions[4,5,6,7,8,9,10,11].

After the primer, the intermediate layer (usually called undercoat) is applied to increase the overall film thickness of the system. The undercoat, usually composed of laminar inhibitive pigments, as micaceous iron oxide (MIO)[12], is specially formulated to improve overall protection and reduce oxygen and water permeability. Generally, the thicker the coating is, the longer will be the usage life[13,14]. Finally, the finishing coating will be the first line of defense against the environment and will also give the aesthetic factor to the final material, giving it the desired color, shine, and appearance[5,15].

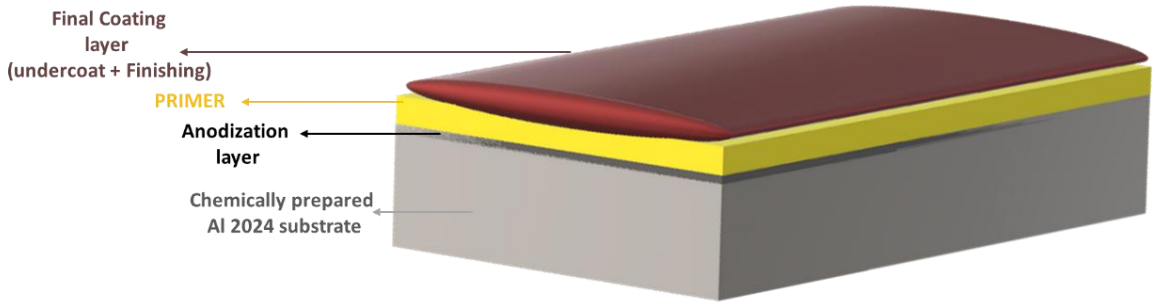

Figure II-1: Classical protection schema for Al 2024. Redraw from Bierwagen, G. et al.[6].

1.2. New approaches to primer elaboration

Most outstanding primer layers innovations to come in the next years will concern green materials, smart-coatings and eco-friendly systems, that could at the same time protect the Al without ignore environmental concerns[16,17] and even improving other aspects, for instance conferring new properties or reducing the coating manufacturing time. The European ECOLAND project started in 2018 is a good and important example about the new direction that Al coatings for aircraft market are pointing. This project looks to the development of a Chromium free coating based on an anaphoretic electrocoating treatment. This process will tend to reduce the total production time from 10-13h to 4.7-6.3h, the VOC (Volatile Organic Compounds) emission in 50% and the energy consumption in 30-45%[18].

Among the rising ideas in that way, the lignocellulose biomass has been taken an important stage as a valuable source of polymers that could confers interesting physico-chemical properties for the creation of anticorrosive coatings. With more or less easiness, biopolymers have already been incorporated in protective coatings as discussed in the works of Ouargaa, A. et al.[19] who developed a "green" anticorrosion system using almond oil and cellulose or of Dastpak, A. et al.[20] with the successful use of cellulose and lignin to hinder the corrosive annoyances. These compounds are also being used in hybrid anticorrosion systems, in which the combine properties of both lignocellulosic biomass and inorganic phase (usually a silicon source) create a more efficient protector system. In the work of Harb Vargas, S. et al.[21] , for instance, lignin was successfully used as a reinforcement phase. The Table II-1 below summarizes some other examples of these bio-based coatings, indicating the biopolymer used, the expected application and the applied technique for the material conception.

Table II-1: Resume of coatings that uses lignin or lignocellulose to create protective systems.

Biopolymer	Technique used	Application	Reference
Kraft Lignin	Hybrid modified lignin and PBAT deposited via Doctor Blade	Create a sustainable alternative coating for papers used as food packages with better mechanical and protective properties against moisture and mechanical stresses.	Shorey, R. and Mekonnen, T.H.[22]
Kraft Lignin	A lignin solution was sprayed over the surface	Develop an anticorrosive coating for a high-strength low-alloy steel combining an anodization layer with a second protective layer of lignin.	Dastpak, A. et al.[23]
Kraft Lignin	Spin-Casting	Create a polyurethane coating from a straight lignin fractionation.	Griffini, G. et al.[24]
Lignocellulose	Hot-Pressing	The fabrication of a coating capable of repeal water (hydrophobic) and retard flame spreading from the combination of lignocellulose biomass, PDMS and stearic acid-$Al(OH)_3$.	Wang, Z. et al.[25]
Kraft Lignin	Manually deposed by a paint brush	The development of a smart-coating (self-healing capacity) capable of increase the corrosion resistance of mild steel substrates from lignin nanocapsules.	Devadasu, S. et al.[26]

In order to achieve these bio-sourced innovative protective layers, different techniques are used to optimize the protection covering factor, to promote a cost reduction and to reduce environmental issues. However, in an industrial approach of thinking (in terms of operative steps number and of sizes of metal parts to protect), some easy ways to execute are even always expected. In this direction, the Dip-Coating process is an extremely interesting alternative, due to i) the quite simple implementation, ii) its ability to be modulated/quantified and iii) its relative low energy consumption.

1.3. Dip-Coating Technique

As quoted before (Chapter I - 1.3 Sol-Gel), the sol-gel method is advantageous because of its capacity to create some homogeneous coatings over almost all kinds of flat surfaces, combining different precursors and organic phases.

The incorporation of the dip-coating will occur during the sol phase, when it can be easily incorporated into the metallic surface where it keeps ageing and drying[27].

This deposition technique stands in the immersion of the substrate in a solution, its removal from the bath at a constant speed followed by a drying step, in which the volatile components (solvent) is evaporated. The (in)organic components aggregate to become a solid layer (a type of xerogel) formed on the surface of the material[28]. These three steps are represented in the Figure II-2 below.

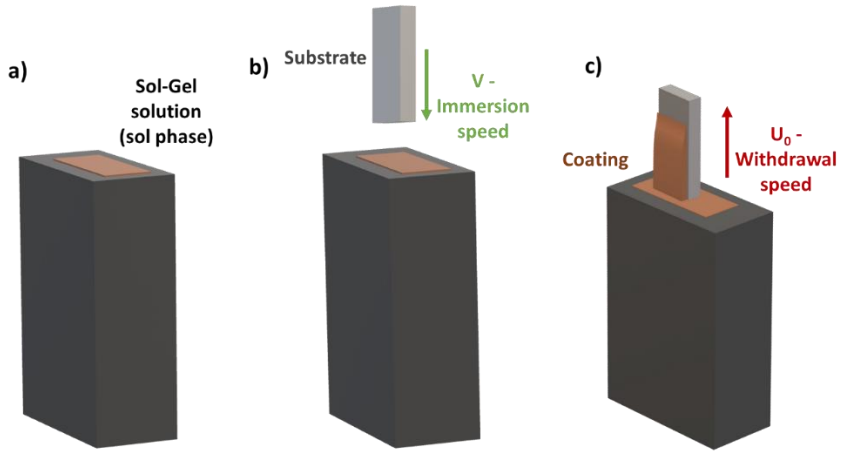

Figure II-2: Dip-Coating schematic process, with the solution inserted on the dip (a), followed by the substrate immersion (b) and its removal with the film formation (c).

During dip, the speed of withdrawal and the deposition environment (with more or less moisture) add to the factors mentioned above as vital to the coating formulation. The environment directly influences the drying rate, evaporation rate of the solvent, and thus the morphology and thickness of the final layer formed[28].

The speed with the substrate is removed from the solution (most important parameter), is directly related to the film thickness and the time the molecules in solution take to bond to the substrate surface. Three velocity regimes are generally considered: capillary, intermediate and drainage, and they involve a parabolic evolution of the film thickness (Figure II-3).

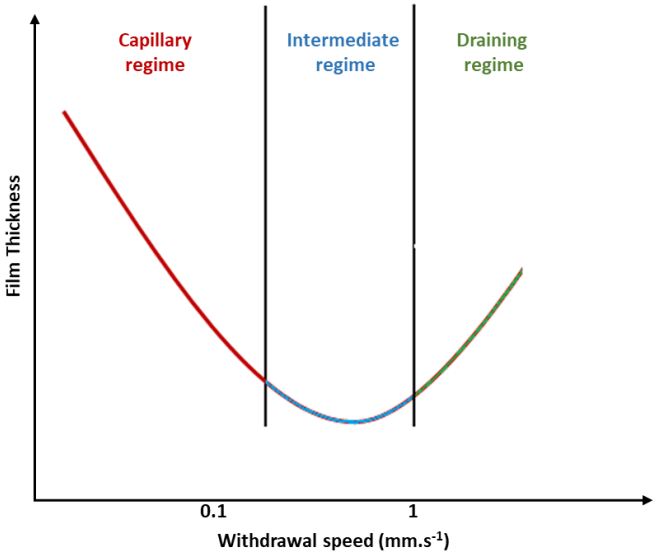

Figure II-3: Film thickness evolution relate to substrate Withdrawal speed.

The first and slowest, the *"capillary regime"*, stands out for evaporation faster than the removal of the substrate itself, generating an inversely proportional relationship between final thickness and speed and making that this regime is normally applied for the creation of extremely thicker films[29]. The following relationship is used to describe this regime:

$$h_0 = \frac{c_i M_i E}{\alpha_i \rho_i L u} \qquad \text{Equation II-1}$$

Where h_o is the final thickness of the film, c is the precursor concentration in mol/cm^3, M is the molar mass in g/mol, E corresponds to the evaporation rate (m^3/s), α is the material percentual in the film, ρ is the solution density in g/cm^3, L is the film width (m) and u the withdrawal speed in mm/s.

Inversely to the capillary, the *"draining regime"* occurs for removal speeds higher than 1 mm/s and it produces intermediate thicknesses. The mathematical estimation of the withdrawal speed relation with the thickness is described by an approximation of the Landau-Levich equation[30]; this equation originally defines Newtonian-fluids behavior[31], what is not the case in sol-gel, due to the viscosity and the concentration changes during the aging phase. So, the equation is the following:

$$h_0 = \frac{0.94\eta_s^{2/3}}{\gamma_s^{1/6}(\rho_s g)^{1/2}} u^{2/3} \qquad \text{Equation II-2}$$

For this equation, η is the solution dynamic viscosity (Pa.s), γ the surface tension in J/m^2 and g the gravity in m/s^2. Due to the higher velocities in the process, the withdrawal speed assumes a direct relation with the thickness and parameters related to the solution properties become more important than the substrate.

Finally, the *"intermediate regime"* is the zone with contributions of both capillary and draining aspects, creating the thinnest coatings and being normally attributed to applications in which the layer must have some few nanometers[29,32]. So, the mathematical relation for this regime is the combination of both previous regimes:

$$h_0 = \frac{c_i M_i}{\alpha_i \rho_i}\left(\frac{E}{Lu} + \frac{0.94\eta_s^{2/3}}{\gamma_s^{\frac{1}{6}}(\rho_s g)^{1/2}} u^{2/3}\right) \qquad \text{Equation II-3}$$

In all those scenarios, after immersion/removal of the substrate of the sol bath, the drying process assumes the last and most significant role of the coating. During this, drying phase is when the film assumes its definite thickness, morphology and shows if it is homogeneously along the substrate surface. So, some methods are intrinsically correlated to this phase, justifying the parameters chosen and the result obtained. The Evaporation Induced Self-Assembly (EISA) is the technique used in this work (defined at Chapter I – 1.3.3) and it appears to be an adapted repeatable process.

2. Materials & Methods

2.1. Al 2024 pre-functionalization

Before the coat of the Al 2024, the samples that were prepared and some of them were even pre-functionalized, in order to create an organo-alkoxide linker coupling molecule that increases the attachment of the hybrid solution. The surface pre-functionalization, used in the NDR coatings deposit procedure, consists in the grafting of 3-(triethoxysilyl) propylsuccinic (TESPSA, 95%, CAS: 93642-68-3 - provided by Merck), on the prepared Al 2024. The surface functionalization steps were:

a) The Al 2024 prepared was immersed in a solution of TESPSA/Toluene (99.5%, ACROS ORGANICS) 2% at 60°C overnight.

b) The sample is recovered and left cooling for 5 minutes under the fumehood.

c) The plate is rinsed with Toluene during 5 minutes at room temperature.

d) Immersion in Toluene at 100 °C for 10 minutes, ensuring the removal of weak bonds.

e) The functionalized substrate is dried under N_2 flow for 1 minute.

The Figure II-4 below shows the surface state after each important step, from the preparation that increases the surficial roughness and hydroxylates it until the final functionalization step, in which the weak bond molecules are eliminated from the Toluene washing[33].

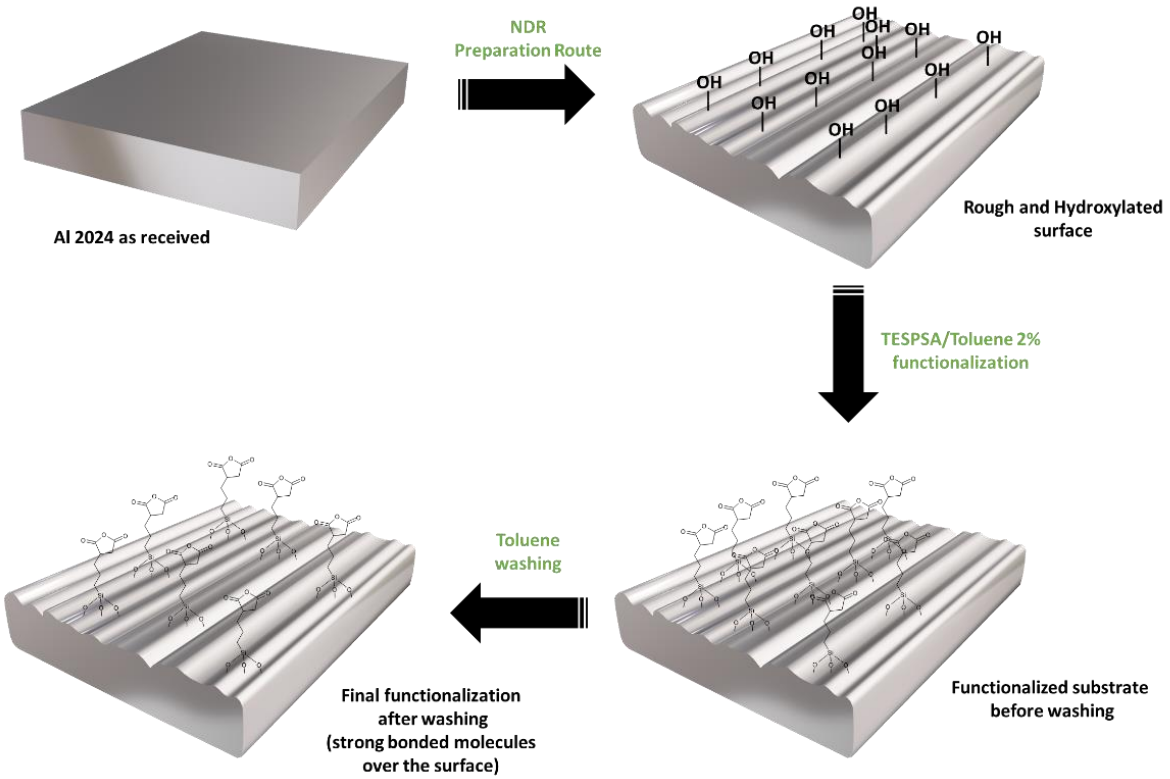

Figure II-4: Schematic representation of the surface state from the surface preparation until the last functionalization step.

All substrates that have undergone this pre-functionalization step have been given the name Non-Direct Route (NDR), and the others were labelled as Direct Route (DR).

2.2. Coatings elaboration

Coating elaboration principle is the same independently of the mode of deposit (DR or NDR). Remind the DR route consists of the direct immersion of the prepared Al 2024 plate in the Solution A when the NDR deposition route includes a pre-functionalization of the alloy surface.

For both paths, the coating was performed by the ACEdip 2.0 dip-coating (SolGelWay, France – Figure II-5 a)) at IPREM - UPPA. The same temperature, relative humidity (RH), withdrawal and immersion speeds, cycle number and immersion time were tested for both paths. The Table II-2 below reports all experimental parameters.

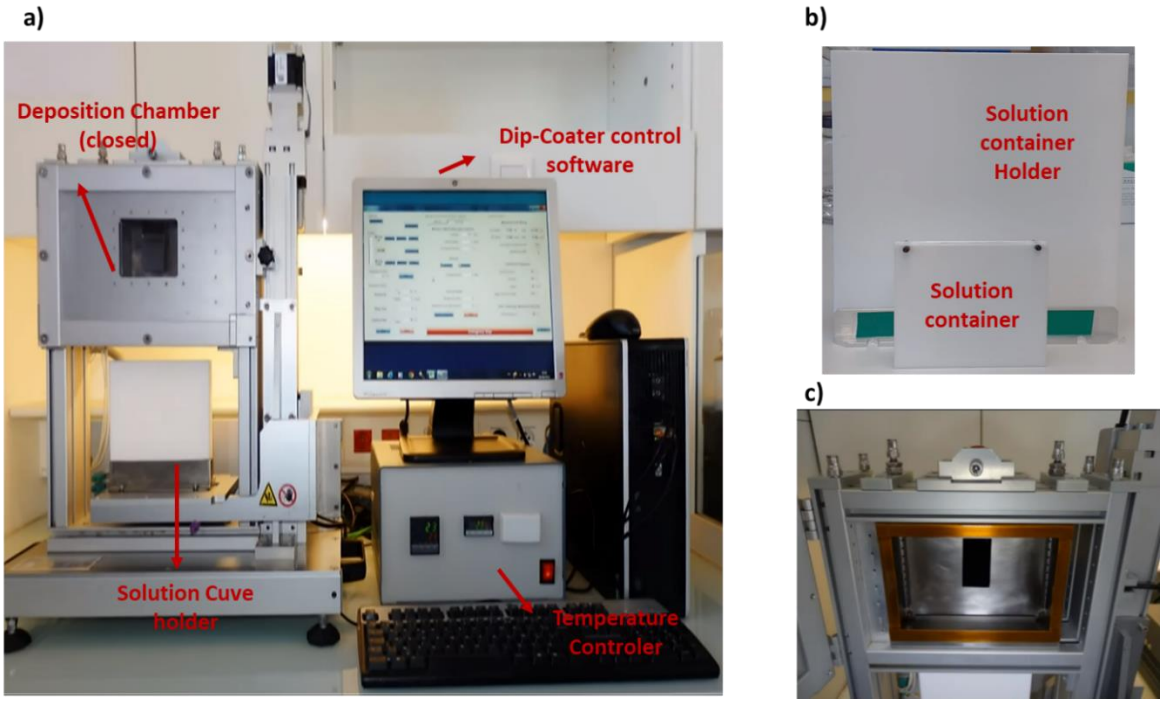

Figure II-5: Dip-Coating system used for the deposition of biohybrid coatings: (a) general view of the system, (b) the solution container and (c) the Al 2024 substrate once positioned inside the deposition chamber.

The RH conditions were varied from 5%, 10%, 50% and 70%, to allow a complete comprehension about the effect of steamy environments over the final coating aspect, adherence. The withdrawal speed was also tested at 3 different values 0.05 mm/s, 0.70 mm/s and 5.00 mm/s, exploring the three dip-coating deposition regimes previously described in the topic 1.3 in this chapter. Immersion speed, immersion time and number of immersion cycles were set at a fixed value as they don't directly impact the coating morphology.

Table II-2: Dip-Coating parameters.

Parameter	Temperature (°C)	Relative Humidity (%)	Immersion speed (mm/s)	Withdrawal speed (mm/s)	Immersion time (sec)	Cycles
Value	Room Temperature	10, 50 and 70	10	0.05, 0.70 and 5.00	5	1

The experimental procedure starts with placing the lignin/silicon solution into the vessel (Figure II-5 b)) and positioning it on the vessel holder. Next, the deposition chamber is opened, the substrate is positioned in the dip-coating chamber (Figure II-5 c)). Then the chamber is locked to maintain a controlled atmosphere. Desired temperature and humidity values are set and a 10min time lapse is mandatory to stabilize experimental conditions.

Once the coating process is effective, samples are left to dry for 3 minutes inside the dip-coater chamber, under the relative humidity atmosphere. Finally, the coated samples are placed in a heat chamber at 120°C for 5 minutes and stored into a desiccator.

2.3. Brief presentation of the characterization techniques

Water Contact Angle (WCA), Optical Profilometry and adhesion tests are employed to describe the wettability and the thickness/roughness of the designed coatings will be briefly detailed here below. A more complete concern is reported in the Appendix – Water Contact Angle and Optical profilometry topics.

2.3.1. Water Contact Angle (WCA)

The water contact angle (WCA) analysis is the measurement of the angle formed by the liquid (water) –vapor – solid interfaces. The Young equation quantifies the wettability of a solid surface (Equation II-4). Each solid, liquid, vapor interface has a specific equilibrium contact angle for a determined temperature / pressure set.

$$\cos\theta = \frac{\gamma_{SA}-\gamma_{SL}}{\gamma_{LA}} \qquad \text{Equation II-4}$$

Depending on the angle obtained, the wettability of the material will be classified as hydrophilic, hydrophobic or superhydrophobic. If the contact angle is between 0 and 90 degrees, the surface is considered hydrophilic, above 90 and below 140 degrees the material is hydrophobic and beyond 140 degrees the surface is superhydrophobic.

The contact angle depends on the medium above the free surface of the liquid, and on the properties of the liquid and solid in contact. It has no correlation with the inclination of the solid relative to the surface of the liquid. It varies with surface forces and therefore with the temperature and the purity of the liquid[34].

2.3.2. Optical Profilometry: Roughness and Thickness Evaluation

Optical Profilometry (OP) is a non-destructive interferometric-based non-contact method that is used for determining roughness/surface topography evaluation and quantification. A light beam is split with one half directed to the surface and another half to the mirror; when beams are recombined, the wavelength scale path difference produced by the topography variations causes interference that can be converted into a topographical pattern[35].

2.3.3. Adhesion Test

In order to assess the suitability of the lignin-based coatings in the manufacturing field, good adhesion ability onto the desired substrates is mandatory. The evaluation of the coating adhesion on the Al 2024 substrate was performed with an Elcometer 1542 Cross Hatch Adhesion Tester Basic Kit. The results were analyzed and interpreted according to the ASTM D 3359-B standard[36].

3. Results

3.1. Direct Route (DR) coatings

3.1.1. Humid Conditions (50% and 70% Relative Humidity)

The first coatings were carried out according to the parameters described in Table II-2. Results presented here below are specific to initial 70% and 50% relative humidity (RH) conditions tested. SEM analysis shows that 50% RH coatings generally appear denser than 70% RH ones. No coating looks really homogeneous, and some defects (for instance holes, dendritic formations and cracks) are observed in random concentration whatever the tested withdrawal speed. At lowest 0.05 mm/s withdrawal speed (capillary regime) some crossing cracks are visible for the thickest coatings of the series (2.92 ± 0.2 µm for 70% RH and 3.29 µm thick for 50% RH – Figure II-6 a) and b) respectively). As reported by Schneller, T. et al.[37], the presence of cracks in the final coating is directly related to some thermal expansion and contraction processes of the created layers, and the phenomenon is enhanced for greater thicknesses. Moreover, as mentioned by Visscher et al.[38], shrinkage of the structure due to the more or less good completion of the drying processes of the film influences both the composition and the final density.

For the intermediate withdrawal speed of 0.70 mm/s, the SEM images (Figure II-6 c) for RH 70% and d) for 50%) did not show the same morphology. The coating with 70% RH seems more covering and denser but would present a heterogeneous porosity and some macro holes defects. On the contrary, the coating configuration under 50% humidity shows lot of metal rubbles probably coming from the surface preparation as already identified on Figure I-16. The observation of such surface details could be associated with the lower thickness measured (2.30 ± 0.2 µm) and maybe a low covering in comparison with the slower regime presented before for 50% RH or a certain heterogeneity of the deposit of the coating created in the capillary regime. The obtained thickness are present in the Table II-3 below.

Table II-3: Thickness of 70% and 50% RH hybrid coatings.

Relative Humidity	Withdrawal Speed		
	0.05 mm/s	**0.70 mm/s**	**5.00 mm/s**
50%	3.29 ± 0.2	1.89 ± 0.2	1.43 ± 0.2
70%	2.92 ± 0.2	2.30 ± 0.2	2.52 ± 0.2

Regarding these observations, the coatings aspect does not seem to follow the expected trend of thinnest layers for the intermediate deposit regime, as expected from Figure II-3. This tendency was also noticed for a humidity of 10% (the lowest used) in the deposit atmosphere; this could possibly mean that the classical dip-coating thickness abacus is not completely adapted for extreme humidity conditions (very steamy or very dry) as the deposition equations (Equation II-1, II-2 and II-3) do not directly consider the relative humidity as a key parameter. However, for the RH of 50%, the withdrawal speed of 0.70 mm/s provided the lowest coating thickness, in adequacy with the Landau-Levich equation.

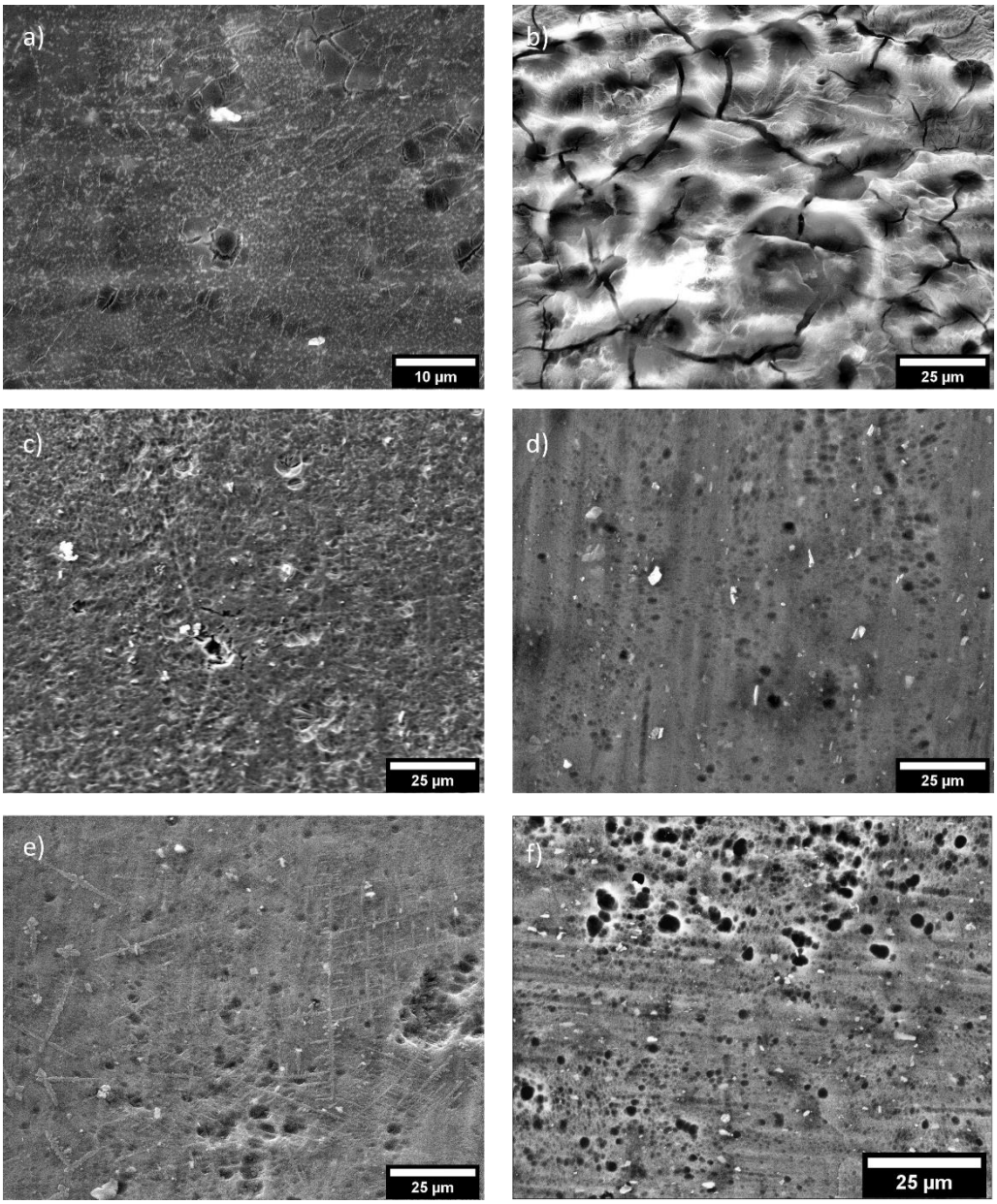

Figure II-6 : SEM images from DR coatings. a) RH 70% with a withdrawal speed of 0.05 mm/s magnified x2500, b) RH 50% with a withdrawal speed of 0.05 mm/s magnified x850, c) RH 70% with a withdrawal speed of 0.70 mm/s magnified x850, d) RH 50% with a withdrawal speed of 0.70 mm/s magnified x850, e) RH 70% with a withdrawal speed of 5.00 mm/s magnified x850 and f) RH 50% with a withdrawal speed of 5.00 mm/s magnified x850.

Finally, for the faster deposition speed (5.00 mm/s), the presence of macro defects is still maintained for 70% RH (Figure II-6 e) condition. For these experimental set, some dendritic structures grew up maybe indicating the precipitation of some entities of the solution during the heat/cooling process. This preferential directional arrangement has been previously reported in a work of Tian, Z. et al.[39] about self-assembly of oxide crystals during post heat/cooling treatments of inorganic based coatings. The same surface over-structure type is not present in the coating made with 50% of RH (Figure II-6 f)), certainly confirming the key role of humidity condition set on the final morphology. Moreover, the 50% RH SEM image clearly highlights the increase of holes concentration with

the enhancement of withdrawal speed. A lowering of the humidity level could indeed increase the solvent evaporation rate during the withdrawal of the substrate out of the dip-coating bath. This would generate the quick extraction of air bubbles impacting the coating morphology.

A complete XPS chemical analysis was systematically done to be sure about the composition of all the samples. Under RH of 70%, at 0.05 mm/s and 5.00mm/s withdrawal speeds, the XPS results revealed a low covering capacity, since the Al substrate was identified in high amounts (8.7 at.% for the 0.05 mm/s speed and 10.2 at.% for the 5.00mm/s speed). At the intermediate regime, only 2.5% of Al is detected.

Meanwhile, as can be observed in the quantification Table II-4 below, the speed of 0.70 mm/s would provide a greater amount of lignin in the material surface, expressed by 70.2 at.% of carbon with same chemical environments than identified in the Kraft lignin (Table I-6). In a reverse view, the capillary and drainage regimes would favor the incorporation of Si from TEOS, in quantities greater than 10 at.%. At this stage, a better covering coating would relate to a high content of Lignin material.

Table II-4: XPS simplified chemical composition table of the DR coatings prepared with RH 70%.

Chemical Element	DR Lignin/Silicon RH 70% _0.05 mm/s	DR Lignin/Silicon RH 70% _0.70 mm/s	DR Lignin/Silicon RH 70%_5.00 mm/s
	Total At. Conc (%)	Total At. Conc (%)	Total At. Conc (%)
Al	8.7	2.5	10.7
C	40.5	70.2	37.8
O	35.8	23.0	37.0
Ca	0.6	0.6	-
Si	12.6	2.6	12.1
Zn	0.1	0.2	-
Cl	1.7	0.9	1.2
N	-	-	1.2
C/Si	3.2	27.0	3.1

XPS data collected for 50% RH samples gave an opposite trend with the detection of more Al signal at 0.7mm/s withdrawal speed (at.% Al > 12%) when it is only about 5% for capillary and drainage regimes. The carbon and silicon percentages reported in the Table II-5 below are reversed. For 0.05mm/s and 5.0mm/s w.s., the C 1s core level spectrum consist of several components, C-C/C=C/C-H, C-O, C=O and COOH and transitions at 284.9 eV, 286.4 eV, 287.9 eV, 289.3 eV and 291.4 eV respectively, as previously observed in the Lignin/Silicon Hybrid (Table

I-9). The π- π* transitions that were identified in the Kraft © lignin were still present in the hybrid coatings, but due to their extremely low content it was not even possible to quantify them.

Finally, thicker coatings do not automatically attest of a homogeneous covering and variations would depend on the relative humidity level which could influence the C/Si ratio in the chemical composition. The lower condition humidity showed less substrate identification after the coating process, indicating that the reduction of humidity may be beneficial to achieve a better covering.

Table II-5: XPS simplified chemical composition table of the DR coatings prepared with RH 50%.

Chemical Element	DR Lignin/Silicon RH 50%_0.05 mm/s	DR Lignin/Silicon RH 50%_0.70 mm/s	DR Lignin/Silicon RH 50%_5.00 mm/s
	Total At. Conc (%)	Total At. Conc (%)	Total At. Conc (%)
Al	4.7	12.2	6.2
C	58.8	36.9	51.2
O	29.8	38.5	31.5
Si	5.5	10.4	9.1
Cl	1.2	2.0	1.4
N	-	-	0.6
C/Si	10.7	3.5	5.6

Despite all these chemical composition differences, both humidity conditions did not meet the necessary requirements for an efficient coating, since Al 2024 substrate is still observed (indicating uncoated zones). In a morphological point of view, the hybrid layers are not homogeneous, stables and offer many surface defects. These aspects (as will be shown further ahead in Chapter IV, when the corrosion phenomenon will be detailed), could be facilitators of corrosive effects.

3.1.2. Dry Condition (10% Relative Humidity)

Then, seeking to improve these points, the humidity was further reduced to 10% to promote a drier atmosphere, and some new coatings were designed with the objective to get a better apparent aspect. In this relative humidity, the mean thickness value varied from 3.75 ± 0.2 µm for the capillary regime, to 2.08 ± 0.2 µm for 0.70 mm/s condition and finally to 1.20 ± 0.2 µm for the draining condition.

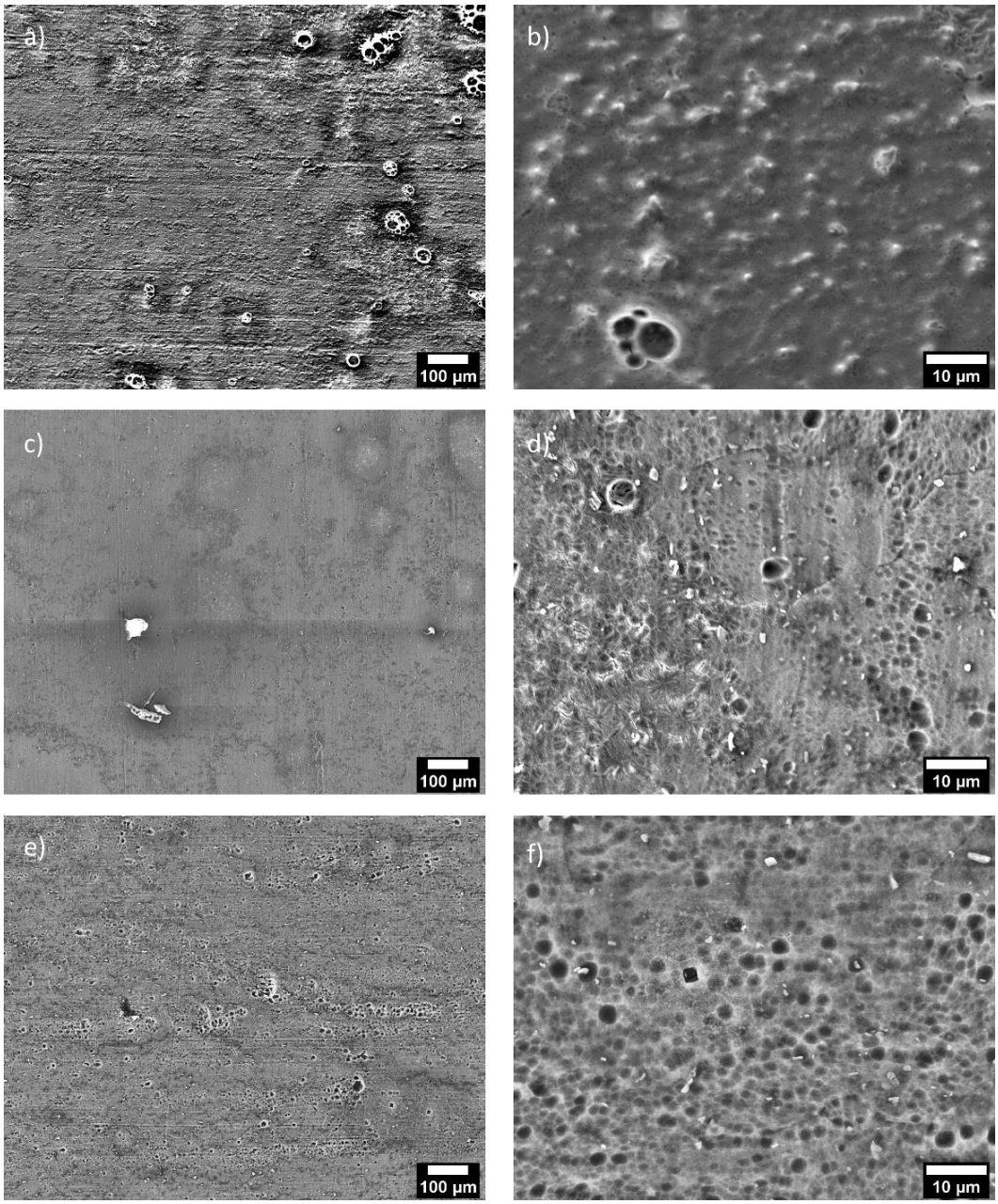

Figure II-7: SEM images from DR coatings 10% RH. a) Withdrawal speed of 0.05 mm/s magnified x150 and b) magnified x1500, c) withdrawal speed of 0.70 mm/s magnified x150 and d) magnified x1500, e) withdrawal speed of 5.00 mm/s magnified x150 and f) magnified x1500.

The SEM investigation showed an apparent significant improvement in the surface coverage, with a much less presence of defects for all speeds. Figure II-7 a) attests of the disappearance of crossing cracks after a 0.05 mm/s withdrawal speed of the substrate; the coating is apparently thick and dense enough to fill in substrate surface asperities. At higher magnification(Figure II-7 b) this trend is confirmed with an uniform aspect; anyway, it is possible to verify the presence of some small particles that seem to have a spherical morphology that remind clusters of lignin as previously seen in Chapter I.

For the intermediate regime, the less magnified image (Figure II-7 c)) indicates a much more homogeneous coating than those obtained in same conditions but for 50% RH and 70% RH , but by zoom in the picture (Figure II-7 d)) some small cracks spread over random areas. Finally, for the highest tested speed, 5.00 mm/s, (Figure II-7 e)), surface seems rougher with the ascertainment of substrate details as initially seen in Figure I-16. When magnifying the SEM image (Figure II-7 f)) some dispersed metal particles are even visible on the coating surface.

Table II-6: XPS chemical composition table of the DR coatings prepared with RH 10%.

Core Peak	DR Lignin/Silicon RH 10%_0.05 mm/s			DR Lignin/Silicon RH 10%_0.70 mm/s			DR Lignin/Silicon RH 10%_5.00 mm/s		
	BE (eV)	at. %	Total At. Conc (%)	BE (eV)	at. %	Total At. Conc (%)	BE (eV)	at.%	Total At. Conc (%)
Al 2p	74.9	1.9	1.9	74.8	1.9	1.9	75.0	1.3	1.5
	-	-		-	-		72.9	0.1	
	-	-		-	-		73.4	0.1	
C 1s	284.9	38.5	60.1	285.0	17	26.3	284.9	19.1	27.8
	286.4	19.6		286.4	8		286.4	7.5	
	288.1	1.1		288.0	0.8		288.0	0.6	
	289.7	0.9		289.4	0.5		289.1	0.6	
O 1s	531.0	1.4	28.4	532.5	45.8	47.3	532.6	45	46.3
	532.5	27.0		530.7	1.5		530.8	1.3	
Ca 2p	347.6	0.2	0.3	-	-	-	-	-	-
	351.1	0.1		-	-		-	-	
Si 2p	103.0	8.2	8.2	103.0	2.6	24.1	103.3	24.4	24.4
Zn 2p	1022.2	0.1	0.1	-	-	-	-	-	-
Cl 2p	198.7	0.8	1.1	199.0	0.3	0.4	199.0	0.2	0.3
	200.4	0.3		200.7	0.1		200.7	0.1	
C/Si	7.6			1.1			1.1		

The Table II-6 reports the detailed information of XPS core levels binding energies and atomic percentage of the coatings designed with 10% RH. Results confirm the better substrate covering with a drastic reduction of the Al content (<2.0 at.%) whatever the withdrawal speed. For example, the general spectrum (Figure II-8 a)) corroborates the Table II-6, with a minor Al 2p peak (1.9 at% - 74.9 eV) and a quite intense signal of carbon and oxygen elements. However, in this dry condition, less evident relationship is made between the good covering of the substrate and a higher content of lignin. An important amount of carbon is recorded in the dip-coating capillary regime with a C/Si ratio 7 times more important than for other withdrawal regimes.

For the 0.05 mm/s w.s. condition, the C 1s spectrum (Figure II-8 b)) is similar to the Kraft © lignin spectrum with 4 components assigned to C-C/ C=C/C-H, C-O, C=O and COOH chemical environment respectively identified

at 284.9 eV, 286.4 eV, 288.1 eV and 289.7 eV, as quoted for the other conditions, the π-π* transitions were not possible to be quantify. Furthermore, XPS signals of Si 2p and O 1s (28.4 at.% and 8.2 at.%) are located at 103.0 eV and 532.5 eV, which would correspond to a siloxane network[40].

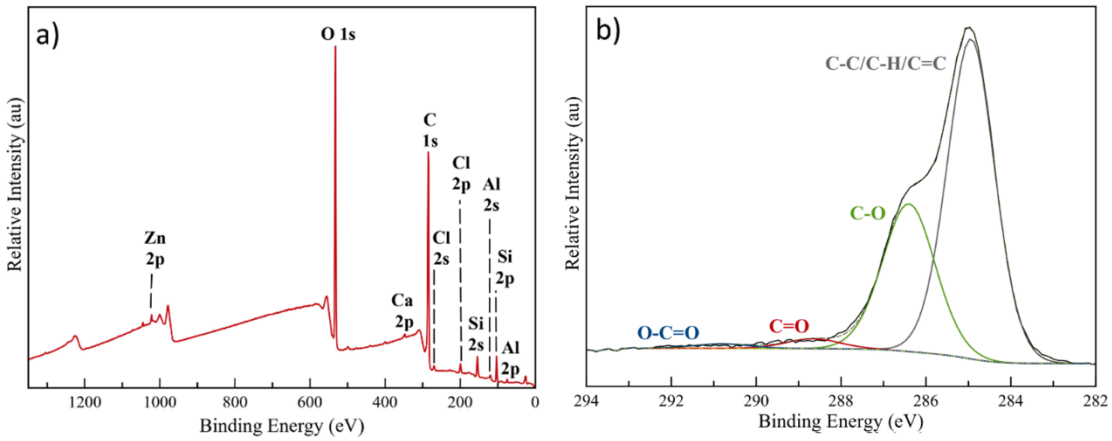

Figure II-8: XPS spectra of DR Al 2024 coated substrate: (a) survey spectrum and (b) C 1s core level spectrum.

To precise the improvement of the covering effect of the designed coating, a XPS chemical mapping was achieved on a 6 mm x 4 mm Al 2024 panel for dip-coating conditions under 10% RH and 0.05mm/s speed. The whole results are presented in the form of chemical elements surface distribution, whose greater intensity in color corresponds to a greater presence of the element checked. Even though the mapping view does not give a quantitative information, Figure II-9 exhibits a heterogenic crossing distribution, certainly related to the presence of lignin polymeric arrangement on the surface. The other elements (Si, O, Al) are mainly detected in zones where carbon is not present. This observation could explain the composition differences noticed in the XPS tables considering the non-uniformity of analyzed zones.

The likely cause of this particular distribution would stem from the nature and strength of the interaction between the mixed layer and the Al 2024 substrate. In particular, the condensation of silanes on aluminum substrates can generally take place via surface hydroxyl groups. However, the high hydrophobicity of lignin may cause microphase separation during solvent evaporation, resulting in a heterogeneous distribution of siloxane bonds over the surface of the aluminum substrate. The post coating thermal treatment of the films can also enhance the segregation process.

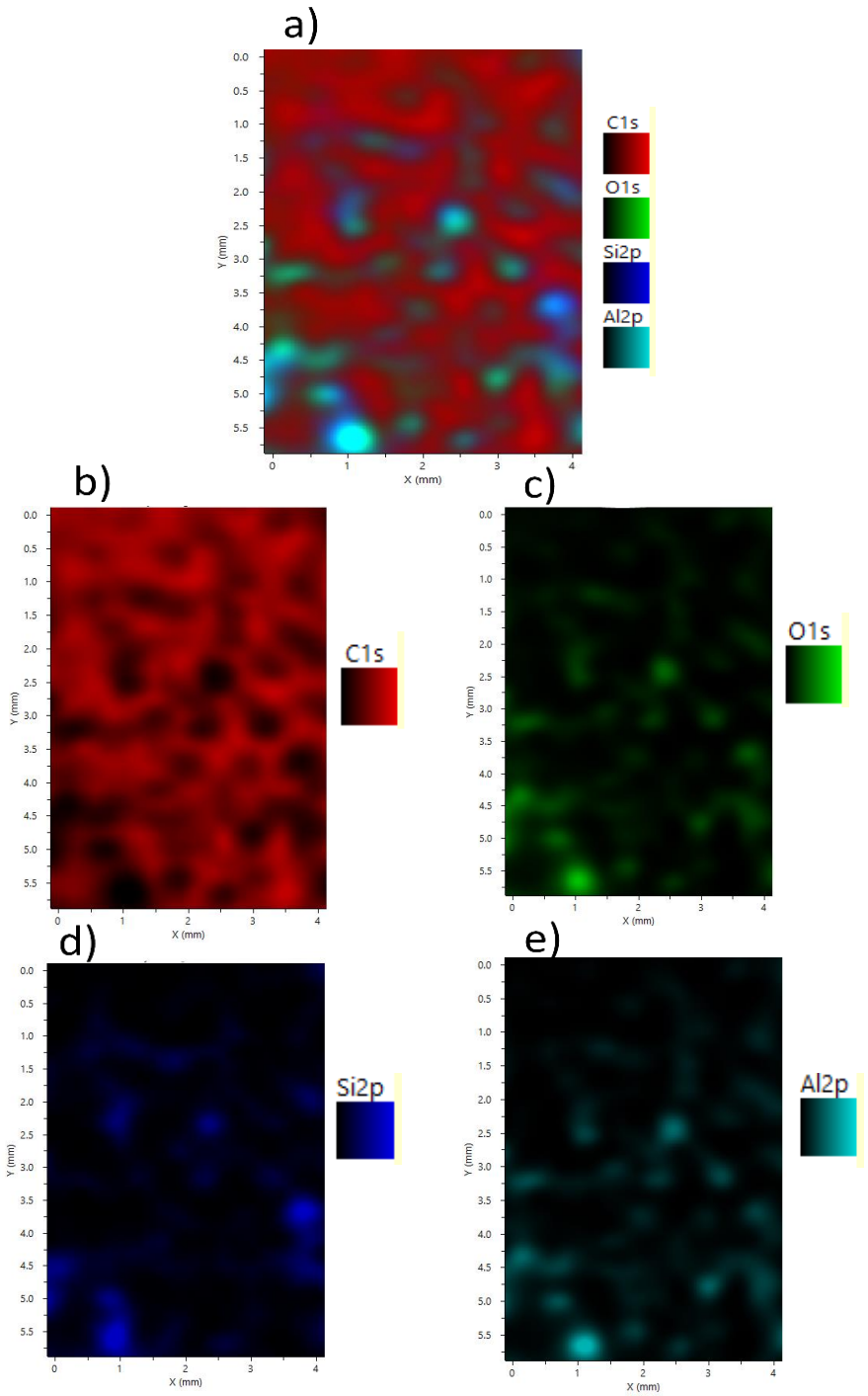

Figure II-9: XPS chemical map of DR RH 10%_0.05 mm/s – Lignin/Silicon Hybrid coating. a) All Elements overlap, b) C 1s distribution on the surface, c) O1s distribution on the surface, d) Si 2p distribution on the surface and e) Al 2p distribution on the surface.

To complete the first knowledge acquired on the surface chemical identification of the designed coating, a FTIR-ATR investigation was done (Figure II-10) to probe more the material bulk (incoming beam penetrates 1.0 to 2.0 µm in-depth). Despite the low Si content recorded at the surface, a siloxane-like network was clearly highlighted with the presence of two specific vibration bands: the first one at 950 cm^{-1} could be correlated to Si-

O-C=OCH_3 bond and the second one at 1050 cm^{-1} would correspond simultaneously to Si-OR and lignin C-H bonds signals. The aromatic vibrations bands and the OH stretching modes associated with the Lignin bio resource were recorded at 1600 cm^{-1} and around 3350 cm^{-1}. They confirm the presence of Kraft lignin like molecules (Figure I-13), in the coating[41].

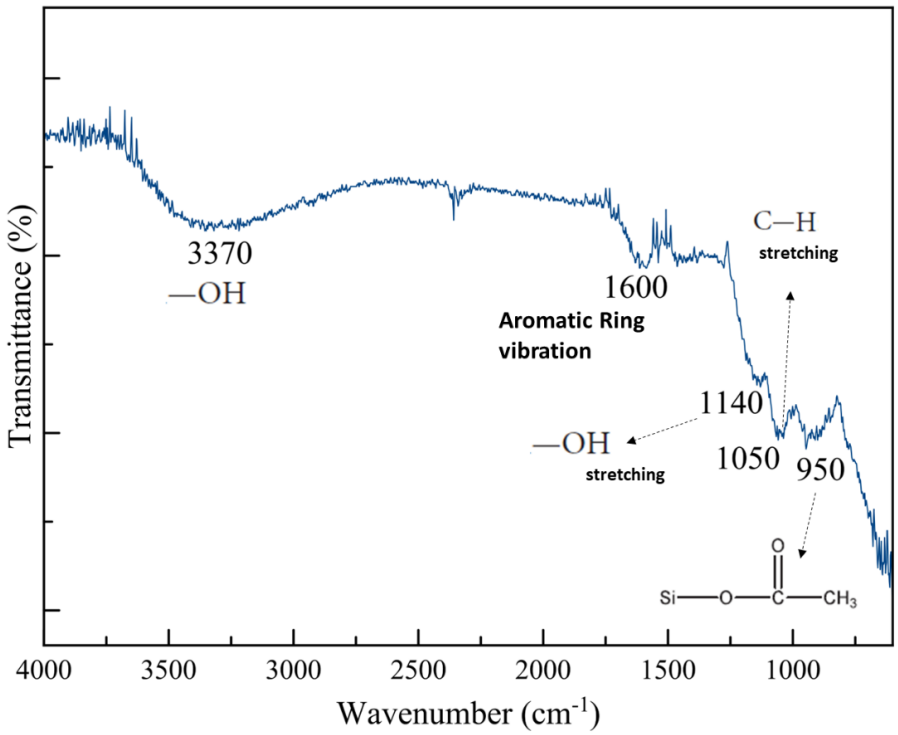

Figure II-10: FTIR spectrum from DR Lignin/Silica Silicon hybrid coating.

Considering the study of these different coatings, it is clear the direct route is not an adapted way to fit with all expected requirements of this work. It produced quite hydrophilic and poor homogeneous hybrid lignin-silicon layers that would probably not protect enough the Al 2024 parts from corrosion.

Finally, to start on valuing the hydrophobic character of the designed coatings, some first wettability tests were performed. Since the objective of this work is to develop anti-corrosion coatings, the creation of hydrophobic primer materials becomes essential. Indeed, for the aeronautical industry, the sector with the most corrosive wear is the one in direct contact with aqueous fluids[42].

The WCA analyses (Figure II-11) did not show great differences for 10% RH coatings with a mean value around 50° (50.3, 51.1 and 49.1 degrees for 0.05 mm/s, 0.70 mm/s and 5.00 mm/s respectively) which is unsatisfactory as it corresponds to extremely hydrophilic behavior.

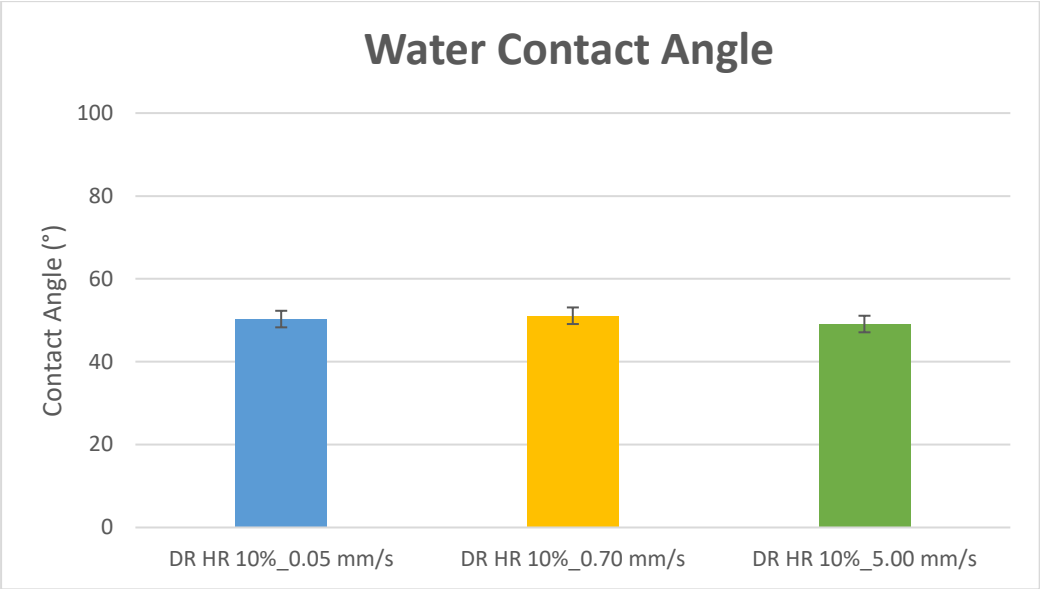

Figure II-11: Water Contact Angle of the different DR coated substrates under 10% RH.

To confirm that the 10% RH deposition parameter was the most satisfactory, the adhesion of the coatings made at the 3 speed regimes was checked and compared (Figure II-12). The result obtained shows that samples made at 0.70 mm/s and 5.00 mm/s (w.s.) were classified as grade 1, the best possible among the 6 grades, with less than 5% of coating being removed by the test. The sample made at 0.05 mm/s was classified as grade 2, the second-best grade, with a percentage between 5% and 15% of coating removal. Even though the result was worse for the sample taken in the capillary regime, it still meets the requirements for an efficient coating.

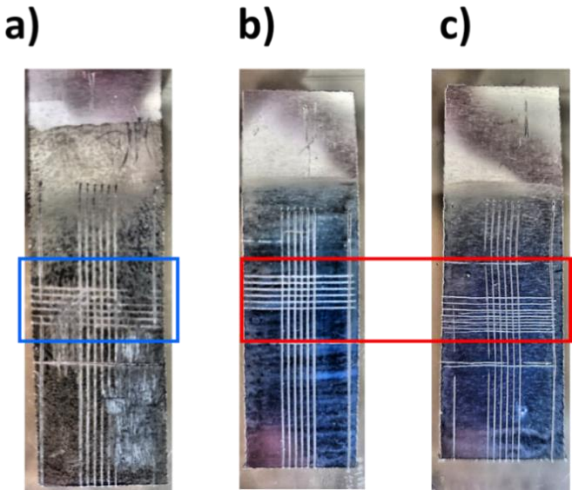

Figure II-12: Adhesion Test results for 10% RH lignin/silicon hybrid for a) 0.05mm/s, b) 0.70 mm/s and c) 5.00 mm/s withdrawal speeds.

Considering the better coating density obtained and the same similar results regarding the Al presence and wettability, the capillary regime (withdrawal speed 0.05 mm/s) was selected as the starting system to further explore and optimize the design of lignin/silicon hybrid bio-sourced primers, even though the slightly worse adhesion grade obtained. A quite thick primer coating is a demanded parameter by aircraft industry coatings, as

reported by Monette, D. L.[43] and Martínez-Viademonte, M. P. et al.[3], so the capillary regime alloy us to be in the correct coating range (> 2µm).

3.2. Non-Direct Route (NDR)

3.2.1. Al 2024 surface pre-functionalization

SEM analysis after the TESPSA pre-functionalization of Al2024 substrate revealed an unchanged morphology in comparison to prepared surface (Figure I-17), keeping the same apparent rough aspect with some dispersed holes and isolated surface particles (Figure II-13 a)). At high magnification, surface details confirm the presence of covering matter on the surface with a foamy aspect (Figure II-13 b)), which could attest of the good efficiency of the treatment.

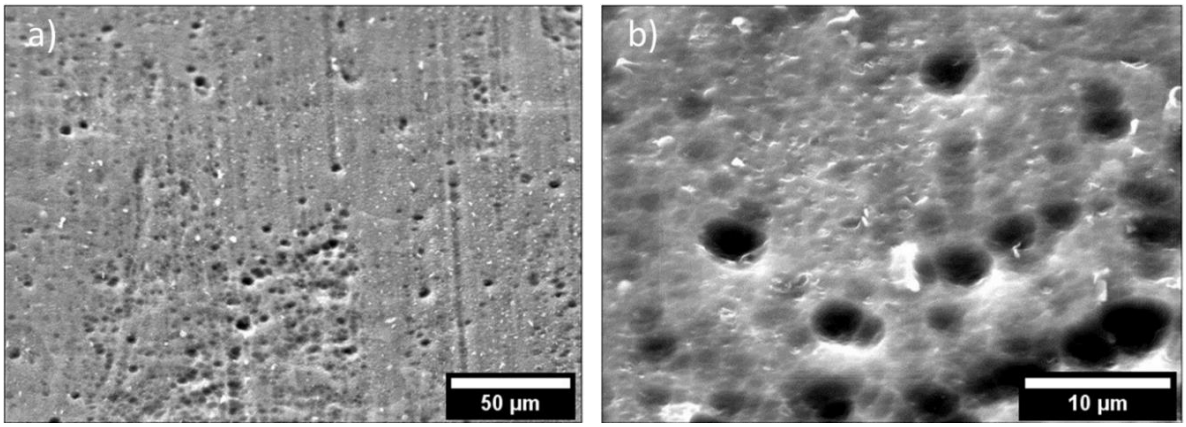

Figure II-13: SEM images from Al 2024 after surface functionalization. a) Magnified x500 and b) x3000.

XPS analysis clearly confirmed a new surface chemical environment, with the presence of silicon signals (Si 2p at 102.5 eV and Si 2s at 153.4 eV, respectively) (Figure II-14 a)). These corresponding binding energies confirm the linking between the coupling agent and the Al 2024 surface, in the form of a $RSiO_3$-Metal[44] bond, matching the exactly expected interaction indicated in Figure II-4.

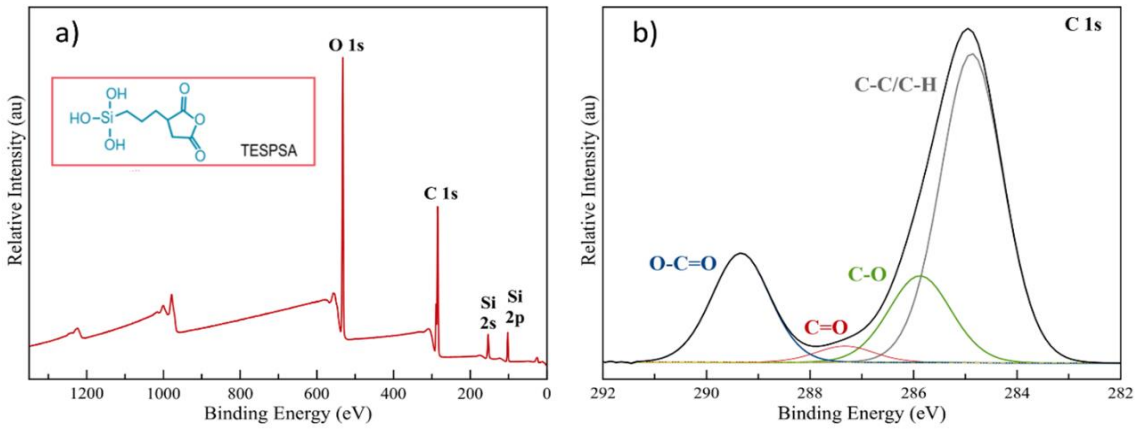

Figure II-14: XPS spectra of TESPSA functionalized Al 2024 substrate: (a) survey spectrum and (b) C1s core level spectrum.

The observation of an intense C 1s component at 289.3 eV ascertained the existence of the O-C=O function of TESPSA molecule (Figure II-14 b)). This peak counts for 12% of the total carbon composition which is in good agreement with the theoretical value of 15%, and the $O_{(O=C)}$/Si ratio of 2.05 (expected value of 2.0) confirmed the grafting of the succinic precursor (Table II-7). The C-C/C-H, C-O and C=O at 284.9 eV, 286.2 eV and 287.3 eV respectively are mainly related to the rest of TESPSA pattern. A remarkable point is the total absence of Aluminum on the analyzed surface, stating the pre-functionalization process uniformity with a layer thicker than 7 nm, the maximal mean XPS depth analysis capacity[45].

Table II-7: XPS quantification of TESPSA functionalized Al 2024 substrate.

Core Peak	Functionalized Al 2024 Substrate		
	BE(eV)	at.%	Total At. Conc (%)
C 1s	284.9	38.3	58.4
	286.2	7.0	
	287.3	0.9	
	289.3	12.1	
O 1s	532.3	18.7	31.0
	533.5	12.3	
Si 2p	102.5	10.7	10.7

3.2.2. Non-Direct Route (NDR) coating

The hybrid lignin/silicon NDR coating elaborated in the same conditions present a homogeneous aspect, but with an extremely high presence of over structures on the top surface (Figure II-15 a)). The magnified SEM image (Figure II-15 b)) allows us to presume that an interconnected network was formed with spherical lignin particles as nodes maybe with some inorganic phase crossing branches. Some small cracks can also be verified and are justified by the important thickness (5.46 ± 0.2 µm) of the layer formed after the dip-coating process as already reported with a TESPSA pre-functionalization of the substrate[46]. Different from what was observed in the direct route, these cracks are not present along the whole surface and present in small quantities.

In order to anticipate the hybrid coating structure, a lignin coating was also designed from a solution without the inorganic precursor, “Solution B” (defined on the Chapter I - 2.3.), and will be used as a reference material for comparative discussion. The produced coating was called NDR-Lignin. The morphological aspect of the coating showed a pretty good homogeneous surface covering layer (Figure II-15 c)) attesting the efficient anchorage of lignin on TESPSA. In addition, the presence of some spherical micro particles is noticed probably referring to aggregated lignin (Figure II-15 and c)).

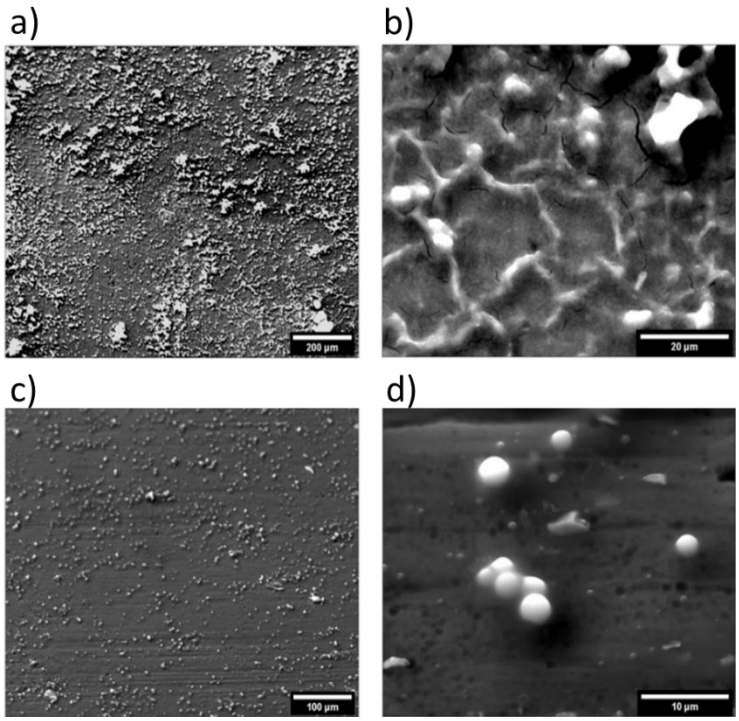

Figure II-15: SEM images of lignin (a, b) coatings on Al 2024 substrate prepared through the NDR route, x250 and x3000 magnified respectively and hybrid lignin/silicon (a, b) via NDR route x250 and x1500 magnified respectively.

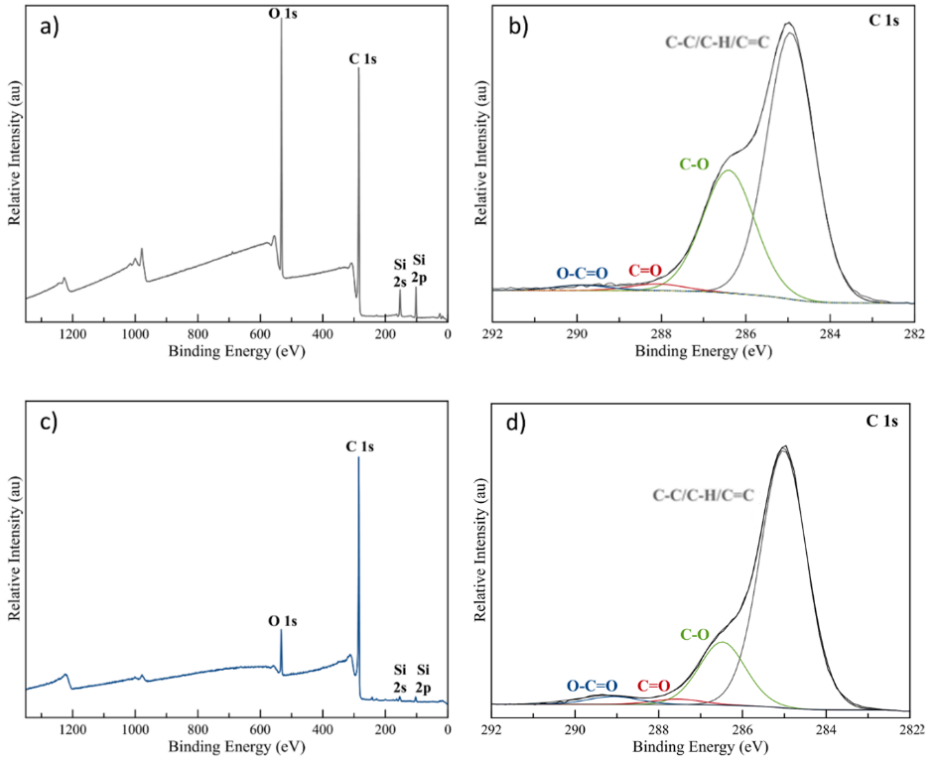

Figure II-16: XPS spectra from NDR Al 2024 substrates: a) Survey spectrum of NDR – Lignin coating, b) Carbon 1s core level spectrum of NDR- Lignin coating, c) Survey spectrum of NDR – Lignin/Silicon coating and d) Carbon 1s core level spectrum of NDR- Lignin/Silicon coating.

XPS analysis was carried out to survey the chemical composition peculiarities with the NDR mode. It can be noticed the carbon content of the NDR Lignin/silicon hybrid material has significantly increased at the same time the silicon signal decreased compared to NDR Lignin coatings (Figure II-16 a) and c) and Table II-8. The chemical quantification also showed that the Si 2p signal for NDR-Lignin was of 7.9 at.% (coming exclusively from TESPSA) , while for the NDR lignin/silicon the content went down to 3.2 at.% in relation with a higher thickness and/or density of the hybrid coating. In addition, the C/O ratio of NDR-Lignin was equal to 3.05 and almost 3.8 for NDR lignin/silicon, a result very close to the 3.7 value of reference Kraft © lignin. Moreover, the NDR lignin/silicon C 1s core level peak profile (Figure II-16 d)) matches almost identically with the NDR lignin and the Kraft lignin reference material. This would tend to confirm the presence of Kraft © lignin on the top surface of the coating.

Table II-8: XPS quantification analysis of NDR-Lignin and NDR-Lignin/Silicon coated samples.

Core Peak	NDR-Lignin			NDR-Lignin/Silicon		
	BE (eV)	at.%	Total At. Conc (%)	BE(eV)	at.%	Total At. Conc (%)
C 1s	284.9	47.9	69.3	285.0	58.7	76.7
	286.5	18.9		286.5	14.6	
	287.9	1.7		287.6	1.3	
	289.5	0.8		289.4	2.1	
	-	-		-	-	
O 1s	533.0	22.8	22.8	532.9	20.1	20.1
Si 2p	102.5	7.9	7.9	103.0	3.1	3.2
C/Si	8.7			24.0		

Moreover, the C/Si ratio increased from 7.6 for DR lignin/silicon to 24 for NDR lignin/silicon, elsewhere enhancing the material stability and improving the lignin deposition. This result tends to show a difference in the coating structure *via* both routes with probably less lignin relative amount within DR coatings in the conditions of deposit.

For the NDR-Lignin comparative material, the value of C/Si ratio is only 8.7, what tends to suggest a synergistic effect of hybridization with TEOS to form a stable organic/inorganic layer. The binding energy values of Si 2p for NDR-Lignin and NDR lignin/silicon in Table II-8 are 102.5 eV and 103.0 eV, respectively. As reported by Paparazzo, E. et al.[47],the binding energy for pure SiO_2 is very close to 104.0 eV. Then, it can be admitted that for both NDR-Lignin and NDR lignin/silicon, SiO_2 chemical environment is not found in the coating composition. The situation is then to consider a less electronegative chemical surrounding around the silicon atoms, decreasing the

identified Si 2p (and Si 2s) binding energies. In this direction, for NDR lignin/silicon coating, the 103.0 eV Si2p BE is characteristic a siloxane network[48,49]. The 102.5eV for the NDR lignin is assigned to the TESPSA sublayers.

As previously done for the DR route coatings, a FTIR-ATR was performed on the NDR Lignin/Silicon coating prepared from the dip-coating process under 10% RH and a 0.05 mm/s withdrawal speed (Figure II-16). Bands related to symmetric and asymmetric stretching vibration of the Si-O-Si bonds were found at 800 cm^{-1} and between 1000-1300 cm^{-1}, respectively, and signals related to asymmetric stretching vibration of the C-O, C-C and C-H bonds of the lignin were recorded. The strong band at 1700-1750 cm^{-1} matches the C=O stretching vibrations from the non-dissociated -COOH, -OC-O-Si or -OC-O-C groups. Finally, as in the Kraft © lignin reference (Figure I-13), the bands at 3370 cm^{-1} and 2920 cm^{-1} corresponds to OH bonds stretching and to the stretching movement of methyl groups, respectively[50].

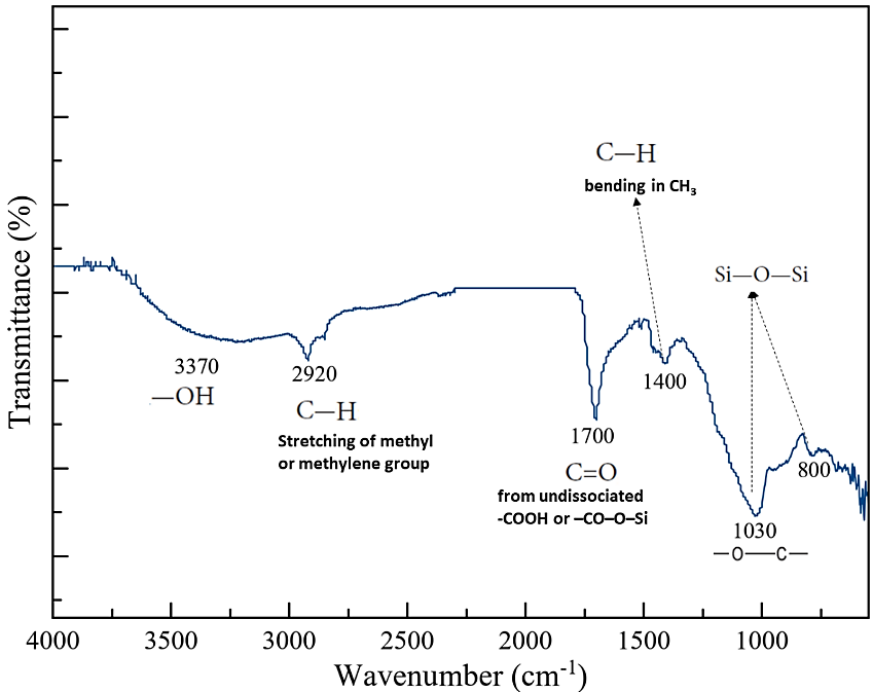

Figure II-17: FTIR spectrum from NDR Lignin/Silicon hybrid coating.

From the collection of the XPS and the FTIR-ATR results, an esterification process, described in Figure II-18, is considered with a possible mechanism responsible for the emergence of lignin particles on the top surface of the coating. Compared to the DR pathway, such a process would increase the stability of the lignin implementation *via* the formation of ester bonds by the reaction between the -OH groups of lignin and the carboxylic acid groups of TESPSA. Furthermore, Chen, R. et al.[51] has shown that cross-linking of TEOS with TESPSA might be considered. In this case, both co-hydrolysis and co-condensation processes occur between the silicon precursor and the carboxylic acid groups of the succinic acid linker. The use of an acid catalyst would facilitate this pre-reaction and would improve the stability of the hybrid coating. These reactions would then contribute to the formation of a strong, interconnected mixed lignin/silica network due to the possibility to create covalent bonds both from both lignin and silicon sources with the succinic linker.

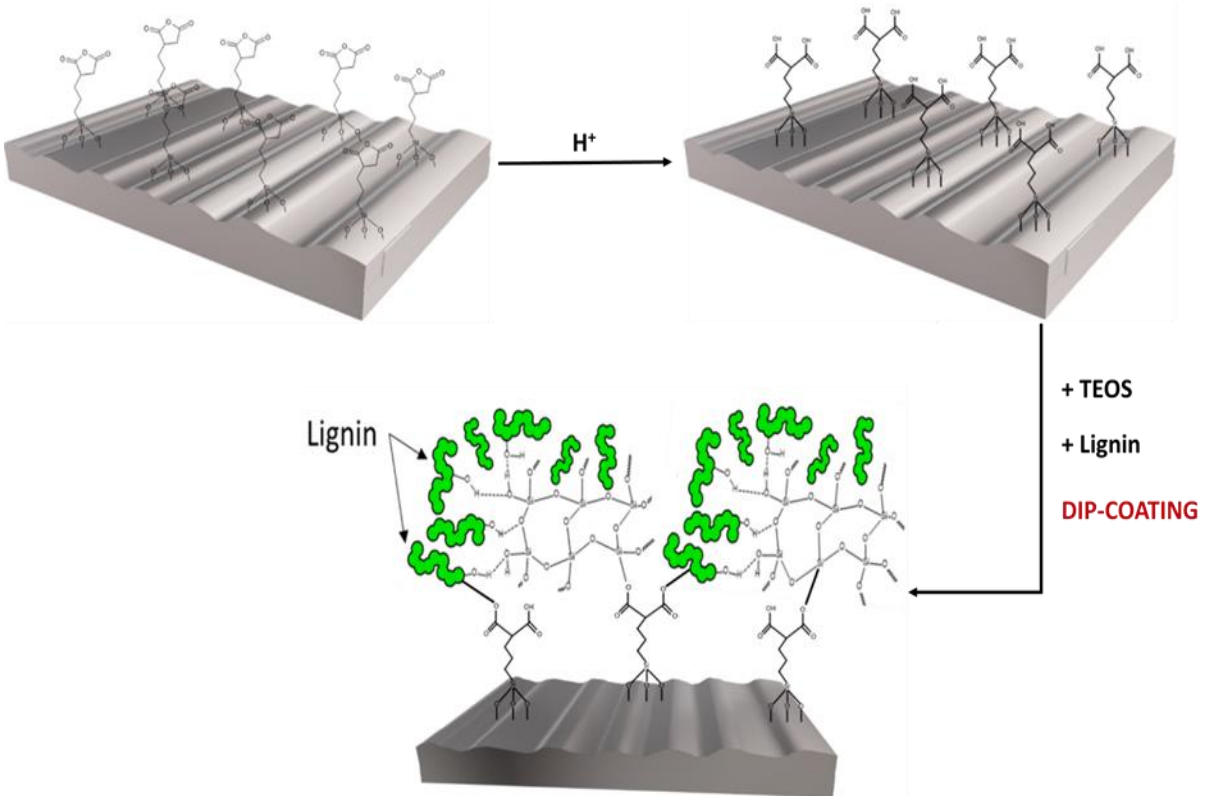

Figure II-18: Proposed esterification mechanism between Lignin/Silicon hybrid and the TESPSA.

Beside the previous study, a complementary XPS specific experiment was initiated with the coupling with a systematic Ar^+ ion etching. The objective of such initiative was to perfectly know about the bonding primer properties that may promote and maintain adhesion between the substrate and the future topcoat (not developed in this work). The experiment consisted of etching cycles to release the coating matter and to access to the inner chemical composition down to the substrate. Each etching cycled was associated with an XPS survey. This XPS depth profile campaign of the NDR Lignin/Silicon coating (Figure II-19 a) was performed accordingly to the settings described in Appendix. The main chemical content of C, O and Si elements was then followed with the etching time evolution Figure II-19 b)).

After 100 seconds of etching (about 0.23 µm of etched material), the Si 2p signal still present the same single component at around 103.0 eV, attesting the already reported carbon species/silicon network[52]. Moreover, the unchanged C 1s core level deconvolution spectrum (Table II-9) always indicates the presence of lignin and the homogeneity of the coating along the coating surface. No aluminum signal is recorded at this stage as can be seen in Figure II-19 d).

Table II-9: XPS quantification analysis of NDR Lignin/Silicon sample before and at different times of Ar^+ etching.

Core Peak	NDR-Lignin/Silicon			NDR-L/S 100 sec etched			NDR-L/S 1000 sec etched		
	BE (eV)	at.%	Total At. Conc (%)	BE (eV)	at.%	Total At. Conc (%)	BE (eV)	at.%	Total At. Conc (%)
Al 2p	-	-	-	-	-	-	73.3	0.6	2.9
	-	-		-	-		73.7	0.3	
	-	-		-	-		74.2	0.3	
	-	-		-	-		75.4	1.7	
C 1s	285.0	58.7	76.8	284.9	70.7	88.6	285.1	41.3	49.6
	286.5	14.0		286.3	12.8		286.4	5.0	
	287.6	1.6		287.7	2.2		287.7	2.2	
	289.3	2.4		289.3	2.9		289.3	1.1	
O 1s	532.7	20.1	20.1	533.0	7.3	7.3	533.3	26.0	26.0
Si 2p	103.0	3.2	3.2	103.2	4.1	4.1	102.4	12.9	21.5
	-	-		-	-		104.1	8.6	
C/Si		24.0			21.6			2.3	

With a longer time of etching (1000 seconds - about 2.5 µm of etched material), the chemical environments evolve. The Si 2p signal splits into two components, at 102.4 eV and 104.1 eV, respectively corresponding to a TESPSA-Metal[54] environment as previously reported and to a SiO_2[53] phase (Figure II-19 e)). After 1000s etching, the XPS analysis probes the metal-coating interface and the Al 2p signal appears with the components assigned to aluminum oxide, Al^0 and the (oxy)hydroxylated aluminum species (Figure II-19 e)).

Through the etching process, a drastically C/Si ratio reduction is observed from the original value of 24.0 to the final one, 2.3, after 1000 sec of etching. This would confirm the previous hypothesis that the lignin tends to be locate more in the top part of on the coating surface, where its concentration is the highest; deeper in the material the lignin content decreases and some SiO2 phases would replace the siloxane network (presence of Si-O vibrations like in SiO_2 was previously noticed in the FTIR-ATR study which probed more the material bulk). This chemical organization highlights the complexity of the NDR lignin/silicon hybrid coating building during the deposition and the anchorage onto the pre-functionalized Al 2024 substrate.

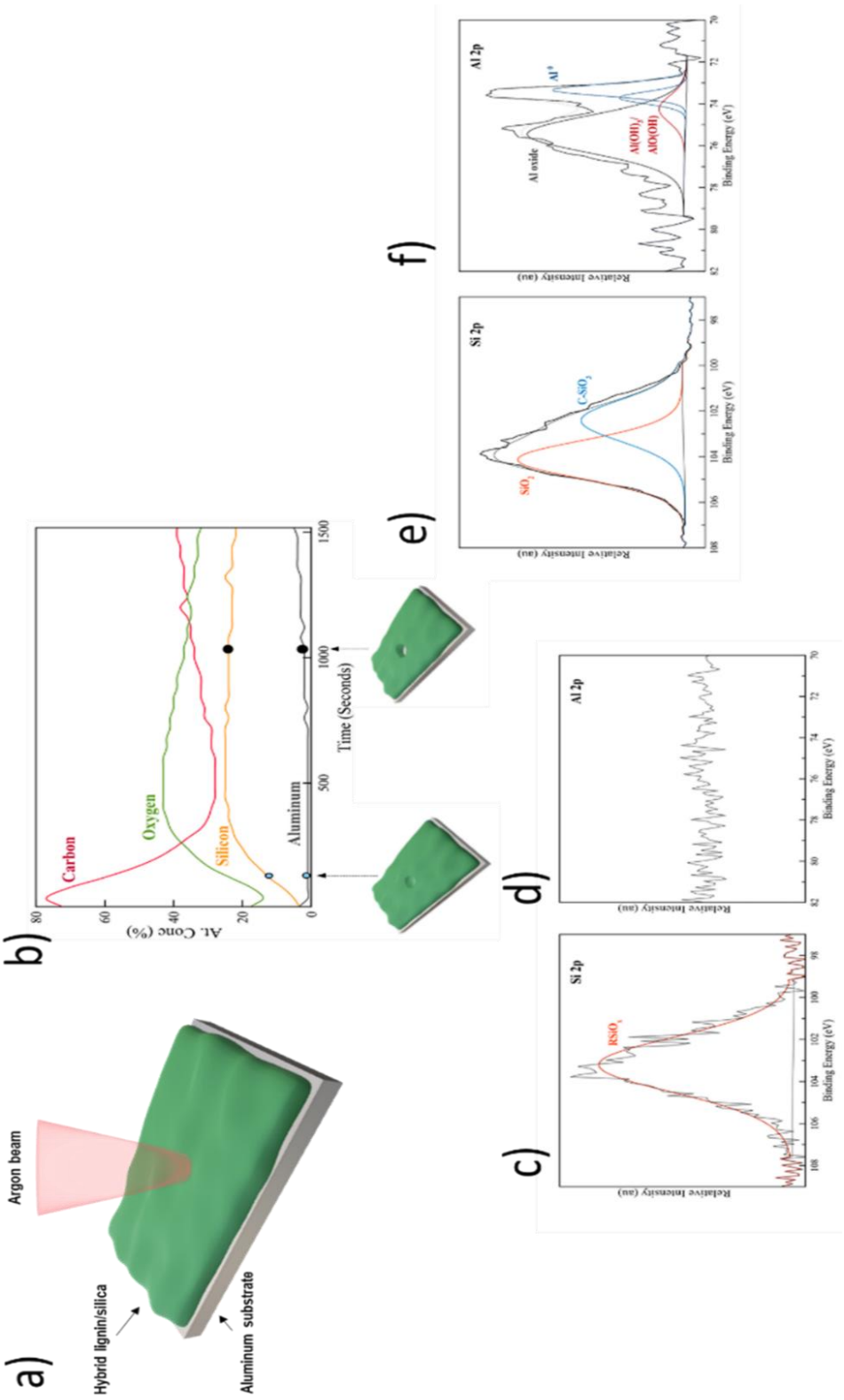

Figure II-19: Depth profile analysis of NDR Lignin/Silicon coating: a) graphical representation of the procedure, b) evolution of the elements concentration (at.%) during the etching process, c) XPS spectra of Al 2p core level spectrum after 100 sec of Ar^+ etching , d) Si 2p core level spectrum after 100 sec of Ar^+ etching ,e) XPS spectra of Al 2p core level spectrum after 1000 sec of Ar^+ etching and f) Si 2p core level spectrum after 1000 sec of Ar^+ etching .

The wettability of the of NDR Lignin/Silicon hybrid was evaluated (Figure II-20) and showed a different behavior than what was observed in the DR samples. Indeed, the NDR hybrid presents a surface hydrophobicity with a more pronounced contact angle of 95°. than the corresponding DR coating (WCA of almost 50°).

Part of the explanation for the wettability enhancement can be found in the variation of the surface roughness, since, as explained by Wang et al.[55] for inhomogeneous materials, t the increase in roughness is directly linked to a lower wettability of the material surface according to the Wenzel's theory[56]. The average roughness for the NDR lignin/silicon samples (10% RH, 0.05mm/s w.s.) is 1.56 ± 0.2 µm, while for a DR coating designed in the same conditions, the value is 0.63 ± 0.2 µm (WCA ~ 50°). Finally, for the "prepared" bare Al 2024 substrate, roughness is only 0.45 ± 0.2 µm (for a WCA < 30°), confirming the trend proposed in the Wenzel hypothesis.

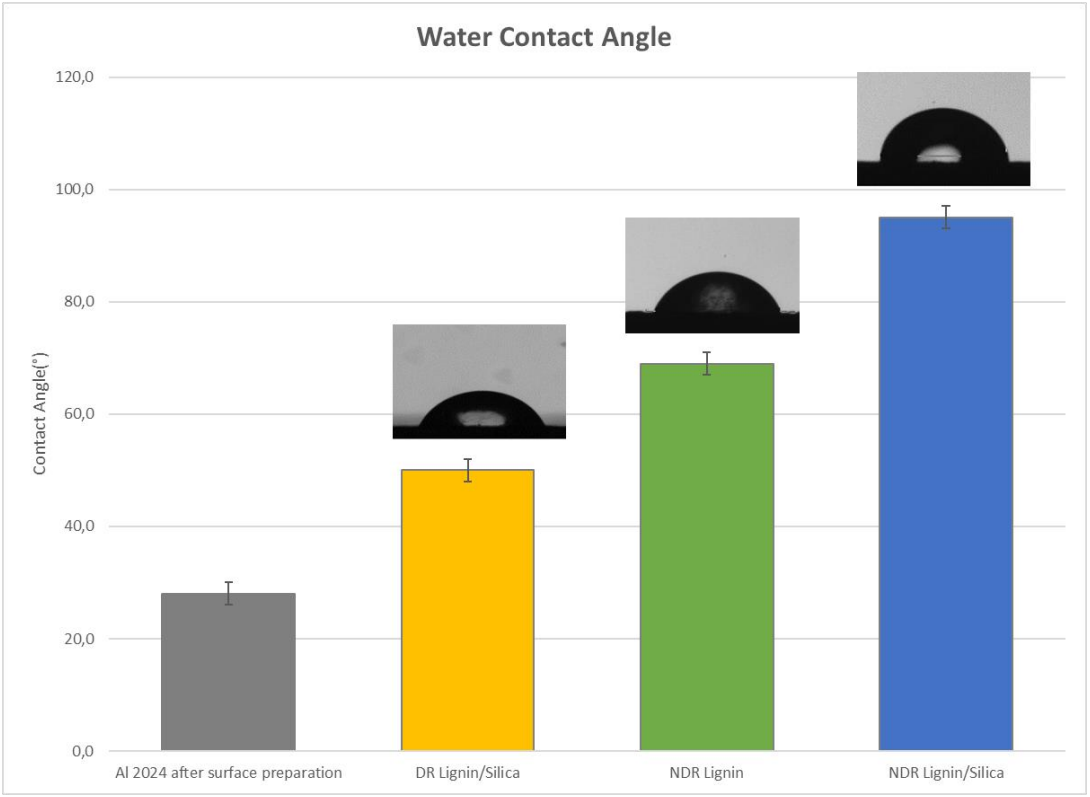

Figure II-20: Comparative water contact angle results of the samples used in this work.

The other part of the explanation around the wettability necessarily depends on the chemical composition of the samples. The esterification reaction on the NDR coating increased the surficial presence of lignin and simultaneously reduced the quantity of OH groups), what improved the hydrophobization[57,58]. The O/C ratio calculation tends to corroborate this point with an inversely proportional tendency already remarked[59]: a value of 1.67 is found for the "prepared" bare Al 2024 substrate, the most hydrophilic material, 0.46 for the DR Lignin/Silicon coating, 0.33 for the NDR Lignin and finally 0.26 for the most hydrophobic NDR Lignin/Silicon surface.

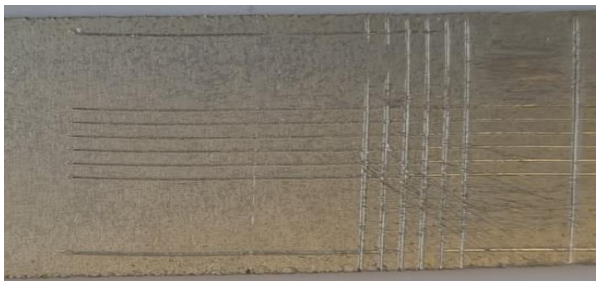

Figure II-21: Adhesion test results for NDR hybrid coating.

The adhesion test in NDR hybrid (Figure II-21) presented the same grade 2 result observed for the DR coating made at 0.05mm/s w.s. This result indicates that, despite the completely different structural organization of the non-direct route, the final adhesion of the "pre-functionalization layer and hybrid coating" arrangement is not impacted.

Chapter Summary

The elaboration of lignin/silicon coatings was conducted from a solution containing silicon and lignin solubilized into tetrahydrofuran (THF). Two routes of coatings preparation have been explored: by lay down the coating directly on the clean Al2024 substrate (DR) or on TESPSA modified Al2024 substrate. The combination of results pointed out the weaknesses of the direct route in making hybrid coatings with an expected good covering aspect and homogeneity, while NDR is more adapted to fill the requirements. Some specific points were highlighted among others:

- The coatings made from DR did not produce coatings with appropriate covering aspect, showing defects whatever experimental conditions and revealing some uncovered substrate zones with a surficial aluminum content varying from 1.5 at.% to 12.2 at.%.
- Under extreme humidity conditions tested of (70% RH), the coatings aspects are full of defects. It could be supposed the high value of moisture leads to different processes within the coating: i) a possible enhancement of the polycondensation of siloxane oligomers instead of a real interconnected lignin/silicon hybrid network, and ii) the expected decrease of the solvent evaporation. These events would penalize the good structuring of the coatings. On the contrary of some organic solvents, the relatively high vapor pressure of THF usually hindered the formation of pores[60]. With water condensation at the surface of the coating, THF should desperately try to get out of the confinement and bubble effect, random surficial defects would be generated.
- Moreover, coatings elaborated with a withdrawal speed of 5.00mm/s appeared the thinnest materials in the series. The effect of the humidity at this stage could even undergo but it seems thickness of siloxane type coatings would generally tend to increase with moisture content[61]. This could correspond to a swelling of the hybrid material when water amounts stay capillary entrapped in the network. Lignin gets a high molecular weight, and, in that case, a quick deposition speed could suffer of inefficiency. There would not be enough time for the hybrid to better bond to the substrate, and consequently, the matter that succeeded to lay down is extremely thin and inhomogeneous.
- Coatings designed at 10% relative humidity by the direct route have shown an improvement that allowed to consider that drier deposition conditions have a beneficial effect on coatings. Indeed, a chemical mapping performed on the DR coating laid down with 0.05mm/s withdrawal speed under 10% RH showed a distribution pattern of the chemical elements over the substrate with a crossing network of the lignin. From these observations, the combination RH 10% with a 0.05mm/s withdrawal speed was determined as the most optimized combination for preparing coatings in adequate aspect. Unfortunately, the water contact angle test for DR coatings underlined their hydrophilic character (WCA of around 50°) and suggested then a bad adequacy with the expected anticorrosion purpose.
- At 10%RH, evaporation ability of THF is reinforced probably leading to a quickest initiation of lignin and TEOS interaction. Leskinen et al.[62] recently reported a sensitive evolution of a lignin molecular solution towards colloid particles with the decrease THF mass concentration in the medium. This work is enough

convincing to understand the appearance of particles of lignin at the surface that are enhanced with the NDR mode of preparation.

- To improve the coatings behavior, especially relate to some covering aspect and anti-corrosion protection, new coatings were designed by implementing a pre functionalization step of the Al2024 substrate with TESPSA molecules. The so-called NDR coatings then prepared in 0.05mm/s withdrawal speed under 10% RH selected conditions offer a much better homogeneous and covering aspect in comparison with DR RH 10 %.
- A precise study of the in-depth structure of the NDR coating conducted with the XPS depth profile methodology revealed a complex organization with some multiple layers of different chemical composition. FTIR-ATR analysis of the NDR lignin/silicon hybrid confirmed this trend with some Silicon based entities-Lignin interactions with a band at 800 cm^{-1} (SiO_2 network) and 1700-1750 cm^{-1}, that among other signals can identify the -OC-O-Si structure. Finally, a better wettability character was measured for NDR Lignin/Silicon coating with a water contact angle of about 95°.

References

1. Zarras, P., & Stenger-Smith, J. D. (2014). *1 - Corrosion processes and strategies for prevention: an introduction* (A. S. H. B. T.-H. of S. C. for M. P. Makhlouf (ed.); pp. 3–28). Woodhead Publishing. https://doi.org/https://doi.org/10.1533/9780857096883.1.3
2. Lee, J., Kim, Y., Jang, H., & Chung, W. (2014). Cr2O3 sealing of anodized aluminum alloy by heat treatment. Surface and Coatings Technology, 243, 34–38. https://doi.org/https://doi.org/10.1016/j.surfcoat.2012.05.071
3. Martínez-Viademonte, M. P., Abrahami, S. T., Hack, T., Burchardt, M., & Terryn, H. (2020). A review on anodizing of aerospace aluminum alloys for corrosion protection. Coatings, 10(11), 1–30. https://doi.org/10.3390/coatings10111106
4. Aircraft, W., Limited, E., Engineered, C., Central, P. P. G., Representative, O., Desoto, P. R. C., Aircraft, W., Limited, E., & No, E. C. (2017). Use of strontium chromate in primers applied by aerospace and defence companies and their associated supply chains.
5. Dolling, C., Roger Hudson, C. P. (2003). Steel Buildings - Chapter 12 Corrosion Protection (The British Constructional Steelwork Association Ltd (ed.)).
6. Bierwagen, G., Brown, R., Battocchi, D., & Hayes, S. (2010). Active metal-based corrosion protective coating systems for aircraft requiring no-chromate pretreatment. *Progress in Organic Coatings*, *68*(1–2), 48–61. https://doi.org/10.1016/j.porgcoat.2009.10.031
7. Nanna, M. E., Bierwagen, G. P., & Dakota, N. (2004). Mg-Rich Coatings : A New Paradigm for Cr-Free Corrosion Protection of Al Aerospace Alloys. *Journal of Coatings Technology and Research*, *1*(2), 69–80. https://doi.org/10.1007/s11998-004-0001-7
8. Prakashiah, B., Shetty, A., & Rani, B. (2019). Improvement of Anticorrosion Properties of Epoxy Primer Coating on Aluminum Alloy 2024-T3 by Thiosemicarbazone Derivatives. *JOM*, *71*. https://doi.org/10.1007/s11837-019-03615-4
9. Gharbi, O., Thomas, S., Smith, C., & Birbilis, N. (2018). Chromate replacement : what does the future hold ? *Npj Materials Degradation*, *February*, 23–25. https://doi.org/10.1038/s41529-018-0034-5
10. Battocchi, D., Simões, A. M., Tallman, D. E., & Bierwagen, G. P. (2006). Electrochemical behaviour of a Mg-rich primer in the protection of Al alloys. *Corrosion Science*, *48*(5), 1292–1306. https://doi.org/https://doi.org/10.1016/j.corsci.2005.04.008
11. Abreu, C. M., Izquierdo, M., Merino, P., Nóvoa, X. R., & Pérez, C. (1999). A New Approach to the Determination of the Cathodic Protection Period in Zinc-Rich Paints. *Corrosion (Houston)*, *55*(12), 1173–1181. https://doi.org/10.5006/1.3283955
12. Snihirova, D., Lamaka, S. V, & Montemor, M. F. (2016). 4 - Smart composite coatings for corrosion protection of aluminium alloys in aerospace applications. In M. F. B. T.-S. C. C. and M. Montemor (Ed.), Woodhead Publishing Series in Composites Science and Engineering (pp. 85–121). Woodhead Publishing. https://doi.org/https://doi.org/10.1016/B978-1-78242-283-9.00004-X

13. Group, S. B. (2009). Guidance Note High performance paint coatings.
14. Peltier, F., & Thierry, D. (2022). Review of Cr-Free Coatings for the Corrosion Protection of Aluminum Aerospace Alloys. In *Coatings* (Vol. 12, Issue 4). https://doi.org/10.3390/coatings12040518
15. Thirumalai, S. V. K. E.-J. (2017). Advanced Multifunctional Corrosion Protective Coating Systems for Light-Weight Aircraft Alloys—Actual Trends and Challenges (p. Ch. 10). IntechOpen. https://doi.org/10.5772/67237
16. Gao, C., Zhao, X., Dong, X., Wang, S., Liu, K., Dong, X., Wang, S., & Kong, F. (2020). Construction of eco-friendly corrosion inhibitor lignin derivative with excellent corrosion-resistant behavior in hydrochloric acid solution. *Materials and Corrosion*, *71*(11), 1903–1912. https://doi.org/https://doi.org/10.1002/maco.202011799
17. Verma, C., Ebenso, E. E., Bahadur, I., & Quraishi, M. A. (2018). An overview on plant extracts as environmental sustainable and green corrosion inhibitors for metals and alloys in aggressive corrosive media. *Journal of Molecular Liquids*, *266*, 577–590. https://doi.org/https://doi.org/10.1016/j.molliq.2018.06.110
18. European Commision|Community Research and Development Information Service (CORDIS). ECOLAND project (2018) - Development of ECO-friendly protection procedures for LANDing gear aluminium alloys.DOI:10.3030/785412.
19. Ouarga, A., Noukrati, H., Iraola-arregui, I., & Elaissari, A. (2020). Progress in Organic Coatings Development of anti-corrosion coating based on phosphorylated ethyl cellulose microcapsules. *Progress in Organic Coatings*, *148*(May), 105885. https://doi.org/10.1016/j.porgcoat.2020.105885
20. Dastpak, A.; Yliniemi, K.; Monteiro, M. C. de O.; Höhn, S.; Virtanen, S.; Lundström, M.; Wilson, B. P. From Waste to Valuable Resource: Lignin as a Sustainable Anti-Corrosion Coating. Coatings 2018, 8 (12). https://doi.org/10.3390/COATINGS8120454.
21. Harb, S. V., Cerrutti, B. M., Pulcinelli, S. H., Santilli, C. V., & Hammer, P. (2015). Siloxane-PMMA hybrid anti-corrosion coatings reinforced by lignin. Surface and Coatings Technology, 275, 9–16. https://doi.org/10.1016/j.surfcoat.2015.05.002
22. Shorey, R., & Mekonnen, T. H. (2022). Sustainable paper coating with enhanced barrier properties based on esterified lignin and PBAT blend. *International Journal of Biological Macromolecules*, *209*, 472–484. https://doi.org/https://doi.org/10.1016/j.ijbiomac.2022.04.037
23. Dastpak, A., Hannula, P.-M., Lundström, M., & Wilson, B. P. (2020). A sustainable two-layer lignin-anodized composite coating for the corrosion protection of high-strength low-alloy steel. *Progress in Organic Coatings*, *148*, 105866. https://doi.org/https://doi.org/10.1016/j.porgcoat.2020.105866
24. Griffini, G., Passoni, V., Suriano, R., Levi, M., & Turri, S. (2015). Polyurethane Coatings Based on Chemically Unmodified Fractionated Lignin. *ACS Sustainable Chemistry & Engineering*, *3*(6), 1145–1154. https://doi.org/10.1021/acssuschemeng.5b00073
25. Wang, Z., Shen, X., Yan, Y., Qian, T., Wang, J., Sun, Q., & Jin, C. (2018). Facile fabrication of a PDMS @ stearic acid-Al(OH)3 coating on lignocellulose composite with superhydrophobicity and flame retardancy. *Applied Surface Science*, *450*, 387–395. https://doi.org/https://doi.org/10.1016/j.apsusc.2018.04.220

26. Devadasu, S., Bagale, U., Sonawane, S. H., & Suranani, S. (2021). Development of ultra-high build self-healing coatings using amino silanized lignin nanocapsules. *Materials Today: Proceedings*, *45*, 5745–5751. https://doi.org/https://doi.org/10.1016/j.matpr.2021.02.576
27. Schuster, F. (2018). Sol Gel Technologies for Glass Producers and Users.
28. Jeffrey Brinker, C., & Hurd, A. J. (1994). Fundamentals of sol-gel dip-coating. *Journal de Physique III*, *4*(7), 1231–1242. https://doi.org/10.1051/jp3:1994198
29. Faustini, M., Louis, B., Albouy, P. A., Kuemmel, M., & Grosso, D. (2010). Preparation of sol-gel films by dip-coating in extreme conditions. *Journal of Physical Chemistry C*, *114*(17), 7637–7645. https://doi.org/10.1021/jp9114755
30. Mayer, H. C., & Krechetnikov, R. (2012). Landau-Levich flow visualization: Revealing the flow topology responsible for the film thickening phenomena. *Physics of Fluids*, *24*(5). https://doi.org/10.1063/1.4703924
31. L. Landau and B. Levich, "Dragging of a liquid by a moving plate," Acta Physicochimica U.R.S.S., Vol. 17, No. 1-2, 1942, pp. 42-54
32. Grosso, D. How to Exploit the Full Potential of the Dip-Coating Process to Better Control Film Formation. J. Mater. Chem. 2011, 21 (43), 17033–17038. https://doi.org/10.1039/c1jm12837j
33. MB, I.; NC, P. A Comparative Study on Surface Treatments in the Immobilization Improvement of Hexahistidine-Tagged Protein on the Indium Tin Oxide Surface. J. Nanomed. Nanotechnol. 2016, 07 (02). https://doi.org/10.4172/2157-7439.1000372.
34. Mahltig, B. (2016). 10 - Smart hydrophobic and soil-repellent protective composite coatings for textiles and leather. In M. F. B. T.-S. C. C. and M. Montemor (Ed.), Woodhead Publishing Series in Composites Science and Engineering (pp. 261–292). Woodhead Publishing. https://doi.org/https://doi.org/10.1016/B978-1-78242-283-9.00010-5
35. Visscher, M., & Struik, K. G. (1994). Optical profilometry and its application to mechanically inaccessible surfaces Part I: Principles of focus error detection. Precision Engineering, 16(3), 192–198. https://doi.org/https://doi.org/10.1016/0141-6359(94)90124-4
36. ASTM. (2017). Standard Test Methods for Rating Adhesion by Tape Test. https://doi.org/10.1520/D3359-09E02
37. Schneller, T., Waser, R., Kosec, M., & Payne, D. (2013). Chemical solution deposition of functional oxide thin films. Chemical Solution Deposition of Functional Oxide Thin Films, 9783211993, 1–796. https://doi.org/10.1007/978-3-211-99311-8
38. Hatte, Q., Dubos, P. A., Guitter, N., Richard-Plouet, M., & Casari, P. (2019). Influence of relative humidity and temperature on the sol-gel transition of a siloxane surface treatment. *Journal of Sol-Gel Science and Technology*, *90*(2), 230–240. https://doi.org/10.1007/s10971-019-04929-0
39. Tian, Z. R., Liu, J., Voigt, J. A., Xu, H., & Mcdermott, M. J. (2003). Dendritic growth of cubically ordered nanoporous materials through self-assembly. Nano Letters, 3(1), 89–92. https://doi.org/10.1021/nl025828t

40. Ouyang, M.; Yuan, C.; Muisener, R. J.; Boulares, A.; Koberstein, J. T. Conversion of Some Siloxane Polymers to Silicon Oxide by UV/Ozone Photochemical Processes. Chemistry of Materials 2000, 12 (6), 1591–1596. https://doi.org/10.1021/cm990770d.
41. Launer, P.; Arkles, B. Infrared Analysis of Organosilicon Compounds; 2013; pp 175–178.
42. Department, U. S., & Transportation, O. (2018). Corrosion Control for Aircraft - Advisory Circular. Aircraft Corrosion Prone Areas / Aeronautics Guide https://www.aircraftsystemstech.com/2019/05/aircraft-corrosion-prone-areas.html
43. Monette, D. L. (2009). 10 - Coating removal techniques in the aerospace industry. In S. B. T.-C. C. in the A. I. Benavides (Ed.), Woodhead Publishing Series in Metals and Surface Engineering (pp. 225–247). Woodhead Publishing. https://doi.org/https://doi.org/10.1533/9781845695538.3.225
44. Aynard, A.; Pessoni, L.; Billon, L. Directed self-assembly in “breath figure” templating of block copolymers followed by soft hydrolysis-condensation: One step towards synthetic bio-inspired silica diatoms exoskeleton. Polymer, 2020, 210, 123047. https://doi.org/10.1016/j.polymer.2020.123047
45. Welker, R. W. (2012). Chapter 4 - Size Analysis and Identification of Particles (R. Kohli & K. L. B. T.-D. in S. C. and C. Mittal (eds.); pp. 179–213). William Andrew Publishing. https://doi.org/https://doi.org/10.1016/B978-1-4377-7883-0.00004-3
46. Chen, Z.; Burtovyy, R.; Kornev, K. G.; Luzinov, I.; Peng, F. Dense and Crack-Free Mullite Films Obtained from a Hybrid Sol-Gel/Dip-Coating Approach. J. Mater. Res. 2017, 32 (9), 1665–1673. https://doi.org/10.1557/jmr.2017.122.
47. Paparazzo, E.; Fanfoni, M.; Severini, E. Studies on the Structure of the SiOx/SiO2 Interface. Appl. Surf. Sci. 1992, 56–58, 866–872. https://doi.org/https://doi.org/10.1016/0169-4332(92)90352-X.
48. Carlos De Haro, J.; Magagnin, L.; Turri, S.; Griffini, G. Lignin-Based Anticorrosion Coatings for the Protection of Aluminum Surfaces. ACS Sustain. Chem. Eng. 2019, 7 (6), 6213–6222. https://doi.org/10.1021/acssuschemeng.8b06568
49. An, L.; Si, C.; Bae, J. H.; Jeong, H.; Kim, Y. S. One-Step Silanization and Amination of Lignin and Its Adsorption of Congo Red and Cu(II) Ions in Aqueous Solution. Int. J. Biol. Macromol. 2020, 159, 222–230. https://doi.org/10.1016/j.ijbiomac.2020.05.072.
50. Zhang, R.; Xiao, X.; Tai, Q.; Huang, H.; Yang, J.; Hu, Y. Preparation of Lignin-Silica Hybrids and Its Application in Intumescent Flame-Retardant Poly(Lactic Acid) System. High Performance Polymers 2012, 24 (8), 738–746. https://doi.org/10.1177/0954008312451476
51. Chen, R.; Qu, H.; Guo, S.; Ducheyne, P. The Design and Synthesis of a Soluble Composite Silica Xerogel and the Short-Time Release of Proteins. J. Mater. Chem. B 2015, 3 (16), 3141–3149.
52. dos Santos, F. C.; Harb, S. v.; Menu, M. J.; Turq, V.; Pulcinelli, S. H.; Santilli, C. v.; Hammer, P. On the Structure of High Performance Anticorrosive PMMA-Siloxane-Silica Hybrid Coatings. RSC Advances 2015, 5 (129), 106754–106763. https://doi.org/10.1039/c5ra20885h.
53. Wagner, C. D. NIST X-Ray Photoelectron Spectrometry Database. NIST Stand. Ref. Database 20, Version 4.1 1991, 1–76.

54. Budnyak, T. M., Aminzadeh, S., Pylypchuk, I. V., Riazanova, A. V., Tertykh, V. A., Lindström, M. E., & Sevastyanova, O. (2018). Peculiarities of synthesis and properties of Lignin–Silica nanocomposites prepared by Sol-Gel method. Nanomaterials,8(11). https://doi.org/10.3390/nano8110950

55. Wang, J.; Wu, Y.; Cao, Y.; Li, G.; Liao, Y. Influence of Surface Roughness on Contact Angle Hysteresis and Spreading Work. Colloid and Polymer Science 2020, 298 (8), 1107–1112. https://doi.org/10.1007/s00396-020-04680-x.

56. Berg, J. C. (2002). Chapter 1 - Semi-empirical strategies for predicting adhesion (D. A. Dillard, A. V Pocius, & M. B. T.-A. S. and E. Chaudhury (eds.); pp. 1–73). Elsevier Science B.V. https://doi.org/https://doi.org/10.1016/B978-044451140-9/50001-9

57. Hua, Q.; Liu, L.-Y.; Karaaslan, M. A.; Renneckar, S. Aqueous Dispersions of Esterified Lignin Particles for Hydrophobic Coatings. Front. Chem. 2019, 7, 515. https://doi.org/10.3389/fchem.2019.00515.

58. Peng, S. X., Chang, H., Kumar, S., Moon, R. J., & Youngblood, J. P. (2016). A comparative guide to controlled hydrophobization of cellulose nanocrystals via surface esterification. Cellulose. https://doi.org/10.1007/s10570-016-0912-3

59. Zhou, G., Xu, C., Cheng, W., Zhang, Q., & Nie, W. (2015). Effects of Oxygen Element and Oxygen-Containing Functional Groups on Surface Wettability of Coal Dust with Various Metamorphic Degrees Based on XPS Experiment. Journal of Analytical Methods in Chemistry, 2015, 467242. https://doi.org/10.1155/2015/467242

60. Lu, P., & Xia, Y. (2013). Maneuvering the Internal Porosity and Surface Morphology of Electrospun Polystyrene Yarns by Controlling the Solvent and Relative Humidity. Langmuir, 29(23), 7070–7078. https://doi.org/10.1021/la400747y

61. Suratwala, T., Hanna, M. L., & Whitman, P. (2004). Effect of humidity during the coating of Stöber silica sols. Journal of Non-Crystalline Solids, 349, 368–376. https://doi.org/https://doi.org/10.1016/j.jnoncrysol.2004.08.214

62. Leskinen, T., Smyth, M., Yao, X., Lintinen, K., Mattinen, M.-L., Kostiainen, M., Oinas, P., & Österberg, M. (2017). Scaling Up Production of Colloidal Lignin Particles. Nordic Pulp and Paper Research Journal, 32, 586–596. https://doi.org/10.3183/NPPRJ-2017-32-04-p586-596

Chapter III.

Surface Modification of hybrid bio coatings by plasma

Figure List

Table List

As described in Chapter II, the general architecture of a protective systems over a metal part is composed of several layers with dissimilar functions. To provide the adequate stability and viability of such covering combination, a good inter-level cohesion is requisite. Then, beside the ambition to design new materials, a key point of the current scientific thinking is to find out the most appropriate ways to make adjacent layers interact themselves. The adhesion or bonding or anchorage are topics of a great interest as much important as the development of coating materials.

Among the different possibilities to increase the interactions within new materials, which are increasingly used in the aerospace R&D, plasma treatments represent an efficient, clean and economical alternative for modifying the functional properties (e.g., adhesive bonding to metal components, to inorganic/organic sub-layers) of many organic surfaces[1,2,3].

This technology generally offers the opportunity to modify the chemical surface state (kind of "activation") and can even increase the density of cross-links or three-dimensional structures[4]. Regarding surface modification, plasma creates reactive polar functional groups at the surface which can intensely increase the surface free energy, improving the wettability and/or enhancing the adhesion with a topcoat for example.

This is the whole context in where, the continuation of the study is supposed to bring new evidence to improve properties of the developed lignin/silicon coatings. This perspective section was dedicated to monitor the capabilities of coatings to boost their wettability and to offer a better active surface state for a subsequent topcoat deposit.

This research was done during an international mobility period at the Laboratory of Surfaces and Thin Films at Federal University of Rio de Janeiro (UFRJ-Brazil) where the plasma technology built the reputation of the group of Pr. R. A. Simão for years now[5,6,7]. It was applied over the main coatings studied previously (DR and NDR at a 10%RH and 0.05 mm/s withdrawal speed) and the Al 2024 alloy substrate for comparison.

The process stands in the philosophy of the present study with a "green dimension" approach, without the generation of toxic/hazardous sub-products. Its details will be explained in the beginning of this chapter, and a brief bibliographical resume will address, among other points, the Plasma Enhanced Chemical Vapor Deposition (PECVD) method operated in the work. In a second moment, the experimental procedure and the results will be discussed.

As far as this project was developed, it was not possible to identify other works getting the same approach than this one, combining the plasma application with bio-sourced hybrid layers and surface pre-functionalization to achieve a significant hydrophobic material. So, besides the good results and the work continuity, it is important to keep in mind the pioneering aspect of this stage that will need further investigations.

1. State of the art

1.1. Plasma

Plasma is defined as the fourth state of matter, usually consisting of a partially ionized gas, which, on average, is electrically neutral and has both ions and charged species, e.g.: free electrons, positive ions, negative ions and molecules. It can therefore improve or provide new properties to de desired surface from the creation of a thin film layer over the material surface[8]. The process of creating a self-sustaining plasma occurs by using an energy source responsible for ionizing the species that make it up. The plasma that follows the process described above is also called "glow discharge"[9]. The formation of ions in a plasma occurs in two distinct ways, which can be divided between physical and chemical reactions. The schematic presentation of CVD process is illustrated in Figure III-1.

- **Physical Reactions:** are based on the principle of elastic and inelastic collisions that will generate the kinetic energy transmission between the atoms. These reactions usually happen in the presence of electric and magnetic fields, involving the ionization of the species and the ions multiplication[9].
- **Chemical Reactions:** these reactions are going to be much more complex, once multiple types of reactions could happen simultaneously depending on ions and molecules present in the atmosphere[10].

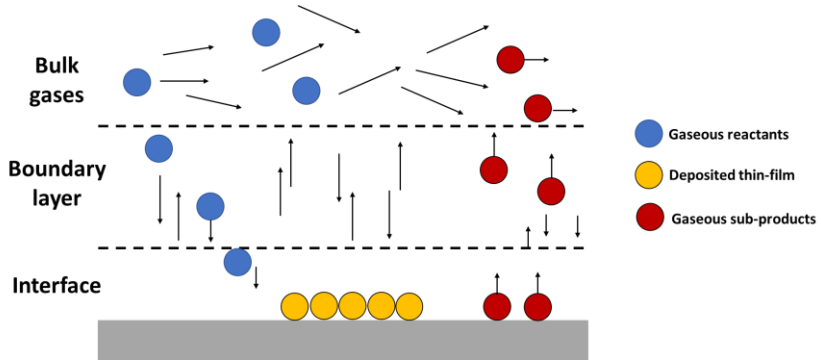

Figure III-1: CVD process schema. Adapted from Spear, K. E[11].

The gas used for this work is the Sulfur hexafluoride - SF_6, and as quoted above several chemical reactions can occur simultaneously during its ionization, as highlighted in the work of Hodak, S. et al.[12].

$$SF_6 \rightarrow SF_5^* + F^*$$

$$SF_5^* \rightarrow SF_4 + F^*$$

$$SF_5^* + SF_6 \rightarrow S_2F_{10} + F^*$$

$$S_2F_{10} \rightarrow 2SF_5^*$$

The plasma provided for this work is called “low-temperature gas discharge” and is created from chemical interactions as mentioned above. This process, that initiates using a gaseous precursor in this work the, belongs to the category of *chemical vapor deposition* events, more specifically to *plasma assisted deposition*.

In these depositions modes, parameters such as working pressure (pressure at which the deposition is done), substrate temperature, gas flow of the plasma reactor and the formation rate of species in the vapor phase are some of the crucial factors that determine the final composition of the thin film created. These and other parameters will be indicated ahead in the Materials and Methods section.

1.2. Chemical Vapor Deposition (CVD)

The chemical vapor deposition (CVD) consists of depositing a solid constituent on a substrate throughout chemical reactions in the gaseous phase, which occur on the material surface (or in the nearest layer closer the surface). The deposition can start itself because of varied chemical reactions, like molecules decomposition or dissociation[13].

Generally, the chemical vapor deposition technique follows a seven steps sequence until the thin film creation[10,14]:

a) Insertion of reactive gases into the deposition chamber.
b) Still within the vapor phase, chemical reactions occur that generates new reactive species and reaction by-products.
c) Mass transport step, during which the specimens generated in step two and the inserted reactive gas are carried to the substrate surface.
d) Surface assimilation and diffusion of the species in the substrate surface (Chemisorption).
e) Chemical reactions and film formation.
f) Desorption of volatile components.
g) Transport of volatiles out of the reaction zone.

1.3. Plasma-Enhanced Chemical Vapor Deposition (PECVD)

As quoted before, the treatment applied on the optimized lignin/silicon hybrid coatings is the PECVD process (Plasma-Enhanced Chemical Vapor Deposition), a derivative of the described CVD; it a plasma as activator of the chemical reactions. The process does not need high temperatures like in CVD[15].

Lower temperatures, but even higher pressures and higher deposition rates are some of the conditions of the PECVD variation[9,10,15].

The production of the thin film by PECVD begins with the introduction of the precursor gases in the reaction chamber and their exposure to the electric field varying with time, which will cause a fraction of the present species to be ionized/excited[16]. Due to their lower masses, the first to react in the field is the free electrons, which will be accelerated and collide (elastically and/or inelastically) with the molecules of the gases used. As electrons are much lighter than the other gas constituents, in most cases, there is no loss of energy in collisions with free electrons. That will generate some highly reactive species and will multiply the free electrons requiring then lower activation energies for deposition on the surface which justifies the lower temperature and higher pressure demand[16,17].

Three plasma reactors can be used for PECVD thin-films production: inductive, capacitive and microwave[10]. In this work the second model was used, which will be detailed below.

The capacitive system, called *Parallel Plates Reactor* or *Reinberg Reactor* (Figure III-2) consists of two symmetrically positioned parallel plates (electrodes) between which the plasma will be formed. In this configuration, known as a direct PECVD process, reactant gases, by-products, substrates and the plasma itself

occupy the same space. The RF source is connected to the upper electrode (anode), while the gas pumping system is connected to the lower plate (cathode)[18].

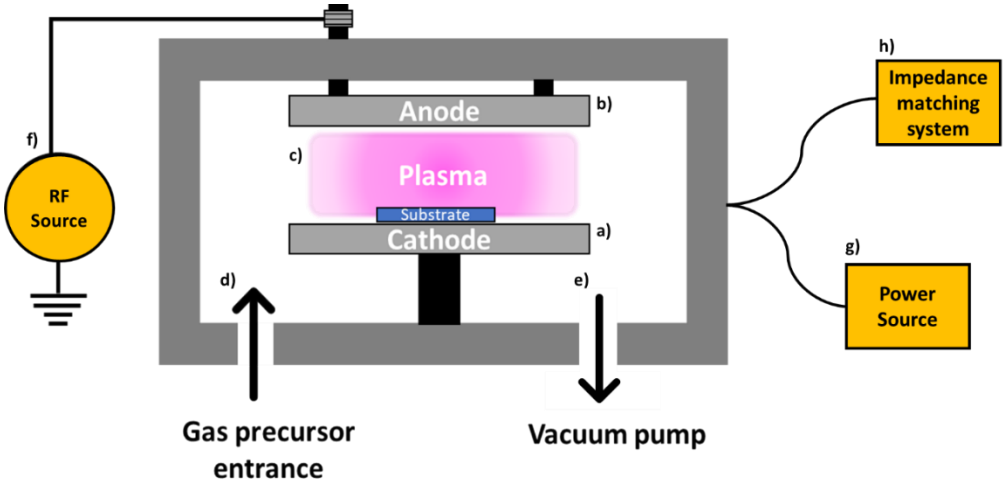

Figure III-2: Schematic representation of a capacitive reactor, indicating the RF source, the vacuum pump, the gas entrance and the plasma formation zone.

The configuration of a diode adopted in the capacitive reactor allows almost every kind of substrates to be recovered in a more uniform and controlled way, when compared to the conventional CVD. With such a flexibility the industrial applications have increased around the material protection and the incorporation of plasma with lignin sourced components.

1.4. Aerospace applications of PECVD/Lignin systems

Some different industrial domains have incorporated PECVD methodology into their manufacturing path to improve or add functionality to their materials. Usually, two groups of applications are related to this technique:

- **Insertion of new properties to the material:** different combinations of precursors (e.g. SF_6, O_2, …) are aligned to materials in order to give them new capabilities, mainly protective aspects (barriers against humidity and hydrophobicity) in the aeronautics and packaging sectors, anti-reflective layers for optical materials, better adhesion from the creation of intermediate nanolayers, enhanced mechanical resistance to wear among others[19,20,21].
- **Surface cleaning:** it's the major use of plasma in the industry with the surface etching created from the plasma (e.g., H_2, Ar, …).

Concerning coatings in the aerospace industry, main focus of this thesis, the work of Haag, J. et al.[22] can be highlighted as an important contribution, once it proves the effectiveness of PECVD to confer an improved adhesion of titanium alloys used in aircrafts after the formation of a thin layer of an organosilicon. For these industrial treatments in larger scales, some big reactors are already available and used, like the systems provided by Kolzer SRL company (Figure III-3) adapted for parts with diameters over one meter[23]. Another promising work to be considered is the precursor study of Kocaman, S. et al.[24] in which PECVD was successfully applied for covering a lignocellulosic based composite system. Study objectives aimed to improve the mechanical and physico-chemical

properties (particularly hydrophobicity and anti-flammability), then proving the capacity to integrate bio-sourced polymers and plasma thin-films.

Figure III-3: Industrial PECVD equipment, provided by Kolzer SRL[23].

Nevertheless the two large groups previously mentioned, this technology is gaining prominence due to its "green" aspect, since: i) it does not produce reaction by-products like most classical chemical reactions, ii) does not expose its users to radiation and toxic gases and iii)neither to dangerous situations like extreme temperatures, as described by Han, Z.J. et al.[25] in their article on nanomaterials fabrication via plasma.

2. Materials & Methods

The reactor used for the coating process of the 2024 aluminum alloy, schematically represented in the Figure III-2, is a Capacitive Coupling System in which the anode and cathode (Figure III-2 a) and b)) are, respectively, 15 cm and 9 cm in diameter and are positioned face to face, creating a plasma formation zone between them (Figure III-2 c)).The substrate is placed in the cathode. To this arrangement are connected an Advanced Energy 13.60 MHz RF source (Figure III-2 f)) with an RFX-600 generator feeding the anode (Figure III-2 g)), an advanced energy impedance matching system (Figure III-2 h)) and an mechanical vacuum pump (Figure III-2 e)). The Figure III-4 below shows the reactor operating and a pink plasma color.

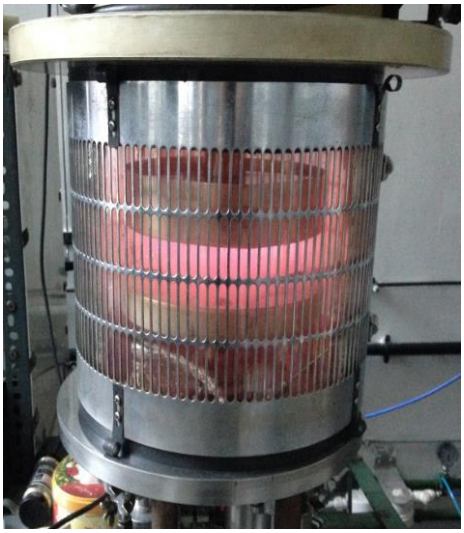

Figure III-4: PECVD reactor used for the plasma deposition.

Coupled to the reactor there is a Sulfur Hexafluoride (SF_6, 99.99% pure from White Martins) (Figure III-2 d)) gas cylinder of, that was used as fluorine source to modify the coatings surface (with the expected creation of a fluorine rich thin overfilm, as explained by Shih et al. [26]). Experimental conditions are presented in Table III-1 below.

Table III-1: Plasma deposition parameters used.

Parameter	Value
Base Pressure (mbar)	2×10^{-2}
Working Pressure (mbar)	2×10^{-1}
Power (W)	135
System Voltage (V)	-10
Time (min)	10

3. Results Discussion

3.1. Al 2024 after PECVD application

A first set of experiments were run on the Al 2024 in order to both optimize the plasma treatment conditions and have a reference result of fluorine species interaction on clean metal substrate as some porosities were observed on designed lignin/silicon coatings and would probably be fill in by fluoride.

After 10min plasma deposit, the contact angle characterization showed the uncoated Al 2024 wettability was highly enhanced, WCA 28° to 77°. This change is the confirmation of the SF_6 film creation over the surface, which generates fluorocarbon or fluorinated aluminum species as previously reported by Dalvi, V. H., & Rossky, P. J.[27] and Satulu, V. et al.[28]. These formed entities have a high capacity to reduce the interactions with water and thus to increase the value of the angle found.

The XPS chemical composition of the plasma modified Al 2024 substrate shows, in which the presence of a F1s peak is highlighted alongside carbon, oxygen, aluminum and silicon signals already been observed in the bare Al 2024 data (Figure III-5 a)) and Table I-7). The complete absence of sulfur at the coating surface can be noticed (Table III-2), indicating, after the decomposition of the SF_6 molecules, the only promotion of fluorine species on the top surface. As stated by the work of Shih, M. et al.[26], sulfur oxyfluorides molecules like SO_2F_2 and SOF_4 are not probable to be formed in low power conditions (below 40 W) in radio-frequency plasmas, what is much less power than what was used in this work. . That could explain the reason why there is not sulfur bonded on the surface. The stoichiometric F/S ratio of initial sulfur hexafluoride also simply explains that much more F is available compared to the S. This fact considerably reduces the opportunities of sulfur to interact with the substrate as already explicited by Koalaga Z. and Andre, P.[29].

Traces of Na and N elements in the composition after the plasma treatment could be related to the presence of some impurities in the plasma deposition chamber.

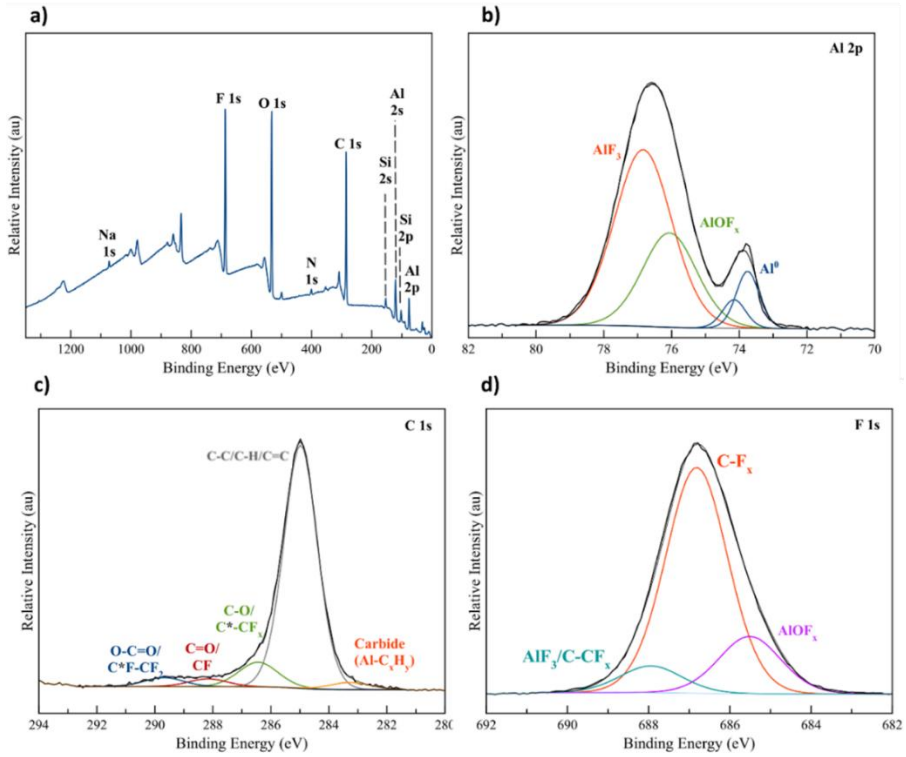

Figure III-5: Al 2024 alloy after SF_6 PECVD treatment.a) General spectrum, b) Al 2p core level spectrum, c) C 1s core level spectrum and d) F 1s core level spectrum. (* for considering carbon in the unit)

The content of aluminum at the alloy surface is multiplied by 3 after the plasma treatment in relation with the strong decrease of the carbon content from 74.7% (Table I-7) to 29.3% after SF_6 exposure. As discussed in the introduction section of plasma technology, an important surface etching effect is noticeable with the release of residues and pollution entities (i.e. hydrocarbon species). The Al 2p core level spectrum (Figure III-5 b)) deconvolution splits into three main species after plasma exposure. The metallic aluminum keeps visible (73.2 - 73.6 eV) but now presenting a BE slightly higher than before, due the presence of electronegative F species in the near surrounding. The two other peaks are related to $AlOF_x$ and AlF_3 respectively at 75.8 eV and 76.5 eV environments[30,31], representing around 64% of the total atomic Aluminum composition of the material. An important consideration is the absence of a clear peak related to Al_2O_3, that may be masked by the presence of the oxyfluorides that appears almost in the same position or because a possible conversion into $AlOF_x$ promoted by the fluorine implementation within the aluminum oxide layer, what has been previously related by Tomko, J. et al.[32].

The C 1s spectrum indicated in Figure III-5 c), in which the referred C is identified with an asterisk, showed the formation of the previously speculated fluorocarbon complexes. As observed in the deconvolution of the peak, bonds referring to C*-CF_x, CF and C*F-CF_2 were created at positions 286.4 eV, 287.9 eV and 289.7 eV respectively[33], overlapping the C-O, C=O and O-C=O bonds previously identified in the bare 2024 alloy. The last identified peak at lower energy is related to the presence of a carbide like structure (Al-C_xH_y - BE 283.3 eV), as already mentioned by DeKoven B.M. and Hagans P.L.[34].

Table III-2: Al 2024 chemical composition after SF_6 PECVD treatment.

Core Peak	BE(eV)	At.%	Total At. Conc (%)
Al 2p	76.5	16.8	29.3
	75.6	1.9	
	73.2	1.0	
	73.6	9.7	
C 1s	285,0	18.2	22.3
	286.4	1.7	
	287.9	0.4	
	289.7	1.2	
	283.3	0.9	
O 1s	532.7	22.1	22.1
N 1s	401.0	1.0	1.1
	404.4	0.1	
F 1s	686.8	15.9	21.9
	685.5	4.1	
	688.0	1.9	
Na 1s	1073.1	0.2	0.2
Si 2p	103.0	3.0	3.1
	99.3	0.1	

Finally, the fluoride spectrum (Figure III-5 d)) showed the results that confirms the previous identifications: AlF_3 and/or CF-CH bonds, a most intense one from fluorocarbon (CF_x) entities and a last one to the metal fluoride respectively identified at 688.0 eV, 686.8 eV and 685.5 eV[35]. Totalizing almost 22 at.% of the elemental composition, the fluorination process is successful.

As observed before, the identified silicon signal is related to the presence of intermetallic particles that constitutes the Al 2024 alloy. Due to the possible conversion of the Al_2O_3 into aluminum oxyfluorides ($AlOF_x$), and consequently its partial dissolution, the XPS investigation was capable of identify a higher amount of the element.

3.2. DR and NDR coatings after plasma treatment

In the case of the DR lignin/silicon coating designed under RH 10% - 0.05mm/s withdrawal speed, the hydrophobicity test proved a substantial increase of the contact angle from 50° to 96°. Let's remind a WCA value of about 90°, corresponds to a hydrophobic character. As can be seen in Figure III-6 a) and b), the interaction of the water droplet with the coating surface is highly reduced after the fluorinated film deposition. The NDR hybrid presented a less pronounced tendency when SF_6 treated, with a 15% WCA increase, from 95° to 108°, Figure III-6 c) and d).

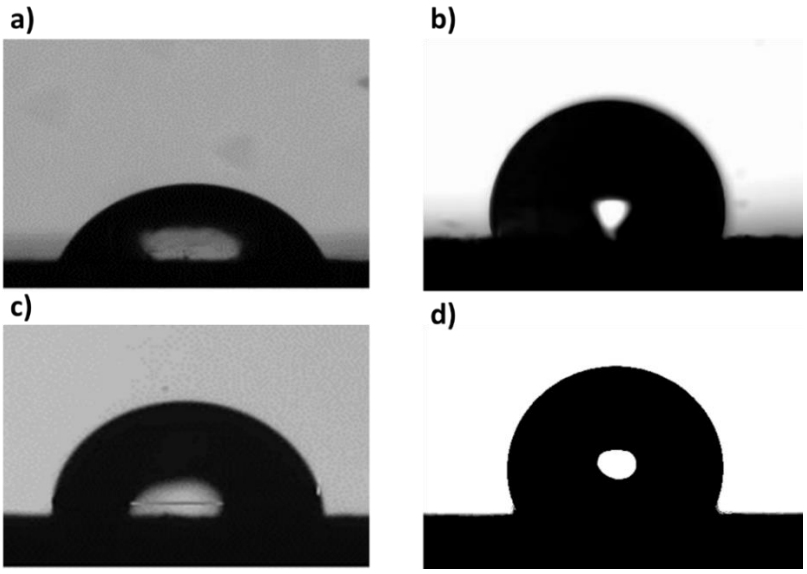

Figure III-6: WCA analysis of a) DR lignin/silicon before plasma deposition , b) DR lignin/silicon after plasma deposition, c) NDR lignin/silicon before plasma and d) NDR lignin/silicon after plasma.

Although both coatings showed an improvement in hydrophobic character, the direct route appears more sensitive to the plasma treatment.

The XPS survey composition of the plasma treated DR sample showed the fluoride was successfully incorporated to the film (Figure III-7 a)). Carbon and oxygen content decreased after the fluorine incorporation. This decay was attributed to the breakage in lignin bonds and replacement by fluorine, according with changes observed in the XPS C1 s spectra. The C 1s core level spectrum (Figure III-7 b)) identified the creation of some new CF_2 and CF_3 bonds with BE at 291.6 eV and 293.7 eV respectively[36], considered as fluorocarbon species with a highly hydrophobic character due to the high concentration of fluorine[37,38]. In Table III-3, they concern 7.2 % of the total chemical composition of the material, which justifies the clear evolution of the hydrophobicity. The reduction in the percentage of the first C1s component (C-C/C=C) after treatment is comparable with the percentage of total number of carbon atoms covalently bonded to fluorine (C-CF, CF_2, CF_3,…) (Table III-3). Some other components, corresponding to C-C/C-H, C-O/C*-CF_x, C=O/CF and O-C=O/C*F-CF_2 bonds are detected at 285.1 eV, 286.7 eV, 288.2 eV and 289.7 eV. On the contrary of the work of A.E.F. Santos et al.[39], content of carboxyl groups did not strongly decline with the plasma treatment ($C_{C-C/C-O}$ decreased of about 10% for treated DR coatings and 20% for treated NDR coatings). Indeed, this evolution could be assigned to some carboxyl groups during the plasma treatment by consumption of the oxygen atoms when the plasma atmosphere in the chamber deposit is not pure enough. The O1s spectrum reports a new component beyond 536.0eV that could be attributed to –OC-F_x chemical environments as in fluorinated polymers[40].

In addition to the fluorocarbon entities that contribute to the wettability reduction, the Al 2p core level on Figure III-7 c) presents a single component referred to AlF_3 bond at 76.9 eV which is the assurance of the covering of the remaining nude substrate areas. On the other hand, the aluminum content after the plasma has been

increased from 1.9 % to 5.8 % (Table II-6 and Table III-3 respectively), probably in relation with the occasional ion damage of lignin films under SF_6 plasma treatment[41].

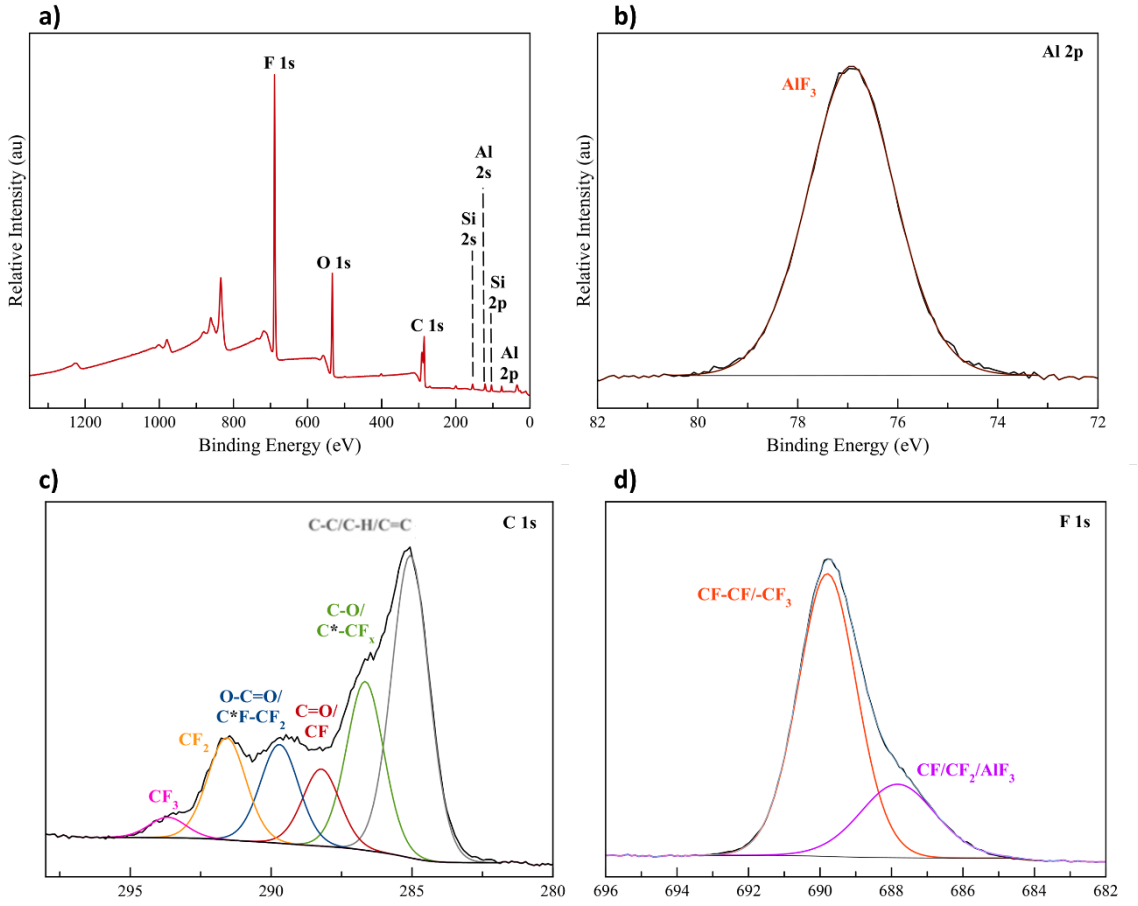

Figure III-7: DR hybrid coating after SF_6 PECVD treatment. a) General spectrum, b) Al 2p core level spectrum, c) C 1s core level spectrum and d) F 1s core level spectrum.

The F 1s spectrum (Figure III-7 d)) was deconvoluted in two main components. The first peak, at 689.8 eV is related to CF-CF and -CF_3 bonds[42]. The low energy side component corresponds to both CF/CF_2 and AlF3 environments (BE = 687.8 eV). The identified silicon (BE 104.4 eV) is referred a SiO_2 phase that could be generated under the plasma treatment and disturbance of the initial siloxane network that was originally identified at 103.0eV (Table II-6)[43,44]. The C/Si content increased from 7.6 (for DR hybrid coating to 11.9 (for SF_6 treated DR hybrid coating)) which may lead to a hypothesis that the PECVD process would generate the replacement of part of Si entities at the surface by fluoride. This could match with the change of resulting chemical environment of remaining silicon and the appearance to SiO_2-like phases, the surface roughness staying quite the same with a 0.61 µm value.

Table III-3: XPS quantification of DR and NDR hybrid coatings after plasma treatment.

	DR RH 10%_0.05mm/s Hybrid coating			NDR RH 10%_0.05mm/s Hybrid coating		
Core Peak	BE(eV)	At.%	Total At. Conc (%)	BE(eV)	At.%	Total At. Conc (%)
Al 2p	76.9	5.8	5.8	-	-	-
C 1s	285.1 286.7 288.2 289.7 291.6 293.7	17.2 9.6 4.4 5.8 6.0 1.2	44.2	285.0 286.3 287.8 289.3 290.9 293.4	33.5 11.4 2.7 6.2 0.6 0.3	54.7
O 1s	533.9 536.1	16.5 1.5	18.0	533.0 534.2	21.8 5.3	27.1
F 1s	689.8 687.8	21.5 6.8	28.3	688.6 687.3	4.5 3.0	7.5
Si 2p	104.4	3.7	3.7	104.2 103.1	2.9 5.4	8.3
S 2p	-	-	-	164.3 165.5	1.6 0.8	2.4
C/Si		11.9			6.6	

For the NDR Lignin/Silicon coating, the XPS survey spectra showed that there were no traces of Al in the composition (Figure III-8 a) and b)). This could traduce the good adequacy between the previous noticed cross-linking of the polymer network and the better film anchorage to the substrate.

Regarding the higher carbon content than treated DR hybrid coating (Table III-3, Figure III-8 c)) and a lower amount of fluoride, one can understand the wettability evolution much less important (+ 15%) for the NDR treated material than the DR ones (+ 90%). On the C1s spectrum, previous observed C^*F_2 and C^*F_3 environments (at 290.9 eV and 293.4 eV respectively) were created during the plasma treatment on the NDR coating surface but in lower relative content. In addition, some sulfur derived species were identified, specifically unbonded thiol units (R-SH with R being a carbonic chain like CH_3 for example) or S^0 (BE 164.3 eV – 165.5 eV)[45,46]. The initial higher content of carbon in NDR compounds and the specific surficial arrangement of lignin/silicon network could explain the reactivity of sulfur on the modified coating.

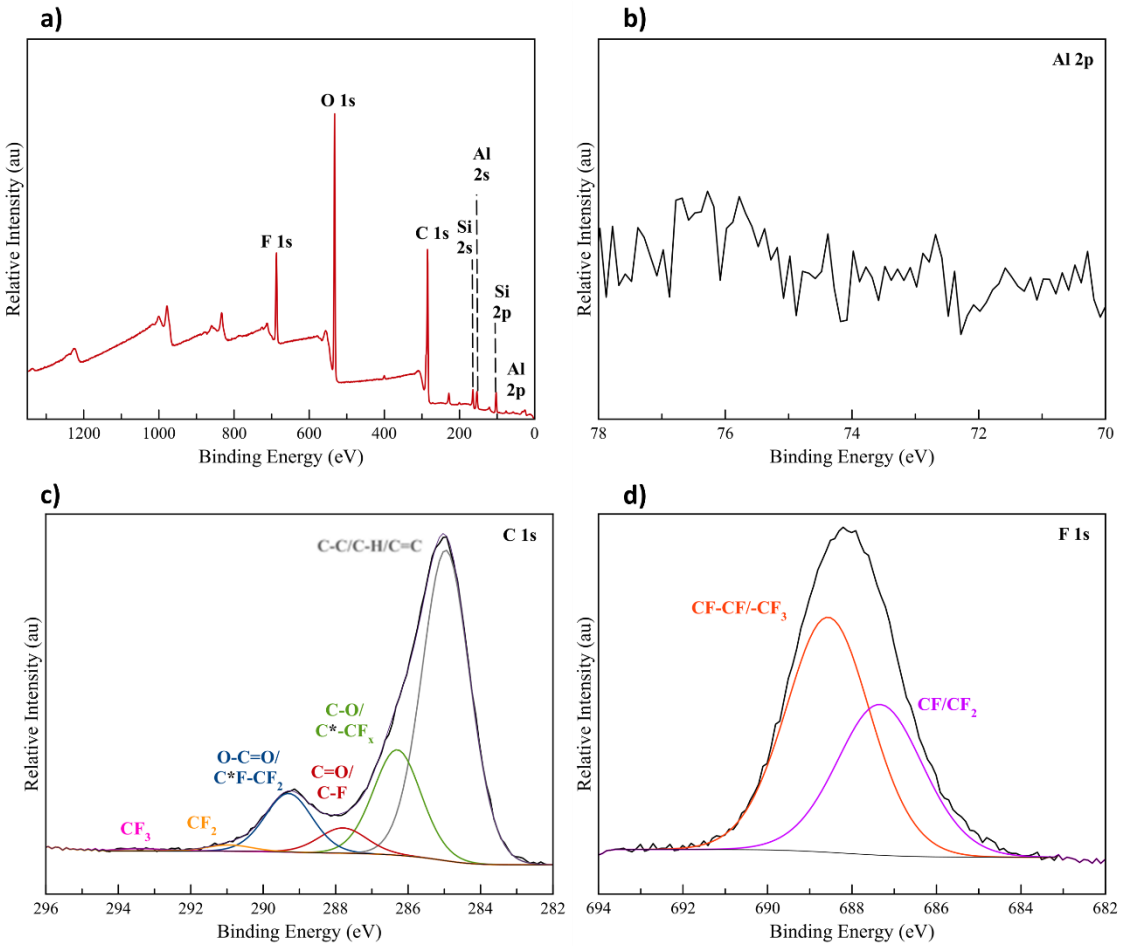

Figure III-8: NDR hybrid coating after SF_6 plasma thin film deposition. a) General spectrum, b) Al 2p core level spectrum, c) C 1s core level spectrum and d) F 1s core level spectrum.

An almost identical F1s pattern was observed (Figure III-8 d)), with the two peaks corresponding to the fluorocarbon bonds and binding energies slightly lower than before (688.6 eV and 687.3 eV). The Si 2p signal showed a total content of 8.3% and differently from what was observed both in the NDR before plasma and in the DR after SF_6 treatment, the signal was split into two components. The first, at 104.2 eV, correlates with SiO_2 appearing with the plasma treatment exposure and corresponding to a coating composition evolution or an effective etching of the surface as the roughness increased to 2.50 mm. Some SiO2 clusters were found deep in the NDR coating after the depth profile Tian et al.[47] have shown some classical SF_6 plasma etching rates for Si based systems of around 90 nm/min whatever the plasma power source. In these conditions, it can be admitted a situation of chemical composition like the depth profile study of NDR hybrid (Table II-9) between Ar^+ etching 100s and 1000s. The second component with lower binding energy (103.1 eV) indicates the siloxane network of the coating.

So, based on these results, a good hypothesis to justify this more significant improvement in the direct route is the much higher amount of fluor content between the DR and NDR routes (almost four times greater – Table III-3). The greater presence of F reduces the wettability of the coating, when for the NDR coating the roughness increase would mitigate the effect.

The FTIR spectra of the DR and NDR coatings also confirmed the formation of carbon–fluorine bonds closer to the bulk of the material. As can be seen in Figure III-9 a) and b) respectively, in addition to the bands shown in the previous spectra (Figure II-10 and Figure II-17), bands related to CF, CF_2 and CF_3 bonds at positions (approximately) 750 cm^{-1}, 690 cm^{-1} and 1340 cm^{-1} respectively[48,49].

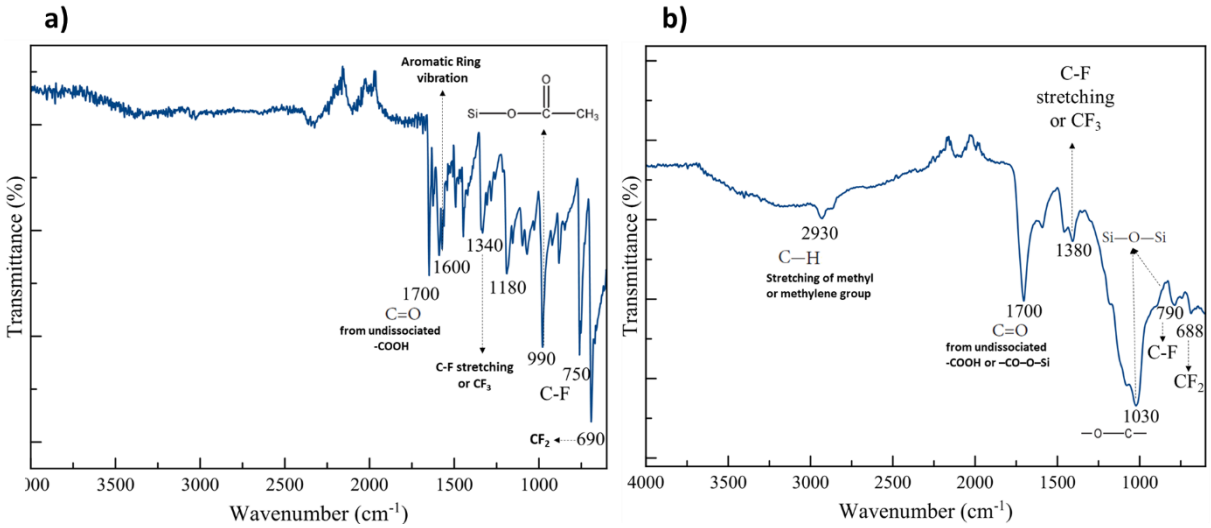

Figure III-9: FTIR spectra plasma treated a) DR hybrid coating and b) NDR hybrid coating.

Chapter Summary

As could be observed throughout the previous presented results, the thin film of SF_6 generated by the PECVD technique brought a clear improvement of the hydrophobicity of materials, conferring substantial enhancement of contact angles. The XPS chemical analysis allowed the confirmation and further comprehension of the new chemical bonds that have been created by the plasma application in relation with the wettability decline. Both fluorocarbon units like $-CF_2$ and $-CF_3$ creation and the pronounced Al-F interactions in the form of AlF_3 and $AlOF_x$. were clearly observed. Besides these points, the following considerations must be taken from this chapter:

- The plasma effect on uncoated Al 2024 substrate has been easily remarked with the remove of carbonaceous species (2.5 times less amount). At the same time the substrate Al signal was more observable as well as fluorine interaction.
- The exposed Al 2024 alloy did not present any traces of sulfur in its composition, what is considered an extremely positive aspect of the formed layer, once the S is a well-known corrosion promoter.
- DR RH 10% 0.05mm/s hybrid coating also present an expressive result, with a WCA almost twice bigger than the previous one, and therefore able to be classified as hydrophobic. This new property is specially related to the intense presence of the highly fluorinated $-CF_2$ and $-CF_3$ bonds. On the other hand, this specimen presented a higher Al content what guide to the conclusion the surface was partially damaged during the SF_6 treatment.
- For the hybrid NDR coating, the hydrophobicity character did not increase that much after plasma exposure in relation with an equilibrium effect between surface fluorination and roughness increase. The absence Al on the composition also is a remarkable point, confirming the still good covering of the hybrid layer. However, the NDR coating was anyway etched as the Si 2p core level peak revealed a SiO_2 phase as previously observed deep in the material. This matches with the simultaneous decrease of the carbon content and the increase of Si amount

References

1. Mainusch, N., Militz, H., Viöl, W., Mai, C., Gascón-Garrido, P., Mainusch, N., Militz, H., Viöl, W., & Mai, C. (2016). Effects of copper-plasma deposition on weathering properties of wood surfaces. Applied Surface Science, 366, 112–119. https://doi.org/https://doi.org/10.1016/j.apsusc.2016.01.060
2. Serrano, J., Ureña, A., Lazcano Ureña, S., & Blanco Varela, T. (2015). New approach to surface preparation for adhesive bonding of aeronautical composites: atmospheric pressure plasma. Studies on the pretreatment lifetime and durability of the bondline. Composite Interfaces, 22(8), 731–742. https://doi.org/10.1080/09276440.2015.1056671
3. Bonizzoni, G., & Vassallo, E. (2002). Plasma physics and technology; industrial applications. Vacuum, 64(3), 327–336. https://doi.org/https://doi.org/10.1016/S0042-207X(01)00341-4
4. Vandenbossche, M., Petit, L., Mathon-Lagresle, J., Spano, F., Rupper, P., Bernard, L., & Hegemann, D. (2018). Formation of lateral chemical gradients in plasma polymer films shielded by an inclined mask. Plasma Processes and Polymers, 15, e1700185. https://doi.org/10.1002/ppap.201700185
5. Prado, M., Marski, S. R. D. S., Pacheco, L. P., Barros, A. W. da C., Gerardo, C. F., Carvalho Prado, M., Marques, F. D., Lunz, J. do N., de Carvalho Silva, G. C., Archanjo, B. S., Lione, V. de O. F., Achete, C. A., & Simão, R. A. (2022). Hexamethyldisiloxane coating by plasma to create a superhydrophobic surface for fabric masks. Journal of Materials Research and Technology, 17, 913–924. https://doi.org/https://doi.org/10.1016/j.jmrt.2022.01.003
6. de Farias, J. G. G., Cavalcante, R. C., Canabarro, B. R., Viana, H. M., Scholz, S., & Simão, R. A. (2017). Surface lignin removal on coir fibers by plasma treatment for improved adhesion in thermoplastic starch composites. Carbohydrate Polymers, 165, 429–436. https://doi.org/10.1016/j.carbpol.2017.02.042
7. Fazeli, M., Florez, J. P., & Simão, R. A. (2019). Improvement in adhesion of cellulose fibers to the thermoplastic starch matrix by plasma treatment modification. Composites Part B: Engineering, 163, 207–216. https://doi.org/https://doi.org/10.1016/j.compositesb.2018.11.048
8. Bhattacharjee, A., & Gurnett, D. A. (Eds.). (2017). Introduction. In *Introduction to Plasma Physics: With Space, Laboratory and Astrophysical Applications* (2nd ed., pp. 1–3). Cambridge University Press. https://doi.org/DOI: 10.1017/9781139226059.002
9. Winkler, R. (2000). The Boltzmann Equation and Transport Coefficients of Electrons in Weakly Ionized Plasmas. In B. Bederson & H. B. T.-A. I. A. Walther Molecular, and Optical Physics (Eds.), *Fundamentals of Plasma Chemistry* (Vol. 43, pp. 19–77). Academic Press. https://doi.org/https://doi.org/10.1016/S1049-250X(08)60121-4
10. Ohring, M. (2001). Materials Science of Thin Films. In *Academic Press* (Vol. 53). https://doi.org/10.1017/CBO9781107415324.004
11. Spear, K. E. "Principles and applications of chemical vapor deposition (CVD)" Pure and Applied Chemistry 54, no. 7 (1982): 1297-1311. https://doi.org/10.1351/pac198254071297

12. Hodak, S., Supasai, T., Paosawatyanyong, B., Kamlangkla, K., & Pavarajarn, V. (2008). Enhancement of the hydrophobicity of silk fabrics by SF6 plasma. Applied Surface Science, 254, 4744–4749. https://doi.org/10.1016/j.apsusc.2008.01.110
13. Nguyen, N.-T. (2012). Fabrication technologies. In *Micromixers*. https://doi.org/10.1016/b978-1-4377-3520-8.00004-8
14. Kodas, T. (1994). Chemical vapor deposition: Principles and applications. Edited by M. L. Hitchman and K. F. Jensen, Academic Press, London 1993, 677 pp., hardback, $ 75, ISBN 0-12-349 670-5. *Advanced Materials*, *6*(1), 87–88. https://doi.org/https://doi.org/10.1002/adma.19940060125
15. Martin, P. M. B. T.-H. of D. T. for F. and C. (Third E. (Ed.). (2010). Chapter 1 - Deposition Technologies: An Overview. In Handbook of Deposition Technologies for Films and Coatings (Third Edit, pp. 1–31). William Andrew Publishing. https://doi.org/https://doi.org/10.1016/B978-0-8155-2031-3.00001-6
16. Reif, R., & Kern, W. (1991). Plasma-Enhanced Chemical Vapor Deposition. In *THIN FILM PROCESSES II*. ACADEMIC PRESS, INC. https://doi.org/10.1016/B978-0-08-052421-4.50015-0
17. Jansen, F. (1998). *Chapter 5.5 - Plasma-Enhanced Chemical Vapor Deposition* (D. M. Hoffman, B. Singh, J. H. Thomas, & J. H. B. T.-H. of V. S. and T. Thomas (Eds.); pp. 711–730). Academic Press. https://doi.org/https://doi.org/10.1016/B978-012352065-4/50075-4
18. Gupta, K., Jain, N. K., & Laubscher, R. (2017). *Chapter 6 - Surface Property Enhancement of Gears* (K. Gupta, N. K. Jain, & R. B. T.-A. G. M. and F. Laubscher (Eds.); pp. 167–196). Academic Press. https://doi.org/https://doi.org/10.1016/B978-0-12-804460-5.00006-7
19. Rastkar, A. R. (2015). Effect of Plasma Enhanced Chemical Vapor Deposition of Tetraethylorthosilicate on the Friction and Wear Loss of Plasma Electrolytic Oxidized Aluminum 6082. 3(2), 29–37. https://doi.org/10.13189/cme.2015.030203
20. Madocks, J., Rewhinkle, J., & Barton, L. (2005). Packaging barrier films deposited on PET by PECVD using a new high density plasma source. Materials Science and Engineering B-Advanced Functional Solid-State Materials, *119*, 268–273. https://doi.org/10.1016/j.mseb.2004.12.080
21. Prado, M., Marski, S. R. D. S., Pacheco, L. P., Barros, A. W. da C., Gerardo, C. F., Carvalho Prado, M., Marques, F. D., Lunz, J. do N., de Carvalho Silva, G. C., Archanjo, B. S., Lione, V. de O. F., Achete, C. A., & Simão, R. A. (2022). Hexamethyldisiloxane coating by plasma to create a superhydrophobic surface for fabric masks. Journal of Materials Research and Technology, 17, 913–924. https://doi.org/https://doi.org/10.1016/j.jmrt.2022.01.003
22. Haag, J., Mertens, T., Kolb, M., Kotte, L., Kaskel, S., Kolb, M., Mertens, T., & Kaskel, S. (2015). Plasma Enhanced Chemical Vapour Deposition (PECVD) at Atmospheric Pressure (AP) of Organosilicon Films for Adhesion Promotion on Ti15V3Cr3Sn3Al and Ti6Al4V. *Journal of Materials Science and Engineering A & B*, *5*, 274–284. https://doi.org/10.17265/2161-6213/2015.7-8.004
23. KOLZER SRL, PVD machines (Online), Available: https://kolzer.com/pvd-machines

24. Kocaman, S., Karaman, M., Gursoy, M., & Ahmetli, G. (2017). Chemical and plasma surface modification of lignocellulose coconut waste for the preparation of advanced biobased composite materials. *Carbohydrate Polymers*, *159*, 48–57. https://doi.org/https://doi.org/10.1016/j.carbpol.2016.12.016
25. Han, Z. J., Levchenko, I., Kumar, S., Yajadda, M. M. A., Yick, S., Seo, D. H., Martin, P. J., Peel, S., Kuncic, Z., & Ostrikov, K. (2011). Plasma nanofabrication and nanomaterials safety. *Journal of Physics D: Applied Physics*, *44*(17), 174019. https://doi.org/10.1088/0022-3727/44/17/174019
26. Shih, M., Lee, W.-J., Tsai, C.-H., Tsai, P.-J., & Chen, C.-Y. (2002). Decomposition of SF6 in an RF Plasma Environment. Journal of the Air & Waste Management Association, 52(11), 1274–1280. https://doi.org/10.1080/10473289.2002.10470864
27. Dalvi, V. H., & Rossky, P. J. (2010). Molecular origins of fluorocarbon hydrophobicity. Proceedings of the National Academy of Sciences of the United States of America, 107(31), 13603–13607. https://doi.org/10.1073/pnas.0915169107
28. Satulu, V., Ionita, M., Vizireanu, S., Mitu, B., & Dinescu, G. (2016). Plasma Processing with Fluorine Chemistry for Modification of Surfaces Wettability. Molecules, 21(12), 1711. https://doi.org/10.3390/molecules21121711
29. Koalaga, Z., & Andre, P. (2010). Composition of a thermal plasma formed from PTFE with copper in non-oxidant atmosphere. Part I: definition of a test case with the SF6. High Temperature Material Processes (An International Quarterly of High-Technology Plasma Processes), 14(3), 285–294. https://doi.org/10.1615/HighTempMatProc.v14.i3.70
30. Ramos, R., Cunge, G., Pelissier, B., & Joubert, O. (2007). Cleaning aluminum fluoride coatings from plasma reactor walls in SiCl 4/Cl2 plasmas. Plasma Sources Science and Technology, 16(4), 711–715. https://doi.org/10.1088/0963-0252/16/4/004
31. Lin, K.-Y., Li, C., Engelmann, S., Bruce, R. L., Joseph, E. A., Metzler, D., & Oehrlein, G. S. (2020). Selective atomic layer etching of HfO 2 over silicon by precursor and substrate-dependent selective deposition. Journal of Vacuum Science & Technology A, 38(3), 032601. https://doi.org/10.1116/1.5143247
32. Tomko, J. A., Boris, D. R., Rosenberg, S. G., Walton, S. G., Hopkinsa, P. E., & Hopkins, P. E. (2019). Thermal conductance of aluminum oxy-fluoride passivation layers. Applied Physics Letters, 115(19), 191901. https://doi.org/10.1063/1.5120028
33. Souza, J. R., Araujo, J. R., Archanjo, B. S., & Simão, R. A. (2019). Cross-linked lignin coatings produced by UV light and SF6 plasma treatments. Progress in Organic Coatings, 128(December 2018), 82–89. https://doi.org/10.1016/j.porgcoat.2018.12.017
34. DeKoven, B. M., & Hagans, P. L. (1986). XPS studies of metal/polymer interfaces — Thin films of Al on polyacrylic acid and polyethylene. *Applied Surface Science*, *27*(2), 199–213. https://doi.org/https://doi.org/10.1016/0169-4332(86)90107-8
35. Metzler, D., Bruce, R. L., Engelmann, S., Joseph, E. A., & Oehrlein, G. S. (2014). Fluorocarbon assisted atomic layer etching of SiO 2 using cyclic Ar/C 4 F 8 plasma . Journal of Vacuum Science & Technology A: Vacuum, Surfaces, and Films, 32(2), 020603. https://doi.org/10.1116/1.4843575

36. Friedman, A. K., Shi, W., Losovyj, Y., Siedle, A. R., & Baker, L. A. (2018). Mapping Microscale Chemical Heterogeneity in Nafion Membranes with X-ray Photoelectron Spectroscopy. Journal of The Electrochemical Society, 165(11), H733–H741. https://doi.org/10.1149/2.0771811jes
37. Kasuya, M. C. Z., Nakano, S., Katayama, R., & Hatanaka, K. (2011). Evaluation of the hydrophobicity of perfluoroalkyl chains in amphiphilic compounds that are incorporated into cell membrane. Journal of Fluorine Chemistry, 132(3), 202–206. https://doi.org/https://doi.org/10.1016/j.jfluchem.2011.01.004
38. Jeffries, B., Wang, Z., Graton, J., Holland, S. D., Brind, T., Greenwood, R. D. R., Le Questel, J.-Y., Scott, J. S., Chiarparin, E., & Linclau, B. (2018). Reducing the Lipophilicity of Perfluoroalkyl Groups by CF2–F/CF2–Me or CF3/CH3 Exchange. Journal of Medicinal Chemistry, 61(23), 10602–10618. https://doi.org/10.1021/acs.jmedchem.8b01222
39. Santos, A. E. F., Bastos, D. C., Silva, M. L. V. J., Thiré, R. M. S. M., & Simão, R. A. (2012). Chemical analysis of a cornstarch film surface modified by SF 6 plasma treatment. Carbohydrate Polymers, 87(3), 2217–2222. https://doi.org/10.1016/j.carbpol.2011.10.049
40. Hantsche, H. (1993). High resolution XPS of organic polymers, the scienta ESCA300 database. By G. Beamson and D. Briggs, Wiley, Chichester 1992, 295 pp., hardcover, £ 65.00, ISBN 0-471-93592-1. Advanced Materials, 5(10), 778. https://doi.org/https://doi.org/10.1002/adma.19930051035
41. Notley, S. M., & Norgren, M. (2010). Surface energy and wettability of spin-coated thin films of lignin isolated from wood. Langmuir, 26(8), 5484–5490. https://doi.org/10.1021/la1003337
42. Lopes, D., Maria, A., Ferraria, A. M., Lopes da Silva, J. D., & Botelho do Rego, A. M. (2003). XPS studies of directly fluorinated HDPE: problems and solutions. Polymer, 44(23), 7241–7249. https://doi.org/https://doi.org/10.1016/j.polymer.2003.08.038
43. Usenko, A. (2010). Silicon Nitride Surface Conversion into Oxide to Enable Hydrophilic Bonding. In ECS Transactions (Vol. 33). https://doi.org/10.1149/1.3483538
44. Tran, T. H., Au, D. B., Diawara, B., Fatyeyeva, K., Marais, S., Ortiz, J., Debarnot, D., & Poncin-epaillard, F. (2019). How the chemical structure of the plasma-deposited SiOx film modifies its stability and barrier properties: FTIR study. Progress in Organic Coatings, 137, 105332.https://doi.org/https://doi.org/10.1016/j.porgcoat.2019.105332
45. Castner, D. G., Hinds, K., & Grainger, D. W. (1996). X-ray Photoelectron Spectroscopy Sulfur 2p Study of Organic Thiol and Disulfide Binding Interactions with Gold Surfaces. Langmuir, 12(21), 5083–5086. https://doi.org/10.1021/la960465w
46. Wagner, C. D. NIST X-Ray Photoelectron Spectrometry Database. NIST Stand. Ref. Database 20, Version 4.1 1991, 1–76.
47. Tian, W.-C., Weigold, J. W., & Pang, S. W. (2000). Comparison of Cl2 and F-based dry etching for high aspect ratio Si microstructures etched with an inductively coupled plasma source. Journal of Vacuum Science & Technology B: Microelectronics and Nanometer Structures Processing, Measurement, and Phenomena, 18(4), 1890–1896. https://doi.org/10.1116/1.1306303

48. Brassard, J. D., Sarkar, D. K., & Perron, J. (2012). Fluorine based superhydrophobic coatings. Applied Sciences (Switzerland), 2(2), 453–464. https://doi.org/10.3390/app2020453

49. Osipov, V. Y., Romanov, N. M., Kogane, K., Touhara, H., Hattori, Y., & Takai, K. (2020). Intrinsic infrared absorption for carbon–fluorine bonding in fluorinated nanodiamond. Mendeleev Communications, 30(1), 84–87. https://doi.org/https://doi.org/10.1016/j.mencom.2020.01.028

Chapter IV.

Ageing and Corrosion Tests on Lignin/Silicon hybrid coatings

Figure List

Table List

This chapter is devoted to the first assays of the coating's durability referring to humid corrosion and UV weathering ageing. After going through the main types of corrosion susceptible to concern the alloy 2024, the tests methodologies will be detailed. Some first results of the cyclic voltammetry, salt spray and UV aging tests will be presented and discussed in relation with some analyses of their chemical composition and electrochemical behavior.

1. State of the art

1.1. General aspects of corrosion

The term corrosion can be described as an interfacial and irreversible electrochemical process in which a surface (usually metallic) is deteriorated due to its interaction with the environment. Consequently, material properties are weakened, and the aggressiveness of the phenomenon usually varies according to the type of material and to external conditions (such as pressure, temperature and water presence[1]).

Three groups of corrosion are often monitored: the corrosion caused by salts/molten metals[2], the dry corrosion[3] and the corrosion in wet environments. In this last case, the type of reaction will be almost always electrochemical, and will occur between the material (electrode) and the medium (electrolyte). The reaction mechanism is the same of a battery, with the creation of an electrical current and a potential (labelled as Corrosion Potential – E_{corr}) result of following equations[1]:

Anodic Reaction: $M \rightarrow M^{n+} + ne^-$ **Equation IV-1**

Cathodic Reaction: $O_2 + 2\,H_2O + 4e^- \rightarrow 4\,OH^-$ **or** $2H^+ + 2e^- \rightarrow H_2$ **Equation IV-2** and **Equation IV-3**

Equation IV-1 indicates metal corrosion (oxidative process) and Equation IV-2 and Equation IV-3 reduction process of chemical compounds present in neutral and acid environments respectively.

Among these three corrosions types the most common and studied is in wet environments, that can be present in eight main different forms in a metallic surface: general, pitting, intergranular (IGC), galvanic, dealloying, crevice, erosion and stress corrosion cracking (SSC)[4]. For Al 2024-T3 alloy, pitting, IGC and SSC are the principal mechanisms. They will be briefly explained in a subsequent topic indicating its electrochemical characteristics and corrosive reactions.

1.2. Corrosion in aluminum and in the 2024 alloy

The pure aluminum is a material with a certain resistance to corrosion and stability in oxidizing media[5]. Although it´s extremely negative oxide-reduction potential (-1660mV/ENH)[6] this material could resist to corrosive effects due to the constant presence of a native thin oxide film over the metal surface, that restricts electrons productions during oxidation reaction and resists to dissolution[7].

The thin layer can achieve a thickness of 10Å[8] only few seconds after its formation and is capable of auto-regeneration when damaged. The formation process can be considered in following reaction:

$$2Al\,(s) + 3/2\,O_2\,(g) \rightarrow Al_2O_3\,(s) \qquad \textbf{Equation IV-4}$$

Thermodynamically, this oxidation reaction has a free energy of about -1675 KJ[9] that is one of the highest among metals, endorsing its stability and tendency to occur naturally. Another vital point that must be considered regarding aluminum corrosion is its relation pH *vs* V, usually described in Pourbaix Diagram (Figure IV-1).

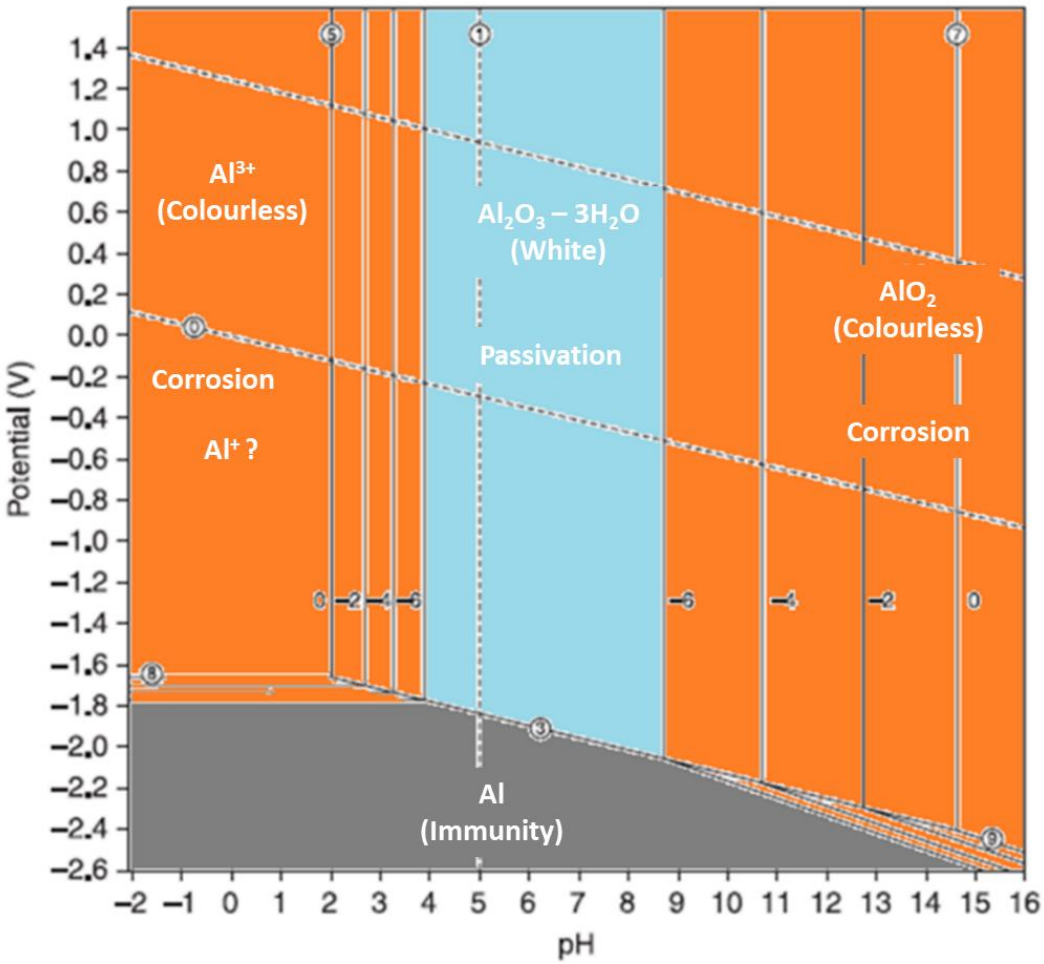

Figure IV-1: Pourbaix Diagram for Al. Redrawn from Birbilis, N. and Hinton, B.[10].

The diagram above shows that in a pH range of 4 until 9, what represents the most part of natural environments, the material owns a passive behavior with the presence of a hydrargillite film ($Al_2O_3.3H_2O$)[10]. On the other hand, for pH lower than 4 or higher than 9 corrosive effects start to act for a determinate potential scale. Aluminum can be described as an amphoteric material, once is stable in more neutral pH unstable in both alkaline and acidic conditions[11], in which the following corrosion mechanism will occur in aqueous medium:

$$Al\ (s) \rightarrow Al^{3+}\ (aq) + 3e^- \qquad \textbf{Equation IV-5}$$

$$3H^+\ (aq) + 3e^- \rightarrow \frac{3}{2} H_2\ (g) \qquad \textbf{Equation IV-6}$$

$$Al\ (s) + 3H^+\ (aq) \rightarrow Al^{3+}\ (aq) + \frac{3}{2}H_2 \qquad \textbf{Equation IV-7}$$

$$\textbf{or}\ Al + 3H_2O\ (aq) \rightarrow Al(OH)_3\ (s) + \frac{3}{2} H_2\ (g) \qquad \textbf{Equation IV-8}$$

As quoted before, Al alloys corrosion resistance is inversely proportional to mechanical improvement promoted by particles and intermetallic. The presence of new phases, precipitates along grain boundaries and alloying elements facilitates corrosive effects in 2024 series.

1.2.1. Pitting Corrosion

Pitting corrosion is a localized phenomenon restrict to small areas and generates the formation of cavities (pits) caused by the action of aggressive conditions (presence of chlorine associated with elevate temperature)[12].

Aluminum surfaces pitting mechanism can be described by breaking the thin oxide passivation film and forming $AlCl_3$[13]. The dissolution of the metallic surface produces Al^{3+} ions, which are going to be hydrolyzed in the presence of the electrolyte causing a drastic reduction in the pH and therefore further favoring the continuation of the alumina dissolution process. The schematic process can be observed in the Figure IV-2.

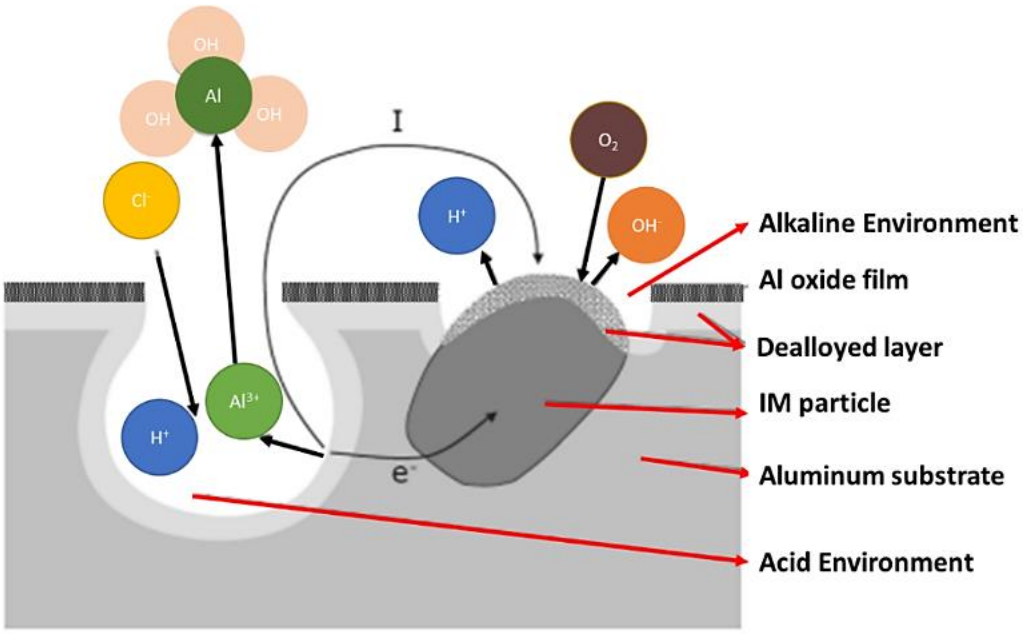

Figure IV-2: General schema for pitting corrosion in aluminum. Redrawn from Kciuk, M et al.[14].

For the 2024 alloy, as stated by Reboul M. and Vieillissement, C.[15] through SEM analysis and corroborated with AFM analysis performed by Warner, T.J. et al.[16], the heterogeneous IM are fragile points that accelerate the pitting corrosion, acting like multiples galvanic cells in relation with the Al matrix.

The nominal composition Cu/Mg ratio is even important to be considered as Al alloys with more magnesium tend to present more pitting corrosion than rich Cu compositions[10].

1.2.2. Intergranular Corrosion (IGC)

The intergranular Corrosion (IGC) is the most common corrosion type in Al 2024 alloys and is directly connected to materials microstructure. The corrosive process will happen by corrosive fluids in small and narrow areas between grains (boundary) due to their higher brittleness. A loss of ductility is noticed with the presence of

impurities in these areas (possible precipitated carbides) and a lack of alloying elements (compared to the grain interior)[17].

The series 2XXX normally presents a great number of heterogeneous precipitates in the grain boundaries and a narrow adjacent zone labeled as solute precipitation free zones (PFZs). The difference in the composition and electrochemical behavior between these zones will then form a galvanic pair that just like in the pitting corrosion will induce the corrosive attack[18], as schematized in Figure IV-3.

Like what occurs in pitting, for intergranular corrosion the presence of intermetallic precipitates has a mandatory role in the mechanism, since the presence of multiple phases is the key factor in the process. But despite these similarities, IGC will be different from the pitting type due to its higher propagation speed and the starting location, since Pitting can start from the material bulk and IGC will start from the grain boundary, depleted zones, obligatorily[19,20].

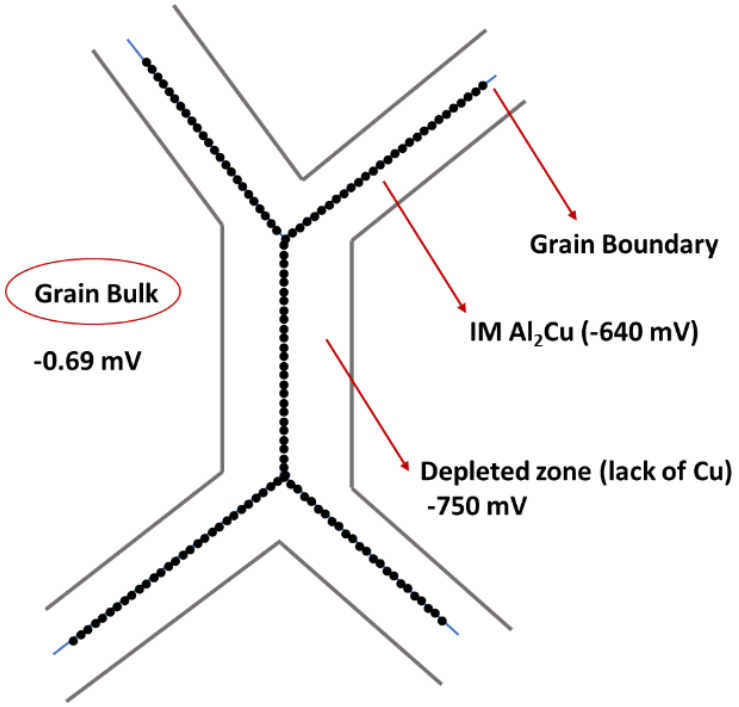

Figure IV-3: IGC schema in the Al 2024. Redrawn from[21].

1.2.3. Stress Corrosion Cracking (SCC)

The third important type of corrosion that could afflict the 2024-T3 alloys is the Stress Corrosion Cracking, in which the corrosive effect will occur due to the combine action of mechanical stress and electrochemical reactions in a corrosive environment (normally containing Cl or Sulphur ions)[22].

The SCC attacks the grain boundaries, in which cracks will appear and spread with time until causing the catastrophic failure of the alloy. Although it also occurs at the grain boundary, this type differs from intergranular corrosion due to the mandatory presence of mechanical actions associated with the aggressive environment, causing, for example, alloys that are not susceptible to IGC to suffer from stress corrosion[23].

Two types of mechanisms are related to SCC propagation, electrochemical reactions (ER) and hydrogen embrittlement (HE). The first case, represented in the Figure IV-4 below, results from the formation of anodic and cathodic zones in the crack region in an aggressive aqueous medium. In this scenario, the crack tip (place of stress concentration) works as the anode and favors the crack propagation[22].

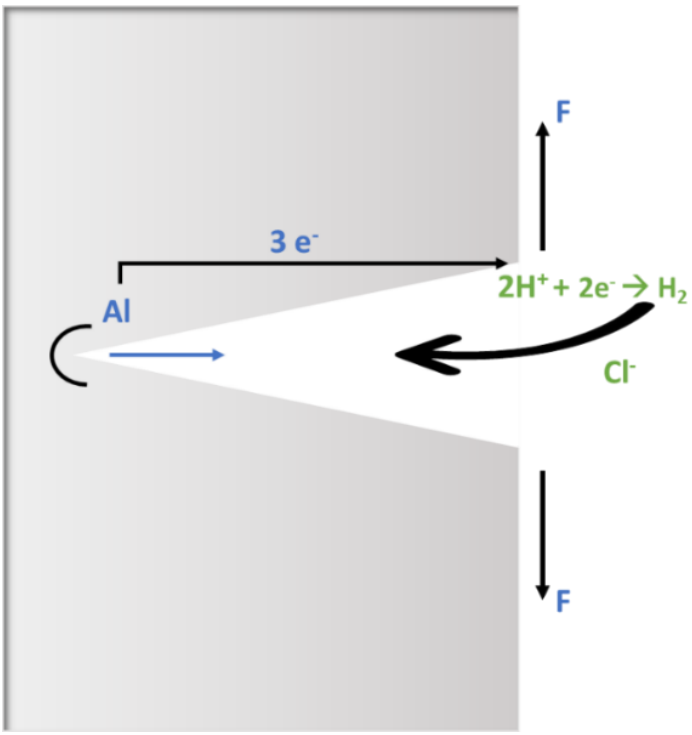

Figure IV-4: SCC schema for the case of electrochemical reactions in an aqueous medium. Obtained and redrawn from[15].

In case two, the corrosion initiates from the presence of residual H that penetrates in the natural layer of alumina during the corrosion, eliminating it and exposing the surface of the material even more.

The Al 2024 will suffer this kind of corrosion due to, among others, metallurgical factors like the presence of heterogeneous particles, different grain sizes and orientations[24].

2. Materials & Methods

2.1. Corrosion Tests

Two kinds of electrochemical evaluations of the coatings (both DR and NDR) were realized: an industrial salt spray test done at INEOSURF (France), and cyclic voltammetry (CV) performed at IPREM – France.

Cyclic voltammetry is a static electrochemical measurement technique that allows the determination of reduction and oxidation potentials of electroactive entities.

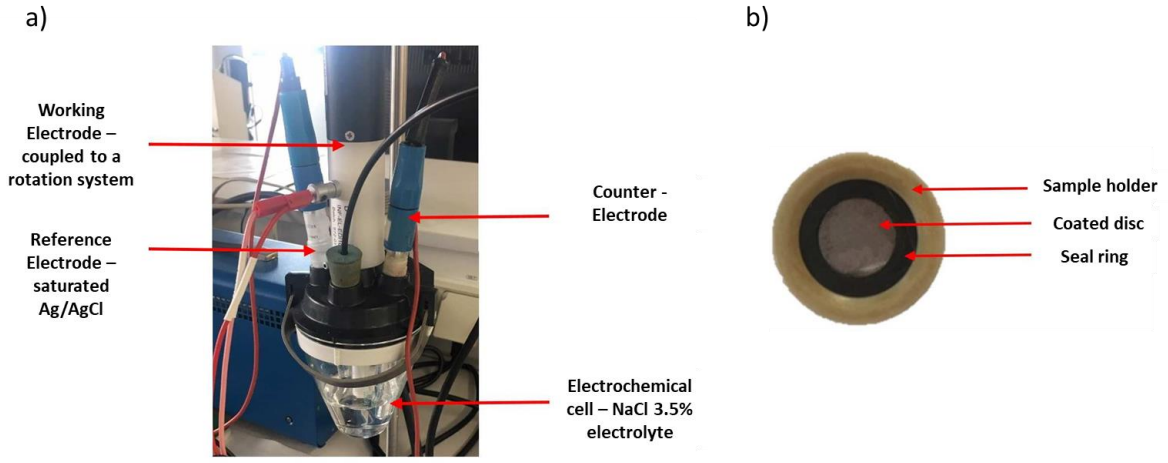

Figure IV-5: Electrochemical cell used in the cyclic voltammetry and the working electrode sample holder.

The experimental setup, given in Figure IV-5 a), consists of an associated cell created from 3 electrodes immersed in a highly semiconducting NaCl solution.

- The working electrode is the place where the electrochemical reactions take place. In our case, it is the Al 2024 coated with the Lignin-Silica hybrid coating.
- The counter-electrode, a platinum wire, which allows the current to flow.
- The reference conductor, whose potential is regulated and constant, allows to manage and measure the potential applied to the surface of the working electrode. In this study, a saturated Ag/AgCl conductor was chosen.

The technique involves applying a potential change between the working and reference electrodes and recording the current (i) resulting from the oxidation or reduction of the working electrode. By plotting the Tafel curve, log(I) vs. potential (V), the corrosion potential (E_{corr}) and corrosion current (i_{corr}) of the material can be determined.

The electrochemical analyses were carried out adapting the work of de Haro, J.C. et al.[25] and the ASTM G44-21 standard[26] .

For the cyclic voltammetry, a Sodium Chloride (NaCl) 3.5% (1.3 mol/l) and pH 7 was used as electrolyte. The working electrode is placed in a sample holder containing a seal ring at the bottom and other at the top to ensure a tight seal (Figure IV-5 b)). The exposed area is the inside diameter of the seal, which is 0.238 cm^2. The sample holder is then connected to the rotating electrode and a rotation of 1000 rpm is applied.

For the measurement, the equilibration time was set to 5 minutes**, with a potential range of -1.6 to 0.4 V and a sweep step of 5 mV/s. Once the Tafel curve was created, both corrosion and current corrosion were determined from the graph. The Figure IV-6 below shows how the key information was obtained.

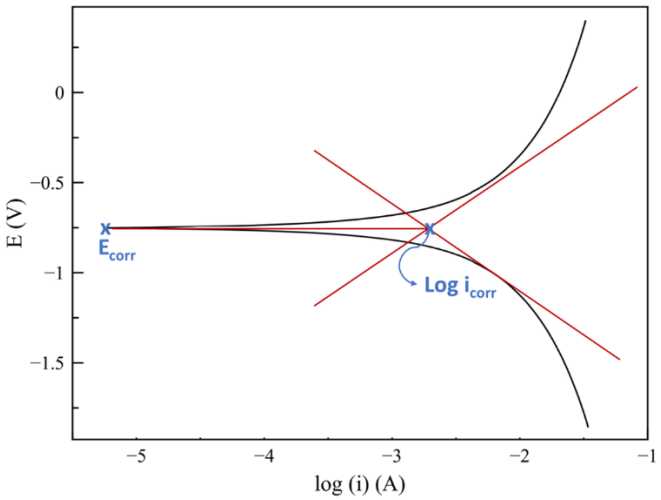

Figure IV-6: Example of theoretical Tafel curve indicating the E_{corr} and i_{corr} measurements.

The salt fog exposure was done over a period of 1 week (168h) with the salt cabinet of Ineosurf Company (Figure IV-7 a)). During the test period, the specimens were exposed to an aggressive alkaline environment capable of magnifying the corrosive process, allowing the verification of the performance and robustness of the coatings. The parameters of temperature, pH, flow rate and concentration of the used corrosive solution were set in accordance with the ISO 9227:2017 standard[27]. The experimental settings consisted in: i) the analyzed specimens are placed in the test cabinet (Figure IV-7 b)) supported with an angle 20 ± 5° from vertical; ii) then, temperature and flow rate are set to 35 ± 2 °C and 1.5 ± 0.5 ml/h respectively. The NaCl solution was prepared in a concentration of 2.3% weight (0.86 mol/l).

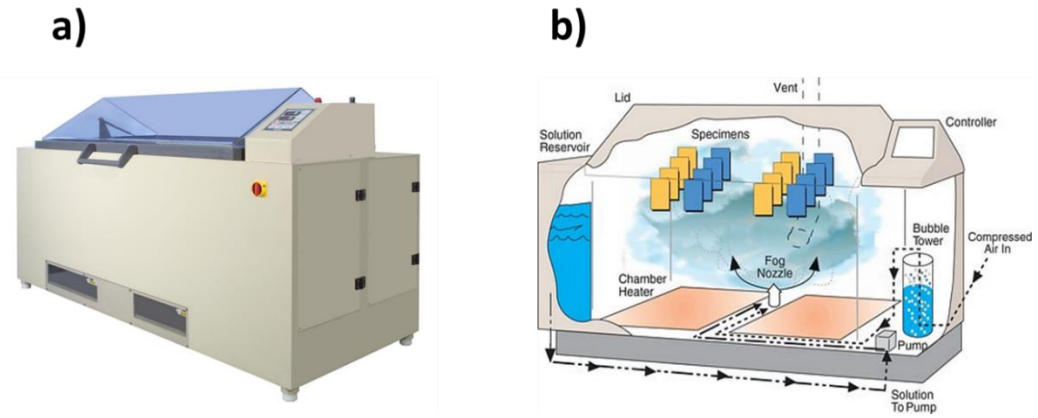

Figure IV-7: a) Salt spray test chamber of Ineosurf company, used for the anticorrosion tests. b) A typical salt-spray chamber has an air saturation tower that stabilizes the salt concentration, a reservoir for the solution itself, an atomization nozzle for the creation of the fog, supporting mechanisms to hold the parts, a method for distributing heat inside the chamber and a tempera ture controller. Photo courtesy of Q-Lab.

The surface investigation was done following the procedure described below:

** : Due to an unexpected problem in the experiments schedule before the summer 2022 period, the cyclic voltammetry campaign was reduced to a day. Samples were then tested after 5min of immersion in alkaline solutions instead of a sequence of 24h, 48h ,72h and 96h for any specimen. They cannot be really compared with industrial neutral spray tests but should give a tendency of resistance behaviour of both DR and NDR coatings.

- All samples (60mm x 20mm) were photographed and had their surfaces state evaluated before insertion into the test chamber.
- After 24h, the surfaces were removed of the chamber and the surfaces once again photographed and analyzed.
- After that, the specimens were water rinsed, dried and repositioned on the sample holder.
- The whole process was repeated until the time of 168 hours (in this study, the specimens damage was at its maximum stage after 96h of exposure).

The results were then elaborated through the photos analysis, in which the following steps were carried out:

- 0.5 cm in relation to all edges were discarded to avoid possible fake results produced by edge effects.
- Color changes on the surface were related.
- The approximated number of pitting points were counted for a same surface area (around 500mm^2) and used to determine the corrosion intensity.

2.2. QUV ageing tests

The UV ageing test was carried out in a QUV equipment provided by the Q-Panel Company, with a lamp type UVA-340 (Figure IV-8). The test was carried out at 60 °C and followed the ASTM G154-16 standard[28], that correspond to a 5000h exposure test.

Figure IV-8: UV ageing test chamber from Q-Panel Company used for the tests.

After the test realization, the visual aspect and the adherence of the coatings were evaluated and compared with the results of the untreated specimens.

3. Results

3.1. Al 2024 corrosion evaluation

The ISO salt fog test performed on the uncoated Al 2024 proved the natural sensitivity of the material to corrosion effects. As can be seen in Figure IV-9, in which the corrosion evolution in relation to the test time is indicated, from the first 24 hours, two new colors have already appeared along the surface of the plate, indicating different states of corrosion. The orange tones are characteristic of corrosive processes. This relation between the color change and corrosion is commonly reported for metals, as for instance in the works of Naik, D. L. et al.[29] for steel surfaces or Zhang Y. et al. for aluminum alloys[30].

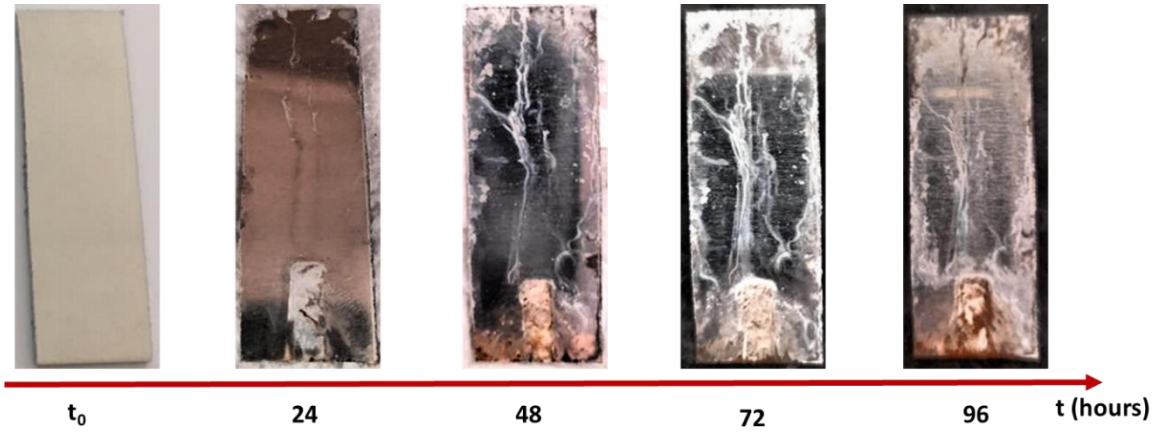

Figure IV-9: 2.3wt % NaCl Salt spray test results evolution through time for the uncoated Al 2024.

After 48 hours, a more deteriorated state is observed, with the appearance of two new brown dark colors and the beginning of a general corrosion product on the bottom of the specimen (represented by the brass color). The corrosion keeps increasing until 96 hours, when the general corrosion phenomenon is easily visualized in both upper and bottom extremities. At this stage, more than 20 pitting points were identified, attesting the tendency of the 2024 alloy to be fragile to this corrosion type when exposed to NaCl solutions[30].

As can be observed in the Tafel plot (Figure IV-10), the calculated E_{corr} from the cyclic voltammetry experiment was approximately -0.75 V vs SCE, what is quite close to the literature[31,32] with common values between -0.85 V and -0.6 V vs SCE for the potentiodynamic polarization curve of Al 2024 in 3.5 wt.% NaCl solution at 30°C.

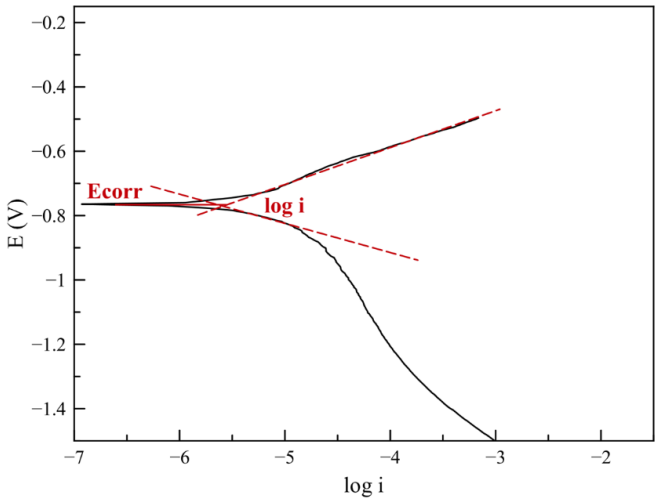

Figure IV-10: Cyclic voltammetry curve for Al 2024 sample immersed in 3.5wt% NaCl.

Besides the corrosion potential, the Tafel curve presented above allowed the estimation of the corrosion density of the 2024 aluminum alloy, which will later be used as a benchmark for comparison against the coatings. The value found was i_{corr} equal to 0.08 mA and corrosion density of 0.34 mA/cm^2.

Finally, a XPS investigation was carried out in the corroded disk to determine the chemical environment and the changes in comparison with the referential Al 2024 (Chapter I - Figure I-16 and Table I-7). The general spectra (Figure IV-11 a)) shows the presence of the chlore and copper and the disappearance of the signals related to zinc and magnesium, indicating the elimination of the IM particles related to these elements in the analyzed point.

The quantification (Table IV-1) reveals a slight increase in the Al content from 9% (raw Al2024) to 11.4 % (corroded Al 2024), with presence of the components assigned to the oxide layer (BE 75.4 eV), Al^0 (BE 72.6 eV – 73.0 eV) and the (oxo)hydroxide aluminum species ($Al(OH)_3$/AlO(OH) (BE 74.0 eV)[33,34] (Figure IV-11 b)). The considerable increase of the hydroxylated entities (from 0.6 % to 3.7 %) can be directly correlated to the corrosive process. As stated by Szunerits, S. and Walt, D. R.[35] in his work about aluminum surfaces corrosion, chloride ions attack the natural Al_2O_3 layer that protects the metallic Al surface creating Al^{3+} entities, which in aqueous media, reacts with water and creates the oxyhydroxy complexes.

The most drastic change after corrosion exposure was the reduction by 2 of the amounts of carbon, (C1s at. conc. 36.4 %). The C1s spectra possess four principal components related to the aliphatic carbon (BE 285.0 eV), C-O bond (BE 286.6 eV), C=O (BE 288.2 eV) and COOH (BE 289.3 eV) and two others that refers to carbides-like environments (BE 283.0 eV)[36] and C-Cl_x environments (BE 290.3 eV)[37].

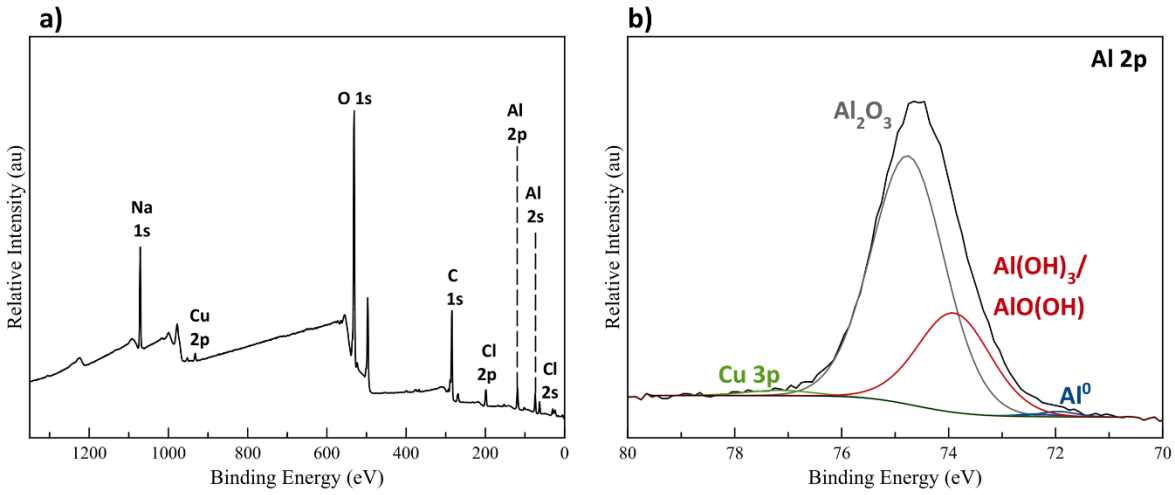

Figure IV-11: XPS spectra of Al 2024 alloy after 3.5wt % NaCl. a) General survey and b) Al 2p core level.

Finally, the appearance of a peak related to Cl and the huge increase in both sodium and oxygen total atomic concentrations were observed. The Cl and the Na augmentation can be explained by the interaction of the Al 2024 with the NaCl solution used on the test, that deposited these elements on the surface. On the other hand, the O 1s core level amount increase is related to the more pronounced presence of oxidized species.

Table IV-1: XPS quantification table of Al 2024 alloy after 3.5wt % NaCl .

Core Peak	BE(eV)	At.%	Total At. Conc (%)
	74.7	7.6	
Al 2p	73.0	0.1	11.4
	72.6	0.0(4)	
	74.0	3.7	
C 1s	285.0	30.1	36.4
	286.6	1.7	
	288.2	0.3	
	289.3	2.2	
	290.3	1.8	
	283.0	0.4	
O 1s	532.1	23.9	30.3
	530.5	4.3	
	536.3	2.1	
Cl 2p	198.9	2.0	3.0
	200.6	1.0	
Na 1s	1071.6	18.6	18.6
Cu 2p	932.9	0.3	0.3

3.2. DR and NDR hybrid coatings corrosion evaluation

The neutral salt spray test presents a much better result for both coatings in comparison with the uncoated material, showing no apparent color changes (no trace of the characteristic orange ton).

The DR coating surface, Figure IV-12 a), showed more than 20 pitting corrosion spots since the first 24h of exposure and this trend that continued until the end of the test. This result is assumed to be unsatisfactory as the coating showed no resistance from the first moments of the test and continued to decrease in performance until 96h.

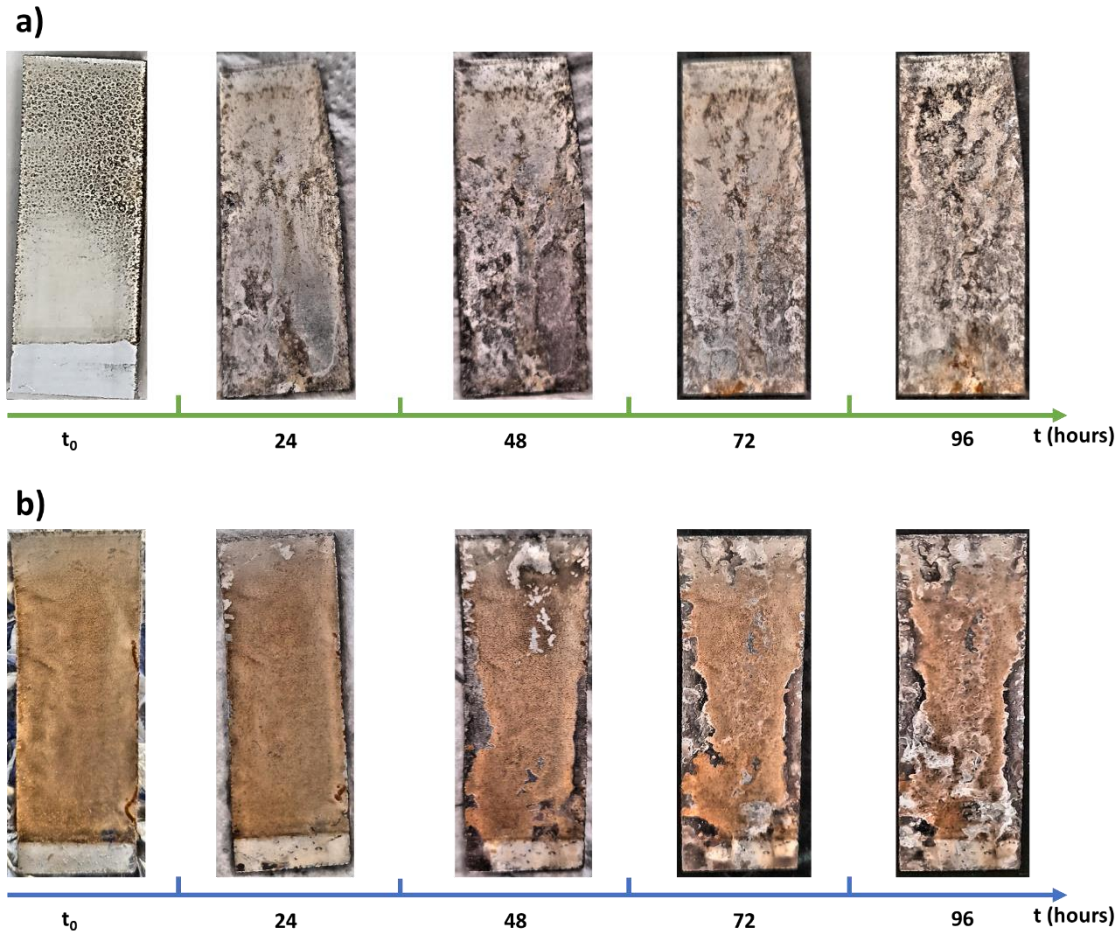

Figure IV-12: 2.3wt % NaCl salt spray test results evolution through time for a) DR hybrid coating and b) NDR hybrid coating.

The aluminum covered with the Lignin/Silicon hybrid elaborated via NDR has no evidence of pitting or surface deterioration, remaining completely intact after 48h (Figure IV-12 b)). After that period of exposure, the sample did not present any color change and slightly more than 20 possible pitting starting points. Despite the non-satisfactory behavior, the NDR coating is very promising in term of compliance requirements.

Indeed, for comparative levels, the commercially available non-chromate AC-131,X-It PreKote pretreatments applied on Al 2024 substrate failed before 24h of neutral spray test (same conditions of the present study)[38]. Keeping a “green” direction, assays achieved with a bio source layer (i.e., chitosan[39]) lead to comparable trend and a 48h resistance can be reached by optimizing the viscosity of the solution. Some other innovative systems show

much enhanced performance, i.e. the Ce inhibitor-Al-O coating of Liu,Y. et al.[40] (until 120h), but the deposit of the protective material is done with a constraining method hard to scale up for industry purpose, i.e. the magnetron sputtering, micro arc oxidation[41].

Although DR and NDR coatings have shown a different response to the salt fog test, the cyclic voltammetry evaluation did not follow the same pattern. According to the data recorded (Figure IV-13) the corrosion potential obtained for both DR and NDR coatings is quite the same (around -0.52 V) and shows a real improvement of the corrosion resistance. A precursor work Abdel-Salam, O.E. et al.[42] on the electrochemical behavior of an anodized Al2024 substrate clogged with lignin already highlighted the capacity of the bio source to affect the material resistance. In this study, the E_{corr} value diminished from -642.4 mV/ Ag/AgCl (Al2024-T3) to -581.2 mV/ Ag/AgCl (anodic bio-coating).

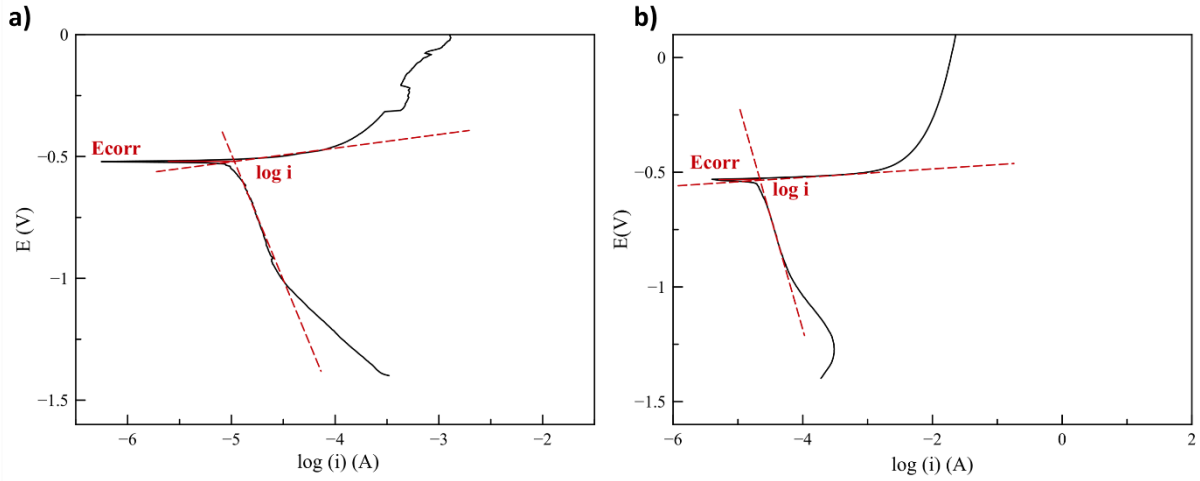

Figure IV-13: Cyclic voltammetry curve for a) DR hybrid Lignin/Silicon coating and b) NDR hybrid Lignin/Silicon coating immersed in 3.5wt % NaCl.

The same behavior was maintained for both corrosion current and corrosion density, that presented a slightly better result for the DR with i_{corr} equal to 0.01 mA and a density of 0.04 mA/cm^2 in comparison with a current of 0.02 mA and 0.09 mA/cm^2 of density for the non-direct hybrid coating.

The XPS chemical analysis of the corroded disks corroborated the Tafel curves above, indicating extremely similar compositions and chemical environments for both coatings. General spectra of the DR and NDR samples in Figure IV-14 a) and c) respectively had almost the same chemical elements identified.

The DR Al 2p core level (Figure IV-14 b)) presents two components related to the Al_2O_3 (BE 74.9 eV) and hydroxylated aluminum entities[43] (BE 74.3eV) and possible aluminosilicate species created after the corrosion, as stated in the work of Frankel, G. S. and Lopez-Garrity, O.[44], in which is shown that an Al 2024 alloy protected the use of a Sodium Silicate could create aluminosilicate entities in the presence of NaCl solution. The total amount of Al, 22.9 % of the total composition, corresponds to an increase of about 20% which confirms the coating deterioration (Table II-6).

The Si 2p core level also had an impressive alteration, with a content reduction from 8.2 % to 0.8% and a slight shift of the binding energy to 102.6 eV (in comparison to BE = 103.0 eV before the corrosion test - Table II-6). This lower BE looks like the TESPSA layer or aluminosilicates like layer[44,45,46].

For the carbon, the whole quantity is half reduced (from 60.1 % to 32.4 %) but kept one of the most important elements present at the surface.

Finally, as expected for a corrosion situation, the oxygen content grew up from 28.4 % to 42.6 %, referring to the formation of highly oxidized species. Completing the identified elements, the Cl (1.3 %) presence is related to the sodium chloride precipitation after the cyclic voltammetry test.

For the NDR hybrid coating (Figure IV-14 d)), same assignments have been done (Table IV-2).

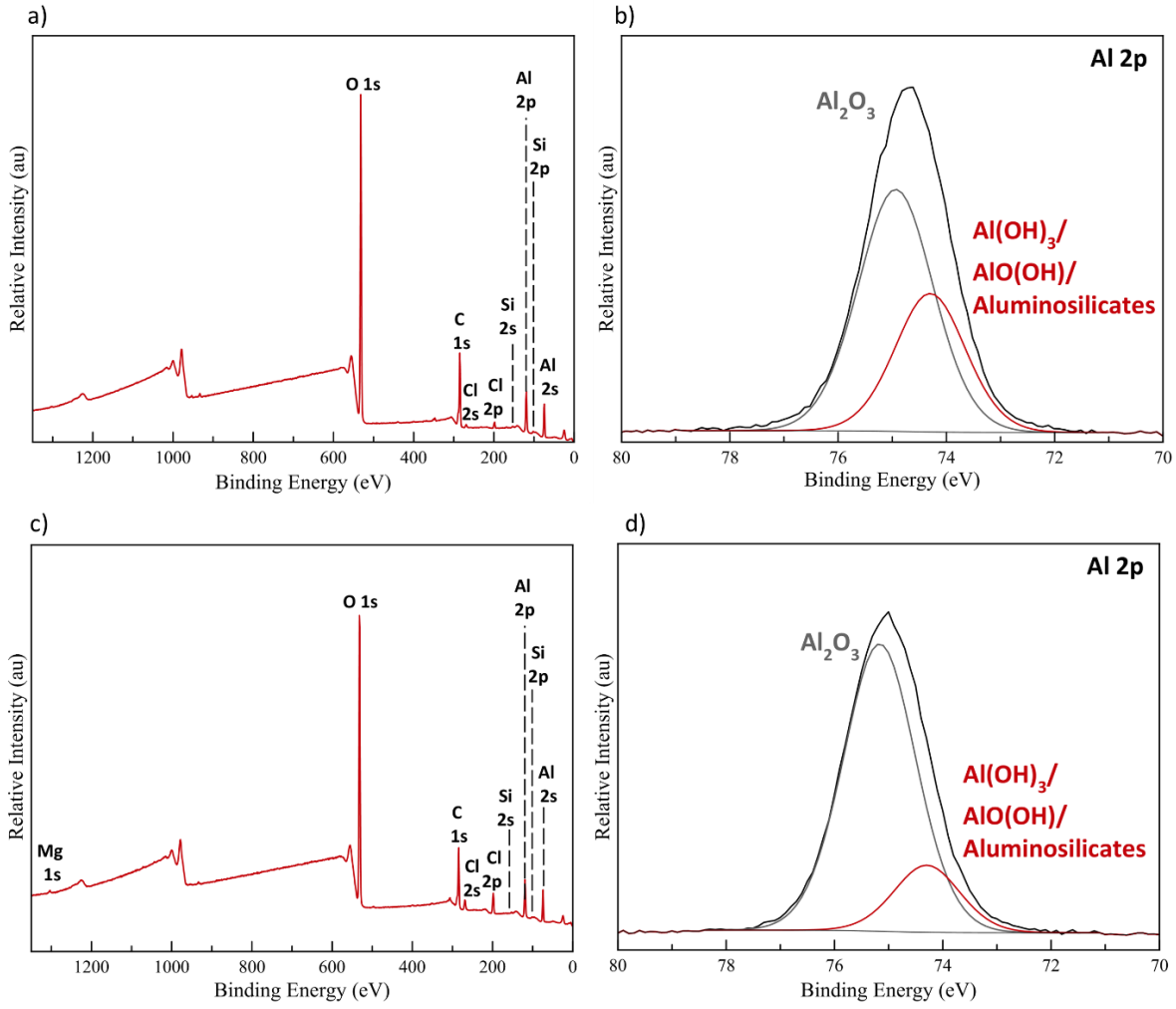

Figure IV-14: XPS spectra from DR and NDR coatings after immersed in 3.5wt % NaCl: a) Survey spectrum of DR Lignin/Silicon hybrid coating, b) Al 2p core level spectrum of DR Lignin/Silicon hybrid coating, c) Survey spectrum of NDR – Lignin/Silicon hybrid coating and d) Al 2p core level spectrum of NDR – Lignin/Silicon hybrid coating.

Table IV-2: XPS quantification results for DR and NDR coating after immersed in 3.5wt % NaCl.

DR Coating - Hybrid Lignin/Silicon				NDR Coating - Hybrid Lignin/Silicon		
Core Peak	BE(eV)	At.%	Total At. Conc (%)	BE(eV)	At.%	Total At. Conc (%)
Al 2p	74.9 74.3	14.9 8.0	22.9	75.0 74.1	19.7 4.1	23.8
C 1s	285.0 286.3 287.8 289.2 290.4 283.2	24.6 3.2 0.8 2.0 1.3 0.6	32.4	285.0 286.3 287.9 289.4 290.6 283.4	21.7 2.2 0.7 1.8 0.6 0.6	27.5
O 1s	532.4 531.1	28.9 13.6	42.6	532.4 531.0	34.8 9.0	43.8
Mg 1s	-	-	-	1304.8	0.2	0.2
Si 2p	102.6	0.8	0.8	102.6	0.7	0.7
Cl 2p	198.9 200.4	0.9 0.4	1.3	198.9 200.5	2.6 1.3	3.9
C/Si		40.5			58.8	

3.3. QUV ageing tests

After the UV weathering exposure, the DR coating surface is quite well conserved and only presented a different color, losing the predominantly brown color from lignin and becoming much whiter (Figure IV-15).

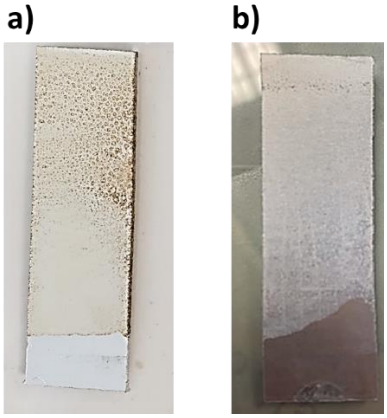

Figure IV-15: DR hybrid (withdrawal speed 0.05mm/s) coatings a) before UV exposition and b) after UV.

This phenomenon has already been related to lignin after its exposure to UV radiation. As quoted by the works of Zahri, S. et al.[47] and Tolvaj, L.[48] about the direct relation between wood (and its constituents) and the UV exposure, the lignin molecule has a tendency to absorb the ultraviolet radiation and then, becomes lighter or darker accordingly to the degradation of its structural components. The lignin discoloration achieved by the DR

sample can also be related to the photodegradation, once it has already been related by Aloui, F. et al.[49] in its review about inorganic UV absorbers.

Despite the probably photodegradation induced by the UV ageing, the coating surface did not present any new defects like cracks or holes, as related by Liao, J. et al.[50] . This positive result would be related to the enhanced mechanical stability provided by the inorganic phase, that has a much better resistance to UV exposition[51].This mechanical stability of the hybrid coating was confirmed by the adherence test, that kept the same result achieved before the exposition, the grade 2 (Figure IV-16).

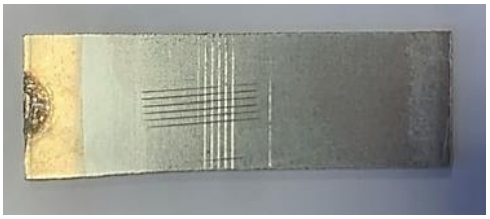

Figure IV-16: Adhesion test from DR hybrid coating exposed to UV ageing.

For a comparison, some polyurethanes coatings, what are ones of the most important in the aircraft use, the study of Usmani A.M. revealed a strong structure damage from 1000h exposure[52] attesting of the pretty good behavior of DR lignin/silicon coating. However, this first test has to be extended to NDR and even to plasma modified coatings. Indeed, UV weathering exposure could involve an appreciable loss of hydrophobicity as reported in the work of Xiu,Y. et al.[53] concerning a SF_6 plasma etched polybutadiene films; hydrophobicity of such treated polymer surface was actually reduced by half after 300h UV exposure. In the future development of the lignin-based materials, this point will be a mandatory issue to focus on.

Chapter Summary

The good anticorrosive results obtained by the NDR sample in the salt spray test and close results between the DR and NDR obtained in the cyclic voltammetry offer real good perspectives for an anticorrosion purpose.

- in a time, the salt spray test confirmed the Al 2024 its susceptibility to corrosion, as after immediate immersion into NaCl, it already presented color change and pitting points to finally finished to corrode in a general way.

  DR and NDR hybrid coatings did not presented color changes and general corrosion points during the salt spray evaluation, already proving a relative improvement in relation to the bare Al 2024. The DR hybrid presented more than 20 pitting points since 24h of exposition, indicating it did not resist efficiently to an aggressive environment.

  On the other hand, the NDR confirmed to be most efficient anticorrosion system, as no corrosion type was noticed even after 48h in the salt spray chamber. Only after 2 days some few pitting points were revealed.
- The Tafel curves extrapolation related very close results for both hybrid coatings, with E_{corr} of -0.52 V and -0.53 V for DR and NDR respectively. This confirms the protective behavior of lignin/silicon formulation.
- A first UV weathering ageing test was carried out onto DR lignin/silicon coating with a quite successful result. Despite a discoloration of the surface, the coating is still covering the Al2024 substrate after 5000h exposure

References

1. Darvell, B. W. (2018). Chapter 13 - Corrosion. Materials Science for Dentistry (Tenth Edition), 382-398. https://doi.org/10.1016/B978-0-08-101035-8.50013-4
2. Subari, F., Maksom, H. F., & Zawawi, A. (2015). Corrosion Behavior of Eutectic Molten Salt solution on Stainless Steel 316L. Procedia - Social and Behavioral Sciences, 195, 2699–2708. https://doi.org/10.1016/j.sbspro.2015.06.465
3. Evans, U. R. (1923). The mechanism of the so-called "dry corrosion" of metals. Transactions of the Faraday Society, 19(JULY), 201–212. https://doi.org/10.1039/TF9231900201
4. Siskou, N., Charalampidou, C., Alexopoulos, N. D., & Kourkoulis, S. K. (2018). Effect of corrosion exposure on aluminum alloy 2024 for different artificial ageing conditions. Procedia Structural Integrity, 10, 79–84. https://doi.org/10.1016/j.prostr.2018.09.012
5. Jones, D. (1996). Principles and Prevention of Corrosion. *Materials & Design*, *14*(3), 572.
6. Li, W., Cochell, T., & Manthiram, A. (2013). Activation of aluminum as an effective reducing agent by pitting corrosion for wet-chemical synthesis. *Scientific Reports*, *3*, 1229. https://doi.org/10.1038/srep01229
7. Agarwala, V. K., & Fort, T. (1976). Nature of the stable oxide layer formed on an aluminum surface by work function measurements. *Surface Science*, *54*(1), 60–70. https://doi.org/https://doi.org/10.1016/0039-6028(76)90087-X
8. Revie, R. W., & Uhlig, H. H. (2008). Corrosion and Corrosion Control. In *British Medical Journal* (Vol. 288, Issue 6412). John Wiley & Sons, Inc. https://doi.org/10.1002/9780470277270
9. Snyder, P. E., & Seltz, H. (1945). The heat of formation of aluminum oxide. *Journal of the American Chemical Society*, *67*(4), 683–685. https://doi.org/10.1021/ja01220a054
10. Birbilis, N., & Hinton, B. (2010). Corrosion and corrosion protection of aluminium. In *Fundamentals of Aluminium Metallurgy: Production, Processing and Applications*. Woodhead Publishing Limited. https://doi.org/10.1533/9780857090256.2.574
11. Snyder, P. E., & Seltz, H. (1945). The heat of formation of aluminum oxide. *Journal of the American Chemical Society*, *67*(4), 683–685. https://doi.org/10.1021/ja01220a054
12. Frankel, G. S. (1998). Pitting Corrosion of Metals: A Review of the Critical Factors. *Journal of The Electrochemical Society*, *145*(6), 2186–2198. https://doi.org/10.1149/1.1838615
13. Shao, M., Fu, Y., Hu, R., & Lin, C. (2003). A study on pitting corrosion of aluminum alloy 2024-T3 by scanning microreference electrode technique. *Materials Science and Engineering A*, *344*(1–2), 323–327. https://doi.org/10.1016/S0921-5093(02)00445-8
14. Kciuk, M., Kurc-Lisiecka, A., & Szewczenko, J. (2010). Structure and corrosion resistance of aluminium AlMg2.5; AlMg5Mn and AlZn5Mg1 alloys. *Journal of Achievements in Materials and Manufacturing Engineering*, *41*.
15. Reboul, M. & Vieillissement, C., (2005). Corrosion des alliages d ' aluminium Corrosion des alliages d ' aluminium. 33(0), 0–21.

16. Warner, T J; Schmidt, M P; Sommer, F; Bellot, D. (1995). *Characterisation of corrosion initiation on 2024 aluminium alloy by atomic force microscopy*. *86*. https://doi.org/https://doi.org/
17. Boag, A., Hughes, A. E., Glenn, A. M., Muster, T. H., & McCulloch, D. (2011). Corrosion of AA2024-T3 Part I: Localised corrosion of isolated IM particles. *Corrosion Science*, *53*(1), 17–26. https://doi.org/10.1016/j.corsci.2010.09.009
18. Luo, C., Zhou, X., Thompson, G. E., & Hughes, A. E. (2012). Observations of intergranular corrosion in AA2024-T351: The influence of grain stored energy. *Corrosion Science*, *61*, 35–44. https://doi.org/10.1016/j.corsci.2012.04.005
19. Zhang, W., & Frankel, G. S. (2003). Transitions between pitting and intergranular corrosion in AA2024. *Electrochimica Acta*, *48*(9), 1193–1210. https://doi.org/https://doi.org/10.1016/S0013-4686(02)00828-9
20. Luo, C., Zhou, X., Thompson, G. E., & Hughes, A. E. (2012). Observations of intergranular corrosion in AA2024-T351: The influence of grain stored energy. *Corrosion Science*, *61*, 35–44. https://doi.org/10.1016/j.corsci.2012.04.005
21. Streicher, M. A., & Begum, S. B. T.-R. M. in M. S. and M. E. (2016). *Corrosion, Intergranular*. Elsevier. https://doi.org/https://doi.org/10.1016/B978-0-12-803581-8.02712-0
22. Jones, D. (1996). Principles and Prevention of Corrosion. *Materials & Design*, *14*(3), 572.
23. Bobby Kannan, M., Bala Srinivasan, P., & Raja, V. S. (2011). Stress corrosion cracking (SCC) of aluminium alloys. *Stress Corrosion Cracking: Theory and Practice*, 307–340. https://doi.org/10.1533/9780857093769.3.307
24. Ge, F., Zhang, L., Tian, H., Yu, M., Liang, J., & Wang, X. (2020). Stress Corrosion Cracking Behavior of 2024 and 7075 High-Strength Aluminum Alloys in a Simulated Marine Atmosphere Contaminated with SO2. *Journal of Materials Engineering and Performance*, *29*(1), 410–422. https://doi.org/10.1007/s11665-019-04537-7
25. Carlos De Haro, J., Magagnin, L., Turri, S., & Griffini, G. (2019). Lignin-Based Anticorrosion Coatings for the Protection of Aluminum Surfaces. ACS Sustainable Chemistry and Engineering, 7(6), 6213–6222. https://doi.org/10.1021/acssuschemeng.8b06568
26. ASTM, 2021. Standard Practice for Exposure of Metals and Alloys by Alternate Immersion in Neutral 3.5 % Sodium Chloride Solution. ASTM G44-21. June 2021. https:// 10.1520/G0044-21
27. ISO,2017. Corrosion tests in artificial atmospheres — Salt spray tests. ISO 9227:2017. https://www.iso.org/standard/63543.html
28. ASTM, 2016. Standard Practice for Operating Fluorescent Ultraviolet (UV) Lamp Apparatus for Exposure of Nonmetallic Materials. ASTM G154-16. December 2016. DOI: 10.1520/G0154-16
29. Naik, D. L., Sajid, H. U., Kiran, R., & Chen, G. (2020). Detection of Corrosion-Indicating Oxidation Product Colors in Steel Bridges under Varying Illuminations, Shadows, and Wetting Conditions. In Metals (Vol. 10, Issue 11). https://doi.org/10.3390/met10111439
30. Mao, Y., Zhu, Y., Deng, C., Sun, S., & Xia, D. (2022). Analysis of localized corrosion mechanism of 2024 aluminum alloy at a simulated marine splash zone. Engineering Failure Analysis, 142(July), 106759. https://doi.org/10.1016/j.engfailanal.2022.106759

31. Tsirimpis, A., Kartsonakis, I., Danilidis, I., Liatsi, P., & Kordas, G. (2010). Synthesis of conductive polymeric composite coatings for corrosion protection applications. Progress in Organic Coatings, 67(4), 389–397. https://doi.org/https://doi.org/10.1016/j.porgcoat.2009.12.010
32. Heidarpour, A., Mousavi, Z. S., Karimi, S., & Hosseini, S. M. (2021). On the corrosion behavior and microstructural characterization of Al2024 and Al2024/Ti2SC MAX phase surface composite through friction stir processings. Journal of Applied Electrochemistry, 51(8), 1123–1136. https://doi.org/10.1007/s10800-021-01567-9
33. Do, T., Mcintyre, N. S., Harshman, R. A., Lundy, M. E., & Splinter, S. J. (1999). Application of parallel factor analysis and x-ray photoelectron spectroscopy to the initial stages in oxidation of aluminium. I. The Al 2p photoelectron line. Surface and Interface Analysis, 27(7), 618–628. https://doi.org/https://doi.org/10.1002/(SICI)1096-9918(199907)27:7<618::AID-SIA550>3.0.CO;2-7
34. Le, A., Kircher, O., Fichtner, M., Schild, D., Léon, A., Kircher, O., Fichtner, M., Rothe, J., & Schild, D. (2006). Evolution of the Local Structure around Ti Atoms in NaAlH4 Doped with TiCl3 or Ti13·6THF by Ball Milling Using X-ray Absorption and X-ray Photoelectron Spectroscopy. The Journal of Physical Chemistry B, 110(3), 1192–1200. https://doi.org/10.1021/jp055100b
35. Szunerits, S., & Walt, D. R. (2002). Aluminum surface corrosion and the mechanism of inhibitors using pH and metal ion selective imaging fiber bundles. Analytical Chemistry, 74(4), 886–894. https://doi.org/10.1021/ac0108257
36. Chen, X., Wang, X., & Fang, D. (2020). A review on C1s XPS-spectra for some kinds of carbon materials. *Fullerenes, Nanotubes and Carbon Nanostructures*, *28*(12), 1048–1058. https://doi.org/10.1080/1536383X.2020.1794851
37. Hoffmann, E. A., Körtvélyesi, T., Wilusz, E., Korugic-Karasz, L. S., Karasz, F. E., & Fekete, Z. A. (2005). Relation between C1s XPS binding energy and calculated partial charge of carbon atoms in polymers. *Journal of Molecular Structure: THEOCHEM*, *725*(1), 5–8. https://doi.org/https://doi.org/10.1016/j.theochem.2005.02.021
38. Kakde, V., & Mannari, V. (2009). Advanced chrome-free organic–inorganic hybrid pretreatments for aerospace aluminum alloy 2024-T3—application of novel bis-ureasil sol–gel precursors. Journal of Coatings Technology and Research, 6(2), 201–211. https://doi.org/10.1007/s11998-008-9142-4
39. Kumar, G., & Buchheit, R. G. (2006). Development and Characterization of Corrosion Resistant Coatings Using the Natural Biopolymer Chitosan. ECS Transactions, 1(9), 101. https://doi.org/10.1149/1.2215582
40. Liu, Y., Huang, J., Qin, L., Claypool, J. B., O'Keefe, M. J., & Jiang, Y. (2018). Effect of Thickness on the Structure and Corrosion Performance of Sputtered Ce-Al-O Coatings on Al 2024-T3 Alloy Substrates. Journal of The Electrochemical Society, 165(7), C395. https://doi.org/10.1149/2.1051807jes
41. Ji, S., Weng, Y., Wu, Z., Ma, Z., Tian, X., Fu, R. K. Y., Lin, H., Wu, G., Chu, P. K., & Pan, F. (2017). Excellent corrosion resistance of P and Fe modified micro-arc oxidation coating on Al alloy. Journal of Alloys and Compounds, 710, 452–459. https://doi.org/https://doi.org/10.1016/j.jallcom.2017.03.303

42. Abdel-Salam, O. E., Shoeib, M. A., & Elkilany, H. A. (2018). Characterization of the hard anodizing layers formed on 2014-T3 Al alloy, in sulphuric acid electrolyte containing sodium lignin sulphonate. Egyptian Journal of Petroleum, 27(4), 497–504. https://doi.org/https://doi.org/10.1016/j.ejpe.2017.07.014
43. White, J. L., Rowberg, A. J. E., Wan, L. F., Kang, S., Ogitsu, T., Kolasinski, R. D., Whaley, J. A., Baker, A. A., Lee, J. R. I., Liu, Y.-S., Trotochaud, L., Guo, J., Stavila, V., Prendergast, D., Bluhm, H., Allendorf, M. D., Wood, B. C., Gabaly, F. El, & El Gabaly, F. (2019). Identifying the Role of Dynamic Surface Hydroxides in the Dehydrogenation of Ti-Doped NaAlH4. ACS Applied Materials & Interfaces, 11(5), 4930–4941. https://doi.org/10.1021/acsami.8b17650
44. Frankel, G. S., Lopez-Garrity, O., & Frankel, G. S. (2014). Corrosion Inhibition of AA2024-T3 By Sodium Silicate. Electrochimica Acta, 130, 9–21. https://doi.org/https://doi.org/10.1016/j.electacta.2014.02.117
45. Wannaparhun, S., Seal, S., & Desai, V. (2002). Surface chemistry of Nextel-720, alumina and Nextel-720/alumina ceramic matrix composite (CMC) using XPS–A tool for nano-spectroscopy. Applied Surface Science, 185(3), 183–196. https://doi.org/https://doi.org/10.1016/S0169-4332(01)00594-3
46. Moulder, J. F., Stickle, W. F., Sobol, W. M., & Bomben, K. D. (1992). Handbook of X-Ray Photoelectron Spectroscop27y: A Reference Book of Standard Spectra for Identification and Interpretation of Xps Data.
47. Zahri, S., Belloncle, C., Charrier - El Bouhtoury, F., Pardon, P., Quideau, S., & Charrier, B. (2013). UV light impact on ellagitannins and wood surface colour of European oak (Quercus petraea and Quercus ASS 2007. May 2014. https://doi.org/10.1016/j.apsusc.2006.11.005
48. Tolvaj, L. (1995). Artificial Ageing of Wood Monitored by DRIFT Spectroscopy and CIE L*a*b* Color Measurements. I. Effect of UV Light. Holzforschung, 49, 397–404.
49. Aloui, F., Ahajji, A., Irmouli, Y., George, B., Charrier, B., & Merlin, A. (2007). Inorganic UV absorbers for the photostabilisation of wood-clearcoating systems: Comparison with organic UV absorbers. Applied Surface Science, 253(8), 3737–3745. https://doi.org/https://doi.org/10.1016/j.apsusc.2006.08.029
50. Liao, J., Brosse, N., Pizzi, A., & Hoppe, S. (2019). Dynamically Cross-Linked Tannin as a Reinforcement of Polypropylene and UV Protection Properties. In Polymers (Vol. 11, Issue 1). https://doi.org/10.3390/polym11010102
51. Huang, W., Zhang, Y., Yu, Y., & Yuan, Y. (2007). Studies on UV-Stable silicone-epoxy resins. Journal of Applied Polymer Science, 104, 3954–3959. https://doi.org/10.1002/app.26188
52. Usmani, A. M., & Donley, M. (2002). Aircraft-coating weathering studies by analytical methods. Journal of Applied Polymer Science, 86(2), 294–313. https://doi.org/https://doi.org/10.1002/app.10960
53. Xiu, Y., Hess, D. W., & Wong, C. P. (2008). UV and thermally stable superhydrophobic coatings from sol–gel processing. Journal of Colloid and Interface Science, 326(2), 465–470. https://doi.org/https://doi.org/10.1016/j.jcis.2008.06.042

Chapter V.

General Conclusion & Perspectives

General Conclusion

One of the main motivations of this thesis project concerned the development of new alternatives to hexavalent chromium in the corrosion protection of metals and alloys. The Cr VI is the main element used for the elaboration of "primers"; the first protective layer applied to Al alloys used in the aircraft industries against corrosion. The soon interdiction to the use of Chromate Conversion Coatings accelerates the urge for new research about alternatives that could combine the protective requirement with the environmental compliance.

The REACH legislation is a strong example of how European countries are making efforts to mitigate the impact of hazardous and pollutant chemical products used in all industrial sectors, by banning those who are harmful to the environment and to human beings. The Chrome Vi is a valuable example of important compound that is going to be banned by REACH. For this, it was chosen to take advantage of the renewable bio-based feedstock on the territory of the University of Pau and Adour with the pine trees forest and the lignocellulosic molecules. Lignin is one of these molecules and today, this biopolymer is not properly valued, its main use serving as fuel for regional paper mills. Its rich and complex molecular structure is, however, an undeniable asset for considering other types of applications with higher technicality. It has already been incorporated into materials to confer new physico-chemical properties.

In this context, the main objective of this work was dedicated to the design, elaboration and comprehension of a bio-sourced pioneering hybrid coating, based on the combination of Kraft Lignin and a Silicon matrix, to emerge as a possible substitute for the currently used primers, on specific for Al 2024 alloy. This alloy is commonly employed by the Aircraft industry for its mechanical abilities, in fuselage for instance. The actual need of the industry is to develop some efficient protective layers with a greener approach in terms of reagents used, energy and time economy. For this purpose, in the present work, the EISA methodology was coupled with the Dip-Coating deposition technique, since they can produce coatings with a small energy demand while maintaining a "sustainable" aspect. The deposit does not require any external energy input as it sets up naturally in aqueous medium according to a hydrolysis-condensation-drying proceeding.

First, our interest was focused on the solubilization of lignin using different solvents, trying to find the one with the least negative impact on the environment. MilliQ water was of course studied as well as organics like ethanol, acetone and THF. These conventional solvents dissolve a wide range of monomer precursors and the resulting polymer products, making them ideal solvents for homogeneous polymerizations. However, they don't fulfill the "green" expectations of this work as they can cause environment depletion. Then DMSO, a slightly oily liquid derived from plants and taken the form of a by-product of papermaking and m-THF, 2 a volatile cyclic ether extracted from corn stover biomass another regional biomass. Comparison of the solvents effect on Lignin dissolution has shown the pretty good efficiency of THF. The low THF evaporation index (I_e = 2.3 relate to ethyl ether according to norm DIN 53170) allows a release in less than one minute completely adapted to the demands of the EISA methodology.

In same section, Al 2024 surface has been chemically prepared to get rid of oils, contaminants and oxides residues present on the surface in order to be able to expose the "bare" substrate and to make it more reactive to further steps. Beside the effective surface cleaning, a substantial roughness increase is observed and a 40% decrease of the native Al2O3 has been estimated from the XPS data. The XPS characterization has also revealed the almost disappearance of Cu, Mg and Zn elements from the surface in relation with dissolution of intermetallic particles.

Finally, first attempts of interaction between TEOS reagent and Lignin bio source were done under EISA protocol. A solid product composed of two phases (a dense matrix of SiO2 and microparticles of Lignin) was evidenced attesting of the good adaptability of the methodology normally devoted to porous inorganic material design.

The second stage of the work then focused on the design of various lignin/silicon coating applied on the Al 2024 alloy, by modeling the dip coating withdrawal speed and the relative humidity in the deposit chamber. The preparation has progressively evolved from the direct application on the coating (Direct Route) to a lignin/silicon post deposit over a pre-layer of bonding organic molecules, TESPSA (Non-Direct Route). The best DR coating aspect (less surficial defects as cracks and holes) was reached under a 10% relative humidity and with a 0.05mm/s withdrawal speed corresponding to the capillary regime of dip coating process. Even though these conditions were selected, the DR coatings were never full covering over the metal substrate. XPS results still reported a clear Aluminum signal suggesting the inhomogeneity of the coatings. Moreover, the mean wettability was not considered pretty high, once the WCA was measured around 50°.

Regarding the demands required for protective uses in the aeronautical sector, the continuation of the work kept on going to an improvement of the material. For this, a pre-functionalization of the Al 2024 surface was performed by a reaction with the TESPSA reagent. A stronger interaction between the organic/inorganic phases and the substrate was identified, with some lignin particles being identified onto the NDR coating top surface (SEM). Whatever the conditions of withdrawal speed and moisture tested, the most impressive point stood in the homogeneity of the hybrid layer well spreading over the whole surface. The XPS analysis confirmed the sole signals associated to both lignin and silicon network, and the SEM observation traduced just about very few defects on the surface. In these improved multilayers architecture, an esterification reaction between the hybrid solution and the organo-alcohol layer created by the functionalization is noticed as the likely cause of the better coating structuring. The wettability of the Al2024 drastically decreased when covered up with NDR hybrid, with a WCA about 95°, and then the emergence of a hydrophobic behavior.

To go further in the structuring of the coating architecture, an XPS depth profile was carried out on the optimized NDR lignin/silicon specimen. A variable in depth composition was surprisingly observed alongside the almost 2 microns thick coating. An interconnected lignin-siloxane network exists in the coating, with an evolutive composition gradient and SiO_2 clusters (or phases) found at the substrate/TESPSA/coating interface. Concerning the general adhesions of both DR and NDR coatings on the aluminum alloy, they seem identical (of a good Grade 2) and the organic layer in the NDR architecture did not enhance this property.

An interesting opening was given to this work with the fluorinated plasma treatment of the elaborate coatings. This technology is currently used as a mean to activate/clean metal surfaces in the industry, and few alternative actions are conducted to improve the hydrophobic properties materials surface. This type of analysis, combining bio-sourced hybrids with SF_6 plasma, has not yet been reported in publications. This part of the work was achieved during a 4 month research mobility in University Federal or Rio de Janeiro (Brazil). After the SF_6 plasma exposure, the DR wettability highly collapsed with a 95% increase of the contact angle generating a pronounced hydrophobic character (WCA of 95°). This new property is specially related to the intense presence of the highly fluorinated -CF_2 and -CF_3 bonds. For the NDR coatings, the surface medication by fluorine entities did not traduce such a drastic hydrophobicity (WCA of 105°). The effective etching effect noticed in that case could mitigate the impact of fluorine entities at the surface.

The work finalized with a very first evaluation of the anti-corrosive property of the coatings. Both DR and NDR coatings showed a clear decrease of the corrosion current and corrosion potential relate to Al2024 confirming the protective behavior. Industrial neutral spray test has allowed to differ the behavior of the coatings along time of exposure under a 2.3%wt NaCl fog. The NDR hybrid system proved to resist 48h which is a very promising result among alternatives to hexavalent chromium conversion layers. To complete this study, a unique UV weathering aging test was carried out to prospect the lignin/silicon response. The optimized DR coating still lays down after 5000h exposure what is a better result than for main of the polymers coatings reported at the present time. Finally, it was possible to conclude that the work successfully achieved its main objective to elaborate and provide the first conclusions about the possibility to create a lignin-based hybrid coating, explaining the possible mechanisms and reasons why the protection was achieved.

Perspectives

All the work carried out during this thesis allowed us to obtain promising results, in particular by the non-direct route applied to hybrid coatings containing a pre-functionalization, which presented the most outstanding results. However, for the continuation of this research work, new studies could be completed in the short, medium and even long term to allow the fully development and progression of this material.

In a short time, deeply investigations should be carried out to complete the understanding of the coatings. So, longer cyclic voltammetry corrosion tests should be done to allow a should be done to allow a higher exposition of the coating to the corrosive solution and then, the visualization of both i_{corr} and E_{corr} after 24h,48h,72h and 96h. In addition, once the hybrid layers are extremely porous, BET analysis could be done to allow a precise observation of this aspect and its correlation with the macro behavior of the samples. Finally, longer exposure QUV tests and chemical analysis of the layers after the material degradation could corroborate to understand the effects of the UV radiation in the lignin/silicon hybrids.

Looking a bit forward, the hybrid solution preparation and its optimization is a step that could be deeply improved. Firstly, the incorporation of new bio-sourced compounds (like Tannin) in the solution could enhance the antioxidative properties of the final product, such as the hydrophobic character. Following, the search for

greener solvents that could efficiently solubilize the lignin (or the combination lignin + other bio-polymer+ silicon matrix) is an important step to reduce the environmental impact of the process. Once this new solubilization study is finalized, a complete characterization of the new solution must be carried out, looking to fully understand parameters like viscosity, morphological organization and chemical composition. For this, XPS, TGA, NMR, SEM, rheological and even computation simulations could be investigated. The functionalization step can also be considered as in key point to be deeper study in the future, find shorter immersion times (during this work, an overnight immersion was set as the most performant) and replace Toluene for a less hazardous may be interesting and innovative points on the process. All these points could be considered as medium terms perspectives.

Finally, as long-term perspectives, an industrial study (with long and standardized tests) of a complete anticorrosion system, with the substrate coated by the hybrid bio-sourced coating, an undercoat application and a finishing layer (painting application for instance) could be carried out. For this moment, large scale mechanical tests would attest the viability to the system to really become an industrial alternative.

Appendix

Figure List

1. X-Ray Photoelectron Spectroscopy (XPS)

The beginning of the X-Ray Photoelectron Spectroscopy (XPS) can be traced back to the year 1887 when the German physicist Heinrich Rudolf Hertz discovered the photoelectric effect, a phenomenon that was only explained in 1905 by Albert Einstein. Two years later, the first XPS spectrum was finally disclosed, in research by P.D. Innes[1].

However, despite this, only almost 50 years later the XPS technique was related to surface analysis. In the late 1950s, at Uppsala University in Sweden, K. Siegbahn and his research group improved and developed a system capable of generating and saving high energy and high resolution XPS spectra. In 1967, Siegbahn released his study on the capability of using XPS technique, then called Electron Spectroscopy for Chemical Analysis (ESCA), for surface verification. Because of his important work, Siegbahn received the Nobel Prize for Physics in 1981[1,2].

This technique was widely used during this thesis work to characterize the raw materials, substrate, solutions and coatings themselves; it is presented in more details in the following paragraphs.

The principle of operation of the XPS consists in the use of the photoelectric effect: the substrate to be analyzed is irradiated by a monoenergetic source of photons (X-rays) with an energy equal to hv, which interact with the atoms of the surface of the material (maximum depth of 10 nm), resulting in the ejection of core/valence electrons. These electrons will then be emitted in multiple directions with specific kinetic energies (KE), photoemission phenomena. Finally, they will be collected and analyzed accordingly to their kinetic energy[3,4]. The photoemission process can be divided in the three following steps, as stated by Hollinger, G.[5]:

a) **Photon absorption by the electron:** A photon of energy hv is excited and then absorbed by a photoelectron of energy E_0.

b) **Electron transport to the surface:** During its path inside the material, the excited electron can collide with others from the material surface, changing its path. Four interaction modes are possible:

- The excited e^- does not collide with any other and after leaving the material it is collected with the same initial energy E_0.
- The excited e^- inelastically collides with one other and leaves the surface with an energy equal to E_0-ΔE.
- The excited e^- inelastically collides multiple times and arrives from the material surface with its initial energy extremely reduced, becoming a secondary electron. The distance traveled between two inelastic shocks is called the inelastic mean free path (IMFP, noted λ) and is mathematically described in the following equations[6]:

$$\lambda = \frac{E}{E_p^2[\beta \ln(E\gamma) - \left(\frac{C}{E}\right) + \left(\frac{C}{E^2}\right)} \qquad \text{Equation 1}$$

Where: $\beta = -0.10 + 0.944\left(E_P^2 + E_g^2\right)^{-\frac{1}{2}} + 0.069\rho^{0.1}$ Equation 2

$$\gamma = 0.191\rho^{-1/2} \qquad \text{Equation 3}$$

$$D = 53.4 - 20.8U \qquad \text{Equation 4}$$

$$C = 1.97 - 0.91U \qquad \text{Equation 5}$$

$$U = \frac{N_v \rho}{M} = \frac{E_P^2}{829.4} \qquad \text{Equation 6}$$

With λ the inelastic mean free path in Å, E the kinetic energy, N_v the number of valence e^- per molecule or crystal lattice, ρ the density of the solid in g/cm^{-3}, M the molar mass of the molecule or the crystal lattice and E_g the energy of the band gap in eV.

- The excited e^- is absorbed by the sample and is no longer recovered. This possibility and the two previous explained are indicated in Figure 1 a) such the probability to recovers an e^- as a function of material depth (Figure 1 b)).

c) **Surface crossing:** it is related to the electron energy loss during due to the single or multiple collisions inside the material. It is divided in three main reasons:

- **Low energy loss:** resulted of the electron-photon interaction (just some tenths of eV).
- **Medium energy loss:** transitions between the bands (or inside the same band) resulted from an electron-electron interaction that provokes the loss of some eVs.
- **Big energy loss:** Collective excitations of the valence electrons that generates an energy loss of until 30 eV.

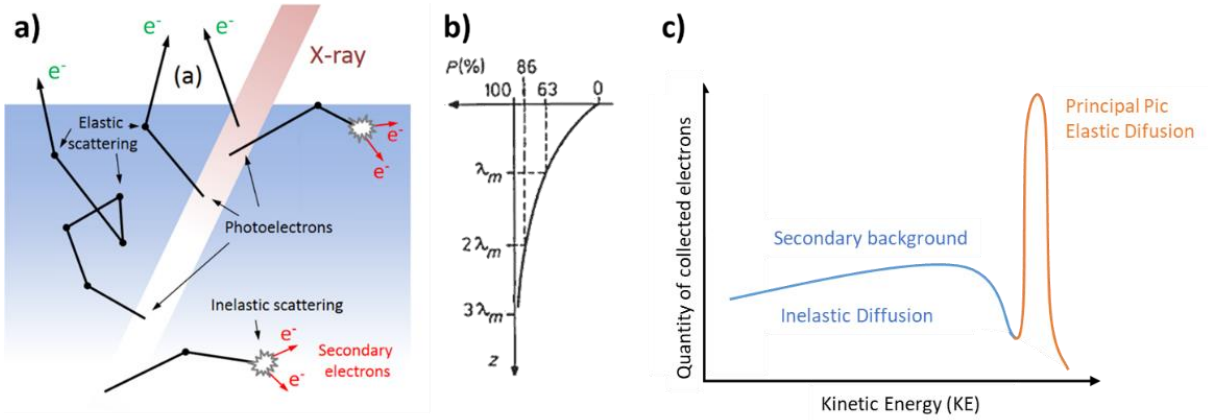

Figure 1: a) Possible electron interactions with the surface, b) probability that a photoelectron arrives at the surface as a function of its inelastic mean free path and c) schematization of an XPS spectrum differentiating the photoelectrons coming from an inelastic scattering from those resulting from elastic scattering. Adapted from references [5] and [6].

1.1. XPS analysis of a chemical environment

Still based on the photoelectron principle, it is possible to obtain an energy conservation equation, which will correlate the kinetic energy (KE), the emitted photon energy (hν), the energetic difference between an electron in the initial state and after the excitation and a work function related to the spectrometer binding energy (BE) in the following equality:

$$h\nu = KE + BE + \phi_{spec} \quad \text{Equation 7}$$

For conductive samples, the Fermi level (highest energy level occupied at absolute zero temperature of the spectrometer and the sample are calibrated to the same level. In addition, the calibration of the instrument allows the quantity ϕ_{spec} to be eliminated, so the previous equation can be simplified and re-organized in the following way[3, 4, 5,7]:

$$BE = h\nu - KE \quad \text{Equation 8}$$

The value of the photon energy (hν) will result in the use of a monoenergetic source to irradiate the samples, which in this work consists of an Al Kα (1486.6 eV) source. Once this variable is known, the BE will depend exclusively on the KE determination, depending on exclusively of the material's nature. The BE determination principle is schematized in Figure 2 below.

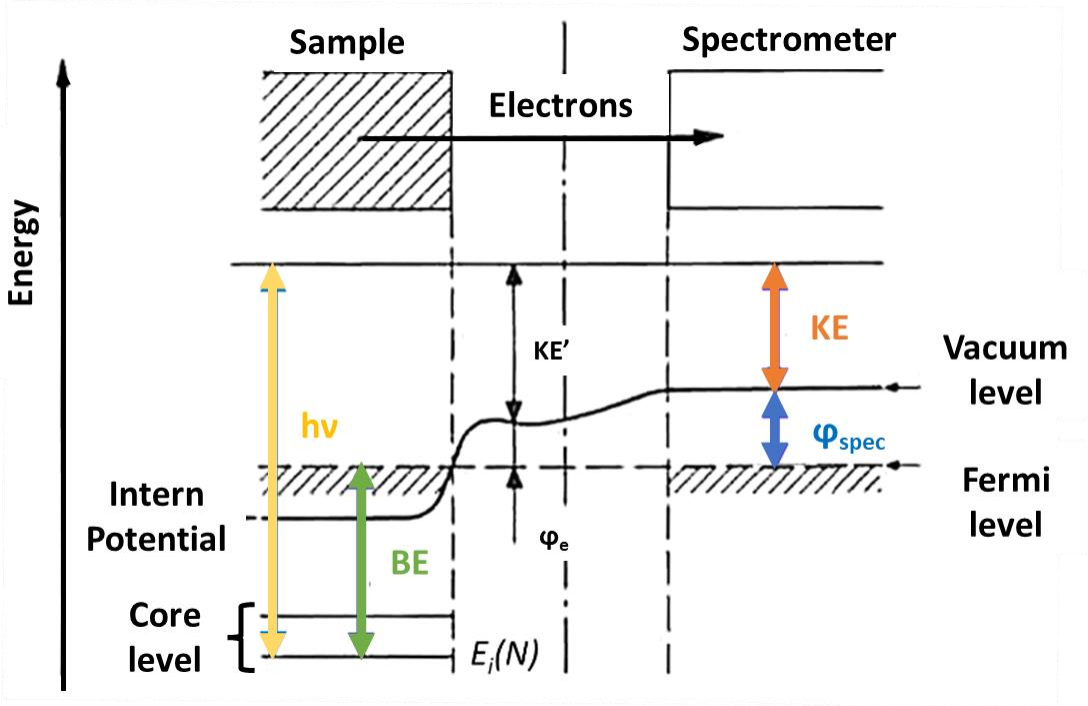

Figure 2:Binding Energy determination principle in XPS. Redrawn from [5].

However, an atom is not really isolated: the sensitivity of an electron to its chemical environment, and thus to the chemical bonds it participates in, changes its binding energy. When an atom is less electronegative, electrons participating in a covalent bond move towards another atom, reducing the repulsion between the e⁻s of that atom and bringing them closer to the nucleus. This increases the binding energy of the central electron of the

atom in question. Similarly, the oxidation of atoms involves the loss of at least one electron, which results in weaker repulsion between electrons and electrons' proximity to the nucleus. The binding energy is thus increased.

The opposite happens when the atom in question is more electronegative or reduced. The binding energy is thus reduced. These phenomena are called initial state effects because the reasoning is based on the state of the atoms prior to photoemission[8].

In addition, the fact that an atom is subject to photoemission interactions means that other phenomena inherent in it (so-called "end-state effects") also change the binding energy. Three contributions related to these effects are highlighted[9]:

- Relaxation after light emission can be identified. When the central electron is ejected, the peripheral orbitals contract around the resulting hole. Therefore, the positive charges tend to be shielded, which means that the energy in the final state of the atom, and therefore the binding energy, is reduced.
- The accumulation of positive charges during analysis (phenomena restricted to insulator or semiconductor samples). The ejection of photoelectrons results in the formation of uncompensated positive charges. The sample is then positively charged. The surface potential arises, and the electrons are delayed, increasing the binding energy. The use of an electron gun can offset the positive charge produced, reducing or even eliminating this charging effect.
- The modification of the Fermi energy (for insulators or semiconductor sample). Since in an insulating compound there are no free electrons (or holes), its Fermi level cannot be set to a spectroscopic-like level. Therefore, the reference is no longer the Fermi level, but the vacuum level. Therefore, the binding energy then depends on the work function of the spectrometer (ϕ_{spec}). However, one solution is to switch to the new current reference by modifying all BEs identically for all electrons of the probed nucleus within a similar material.

1.2. Spin-orbit coupling and multi-electronic processes

The electronic orbitals will possess two different movements, the intrinsic angular momentum (spin S, with S= ±1/2) and the orbital momentum (L, with L =0, 1, 2 or 3 for the s, p, d and f orbitals, respectively), that will interact with each other creating a so-called "spin-orbit coupling" effect. This phenomenon consists in the splitting of the peaks that do not have their orbital moment equal to zero, thus generating a double peak in the XPS spectrum. These two peaks created will be spaced by a certain binding energy that will vary accordingly to the verified atom.

The intensity of the peaks is normally given by the 2J+1 multiplicity rule, once that the total angular momentum J of an e^- on a given layer is defined by the relation J = L+S.

Some other kinds of peaks may appear in the XPS spectrum, the most important are:

- Auger peaks: The energy released from the displacement of an electron from the upper layer to a hole (created during photoelectron ejection) is not dissipated as radiation, but is transferred to

another electron, causing it to eject. If this electron is detected, it is associated with the formation of the Auger peak in the XPS spectrum.

- **Peaks associated with spin multiplet structures**: After photoionization, coupling occurs between unpaired core electrons and unpaired valence electrons (paramagnetic compounds). This coupling induces different final states, resulting in different peaks.
- **Satellite peaks**: In response to the gap created during photoionization, a relaxation effect occurs that excites weakly bound valence electrons: these valence electrons can be sent to unoccupied energy levels. Therefore, for the emitted photoelectrons with a certain kinetic energy.

1.3. XPS Spectra: Concepts and Processing

When performing an XPS experiment, the first step is to obtain a general spectrum (also called survey spectrum). This spectrum will be made from high energy variation and low-resolution quality and will have two distinct energy regions. The first will be the core level peaks (BE > 30 eV), which will allow the identification of all the chemical elements that constitute the sample (except by Hydrogen and Helium), and the determination of which components should be evaluated in high-resolution (Figure 3 a)), which allows the identification of the chemical environment related to the studied chemical element. The second region, the so-called valence band (BE < 30 eV), corresponds to an experimental visualization of the density of occupied electronic states of the solid and are thus often referred to as a "fingerprint" of a material (Figure 3 b))[4].

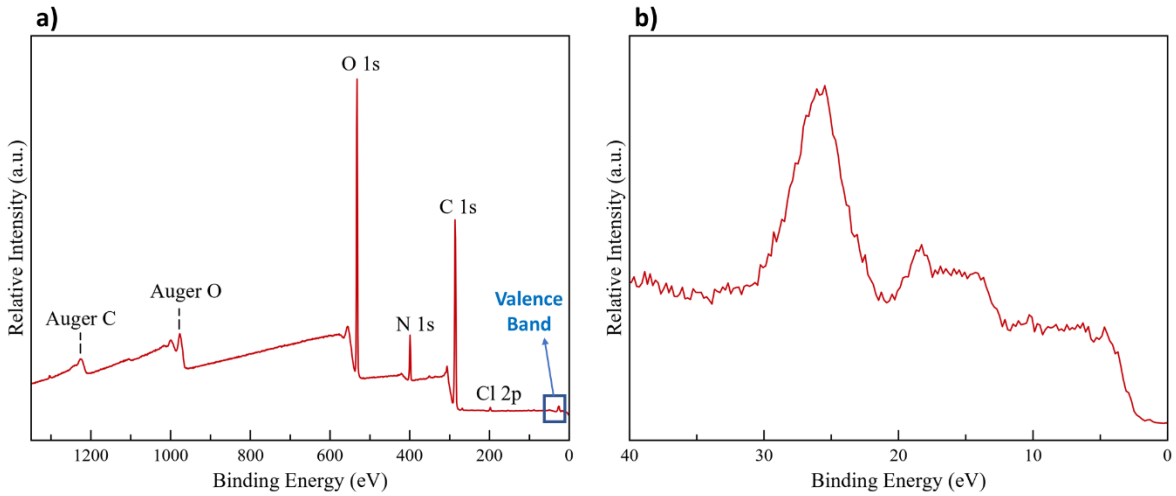

Figure 3: XPS general spectrum (a) and valence band, with lower energies (b).

The treatment of the XPS spectra from the different materials presented in this manuscript is as follows:

- Calibration of the C 1s line with respect to the peak related to C-C/C-H lignin bonds, which was set at 285.0 eV (± 0.1 eV). This peak, therefore, will comprise both aliphatic carbons and carbons of aromatic structures of the organic phase. This approach has already been used in the literature, due to the energetic proximity between the types mentioned above[10,11].

- For modeling the continuum background, a Shirley type was chosen. This background chose allows an extensive comparison of the obtained results with the published results about the subject, which are mostly based on the Shirley background.
- Deconvolution of the core peaks using CasaXPS software, mainly based on XPS analyses of reference compounds (that are going to be shown and discuss throughout the Chapter 3) performed in the framework of this thesis work but also on results from the literature. The components resulting from the symmetric peaks deconvolution correspond to the product of a Gaussian function (70%) and a Lorentzian function (30%), labelled GL (30) in the software.
- For the core peaks, the atomic percentages (at.%) relative to each component were calculated using the corrected areas (A_i^{correc}) of each component:

$$\text{at.}\,\% = \frac{A_i^{correc}}{\sum_i A_i^{correc}} \qquad \text{Equation 9}$$

where:

$$A_i^{correc} = \frac{A^{raw}}{RSF\ x\ TxMFP} \qquad \text{Equation 10}$$

The variable T is relative to the transmission function of the spectrometer (which combines the transmission factor of the analyzer and the efficiency of the detector, whose values are given by the manufacturer of the spectrometer), MFP is the mean free path and RSF "Relative Sensitivity Factor" is the atomic sensitivity factor, which depends on the effective section (probability that the incident photon causes the ejection of the electron). The values of RSF and MFP used for these thesis works are based on semi-empirical databases provided by the manufacturer of the spectrometer (Scofield cross sections database).For the alumina oxide layer, the estimation of its thickness was calculated from the following equation:

$$(\mathrm{d_{Al2O3}})(\mathrm{nm}) = \lambda_o osin\theta . sin\theta \left(\frac{N_m \lambda_m I_o}{N_o \lambda_o I_m} + 1\right) \qquad \text{Equation 11}$$

N_m and N_o are the metal and oxide densities respectively (N_m =2.7 g/cm^3 and N_o=3.95 g/cm^3), λ is the inelastic mean free path (IMFP) calculated in Flores-Mancera, M. A et al.[12] and reported as 26 nm for the Al metal and 28 nm for Al oxide. The oxide to metal peak ratio (I_o/I_m) was obtained from XPS quantification. The theta (θ) angle used was 54.7 degrees and depends on the inner optical configuration of the spectrometer.

1.4. XPS parameters used in this thesis

XPS analysis were performed in a Thermo K-alpha spectrometer working with a hemispherical analyzer and a micro focused (400 µm diameter microspot), equipped with a monochromatic X-ray radiation source (Al Kα, 1486.6 eV) operating at 72 W. The analysis chamber of this equipment is kept in ultra-high vacuum (10^{-9} mbar) and is connected to an intermediate chamber also under ultra-high vacuum (10^{-7} mbar). This last one is directly

connected to a glove box that is kept under a protective atmosphere (argon), whose O_2 and H_2O levels are maintained lower than 1 ppm. The machine can be seen in the Figure 4 below.

Figure 4: Thermo K-alpha spectrometer used for all XPS analysis.

Even though the investigated substrate is metallic, and the hybrid lignin-silica coatings has a metallic phase, the natural oxide layer of Al_2O_3 that covers the Al 2024 alloy, and the thick organic phase of the coating could create an insulant aspect on the samples, hindering the analysis due to the appearance of charge effects. To compensate this phenomenon, a dual beam charge neutralization system ("flood gun" - low energy electrons and Ar^+ ions) was used during the analysis, providing consistent charge compensation.

Three analysis types were used during this thesis:

- **Single surface point:** this analysis starts with the obtention of a general spectrum, with low resolution and a binding energy range from 0 until 1350 eV. During this acquisition, the pass energy is adjusted to 20 eV with an energy step of 1.0 eV. Once all constituent elements are determinate, the core peaks of each one of them are acquired. In this moment, the energy step is adjusted to 0.1 eV. All spectrums were deconvoluted following the methodology described in the topic 7.3 (XPS Spectra: Concepts and Processing) of this chapter.
- **Chemical mapping:** this investigation starts exactly as the previous one, with the general survey spectra obtention and the chemical elements identification. Once it is done, a large area of 560 points is defined on the sample surface. The pass energy was set to 80 eV and a 20 µm step was defined. Differently of the other analysis types, the obtained chemical map is analyzed in the Thermo Scientific™ Avantage Data System for surface analysis, which allows the creation of an overlapped image with all elements and how they are distributed on the surface.
- **Depth profile:** for the depth profile, the same pass energy and energy step of the single point analysis were used. An Ar^+ ion beam at 3000 eV energy and high current was used in order to etch the surface and allow the investigation of deeper layers. The sample was etched for 40 seconds/cycle, and a total of 60 cycles was performed, assuring the etching until reach the substrate.

2. Scanning Electron Microscopy (SEM)

Currently being one of the most important techniques to the topographical investigation of a material, the basis of the electron microscopy dates at the end of the 1920s, with Busch's studies concerning the trajectory of charged particles in electric and magnetic fields, and de Broglie's research with the definition of the where-particle duality. However, it was only almost 20 years later, in 1942, that Zworykin, a Russian engineer, developed the first SEM. This microscope, the first to use secondary electrons for the investigation of the analyzed topography, reached a maximum resolution of 50 nanometers[13].

SEM is based on the principle of interaction of the material surface with a beam of primary electrons, which, as they impinge on the surface, are converted into different energy forms, e.g. secondary electrons, backscattered electrons and X-ray, which are used for different analyses[14]. Figure 5 below schematizes the process described above, highlighting the depth of emission of each type of energy.

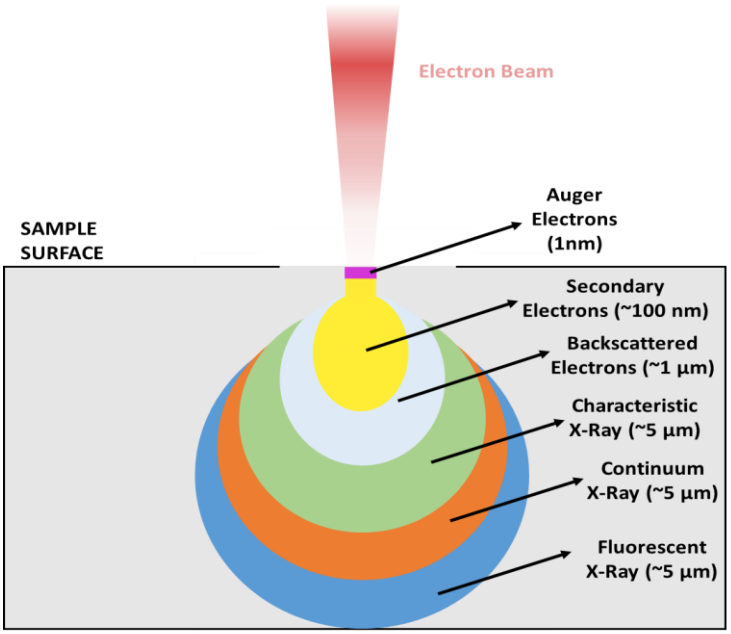

Figure 5: Electron bean conversion after the contact with the surface, indication the created energy and its depth.

The SEM image is formed from secondary and backscattered electrons. Once the primary electron beam hits the surface, secondary electrons (SE) are formed at relatively high energy, but in order to create a pair, they share their energy with another electron of the material, this being of low energy level, thus forming 2 low energy SEs. This process keeps repeating itself successively over the entire surface, in a process called "cascade". These low energy SEs are then finally attracted by an electron collector attached to the machine and transformed into a topographic image of the surface of the analyzed material[15].

Backscattered electrons, meanwhile, lose less energy than secondary electrons and have a greater depth than previous electrons. Once emitted, they are deflected into the main beam and collected by a collector. These are used to distinguish ranges of elements with different atomic numbers. Heavier elements, i.e. with higher atomic numbers emit more backscattered electrons and appear brighter than elements with lower atomic numbers[16].

As explained, for SEM analysis, the material needs to be conductive, thus allowing the diffusion of electrons on its surface. Therefore, insulating materials and/or materials with a high non-conductive character, as is the case of lignin, must be submitted to a previous preparation to become conductive. This is usually done by applying a thin metallic layer over the material, usually by sputtering.

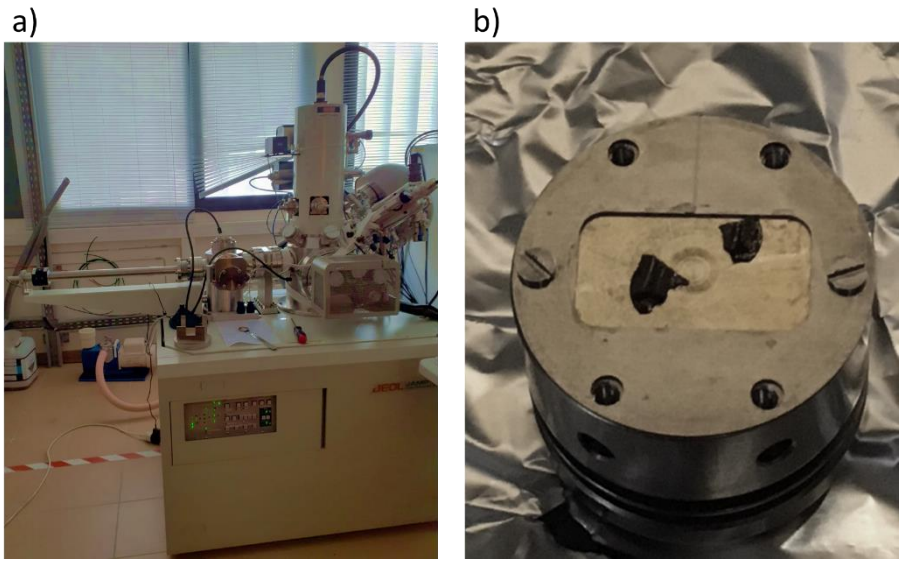

Figure 6: SEM instrument used for the images obtention of this thesis.

Before been inserted in the SEM equipment (Figure 6 a)), a JEOL JAMP-9500F Field Emission dual Auger-SEM Microprobe equipment under ultrahigh vacuum (10^{-8} mbar), the lignin was coated with a thin layer of gold generated from a DESK V (Denton Vacuum) metallizer for 1 minute at 50 mA. After that, the samples were glued on the sample holder with a 20 mm diameter carbon tape (Figure 6 b)) and finally inserted into the machine. For image acquisition, the equipment was operated at 30 kV and 5 nA. All other analyzed materials followed the same methodology and conditions, except for the metallization step.

3. Attenuated Total Reflection - Fourier Transform Infrared Spectroscopy (ATR -FTIR)

Widely used for the evaluation of chemical composition (from the types of bonds in the material), the origin of FTIR spectroscopy dates back to 1900, when Michelson invented the first interferometer in 1880 and Rayleigh, in 1892, theorized and proposed the possibility of converting the interference patterns produced by Michelson's apparatus into real spectra to be analyzed. However, only almost 80 years later the first industrially capable FTIR was manufactured, expanding the use of this technique[17].

The working principle of this Infrared Spectroscopy is based on the interaction infrared (IR) radiation and material. Once emitted onto the material to be analyzed, the IR radiation stimulates the atoms to start vibrating around their bonds, while the entire molecule performs a continuous translation and rotation movement[18,19].

The FTIR technique will take this vibrational concept in incorporate in a specific equipment arrangement, with the use of an interferometer with the Fourier Transformation mathematical approach, allowing a fast

spectrum creation. Finally, the ATR methodology will facilitate the analysis due to the non-necessity of a previous sample preparation, allowing the analysis a solid product. A crystal with a high refractive index will be placed in the equipment, making that a great number of internal reflections occurs before the laser leaves the crystal to the sample, increasing its analysis capacity[20].

The FTIR analysis were performed both at IPREM – UPPA France and UFRJ Laboratory of Surfaces and Thin Films – Brazil, for the obtention of both pure lignin and coatings chemical composition. The equipment was a Nicolet Spectrometer model 6700 (Thermo Scientific) in ATR mode. The coatings were removed from the substrate by scraping and collected as a powder, then fixed on the crystal for analysis and analyzed. The totality of the spectra was acquired in transmittance mode, in a range of 600 cm^{-1} to 4000 cm^{-1} in the transmittance mode, 64 scans were performed with a step of 2 cm^{-1} and resolution of 4 cm^{-1}.

4. Water Contact Angle (WCA)

The WCA is a common analysis used to determine the degree of hydrophobicity from a material. Its principle is based on two main concepts, the surface tension and the wettability. The first, is the force opposing the creation of a new surface, the inverse of the surface energy, which is defined as the required energy to create a new unit of surface area on the material. On the other hand, the wettability is the ability of a liquid phase to spread over the surface of the solid it interfaces with and will be measured by the Contact Angle[21].

Contact Angle (θ) is the evaluation of the angle that is formed between the boundary of the liquid and solid phases and is defined by Young's equation[22]:

$$\cos\theta = \frac{\gamma_{SA} - \gamma_{SL}}{\gamma_{LA}} \qquad \text{Equation 12}$$

Where: γ_{SA}, γ_{SL} and γ_{LA} are the surface tension between solid-air, solid-liquid and liquid-air phases, respectively.

The experimental procedure was divided in two phases, the first one at UPPA - France, was done on a Teclis Scientific Tracker Automatic Drop tensiometer. No prior preparation was necessary, consisting directly in placing the Al 2024 (pure and coated) on the machine sample base and depositing the water drop on it. The volume of the water droplet was kept 3 µL for all measurements at 25°C and for an acquisition time of 5 minutes. The acquisition software provided the results and assured the correct volume.

In the second phase, the samples coated with the hybrid coating and the plasma film were analyzed in the UFRJ Laboratory of Surfaces and Thin Films – Brazil, in a A-100 NRL goniometer from Ramé-Hart. The drop temperature and volume used were exactly the same as above, but 8 different points on the surface were investigated, with each acquisition lasting 2 minutes. The acquisition software provided the results and assured the correct volume.

5. Dynamic Laser Scattering (DLS)

Used to verify that the kraft lignin was completely solubilized after the solubility tests (experiments and results will be discussed in the next chapters), this technique is based on the use of a monochromatic beam, which is incident on a solution containing dispersed macromolecules. The light is then scattered in all directions, depending on the size and shape of the macromolecules. In static light scattering, the method used in this work, the intensity of the scattered light is analyzed as a time-averaged intensity, which provides useful information about the molecular weight and radius of gyration of the macromolecules[23].

Specifically in this work, the technique was used to check whether particles were still present even after apparent solubilization. This process consists of positioning the container containing the solution between the equipment, a Batch-mode Dynamic Light Scattering (DLS) analyses were performed using a VASCO-2 particle size analyzer (Cordouan Technology, France) equipped with a 65 mW laser (657 nm wavelength). The sample-laser distance was 8 cm. Afterwards the spectrum was obtained with the software nanoQ v 6.2.2 and analyzed. The Figure 7 below illustrates the experimental arrange.

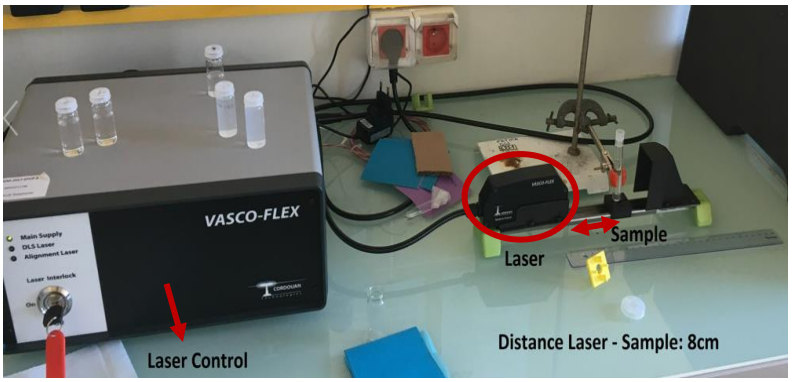

Figure 7: Schematic arrange of DLS measure.

6. Optical Profilometry: Roughness and Thickness Evaluation

Used to determine the roughness of pure Al 2024 substrate and after coating, optical profilometry is a simple and non-destructive method. A light source is used to scan the surface of the sample and the beam diffracted by the surface roughness is collected on a mirror. The resulting image is the deflection of the beam on the mirror. Using this technique, roughness can be estimated down to the nanometer range[24].

A Micromesure CHR150 profilometer (STIL Society), providing 2D and 3D profiles, equipped with a high-resolution sensor that allows measurements until nanometric scales was used. The data was acquired in the SurfaceMap Software and then the results treated by the software MountainsMap®Scanning Topography 7.4.9391, that provided the root main square height (Sq) following ISO 25178 standard. Five different points over each surface were analyzed and the result considered is the average of them all.

References

1. The International XPS Database. The History of XPS, Available Online. https://xpslibrary.com/history-of-xps/
2. Siegbahn, K. (1982). Electron Spectroscopy for Atoms, Molecules, and Condensed Matter. Science, 217(4555), 111–121. http://www.jstor.org/stable/1689700
3. Stevie, F. A., & Donley, C. L. (2020). Introduction to x-ray photoelectron spectroscopy. Journal of Vacuum Science & Technology A, 38(6), 063204. https://doi.org/10.1116/6.0000412
4. Moulder, J. F., Stickle, W. F., Sobol, W. M., & Bomben, K. D. (1992). Handbook of X-Ray Photoelectron Spectroscop27y: A Reference Book of Standard Spectra for Identification and Interpretation of Xps Data.
5. Guy Hollinger. (1986). Spectroscopies de photoélectrons: XPS ou ESCA et UPS. Techniques de l'Ingénieur, 33(0).
6. Tanuma, S., Powell, C. J., & Penn, D. R. (2003). Calculation of electron inelastic mean free paths (IMFPs) VII. Reliability of the TPP-2M IMFP predictive equation. *Surface and Interface Analysis*, *35*(3), 268–275. https://doi.org/10.1002/sia.1526
7. Charles Kittel, H. K. (1980). *Thermal physics* (W.H.Freeman & Co Ltd (ed.); 2nd ed.).
8. Roberts, F. S., Anderson, S. L., Reber, A. C., & Khanna, S. N. (2015). Initial and Final State Effects in the Ultraviolet and X-ray Photoelectron Spectroscopy (UPS and XPS) of Size-Selected Pdn Clusters Supported on TiO2(110). The Journal of Physical Chemistry C, 119(11), 6033–6046. https://doi.org/10.1021/jp512263w
9. Köhler, L., & Kresse, G. (2004). Density functional study of CO on Rh(111). Phys. Rev. B, 70(16), 165405. https://doi.org/10.1103/PhysRevB.70.165405
10. Bañuls-Ciscar, J., Pratelli, D., Abel, M. L., & Watts, J. F. (2016). Surface characterisation of pine wood by XPS. *Surface and Interface Analysis*, *48*(7), 589–592. https://doi.org/10.1002/sia.5960
11. Bañuls-Ciscar, J., Abel, M.-L., & Watts, J. F. (2016). Characterisation of cellulose and hardwood organosolv lignin reference materials by XPS. *Surface Science Spectra*, *23*(1), 1–8. https://doi.org/10.1116/1.4943099
12. Flores-Mancera, M. A.; Villarrubia, J. S.; Massillon-Jl, G. Electron Inelastic Mean Free Paths for LiF, CaF2, Al2O3, and Liquid Water from 433 KeV down to the Energy Gap. ACS Omega 2020, 5 (8), 4139–4147. https://doi.org/10.1021/acsomega.9b03872.
13. Bogner, A., Jouneau, P.-H., Thollet, G., Basset, D., & Gauthier, C. (2007). A history of scanning electron microscopy developments: Towards "wet-STEM" imaging. *Micron*, *38*(4), 390–401. https://doi.org/https://doi.org/10.1016/j.micron.2006.06.008
14. Watts, J.F. and Wolstenholme, J. (2003). Electron Spectroscopy: Some Basic Concepts. In An Introduction to Surface Analysis by XPS and AES (pp. 1–15). https://doi.org/https://doi.org/10.1002/0470867930.ch1
15. Joy, C., & Joy, D. C. (1991). The theory and practice of high-resolution scanning electron microscopy. *Ultramicroscopy*, *37*(1), 216–233. https://doi.org/https://doi.org/10.1016/0304-3991(91)90020-7
16. McCall, J. L., Mueller, W. M., Society, I. M., Metals, A. S. of for, ASM, Metals, A. S. of for, & A.S.M. (1973). *Microstructural analysis tools and techniques* (1st ed. 19). New York. https://doi.org/10.1007/978-1-4615-8693-7

17. Subramanian, A., & Rodriguez-saona, L. (2009). *Chapter 7 - Fourier Transform Infrared (FTIR) Spectroscopy* (D.-W. B. T.-I. S. for F. Q. A. and C. Sun (ed.); pp. 145–178). Academic Press. https://doi.org/https://doi.org/10.1016/B978-0-12-374136-3.00007-9
18. El - Azazy, M., & Access, O. (2018). Introductory Chapter: Infrared Spectroscopy - A Synopsis of the Fundamentals and Applications. https://doi.org/10.5772/intechopen.82210
19. Ismail, A. A., van de Voort, F. R., & Sedman, J. (1997). Chapter 4 Fourier transform infrared spectroscopy: Principles and applications. In J. R. J. Paré & J. M. R. B. T.-T. and I. in A. C. Bélanger (Eds.), *Instrumental Methods in Food Analysis* (Vol. 18, pp. 93–139). Elsevier. https://doi.org/https://doi.org/10.1016/S0167-9244(97)80013-3
20. Larkin, P. J. (2018). Chapter 3 - Instrumentation and Sampling Methods (P. J. B. T.-I. and R. S. (Second E. Larkin (ed.); pp. 29–61). Elsevier. https://doi.org/https://doi.org/10.1016/B978-0-12-804162-8.00003-3
21. Kohli, R. (2012). Chapter 3 - Methods for Monitoring and Measuring Cleanliness of Surfaces (R. Kohli & K. L. B. T.-D. in S. C. and C. Mittal (eds.); pp. 107–178). William Andrew Publishing. https://doi.org/https://doi.org/10.1016/B978-1-4377-7883-0.00003-1
22. Gao, L., & McCarthy, T. J. (2006). Contact Angle Hysteresis Explained. Langmuir, 22(14), 6234–6237. https://doi.org/10.1021/la060254j
23. Stetefeld, J., Mckenna, S. A., & Patel, T. R. (2016). Dynamic light scattering : a practical guide and applications in biomedical sciences. Biophysical Reviews, 409–427. https://doi.org/10.1007/s12551-016-0218-6
24. Mabilleau, G., & Sabokbar, A. (2008). 7 - In vitro biological test methods to evaluate bioresorbability. In F. B. T.-D. R. of B. M. Buchanan (Ed.), *Woodhead Publishing Series in Biomaterials* (pp. 145–160). Woodhead Publishing. https://doi.org/https://doi.org/10.1533/9781845695033.3.145

Resumé

Dans le contexte actuel des développements technologiques anticorrosion du secteur aéronautique, de nouvelles alternatives aux revêtements classiques à base de chrome hexavalent sont étudiées et se veulent plus éco-durables, comme attendu par la législation Européenne REACH. Une nouvelle approche de la protection des alliages d'aluminium 2024 a été engagée avec l'élaboration d'un revêtement hybride innovant combinant une matrice de silice interconnectée avec de la lignine kraft telle que celle extraite de la Forêt des Landes de Gascogne.

Bien qu'elle soit le deuxième biopolymère le plus abondant sur Terre et qu'elle ait une structure moléculaire riche la lignine est malheureusement peu utilisée dans des applications à haute valeur ajoutée technologique ; elle a en effet pour principal usage, celui d'être une source de chaleur et d'énergie par simple combustion.

Dans ce travail de thèse, la conception du bio revêtement s'appuie sur l'auto-organisation naturelle des phases en présence permise par la technique de "Evaporation Induced Self-Assembly (EISA)". Le procédé ne nécessite aucun apport d'énergie externe pour s'activer et se développer et s'inscrit dans une démarche environnementale. Le mélange bio ressource/agent silicique est appliqué sur le substrat par la méthode du Dip-Coating, simple à mettre en œuvre, dans laquelle des paramètres importants comme l'humidité relative (HR) et la vitesse de retrait ont été optimisés. Le processus de protection de l'alliage a ensuite été renforcé par un post-traitement de plasma SF6 de la surface du revêtement. Dans ces conditions, il a été observé une très nette augmentation de l'hydrophobicité des matériaux élaborés en adéquation avec les objectifs scientifiques attendus.

Techniquement, deux voies différentes de préparation des revêtements ont été évaluées dans ce travail : une voie dite « directe » (DR) et une voie dite « non directe » (NDR), dans laquelle une fonctionnalisation préalable de la surface du substrat métallique à protéger a été effectuée avec un agent organo-alcoolique, le TESPSA. Les résultats ont montré que les revêtements « non directs » présentaient une couverture plus homogène à la surface de l'alliage Al2024 et que leur hydrophobicité était naturellement bien plus importante que celle des revêtements « directs ». Dans la continuité de ces observations, les caractérisations physico-chimiques SEM et XPS ont mis en lumière la tendance de la lignine à s'organiser sur la phase silicique, jouant très certainement un rôle majeur dans la protection finale. Par ailleurs, les bilans montrent qu'il semble opportun de réaliser les dépôts avec des vitesses de retrait des bains plus lentes tout en opérant dans un environnement plutôt sec (Humidité Relative autour de 10%). Ces conditions assureraient en effet une meilleure homogénéité des revêtements, réduisant également sensiblement leur mouillabilité et les rendant plus épais, soient des exigences attendues par les certifications de l'industrie aéronautique. Pour les matériaux élaborés, les tests d'adhésion réalisés ont indiqué un bon degré d'adhésion sur l'alliage d'aluminium.

Finalement, des essais de corrosion ont été menés pour tester le comportement des revêtements hybrides (mesures électrochimiques et tests de brouillard salin). Ces premières études se sont révélées prometteuses puisque la couche de protection optimisée (NDR/vitesse de retrait : 0,05mm.s-1/HR 10%) a résisté 48h sans aucune piqûre de corrosion confirmant le très faible courant de corrosion mesurée. Le post-traitement de plasma SF6 appliqué sur les revêtements a pour sa part multiplié le caractère hydrophobe de ces derniers avec des angles de contact d'environ 95 degrés pour les revêtements DR et d'environ 105 degrés pour les revêtements NDR.

Abstract

In the current context of anti-corrosion technological developments in the aeronautical sector, new alternatives to the traditional Cr VI -based coatings are being studied and are intended to be more eco-sustainable, as required by the European REACH legislation. A new approach to the protection of 2024 aluminum alloys has been initiated with the development of an innovative hybrid coating combining an interconnected silica matrix with kraft lignin, such as that extracted from the Landes de Gascogne Forest.

Although it is the second most abundant biopolymer on Earth and has a rich molecular structure, lignin is unfortunately little used in high value-added technological applications; indeed, its main use is as a source of heat and energy by simple combustion.

In this thesis, the design of the bio-coating is based on the natural self-organization of the phases in presence allowed by the technique of "Evaporation Induced Self-Assembly (EISA)". The process does not require any external energy to activate and develop and is environmentally friendly. The bio-resource/silica mixture is applied to the substrate using the easy-to-implement Dip Coating method, in which important parameters such as relative humidity (RH) and shrinkage rate have been optimized. The alloy protection process was then enhanced by SF_6 plasma post-treatment of the coating surface. Under these conditions, it was observed a clear increase of the hydrophobicity of the elaborated materials in adequacy with the expected scientific objectives.

Technically, two different ways of preparation of the coatings were evaluated in this work: a way called "direct" (DR) and a way called "non direct" (NDR), in which a preliminary functionalization of the surface of the metallic substrate to be protected was carried out with an organo-alcoholic agent, the TESPSA. The results showed that the NDR coatings presented a more homogeneous coverage on the surface of the Al2024 alloy and that their hydrophobicity was naturally much higher than that of the DR ones. In the continuity of these observations, the physico-chemical characterizations SEM and XPS highlighted the tendency of the lignin to organize itself onto the silicic phase, playing certainly a key role in the final protection. Moreover, the results show that it seems appropriate to carry out the deposits with slower speeds of withdrawal of the baths while operating in a rather dry environment (Relative Humidity around 10%). These conditions would indeed ensure a better homogeneity of the coatings, also significantly reducing their wettability and making them thicker, which are the requirements expected by the aeronautical industry certifications.

Finally, corrosion tests were performed to evaluate the behavior of the hybrid coatings (electrochemical measurements and salt spray tests). These first studies proved to be promising since the optimized protective layer (NDR/shrinkage rate: 0.05mm.s-1/HR 10%) resisted 48h without any corrosion pitting confirming the very low corrosion current measured.

The SF_6 plasma post-treatment applied on the coatings has multiplied their hydrophobic character with contact angles of about 95 degrees for DR coatings and about 105 degrees for NDR coatings. These important evolutions open a large field of perspectives for the protection of metallic parts in the Aeronautics industry by associating future technologies to the valorization of bio resources.

ECOLE DOCTORALE :

ECOLE DOCTORALE :
Sciences Exactes et leurs Applications

LABORATOIRE :
IPREM